



**UNIVERSITAT
JAUME I**

Doctoral Program in Sciences

Doctoral School of the Universitat Jaume I

**Solid-State Hosts Based on Fluorides with Europium:
From the Crystal Structure toward the Optical
Performance**

Report submitted by Pablo Serna Gallén in order to be eligible for a

Doctoral Degree awarded by the Universitat Jaume I

International Doctorate Distinction

Doctoral Candidate

Pablo Serna Gallén

Director and Tutor

Eloísa Cordoncillo Cordoncillo

Co-director

Héctor Beltrán Mir

Castelló de la Plana, December 2023

Funding

The present Doctoral Thesis has been carried out thanks to the award of a predoctoral contract for the *Formation of University Professors (Formación de Profesorado Universitario, FPU, FPU18/04511*; score obtained: 81.2/100, maximum score in the area of Chemistry) granted by the Spanish Ministry of Science and Innovation (MCIN) and funded by MCIN/AEI /10.13039/501100011033 and by “ESF Investing in your future”.

It was also possible to make an international research stay thanks to the FPU subprogram of the MCIN *Complementary grants for beneficiaries of FPU contracts: short stays and temporary mobilities (EST22/00090*; score obtained: 100/100). The research stay was conducted from 12/09/2022 to 11/12/2022 at the University of Aveiro (Portugal) in the Department of Physics under the supervision of professor Luís D. Carlos.

The research activity has been supported financially by the Spanish Ministry of Economy and Competitiveness (Project MAT2016-80410-P), the Spanish MCIN (Grant PID2020-116149GB-I00 funded by MCIN/AEI/10.13039/501100011033) and the Universitat Jaume I (Project UJI-B2019-41).

Creative Commons License



Attribution-ShareAlike CC BY-SA

Publications

Thesis by compendium of the following publications:

- 1 Title:** **Tuning the optical and photoluminescence properties of high efficient Eu³⁺-doped KY₃F₁₀ phosphors by different synthetic approaches**

Authors: P. Serna-Gallén, H. Beltrán-Mir, E. Cordoncillo

Citation: Optics & Laser Technology, 136 (2021) 106734.
<https://doi.org/10.1016/j.optlastec.2020.106734>

IF: 4.939 (Q1)
- 2 Title:** **Unraveling the superior role of dicarboxylic acids as surface chelators in Eu³⁺-doped yttrium fluorides: A systematic modulation of the crystal phases and morphologies for highly tuned optical performance**

Authors: P. Serna-Gallén, H. Beltrán-Mir, E. Cordoncillo

Citation: Journal of Alloys and Compounds, 883 (2021) 160847.
<https://doi.org/10.1016/j.jallcom.2021.160847>

IF: 6.371 (Q1)
- 3 Title:** **The unexplored δ -phase of KY₃F₁₀: Toward novel Eu³⁺-doped nanoplates with a ‘super-diamond’ structure for optical applications**

Authors: P. Serna-Gallén, H. Beltrán-Mir, E. Cordoncillo

Citation: Journal of Materials Research and Technology, 15 (2021) 6940–6946. <https://doi.org/10.1016/j.jmrt.2021.11.060>

IF: 6.267 (Q1)
- 4 Title:** **The pH-dependent reactions in the sonochemical synthesis of luminescent fluorides: the quest for the formation of KY₃F₁₀ crystal phases**

Authors: P. Serna-Gallén, H. Beltrán-Mir, E. Cordoncillo

Citation: Ultrasonics Sonochemistry, 87 (2022) 106059.
<https://doi.org/10.1016/j.ultsonch.2022.106059>

IF: 8.4 (Q1)

- 5 **Title:** A site-selective fluorescence spectroscopy study of the crystal phases of KY_3F_{10} : leveraging the optical response of Eu^{3+} ions
Authors: P. Serna-Gallén, H. Beltrán-Mir, E. Cordoncillo, R. Balda, J. Fernández
Citation: Journal of Alloys and Compounds, 953 (2023) 170020.
<https://doi.org/10.1016/j.jallcom.2023.170020>
IF: 6.2 (Q1)
- 6 **Title:** Kinetics or thermodynamics? Extolling their role to modulate the crystal phases and luminescence of $\text{KY}_3\text{F}_{10}:\text{Eu}^{3+}$ powders
Authors: P. Serna-Gallén, H. Beltrán-Mir, E. Cordoncillo
Citation: CrystEngComm, 25 (2023) 5918–5931.
<https://doi.org/10.1039/D3CE00614J>
IF: 3.1 (Q1)
- 7 **Title:** Practical guidance for easily interpreting the emission and physicochemical parameters of Eu^{3+} in solid-state hosts
Authors: P. Serna-Gallén, H. Beltrán-Mir, E. Cordoncillo
Citation: Ceramics International (2023)
<https://doi.org/10.1016/j.ceramint.2023.01.141>
IF: 5.2 (Q1)

This Thesis has been accepted by the co-authors of the publications listed above that have waved the right to present them as a part of another Ph.D. Thesis.

Additional publications

During the development of this Thesis the following additional researches (including also of academic character) have been published:

- Title:** Site-selective symmetries of Eu³⁺-doped BaTiO₃ ceramics: a structural elucidation by optical spectroscopy

Authors: P. Serna-Gallén, H. Beltrán-Mir, E. Cordoncillo, A. R. West, R. Balda, J. Fernández

Citation: Journal of Materials Chemistry C, 7 (2019) 13976–13985.
<https://doi.org/10.1039/C9TC03987B>

IF: 7.059 (Q1)
- Title:** A way to understand the solid-state chemistry for high level education students: the case of a ceramic pigment

Authors: S. Torresi, A. Bou-Gil, P. Escámez-Gutiérrez, N. Peña-Recuenco, S. Chouli, P. Serna-Gallén, H. Beltrán-Mir, E. Cordoncillo

Citation: EDULEARN20 Proceedings, (2020) 974–981. ISBN: 978-84-09-17979-4
- Title:** A new series of environment-friendly reddish inorganic pigments based on AFeO₃ (A = Ln, Y) with high NIR solar reflectance

Authors: M. Fortuño-Morte, P. Serna-Gallén, H. Beltrán-Mir, E. Cordoncillo

Citation: Journal of Materiomics, 7(5) (2021) 1061–1073.
<https://doi.org/10.1016/j.jmat.2021.02.002>

IF: 8.589 (Q1)
- Title:** The influence of Ca²⁺ and Zn²⁺ doping on the development of sustainable pigments based on GdFeO₃ perovskite: From a reddish colour towards a pure black

Authors: M. Fortuño-Morte, P. Serna-Gallén, H. Beltrán-Mir, E. Cordoncillo

Citation: Ceramics International, 48(15) (2022) 21469–21478.
<https://doi.org/10.1016/j.ceramint.2022.04.111>

IF: 5.2 (Q1)

- 5 **Title:** “MasterChemist”: A Novel Strategy for Reviewing Stoichiometry and Introducing Molecular Gastronomy to Chemistry Students
- Authors:** P. Serna-Gallén, M. Fortuño-Morte, H. Beltrán-Mir, E. Cordoncillo
- Citation:** Journal of Chemical Education, 99(10) (2022) 3443–3451.
<https://doi.org/10.1021/acs.jchemed.2c00250>
- IF:** 3.0 (Q2)

Conferences

Some of the main results of this Thesis have been presented in several conferences of national and international relevance:

- Title:** **Development of synthetic routes and their influence on the optical properties of Eu³⁺-doped KY₃F₁₀ materials**

Authors: P. Serna-Gallén, H. Beltrán-Mir, E. Cordoncillo

Contribution: Poster

Conference: Photoptics 2021 (9th International Conference on Photonics, Optics and Laser Technology). Online streaming (2021)
- Title:** **Employing dicarboxylic acids in the KF-YF₃ system to modulate the crystal phase and optical response of Eu³⁺-doped materials**

Authors: P. Serna-Gallén, H. Beltrán-Mir, E. Cordoncillo

Contribution: Oral

Conference: 3rd Advanced Materials Science World Congress. Online streaming (2022)
- Title:** **New avenues in the formation of luminescent fluorides prepared by sonochemical approaches**

Authors: P. Serna-Gallén, H. Beltrán-Mir, E. Cordoncillo

Contribution: Poster

Conference: XXXVIII Reunión Bienal de la Sociedad Española de Química (RSEQ). Granada, Spain (2022)
- Title:** **Crucial and innovative strategies to obtain the KY₃F₁₀ crystal phases and related fluorides for photoluminescence applications**

Authors: P. Serna-Gallén, H. Beltrán-Mir, E. Cordoncillo

Contribution: Oral

Conference: XXX Simposio del Grupo Especializado de Cristalografía y Crecimiento Cristalino (GE3C). Benidorm, Spain (2023)

- 5 **Title:** **Intriguing solid-state hosts based on yttrium complex fluorides for photoluminescence**
- Authors:** P. Serna-Gallén
- Contribution:** Oral
- Conference:** International Workshop “Multifunctional Materials: From Basic Research to the Development of New Technologies”. Castelló, Spain (2023)
-
- 6 **Title:** **Chemical pressure driving phase transition and morphology in Eu³⁺-doped KY₃F₁₀: An experimental and theoretical insight**
- Authors:** P. Serna-Gallén, S.C.S. Lemos, L. Gracia, E. O. Gomes, H. Beltrán-Mir, E. Cordoncillo, J. Andrés
- Contribution:** Oral
- Conference:** 18th European Conference on Solid State Chemistry. Prague, Czech Republic (2023)
-
- 7 **Title:** **Fluorescence line narrowing as a powerful tool to unveil the Eu³⁺ crystal symmetries in mixed oxides**
- Authors:** P. Serna-Gallén, H. Beltrán-Mir, E. Cordoncillo, R. Balda, J. Fernández
- Contribution:** Oral
- Conference:** 8th International Sol-Gel Society Workshop (SUSGEM 2023). Castelló, Spain (2023)

Additional conferences

It has also been possible to contribute in other conferences with scientific collaborations or being a panelist in high-relevance events:

- Title:** **Los lantánidos: una alternativa para el desarrollo de pigmentos cerámicos multifuncionales**

Authors: M. Fortuño-Morte, P. Serna-Gallén, H. Beltrán-Mir, E. Cordoncillo

Contribution: Oral

Conference: LVII Congreso Nacional de Cerámica y Vidrio. Castelló, Spain (2020)
- Title:** **Desarrollo de pigmentos negros sostenibles con elevada reflectancia NIR basados en la perovskita $GdFeO_3$ dopada con Ca^{2+} y Zn^{2+}**

Authors: M. Fortuño-Morte, P. Serna-Gallén, H. Beltrán-Mir, E. Cordoncillo

Contribution: Poster

Conference: QIES22 (XIX Reunión del Grupo Especializado de Química Inorgánica, XIII Reunión del Grupo Especializado de Química de Estado Sólido). Sevilla, Spain (2022)
- Title:** **Novel reddish ‘cool pigments’ based on $AFeO_3$ ($A = Ln, Y$)**

Authors: M. Fortuño-Morte, P. Serna-Gallén, H. Beltrán-Mir, E. Cordoncillo

Contribution: Oral

Conference: 4th International Conference on Material Science & Nanotechnology (ICMSN 2022). Online streaming (2022)
- Title:** **Future and social responsibility of chemistry: the view of the young generation**

Authors: Bert Meijer (Chair), Alena Budinska, Thomas Ebbesen, Yamuna Krishnan, Pablo Serna Gallén, Hennie Valkenier

Contribution: Panelist

Conference: 100th Anniversary of the First Solvay Conference on Chemistry. Brussels, Belgium (2022)

- 5 **Title:** **Química y nuevas competencias profesionales ante el Pacto Verde Europeo**
Authors: Carlos Negro (Chair), M^a Carmen Cruzado, Pablo Serna Gallén, M^a Isabel Fernández, Salvador Viera
Contribution: Panelist
Conference: Smart Chemistry Smart Future: Green Deal Edition (Expoquimia). Barcelona, Spain (2023)
- 6 **Title:** **Matèries primes i economia circular**
Authors: María Dolores Parra (Chair), Antonio Gallardo, Pablo Serna Gallén, Jose Planas, Jordi Llop, Luis Oria, Sergio Chiva
Contribution: Panelist
Conference: Fira Científica, Tecnològica i d'Innovació: Destaca en Ruta. L'Alcora, Spain (2023)
- 7 **Title:** **Homenatge a Fernando Latre. De la química a la societat**
Authors: Pablo Serna Gallén, Juan Hernández, Vicente Blasco, José Usó, Vicente Doménech
Contribution: Chair
Conference: Fira Científica, Tecnològica i d'Innovació: Destaca en Ruta. L'Alcora, Spain (2023)

Achievements

Apart from the research tasks of the Thesis, the scientific formation has been complemented with other activities focused on the development of leadership, innovation, dissemination, or academic excellence skills. Accordingly, several achievements have been obtained, among which is of relevance highlighting the selection as one of the 21 Europe's outstanding Ph.D. students by Cefic (European Chemical Industry Council) with the support of Feique (Federación Empresarial de la Industria Química Española). Thus, it allowed me to be the Spanish representative in the *Honour Science & Chemistry* event held in Brussels on May 30, 2022, and to continue the collaboration with Cefic during the whole year. Further details can be found in Appendix 3.

- 1 Vice president of the Chemists Association of the Valencian Community**
Start Year: 2023
- 2 Delegate in Castellón of the Official Chemists College of the Valencian Community**
Start Year: 2022
- 3 Spanish representative in the European *Honour Science & Chemistry Event* held in Brussels on May 30. Organized by Cefic**
Year: 2022
- 4 Member of the Governing Board of the Official Chemists College of the Valencian Community**
Start Year: 2020
- 5 Coordinator of the Technical Research Section of the Chemists Association of the Valencian Community**
Start Year: 2021
- 6 Full member of the Spanish Society of Academic Excellence (SEDEA)**
Start Year: 2021

- 7 **Member of the Centre Board of the School of Technology and Experimental Sciences (ESTCE) of the Univesitat Jaume I**
Start Year: 2022
- 8 **Member of the Governing Council of the Department of Inorganic and Organic Chemistry of the Univesitat Jaume I**
Start Year: 2019
- 9 **Jury of the “Literary Prize in Valencian of Scientific and Technological Divulagation of the School of Technology and Experimental Sciences (ESTCE)”**
Editions: 2019, 2020, 2021
- 10 **Jury of the “Crystallization at School” Contest of the Valencian Community**
Edition: 2022
- 11 **Organization committee of the XXX Simposio del Grupo Especializado de Cristalografía y Crecimiento Cristalino (GE3C)**
Year: 2023
- 12 **Organization committee of the Chemistry Olympiad in the Valencian Community**
Year: 2023
- 13 **Local organization committee of the XXXVI Spanish National Chemistry Olympiad**
Year: 2023
- 14 **Preselection jury of the “Women in Chemistry” National Contest, 1st edition**
Edition: 2023
- 15 **Member of the Educational Innovation Group on Solid Inorganic Materials**
Start Year: 2021
- 16 **Contribution of 7 patterns to the Powder Diffraction File-Release 2024 of the International Centre for Diffraction Data (ICDD)**
Year: 2023

Preface

Being embarked on the crazy adventure of a Ph.D. cannot be summarized in a few paragraphs. However, I would like to start the opening of this Thesis with a small preface that only intends to compile some of the perspectives that I have got time to develop during this period. Thus, only pay attention to the *true* meaning of the abbreviation Ph.D., Doctor of Philosophy, which transcends more than three simple letters to be added in the C.V.

I do remember that some years ago I was labeled “an alchemist of the letters” during an interview about scientific dissemination. And I could not agree more with this assertion because I strongly believe that *true alchemists do not change lead into gold; they change the world into words* (William H. Gass).

These brief comments lead me to the conclusion that for being at the cutting edge of science, being an innovator is by far something more than obvious. Over time, history has witnessed several periods where creativity shed light on the perceptions toward not only such incipient glimpses of science but also toward arts, literature, culture, and even the economy. Would not it be for the thinking of the Renaissance, the Enlightenment, the passion for opening up new paths and finding ways to cut through the biases of the precedent epochs, we, and what we now know as science, would not be the same.

Sir Isaac Newton, Robert Boyle, Paracelsus... all of them were alchemists. But does it mean that they were in pursuit of the philosopher’s stone, as perhaps it might be thought after reading the word *alchemy*? Absolutely not, they just were ahead of their time, thinking out of the box, trying to apply chemistry, physics, medicine... to solve

problems: and this is the main objective of the research.

At this point, I would like to take the humble privilege of saying that we must be the *Da Vincis* of the XXI century. The discoveries must break the actual rules of science, they have to culminate in theories inconceivable, a priori. Only by doing this, our society will be prepared to improve and overcome some of the current problems in particular fields. And for that purpose, the next generation of scientists is committed to being innovative, creative; to be the *artists* that play on the stage in this scenario.

Such a conception is closely linked to some common literary topics, like *Beatus ille* or *Locus amoenus*, that try to extol the virtues of nature and its direct connection with life. It is known that human beings established the first scientific theories based on the contemplation of nature and the processes involved in different phenomena. If not, just think about the *Physis* of the philosopher Aristotle. *Nature must be the foundation and model of science; thus, Art works according to Nature in everything it can. Therefore, it is necessary that the Artist follows Nature and operates according to her* (St. Albertus Magnus).

Interdisciplinarity in science is something to which we are used to; however, broadening our minds to fields apparently far away from our profession, as the above-mentioned scientists made, will be the conjunction to become the new *Da Vincis* and coin (not only in gold) the new meaning for the word *alchemy*. We have to adapt our perspectives, but it will only require a shred of fruitful imagination and a lot of passion since *if you are an alchemist, make gold of that* (William Shakespeare).

The major advantage that we can have in this long journey of inspiration is to know our weaknesses, be aware of them, and deal with any concerns we might have that leave us with the worst of fears. Complicate, though, *happiness can be found, even in*

the darkest of times, if one only remembers to turn on the light (Albus Dumbledore).

First and foremost, we are researchers, then, *cerca trova*.

Acknowledgments

This Doctoral Thesis represents, as could not be otherwise, the harmonious and peculiar connection created among science, researchers, and many people that I have to acknowledge from the very first moment that I was embarked on the adventure of being a Chemist. All of them have fondly contributed to my personal evolution of becoming a science-minded researcher with a solid-principle perspective and a thankful soul. As we say in Spanish, *es de bien nacido ser agradecido*.

Así pues, me gustaría empezar con mi Familia. Esas personas que me han cuidado cada día, me han apoyado siempre, han reído conmigo, y también llorado junto a mí. Bien por alegrías o por momentos no tan placenteros que la vida nos ha presentado. Bonito, no siempre lo es todo, mas como digo, *virtus unita fortior*. Papá, mamá, tía M. Ángeles, yaya María, desde lo más profundo que puedo ahondar en mi ser, infinitas gracias. Porque para construir un científico no sólo se necesitan bloques de conocimiento, sino también son necesarios unos buenos cimientos de valores que me habéis proporcionado desde mi infancia. La ciencia nos enseña que no todo lo tangible es real y que no todo lo intangible es ficticio. *Visibilia omnia et invisibilia* concuerda bastante bien con la dualidad onda-corpúscular de la materia y las teorías cuánticas. Acabadas estas palabras, tomo de nuevo mi afecto y me dirijo a aquellos que, aunque invisibles para mis sentidos, eternamente me aman y velan por mí desde *lo más alto*.

It is now the moment of acknowledgment to my directors, Eloísa and Héctor. Strange thing the time... isn't it? It seems like only yesterday that I was starting my collaboration on the Solid State Chemistry Research Group. *Tempus fugit...* because nine years ago I was just a first-year student of the Bachelor's Degree in Chemistry. I am grateful for allowing me to grow, personally and scientifically, and transmitting

your knowledge. I appreciate the chance that I have got to take part and learn different disciplines of this field of science. After finishing the Bachelor's Degree and just starting my Master's Degree, I had the huge privilege of choosing between the two main lines of research in which I had been working the previous years: my passion about optical materials and their applications was proved then. I believe that this open-minded attitude of my directors boosted the incipient researcher passion and creativeness. I also appreciate that you completely trusted in me for creating the research projects on my own, modulating, and conducting them, as well as for the opportunity of opening up new lines of research in our group.

Dear Elo, what could I say that I have not told you yet? I remember the talk that we had when we visited the first year Inma Usó, to whom I also acknowledge her help and extreme dedication. I was enrolled in the "Study and Research at UJI" program that allowed me to collaborate in this research group since my first steps at the University, and you were my supervisor. Thank you for that inspiring conversation and for announcing something that you would repeat during my career: *Hay que tener la maletita preparada para el momento adecuado*. All these years working with you have been wonderful. I admire that you have not only been a professor, you have worried in the darkest of times, you have encouraged me with calmness, and help me with anything in your reach. I would tell you by phone to also transmit some warm words to Maite, but as we both know, your phone is crazy and it is not always the best option to contact you.

Héctor, thank you again for your continuous support, even from the first lesson of General Chemistry that you gave me while studying the Degree. We have all grown together as a research team. Be sure that I will not forget my first conference of Electroceramics in Cuenca, it was a pleasure to assist such an event for a third-year

student of Chemistry. From that moment on we have learnt two important points: the first one, check that the hotel has air conditioner in summer; and the second one, be prepared in life for any unforeseen circumstances, such as having a flat tire. You have also encouraged me and have revealed that in the bad and in the best moments a good *cerveseta* is always an exceptional option. Complicate to forget, as well, is your “Yes, of course!” after asking you “*Mone*” a *esmorzar*? at 10:30 AM.

I would also like to express my gratitude to the rest of professors that have made me feel highly comfortable from the very first moment: Juan, Mario, Guillermo, and Vicente.

But most of the time –including headaches, frustration about why the reactions do not work properly, and wonderful moments of happiness and burst of laughter– have taken place in the lab. So, it is time to recall those colleagues who have become truly friends.

En primer lloc, cal fer menció especial a Maria. Hem treballat junts vora huit anys i, òbviament, això ha creat un vincle d'amistat especial que no vull oblidar mai. Els teus “mareee...” quan algun comentari et sorprenia crec que són més que fantàstics i a tots ens han fet riure. Els teus pigments han donat color a l'ambient del laboratori i, en alguns viatges de cursets que hem compartit, ens ho hem passat d'allò més bé. Eres una persona amb una gran serenitat i constància, et mereixes molt ser la química que desitges. Perquè també ens hem donat suport en els moments més “fotuts”, i sé que dur a terme una tesi i estudiar per a les oposicions no fou una tasca fàcil. Gràcies per tots els moments!

E agora, é minha vez de lembrar meu amigo Emerson (desculpe, devo dizer, Emersoncito). Você sabe quantas vezes já rimos e filosofamos juntos? Estou muito orgulhoso de nosso bom relacionamento e do fato de ter sido eu quem te ajudou na

UJI durante suas primeiras semanas na Espanha. Vi por minha própria experiência que ir ao exterior em uma aventura não é fácil. Mas você é uma grande pessoa, um amigo de seus amigos, e aprendeu a falar espanhol muito melhor do que eu consegui falar português, mas estou tentando... Você tem sido um grande companheiro de viagem nesta aventura da tese, e você pode ter certeza de que isto nos marcou para sempre. Mesmo que você não aprecie minhas boas piadas, você sabe que no fundo não sou tão louco. Você é um grande pesquisador. Muito obrigado ao brasileiro *tranquilo!*

I, com no, el senyor Samuel Porcar, Sam, també ha contribuït enormement a fer d'aquests anys una agradable etapa de la meua vida. Perquè, com ben bé diem nosaltres dos, qui entén les nostres gràcies? Només uns pocs tenen reservada la capacitat de fer bromes i jocs de paraules que, encara que ens els tatxen d'acudits roïns..., nosaltres gaudim SEMpre. Des que compartirem el despatx de becaris al màster o al principi del doctorat, la tauleta de xocolata a mode de permuta pels meus "briconsejos" científics ha sigut una bona manera de captivar l'amistat. Ai, Sam, reconeixem que de vegades tens unes idees descabellades..., però el teu propi univers és el que fa de tu una ment brillant per a seguir avançant en el món de la investigació. Espere que no oblidés llegir estes paraules, perquè durant aquests anys ja no duc el compte de totes les coses que has oblidat o perdut. Gràcies, amic!

Por extensión, me gustaría agradecer los buenos ratos pasados junto a todos los integrantes del Grupo de Investigación de Química del Estado Sólido: nuestra *baby* Silvia, Abde, Diego, Marc Sedano, mi "pupilo" Guillem y muchas otras personas más que me dejo en el tintero ("teclado"). Y, cómo no, ¡a mi compi de despacho, Nuria!

Però el viatge químic va començar durant la carrera, on he d'agrair eixos meravellosos moments de la meua vida als Químics Escèptics, particularment a Alberto, Juanjo i Sergio. Hem creat un vincle que espere que, de tot cor, siga per

sempre. Perquè quan comparteixes frustracions i passes més hores a l'UJI que a casa... l'amistat generada no pot ser sinó exergònica: tot flueix espontàniament. Moltíssimes gràcies companys per tots els bons moments!! Des de sopars fins a partides de cartes, quedades, recolzament, viatges, i més que ens queda. I, per descomptat, menció especial a Mr. Alberto Pla, el meu company de laboratori a totes les pràctiques de la carrera; ja saps, *always Lab's Team!*

I baixem de la quarta planta dels Químics a la primera dels Físics, i ens trobem amb el *nanomaker* Sergio. Com tu dius, “primo”, ha molat dur a terme idees en conjunt, i aprendre l'un de l'altre: el químic que es fa físic, i el físic que es fa químic. Com les nostres coses van de plasmons, no podia evitar plasmar-ho ací.

As part of my immersion in the photonics field, I must acknowledge Prof. Rolindes and Prof. Joaquín from Bilbao. Thank you so much for kindly welcoming at your university during my final year of the Chemistry studies. I am excited (as the lanthanide ions under a laser pulse) about having continued our collaboration since that moment up to date and I hope that it goes on for many years. *Eskerrik asko!*

I have also to express my acknowledgement for all the people who contributed to make warm my research stay in Aveiro (Portugal). Muito obrigado aos físicos e químicos do grupo *Phantom-G*. Estou realmente contente por ter aprendido muitos conhecimentos no campo da física óptica. Por isso, gostaria de agradecer ao Professor Luís D. Carlos por ter melhorado o meu potencial e me ter ensinado novos conhecimentos físicos. Também ao Carlos e aos meus colegas Julio, Miguel, Rodolfo, Joana e Bruno. Sobre todo, non me esquecerei das *canecas*, escapadas e pausas café (*um abatanado e meia de leite*) con Julio. Aprendemos que as cousas portuguesas van *com calma meninos...*, sobre todo cando se trata de activar unha tarxeta. Moitas grazas

amigo por ter estado nos bos momentos e nalgúns peores que lembraremos... O vínculo galego-valenciano está selado!

Continuando com mais algumas palavras em português, gostaria de expressar o bom companheirismo e a amizade dos amigos brasileiros: Emerson, novamente, Samantha, Edu, Rafa e Marcelo. Um cafezinho é sempre bom para desconectar!

Y, sin duda alguna, no puedo olvidarme de mis colegas del Colegio de Químicos y Asociación de Químicos de la Comunidad Valenciana. Gracias por confiar en mí y hacerme partícipe de los retos a los que nos enfrentamos y de las actividades que llevamos a cabo. Formar parte de estas instituciones y, más aún si cabe, como miembro de la Junta Directiva, me ha brindado una gran red de contactos multidisciplinar, de ámbitos químicos totalmente alejados del perfil investigador. ¡Muchas gracias compañeros! Especialmente, con afecto a Vicente Esteve por descubrirme este “mundo”, a José Guaita, Juan Hernández, Dulce, Juan Antonio, Sergio Menargues, y a mi “compi” *escéptico* José Juan.

Pero no podía acabar los agradecimientos sin acordarme de Cristina González y Esmeralda Honrubia de Feique. Aquel premio *SusChem 2019 FUTURA* nos puso en común y hemos podido estar en contacto desde entonces. Gracias por promoverme y ayudarme, por vuestra pasión, consejos, y apoyo en la selección para el evento del Cefic. Given the above, I must solemnly express my acknowledgement to Cefic for their support and giving me the chance to assist at incredible events that boosted and broadened my perspectives and horizons as a chemist. And, for sure, not all was about Chemistry; I have now a collection of friends all around Europe. Best wishes for my colleagues of the *CB Team*: Kata, Robert, and Branislav.

**I per concloure, gràcies a l'UJI per haver sigut una veritable casa acollidora
durant tots aquests anys!**

Abstract

The present Doctoral Thesis, which is entitled *Solid-State Hosts Based on Fluorides with Europium: From the Crystal Structure toward the Optical Performance*, is framed within the area of Solid-State Chemistry and Materials Science. Driven by a profound interest in conducting research that integrates both fundamental and applied scientific principles, the primary objective of this Doctoral Thesis is to formulate host lattices based on yttrium complex fluorides, with a specific focus on their application in photoluminescence. Therefore, there is always a close connection with other disciplines such as Crystallography and Physics.

This thesis, presented as a compendium of articles, consists of ten chapters. Among them, seven chapters directly align with the published papers. These are preceded by two chapters, which outline a general introduction and the main objectives. Finally, the thesis concludes with a final chapter summarizing the key findings and conclusions.

Chapter 1 serves as an introduction, offering a comprehensive overview of the key subjects explored in this thesis. It provides valuable insights into luminescence and lanthanides, enhancing the reader's comprehension of the research conducted. Subsequently, in **Chapter 2**, the general and specific objectives of the Doctoral Thesis are presented.

Chapter 3 (Article 1) discusses the preparation of Eu^{3+} -doped $\alpha\text{-KY}_3\text{F}_{10}$ materials with different dopant levels, highlighting the importance of reaction conditions in determining product characteristics. Changes in photoluminescence spectra and lifetimes are observed due to energy transfers between Eu^{3+} ions, offering the potential

for high quantum efficiencies. The study underscores the complexity of fluoride-based systems and the color-tunable emissions of the phosphors (orange-yellow), which could be interesting for their application in white light-emitting diodes through their combination with blue chips.

In **Chapter 4 (Article 2)**, Eu^{3+} -doped YF_3 and $\alpha\text{-KY}_3\text{F}_{10}$ phosphors are prepared hydrothermally at various pH values with and without surface chelators. The role of dicarboxylic acids in modulating surface and crystal phases is explored, leading to tunable photoluminescence with high quantum efficiencies. Relationships between optical performance and physicochemical properties are established, highlighting potential applications in various fields.

Chapter 5 (Article 3) introduces a sonochemical method to synthesize the $\delta\text{-KY}_3\text{F}_{10}\cdot x\text{H}_2\text{O}$ compound with a 'super-diamond' structure. It is important to note that this new synthesis approach and this paper is the first one contemplating the study of this crystal phase since it was first discovered more than twenty years ago and fell into complete oblivion. Additionally, the growth mechanism underlying the formation of the nanomaterials and their connection with the pH of the medium is explored. The material's potential for optical applications, particularly when doped with Eu^{3+} , is also demonstrated.

Given the previous results, a comprehensive and detailed study of the chemical mechanisms that allow tuning the crystal structures of different yttrium fluorides is presented in **Chapter 6 (Article 4)**. Eu^{3+} -doped fluorides are synthesized via ultrasound-assisted processes at different pH values (from 4.0 to 9.0). Both $\alpha\text{-KY}_3\text{F}_{10}$ and $\delta\text{-KY}_3\text{F}_{10}\cdot x\text{H}_2\text{O}$ phases are obtained, along with yttrium hydroxyfluorides, $\text{Y}(\text{OH})_{3-x}\text{F}_x$. These materials exhibit highly tunable optical responses, with various color emissions, lifetimes, and quantum efficiencies. Sonochemistry's importance in

controlling crystal structures is emphasized.

With a particular focus on photonics and photophysical processes, **Chapter 7 (Article 5)** delves into the luminescent response of Eu^{3+} ions in KY_3F_{10} with different crystal phases using time-resolved fluorescence line-narrowing (TRFLN). Another alternative and very low time-consuming method is developed to obtain nanospheres of the δ -phase. The site-selective symmetries of the dopant are explored in single δ -phase, single α -phase, and mixed-phase samples. As a landmark, it is worth highlighting that the site-selective emission of the Eu^{3+} -doped δ -phase is up to 20 times more intense than that of the α -phase.

Chapter 8 (Article 6) focuses on the capability of isolating both the thermodynamic α -phase and the metastable δ -phase of KY_3F_{10} using a coprecipitation method. It also discusses how reaction temperature and time affect polymorph formation and particle morphology: an interplay between thermodynamics and kinetics. The luminescent response of Eu^{3+} -doped powders is used to understand structural stability.

Chapter 9 (Article 7) emphasizes the significance of Eu^{3+} as a luminescent ion for the straightforward calculation of its physicochemical parameters. The chapter offers guidance on interpreting emission spectra and practical insights into the theoretical concepts involved, especially those devoted to solid-state host lattices.

Finally, **Chapter 10** offers the general conclusions of findings and implications drawn from the research detailed in the preceding Chapters.

Resumen

La presente Tesis Doctoral, titulada *Solid-State Hosts Based on Fluorides with Europium: From the Crystal Structure toward the Optical Performance*, se enmarca en el campo de la Química del Estado Sólido y la Ciencia de Materiales. Impulsada por un profundo interés en llevar a cabo investigaciones que integren principios científicos tanto fundamentales como aplicados, el objetivo principal es la formulación de redes huésped basadas en fluoruros complejos de itrio, con un enfoque específico en su aplicación en la fotoluminiscencia. Por ello, siempre se mantiene una estrecha conexión con otras disciplinas como la Cristalografía y la Física.

La tesis, presentada por compendio de artículos, consta de diez capítulos, de los cuales siete corresponden a los artículos publicados. Estos son precedidos por dos capítulos que describen una introducción general y los principales objetivos. Finalmente, se concluye con un último capítulo que resume los principales resultados obtenidos y las conclusiones.

El **Capítulo 1** sirve como introducción, ofreciendo una visión global de las temáticas clave exploradas a lo largo del contenido de la tesis. Proporciona una perspectiva valiosa sobre el fenómeno de luminiscencia y los lantánidos, mejorando con ello la comprensión del lector sobre la investigación llevada a cabo. Seguidamente, en el **Capítulo 2**, se presentan los objetivos generales y específicos de la Tesis Doctoral.

El **Capítulo 3 (Artículo 1)** aborda la preparación de materiales con estequiometría α -KY₃F₁₀ dopados con diferentes concentraciones de Eu³⁺, resaltando la importancia de las condiciones de síntesis en la determinación de las características del producto. Se observan cambios en los espectros de fotoluminiscencia y en los tiempos de vida

debido a las transferencias de energía entre los iones Eu^{3+} , lo que permite obtener altas eficiencias cuánticas. El estudio pone de manifiesto la complejidad de los sistemas basados en fluoruros y la capacidad de modular el color de las emisiones (naranja-amarillo) de los materiales, que podrían ser interesantes para su aplicación en diodos emisores de luz blancos mediante su combinación con chips azules.

En el **Capítulo 4 (Artículo 2)**, se preparan hidrotermalmente compuestos de YF_3 y $\alpha\text{-KY}_3\text{F}_{10}$ dopados con Eu^{3+} a diferentes valores de pH, con y sin agentes quelantes. Se explora el papel de los ácidos dicarboxílicos en la modulación de la superficie de las partículas y las fases cristalinas, lo que conlleva también una fotoluminiscencia modulable con altas eficiencias cuánticas. Además, se establecen relaciones entre la respuesta óptica y las propiedades fisicoquímicas.

El **Capítulo 5 (Artículo 3)** presenta un método sonoquímico para sintetizar el compuesto $\delta\text{-KY}_3\text{F}_{10}\cdot x\text{H}_2\text{O}$, el cual exhibe una estructura de “súper-diamante”. Es importante destacar que tanto el nuevo enfoque de síntesis como este artículo son los primeros en contemplar el estudio de dicha fase cristalina desde que fue descubierta por primera vez hace más de veinte años y cayó en completo olvido. Además, se explora el mecanismo de crecimiento que subyace en la formación de los nanomateriales y su conexión con el pH del medio. También se demuestra el potencial del material para aplicaciones ópticas, especialmente cuando está dopado con Eu^{3+} .

Dado los resultados anteriores, en el **Capítulo 6 (Artículo 4)** se describe un estudio exhaustivo y detallado de los mecanismos químicos que permiten formar las diferentes estructuras cristalinas de fluoruros de itrio. Se sintetizan fluoruros dopados con Eu^{3+} mediante procesos asistidos por ultrasonidos a diferentes valores de pH (de 4,0 a 9,0). Se obtienen las fases $\alpha\text{-KY}_3\text{F}_{10}$ y $\delta\text{-KY}_3\text{F}_{10}\cdot x\text{H}_2\text{O}$, junto con hidroxifluoruros de itrio, $\text{Y}(\text{OH})_{3-x}\text{F}_x$. Estos materiales exhiben respuestas ópticas altamente ajustables,

con diversas emisiones de color, tiempos de vida y eficiencias cuánticas. Se enfatiza la importancia de la sonoquímica en el control de las estructuras cristalinas.

Con un enfoque particular en la fotónica y los procesos fotofísicos, el **Capítulo 7 (Artículo 5)** profundiza en la respuesta luminiscente de los iones Eu^{3+} en compuestos de KY_3F_{10} con diferentes fases cristalinas utilizando la técnica de fluorescencia de estrechamiento de línea resuelta en tiempo (TRFLN, del inglés, *time-resolved fluorescence line-narrowing*). Se desarrolla otro método alternativo y eficaz que permite obtener nanoesferas de la fase δ . Además, se exploran las simetrías de sitio selectivo del dopante en muestras de fase δ pura, fase α pura, y mezcla de ambas fases. Es importante destacar que la emisión de sitio selectiva de los iones Eu^{3+} en la fase δ es hasta 20 veces más intensa que la de la fase α .

El **Capítulo 8 (Artículo 6)** se centra en la capacidad de aislar tanto la fase termodinámica α como la fase metaestable δ del KY_3F_{10} mediante un método de coprecipitación. También se discute cómo la temperatura y el tiempo de reacción afectan a la formación de los distintos polimorfos y a la morfología de las partículas, lo que implica una interacción entre la termodinámica y la cinética. La respuesta luminiscente de los productos dopados con Eu^{3+} se utiliza para dilucidar la estabilidad estructural.

El **Capítulo 9 (Artículo 7)** enfatiza la importancia del Eu^{3+} como ion luminiscente para el cálculo directo de sus parámetros fisicoquímicos. El capítulo ofrece orientación sobre la interpretación de los espectros de emisión e ideas prácticas sobre los conceptos teóricos involucrados, especialmente los relacionados con las redes huésped en estado sólido.

Por último, el **Capítulo 10** ofrece las conclusiones generales de los resultados y las implicaciones extraídas de la investigación detallada en los capítulos anteriores.

Contents

Chapter 1	Introduction	1
1.1.	Advanced inorganic materials	3
1.2.	Fluoride-based materials for optical applications	5
1.2.1.	The KY_3F_{10} crystal structure	9
1.2.1.1.	α - KY_3F_{10}	9
1.2.1.2.	δ - $KY_3F_{10} \cdot xH_2O$	11
1.2.2.	The YF_3 crystal structure	12
1.2.3.	The $Y(OH)_{3-x}F_x$ crystal structure	13
1.3.	Basics of luminescence	15
1.3.1.	General considerations	15
1.3.2.	Photoluminescence	17
1.3.2.1.	<i>Excitation and emission spectra</i>	19
1.3.2.2.	<i>Time-resolved fluorescence spectroscopy</i>	21
1.3.2.3.	<i>Quantum yield</i>	24
1.4.	Lanthanides	27
1.4.1.	Electronic structure	27
1.4.2.	Luminescent applications of lanthanides	31
1.4.2.1.	<i>Lanthanides in lighting and displays</i>	32
1.4.2.2.	<i>Lanthanides in lasers</i>	34
1.4.2.3.	<i>Lanthanides for anti-counterfeiting</i>	34
1.4.3.	The Eu^{3+} ion	35
1.5.	Synthesis methods	37
1.5.1.	Coprecipitation method	37
1.5.2.	Sonochemical synthesis	38
1.5.3.	Hydrothermal synthesis	39
	References	41
Chapter 2	Objectives	55
Chapter 3	Tuning the optical and photoluminescence properties of high efficient Eu^{3+}-doped KY_3F_{10} phosphors by different synthetic approaches	61
	Abstract	65
3.1.	Introduction	66

3.2.	Experimental section	70
3.2.1.	Materials	70
3.2.2.	Synthesis of Eu ³⁺ -doped KY ₃ F ₁₀ compounds	70
3.2.2.1.	<i>Synthetic Routes with an Ultrasonication Common Step (Routes 1–3)</i>	71
3.2.2.2.	<i>Synthetic Routes with a Continuous Stirring Common Step (Routes 4–6)</i>	73
3.2.2.3.	<i>Synthetic Routes with a Coprecipitation Common Step (Routes 7–8)</i>	73
3.2.3.	Characterization	74
3.3.	Results and discussion	75
3.3.1.	Structural characterization	75
3.3.2.	Morphological characterization	78
3.3.3.	Photoluminescence studies	80
3.3.3.1.	<i>Emission spectra</i>	80
3.3.3.2.	<i>Judd-Ofelt and Asymmetry Ratio Calculations</i>	88
3.3.3.3.	<i>Lifetimes and Quantum Efficiencies Analysis</i>	90
3.4.	Conclusions	94
	Acknowledgments	96
	References	96
S3.	Supporting Information	103
Chapter 4	Unraveling the superior role of dicarboxylic acids as surface chelators in Eu³⁺-doped yttrium fluorides: a systematic modulation of the crystal phases and morphologies for highly tuned optical performance	111
	Abstract	115
4.1.	Introduction	116
4.2.	Experimental section	119
4.2.1.	Materials	119
4.2.2.	Synthesis of Eu ³⁺ -doped compounds	120
4.2.3.	Characterization	121
4.3.	Results and discussion	122
4.3.1.	Structural characterization	122
4.3.2.	Morphological characterization	126
4.3.2.1.	<i>Samples prepared without the incorporation of surface chelators</i>	127

	4.3.2.2. <i>Samples prepared with the incorporation of surface chelators</i>	128
	4.3.3. Photoluminescence studies	129
	4.3.3.1. Excitation spectra	129
	4.3.3.2. <i>Emission spectra</i>	130
	4.3.3.3. <i>Judd-Ofelt and Asymmetry Ratio Calculations</i>	135
	4.3.3.4. <i>Lifetimes and Quantum Efficiencies Analysis</i>	139
4.4.	Conclusions	144
	Acknowledgments	145
	References	146
S4.	Supporting Information	153
Chapter 5	The unexplored δ-phase of KY_3F_{10}: Toward novel Eu^{3+}-doped nanoplates with a ‘super-diamond’ structure for optical applications	157
	Abstract	161
5.1.	Introduction	162
5.2.	Experimental	164
5.3.	Results and discussion	165
	5.3.1. Crystal structure and growth mechanism	165
	5.3.2. Thermal analysis	168
	5.3.3. Photoluminescence studies	169
5.4.	Conclusions	172
	Acknowledgments	173
	References	173
S5.	Supporting Information	177
Chapter 6	The pH-dependent reactions in the sonochemical synthesis of luminescent fluorides: the quest for the formation of KY_3F_{10} crystal phases	183
	Abstract	187
6.1.	Introduction	188
6.2.	Experimental section	190
	6.2.1. Materials	190
	6.2.2. Synthesis of Eu^{3+} -doped compounds	190
	6.2.3. Characterization	191
6.3.	Results and discussion	192
	6.3.1. Structural characterization	192

6.3.2.	Reaction mechanism	196
6.3.2.1.	<i>Formation of compounds with initial pH ≤ 7</i>	199
6.3.2.2.	<i>Formation of compounds with initial pH > 7</i>	200
6.3.3.	Morphological characterization	202
6.3.4.	Photoluminescence studies	204
6.3.4.1.	<i>Excitation and emission spectra</i>	204
6.3.4.2.	<i>Asymmetry ratio and Judd-Ofelt parameters</i>	207
6.3.4.3.	<i>Time-resolved luminescence and quantum efficiencies</i>	209
6.4.	Conclusions	211
	Acknowledgments	212
	References	212
S6.	Supporting Information	217
Chapter 7	A site-selective fluorescence spectroscopy study of the crystal phases of KY₃F₁₀: leveraging the optical response of Eu³⁺ ions	229
	Abstract	233
7.1.	Introduction	234
7.2.	Experimental section	238
7.2.1.	Materials	238
7.2.2.	Synthesis of materials	239
7.2.2.1.	<i>Preparation of δ-KY₃F₁₀:Eu³⁺</i>	240
7.2.2.2.	<i>Preparation of (δ+α)-KY₃F₁₀:Eu³⁺</i>	240
7.2.2.3.	<i>Preparation of α-KY₃F₁₀:Eu³⁺</i>	241
7.2.3.	Characterization	241
7.3.	Results and discussion	242
7.3.1.	Structural and thermal characterization	242
7.3.2.	Morphological characterization	246
7.3.3.	Site-selective time-resolved fluorescence line-narrowing spectroscopy	248
7.3.3.1.	<i>General grounds</i>	248
7.3.3.2.	<i>Interpretation of the TRFLN spectra</i>	249
7.3.3.3.	<i>Experimental results and discussion</i>	252
7.4.	Conclusions	260
	Acknowledgments	261
	References	261
S7.	Supporting Information	267

Chapter 8	Kinetics or thermodynamics? Extolling their role to modulate the crystal phases and luminescence of KY₃F₁₀:Eu³⁺ powders	271
	Abstract	275
8.1.	Introduction	276
8.2.	Experimental section	279
	8.2.1. Materials and methods	279
	8.2.2. Characterization techniques	281
8.3.	Results and discussion	281
	8.3.1. Structural characterization	281
	8.3.1.1. <i>Understanding the ($\alpha + \delta$)$\rightarrow\delta$ transformation</i>	287
	8.3.2. Morphological characterization	289
	8.3.3. Photoluminescence properties	292
	8.3.3.1. <i>Excitation and emission spectra</i>	292
	8.3.3.2. <i>The crystal environment of Eu³⁺ ions</i>	295
	8.3.3.3. <i>Time-resolved luminescence</i>	298
8.4.	Conclusions	303
	Author contributions	304
	Acknowledgments	304
	References	304
S8.	Supporting Information	309
Chapter 9	Practical guidance for easily interpreting the emission and physicochemical parameters of Eu³⁺ in solid-state hosts	317
	Abstract	321
9.1.	Introduction	322
9.2.	Electronic features	323
	9.2.1. Energy levels	323
	9.2.2. Some basics about symmetry and electronic transitions	324
	9.2.3. Understanding the character of electronic transitions in lanthanides	327
9.3.	Some useful considerations about the emission spectra	329
	9.3.1. General assignment of the bands	329
	9.3.2. The phonon energy and how to properly discriminate emissions from higher excited states	330
	9.3.3. The emission color: CIE xy coordinates	335
9.4.	The asymmetry ratio	336
	9.4.1. Determination of the branching ratios	336
	9.4.2. The Jacobian transformation: to do, or not to do	337

9.4.3.	Avoid emissions from higher excited states	339
9.4.4.	“Unexpected” values and controversy about the asymmetry ratio	340
9.5.	Judd-Ofelt parameters of Eu^{3+}	341
9.5.1.	Theory and applications: a 60-year history	341
9.5.2.	The particular case of Eu^{3+}	343
9.5.3.	Calculus by computational programs	345
9.5.4.	No data available for the refractive index	347
9.6.	Inferring the site-selective symmetries of Eu^{3+}	350
9.7.	Conclusions	352
	Acknowledgments	353
	References	354
Chapter 10	Conclusions	363
Appendix 1		367
Appendix 2		373
Appendix 3		379

Chapter 1

Introduction

1.1. Advanced inorganic materials

Our society is confronted with significant challenges in the form of an energy crisis and the accompanying environmental pollution. In a time when our destiny is tied to perpetually advancing scientific progress, inorganic materials are the unseen creators of revolutionary transformation [1].

These materials showcase a plethora of compositions and functionalities, which range from the fundamental semiconductors that power our digital world to the enigmatic superconductors, capable of revolutionizing energy transportation. Each material category within this sphere has developed its area of specialty, advancing innovation in areas such as electronics, energy storage, catalysis, optics, and a range of other major aspects of our modern lives [2]. As a summary, some examples of different areas are explained below.

In this context, an area that cannot go unnoticed is the field of advanced ceramics. They are distinguished from traditional ceramics due to their elevated strength, customizable properties, enhanced toughness, and the ability to withstand higher operating temperatures. These attributes collectively constitute the defining characteristics of contemporary ceramic components. From airplane components to long-lasting dental implants, these components signify the changed capacity of advanced inorganic elements to reconceptualize long-established industries [3].

At the foundation of the technological revolution lie semiconductor materials, with silicon occupying a prevailing position. Semiconductor materials offer the ability to adjust their electrical properties through the deliberate introduction of impurities, the application of electrical fields, or exposure to light [4]. As a result, semiconductor-based devices find applications in amplification, switching, and energy conversion, to name but a few. Materials based on Ga-N and SiC compounds have also promoted

power electronics, such as speedy communication through mobile devices [5].

Superconducting materials have the potential to revolutionize electric power and high-field magnet technology, paving the way for highly efficient power generation, compact and light-weight electrical devices, the creation of ultra-powerful magnetic fields for advanced applications such as high-resolution magnetic resonance imaging (MRI) systems, nuclear magnetic resonance (NMR) systems, future advanced high-energy particle accelerators, and nuclear fusion reactors, among others. While numerous superconductors have been identified, only a few possess practical significance, including Nb-Ti, Nb₃Sn, copper-based oxide superconductors, MgB₂, and iron-based superconductors [6].

Ferroelectrics, characterized by having spontaneous electric polarization, have a high permittivity and can retain a large, residual polarization of charge after an electric field has been removed [7]. They supply power to ultrasonic sensors, facilitate precise actuators, and provide non-volatile memory gadgets. One of the most known and versatile ferroelectric materials is BaTiO₃, where the polarizability depends on the polymorph that this structure exhibits at a certain temperature [8].

It is also important to include in this section of advanced inorganic materials those that are found at the nanoscale, i.e., nanomaterials. Innovative and uncommon characteristics which were formerly confined to the area of mythology, now are confined to the laws of quantum mechanics. Because of that, nanomaterials find a wide range of applications: biomedical, energy generation, solar cells, optoelectronics, or catalysis [9,10].

Finally, it must be highlighted that inorganic materials play a crucial role in photonic applications, where the manipulation and control of light are central to the functionality of devices and systems. These materials are chosen for their unique

optical properties and capabilities [11–14]. In this context, as presented in the forthcoming sections, fluoride-based inorganic host lattices have risen to prominence as a preeminent category of materials for advanced optical applications when juxtaposed with other material types [15–18]. Consequently, owing to the pressing need for discovering and precisely tailoring new prospects with the potential to revolutionize the realm of photonics, this Doctoral Thesis will delve into an extensive investigation concerning the analysis of the optical characteristics inherent to fluoride-based systems.

1.2. Fluoride-based materials for optical applications

Fluorides have a highly ionic bond character, resulting in low phonon energies (generally $300\text{--}550\text{ cm}^{-1}$) compared to oxide materials ($> 550\text{ cm}^{-1}$), which means they have weak vibrational interactions that can lead to lower energy losses during optical transitions [19–21]. This characteristic makes them suitable for hosting rare-earth ions and other dopants that can generate laser action and exhibit interesting optical phenomena. Moreover, fluorides exhibit exceptionally large band gaps, see **Figure 1.1** [22], leading to ultraviolet absorption edges at lower wavelengths than most oxides. This property makes them suitable for applications in ultraviolet and vacuum ultraviolet wavelength ranges, particularly for laser, window, and lens applications [23,24].

When doped with lanthanide ions (Ln^{3+}), fluorides show weaker non-radiative de-excitation probabilities compared to oxides, making them more efficient for luminescence applications. In contrast to fluorides, many oxide laser hosts exhibit multiphonon relaxation processes that increase non-radiative decay rates and, therefore, exhibit lower quantum yields [25,26]. Moreover, the presence of a weak

crystal field in fluorides results in decreased probabilities of cross-relaxation between luminescent active ions, consequently leading to a significant enhancement in their luminescence properties [27]. Furthermore, the long excited state lifetimes in fluorides facilitate upconversion processes, which are beneficial for generating blue and ultraviolet lasers [28].

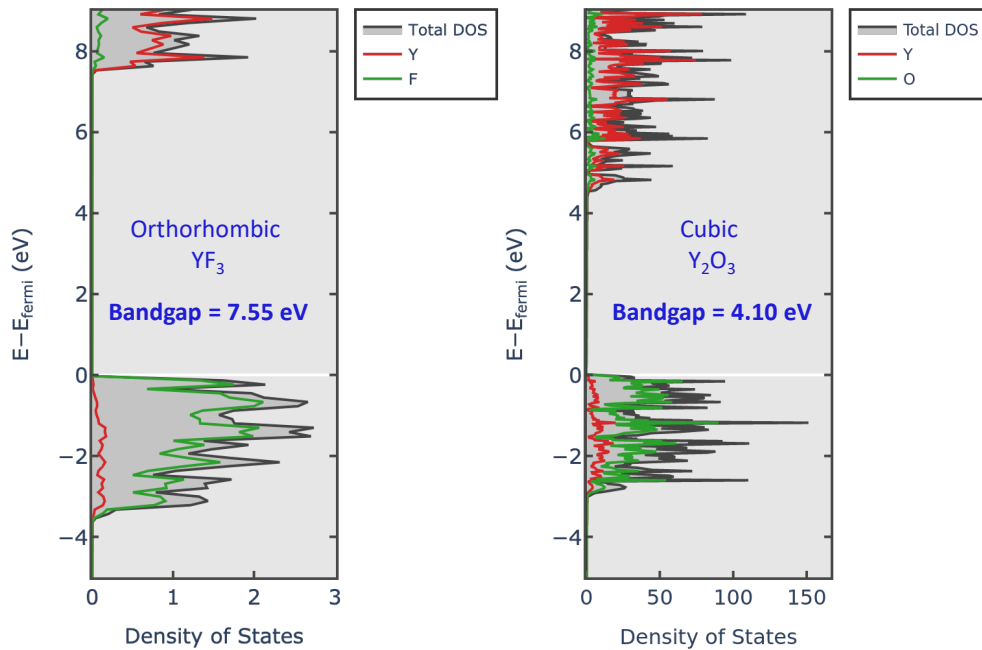


Figure 1.1. Comparison of bandgaps of the orthorhombic YF_3 fluoride and the cubic Y_2O_3 oxide. DOS (Density of States) diagrams obtained from Materials Project database and core program [22].

These unique optical properties make fluorides attractive candidates for a wide range of optical applications. In addition, the morphology and luminescence of fluorides can be highly influenced by the synthesis method employed during their formation. Different synthesis techniques can lead to variations in the shape, size, and arrangement of the fluoride particles, as well as affect their luminescent properties. As an example, **Figure 1.2** showcases how the synthetic conditions have a profound

influence in the resulting morphology of the compounds [29]. Therefore, the luminescence dynamics of the trivalent lanthanide ions can be significantly impacted by various factors, including particle size and morphology (as commented) but also surface characteristics, strain, and crystal phase [30].

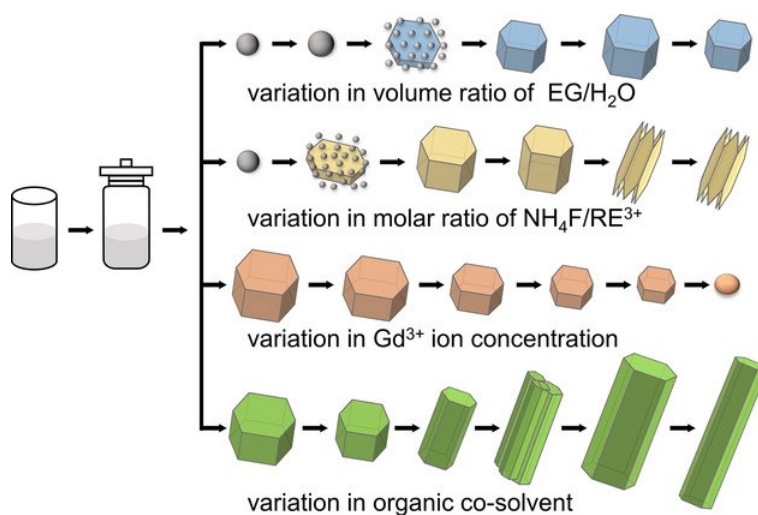


Figure 1.2. Different factors affecting the size and morphology in the solvothermal synthesis of Ln^{3+} -doped NaYF_4 fluorides. Reprinted with permission from reference [29].

Depending on their specific application, different Ln^{3+} -doped fluorides have been extensively studied in the literature. These host lattices encompass simple, binary structures but also more complex structures, including ternary and quaternary fluorides or multi-doped systems. Some common host lattices are BaF_2 [31,32], CaF_2 [33,34], YLiF_4 [35,36], NaYF_4 [37,38], or compounds of the related $\text{KF}-\text{YF}_3$ binary system (YF_3 , KYF_4 , KY_3F_{10} , K_2YF_5 , etc.) [39–42]. Among all of them, it is important to note that fluorides with trivalent lattice cations, as it is Y^{3+} , are particularly appealing for luminescence applications due to their ability to facilitate the isovalent substitution of a Ln^{3+} ion and also due to the similitude between the Y^{3+} and Ln^{3+} ionic radii [43,44].

Frequently, NaYF_4 is regarded as one of the most efficient fluoride matrices. However, it has been demonstrated that for some applications other compounds, such as YF_3 or KY_3F_{10} , can exhibit better optical response [45–47]. Therefore, great interest has been paid to these materials in the last few decades, specially to KY_3F_{10} [48–54]. However, certain preparation methods are often challenging to utilize due to the intricacy and difficulties associated with reproducing the final product [49]. Moreover, there is still a lack in the profound knowledge of the relationship between the synthesis-structure-properties of KY_3F_{10} acting as a host material for lanthanide doping. Additionally, exploring the structure's response to external stimuli, such as temperature or pressure, can unlock new possibilities for advanced optical materials and devices. It is the aim that a comprehensive research into the KY_3F_{10} structure will pave the way for innovations in lasers, imaging systems, and other optical technologies, thereby advancing various scientific, industrial, and medical applications. By all the aforementioned, KY_3F_{10} will be the main crystal structure under study in this Doctoral Thesis.

The following subsections provide a concise crystallographic overview of all the compounds discussed in the different articles herein presented. More comprehensive details will be presented in the forthcoming Chapters. In the context of the current Doctoral Thesis research, primary attention has been dedicated to KY_3F_{10} , as previously mentioned. However, it's worth noting that other intriguing materials, including YF_3 or $\text{Y}(\text{OH})_{3-x}\text{F}_x$, have also been studied due to the intricate and delicate synthesis.

1.2.1. The KY_3F_{10} crystal structure

Currently, there are three known crystal phases of KY_3F_{10} : α - KY_3F_{10} (the most stable thermodynamic phase), δ - $\text{KY}_3\text{F}_{10}\cdot x\text{H}_2\text{O}$ (a hydrated metastable phase), and a high-pressure phase with $Pm\bar{3}m$ space group [55].

However, until now, researchers have exclusively directed their attention towards the prevalent α -phase of KY_3F_{10} aiming to comprehensively elucidate its physicochemical characteristics and potential applications [49–52,56]. In 2000, Le Berre *et al.* [57] made a noteworthy discovery of a novel crystal phase of this compound, known as the hydrated δ -phase (a metastable phase). However, despite its significance, subsequent research on this phase was overlooked, and no further investigations were pursued. Henceforth, the primary endeavors of this Doctoral Thesis have been dedicated to profoundly investigating the characteristics of α - KY_3F_{10} and δ - $\text{KY}_3\text{F}_{10}\cdot x\text{H}_2\text{O}$ as host lattices for the incorporation of luminescent lanthanide ions, as well as to exploring novel and enhanced synthetic pathways for obtaining these substances. Furthermore, a concerted effort has been made to establish a robust correlation amongst the synthesis–structure–property triad.

1.2.1.1. α - KY_3F_{10}

Under ambient temperature and pressure conditions, α - KY_3F_{10} crystallizes in a fluorite-type cubic structure with the $Fm\bar{3}m$ (no. 225) space group. The lattice parameter is $a = 11.536 \text{ \AA}$, and the cell volume is $V = 1535.20 \text{ \AA}^3$. There are 8 formula units per unit cell ($Z = 8$) [58].

Traditionally, the crystal structure has been described as a $2 \times 2 \times 2$ superstructure of fluorite ($Z = 8$). The structure can be described by means of square antiprisms formed by YF_8 units. A central yttrium cation is bonded to two squares of fluorine anions with

different Wyckoff positions [59]. One square is formed by the anions in the $32f$ position (F1), and the other by the anions in the $48i$ position (F2), as shown in **Figure 1.3(a)**. Considering this, the resulting symmetry of Y^{3+} is C_{4v} . The union of six antiprisms generates a cluster-like unit in which the vertices are shared, leaving an empty cuboctahedron in the center formed by the ions in position F2, see **Figure 1.3(b)**. The empty cuboctahedron is located in the center of the unit cell and in between the edges, as depicted in **Figure 1.3(c)**. Potassium cations are distributed along channels formed in the structure parallel to the crystallographic axes a , b , and c , see **Figure 1.3(d)** [60].

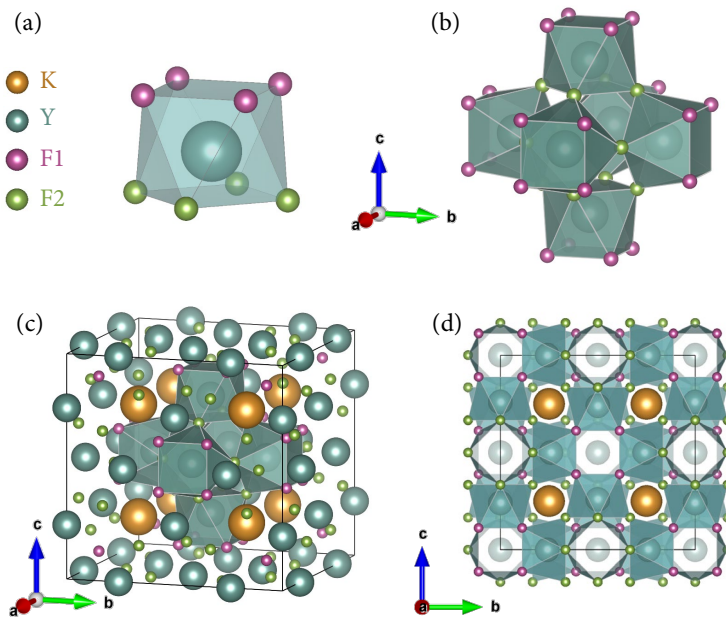


Figure 1.3. Structure of cubic α - KY_3F_{10} : (a) basic unit composed of YF_8 square antiprisms, (b) cluster assemblage of six antiprisms, (c) unit cell, and (d) view along the $[100]$ direction.

1.2.1.2. $\delta\text{-KY}_3\text{F}_{10}\cdot x\text{H}_2\text{O}$

The $\delta\text{-KY}_3\text{F}_{10}\cdot x\text{H}_2\text{O}$ compound has a cubic structure with $\text{SG} = Fd\bar{3}m$ (no. 227), $Z = 16$, and $a = 15.492 \text{ \AA}$ (cell volume $V = 3717.90 \text{ \AA}^3$) [57]. The crystal structure exhibits a remarkable arrangement consisting of six YF_8 square antiprisms, collectively referred to as the unit of octahedral antiprism (UOA), see **Figure 1.4(a,b)**. These UOAs are connected through shared edges and corners, forming an intricate three-dimensional cage-like structure [61].

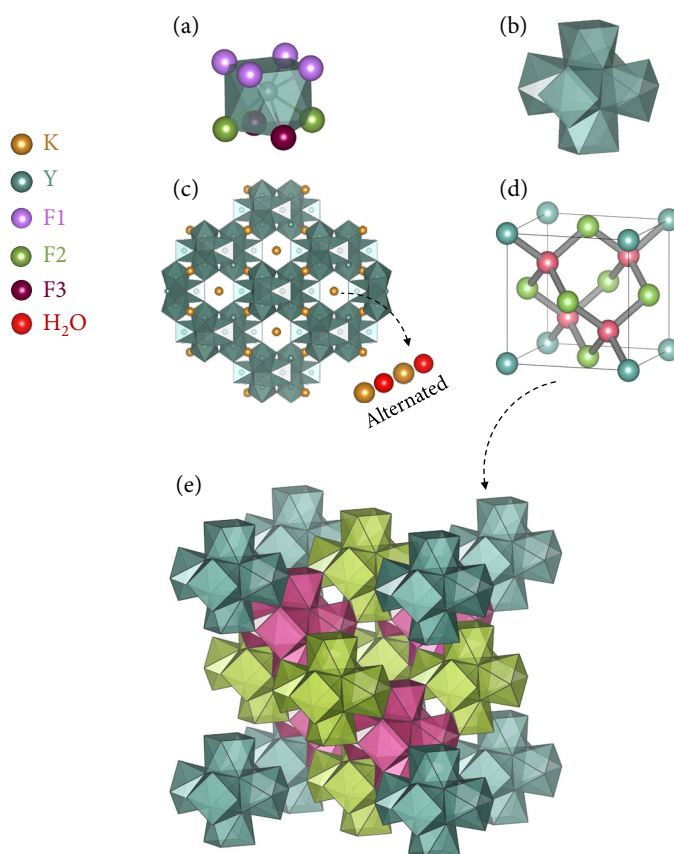


Figure 1.4. (a) YF_8 square antiprism. (b) Schematic representation of the unit of octahedral antiprism. (c) Three-dimensional cage-like with cavities and channels, where K^+ and H_2O are alternated. (d) Corresponding view of the diamond structure with C atoms represented as spheres. (e) ‘Super-diamond’ structure view of $\delta\text{-KY}_3\text{F}_{10}\cdot x\text{H}_2\text{O}$.

Within these cavities, potassium ions and water molecules are present, **Figure 1.4(c)**. The presence of water molecules allows for mobility through the tunnels, giving rise to a zeolitic behavior in this unique phase. Describing the three-dimensional network, it resembles a diamond-type stacking of UOAs. Interestingly, each UOA contains a central vacancy, akin to the position of a carbon atom in the diamond structure [62,63], **Figure 1.4(d,e)**. For clarity in comparing structures, the ‘super-diamond’ view of δ - $\text{KY}_3\text{F}_{10}\cdot x\text{H}_2\text{O}$ has retained the respective colors of UOAs to indicate their similarity to C atoms.

In summary, while both α - KY_3F_{10} and δ - $\text{KY}_3\text{F}_{10}\cdot x\text{H}_2\text{O}$ are different crystalline phases of the KY_3F_{10} compound, the latter is distinct due to its ability to incorporate varying amounts of water into its crystal structure. These differences in crystallographic phase and hydration state lead to variations in their overall properties, making them important considerations in material science and chemistry, especially in the design of luminescent compounds.

1.2.2. The YF_3 crystal structure

Under ambient temperature and pressure conditions, YF_3 crystallizes into an orthorhombic structure with $\text{SG} = Pnma$ (no. 62), $Z = 4$, and lattice parameters $a = 6.353 \text{ \AA}$, $b = 6.850 \text{ \AA}$, $c = 4.353 \text{ \AA}$ (cell volume $V = 189.43 \text{ \AA}^3$) [64].

The structure can be described by means of tricapped trigonal prisms formed by YF_9 units. A central yttrium cation is bonded to six fluorine anions in the $8d$ Wyckoff position (F1) and three in the $4c$ position (F2), as shown in **Figure 1.5(a)**. Each YF_9 unit exhibits only one possible symmetry operation, which is reflection in a plane perpendicular to the crystallographic axis b [65]. Thus, the symmetry of Y^{3+} is C_s , as illustrated in **Figure 1.5(b)**. In one unit cell of YF_3 , there are 4 Y^{3+} cations and 12 F^-

anions ($Z = 4$). **Figure 1.5(c)** displays the four YF_9 units within the unit cell. As can be seen, the polyhedra are interconnected by sharing faces and edges, as depicted in **Figure 1.5(d,e)**.

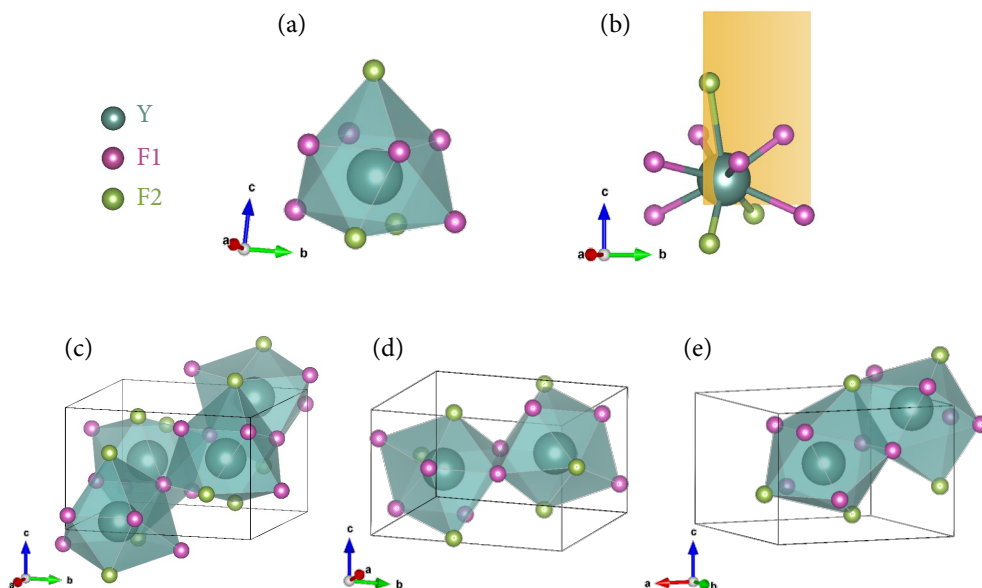


Figure 1.5. (a) YF_9 units forming a tricapped trigonal prism with the central yttrium cation. (b) Detail of the symmetry plane perpendicular to the crystallographic axis b . (c) Unit cell of YF_3 characterized by tricapped trigonal prisms. (d) Detail of the prisms connected by sharing edges and (e) sharing faces.

1.2.3. The $Y(OH)_{3-x}F_x$ crystal structure

$Y(OH)_{3-x}F_x$ is a hexagonal structure with $SG = P6_3/m$ (no. 176), and $Z = 2$ [66]. The compound can be described as a partial substitution of hydroxide anions (OH^-) in $Y(OH)_3$ by fluoride anions (F^-). Fluoride ions are smaller than hydroxide ions, and this change in anion size can affect the crystal structure and lattice parameters of the compound, as well as the ideal local symmetry of the Y^{3+} site (C_{3h}).

The hexagonal $Y(OH)_{3-x}F_x$ can exhibit different physical and chemical properties

compared to the original $\text{Y}(\text{OH})_3$ due to the altered crystal structure. Additionally, the luminescence properties of the compound may also change as a result of the substitution, making it potentially useful in luminescent applications [67,68]. **Figure 1.6(a)** showcases the coordination polyhedron of Y^{3+} , **Figure 1.6(b)** depicts the unit cell of the compound where the polyhedra are interconnected by sharing edges, and **Figure 1.6(c)** corresponds to the view along the $[001]$ direction to easily appreciate the C_3 symmetry element in each coordination polyhedron.

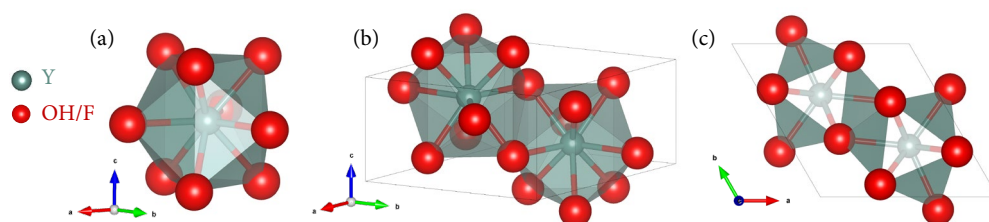


Figure 1.6. Structure of hexagonal $\text{Y}(\text{OH})_{3-x}\text{F}_x$: (a) coordination polyhedron of Y^{3+} , (b) unit cell, and (c) view along the $[001]$ direction.

1.3. Basics of luminescence

1.3.1. General considerations

The term luminescence, derived from the Latin words *lumen* (light) and *essentia* (essence or nature), was introduced by the German physicist Eilhard Wiedemann in 1888. Wiedemann coined this term to distinguish a particular phenomenon of light emission from incandescence, which is the emission of light caused by heat alone. Luminescence encompasses a broader range of physical processes in which the emission of light is not solely dependent on an increase in temperature [69].

According to the International Union of Pure and Applied Chemistry (IUPAC) Gold Book, luminescence can also be defined as the spontaneous emission of electromagnetic radiation by electronically excited species that are not in thermal equilibrium with their surroundings, a definition that intentionally excludes incandescence phenomena [70]. The interaction of light with matter is a fundamental concept in physics, and it plays a significant role in understanding the electromagnetic spectrum. When light interacts with matter, it can be absorbed (and then emitted), transmitted, reflected, refracted, scattered, or diffracted, depending on the properties of the material and the characteristics of the light [71,72], see **Figure 1.7**.

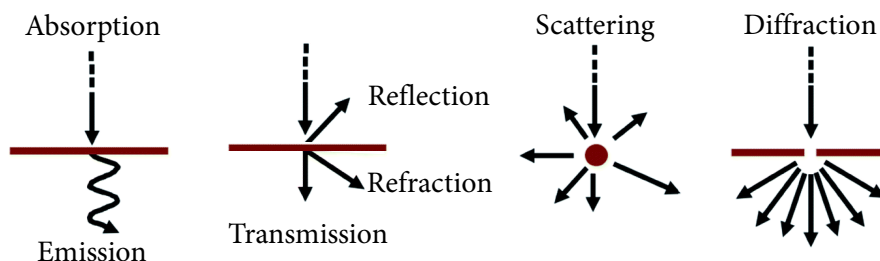


Figure 1.7. Different processes resulting from light-matter interactions. Adapted with permission from reference [72].

The electromagnetic spectrum covers a wide range of wavelengths or frequencies of electromagnetic radiation, including radio waves, microwaves, infrared radiation, visible light, ultraviolet radiation, X-rays, and gamma rays, as depicted in **Figure 1.8** [73]. Each region of the spectrum interacts with matter in different ways, and these interactions are based on the principles of quantum mechanics and electromagnetism. However, luminescence phenomena primarily focus on electromagnetic waves in the ultraviolet, visible, and near-infrared (NIR) spectral ranges.

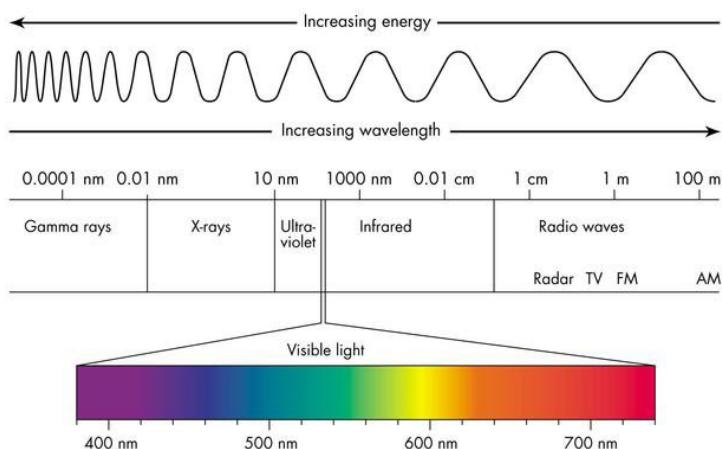


Figure 1.8. Electromagnetic spectrum highlighting the visible light range [73].

Luminescence phenomena can be classified depending on the type of excitation energy, as summarized in **Table 1.1** [74]. Among all of them, photoluminescence is of particular interest since it will be the luminescent phenomenon addressed in the present Doctoral Thesis. Photoluminescence refers to the emission of light from a material after it absorbs photons of higher energy (in the UV, visible, or NIR spectral range). When a material absorbs photons, its electrons become excited and move to higher energy levels. As these electrons return to their original energy levels, they release energy in the form of photons, resulting in the emission of light. As discussed

in detail in the following Section, photoluminescence can be formally divided into two categories: fluorescence and phosphorescence.

Table 1.1. Classification of luminescence phenomena according to the excitation source. Adapted with permission from reference [74].

Phenomenon	Excitation source	Example
Photoluminescence	Photons (UV, Vis, NIR)	Rhodamine
Chemiluminescence	Energy of chemical reactions	Luminol + H ₂ O ₂ + OH ⁻ + Fe ³⁺
Bioluminescence	Chemiluminescence in biological systems	Deep sea animals
Crystalloluminescence	Chemiluminescence in crystallization	Crystallization of As ₂ O ₃
Electroluminescence	Electric potential difference	Electronic displays
Cathodoluminescence	Electron beam	Cathode ray tubes
Thermoluminescence	Luminescence stimulated by heat (comprises the previous formation of excited states)	Chlorophan
Triboluminescence	Mechanic energy, friction	Sodium tartrate
Fractoluminescence	Mechanic energy, fracture	Ice
Piezoluminescence	Mechanic energy, pressure	KCl
Radioluminescence	Ionizing radiation (X-rays, γ -rays and β -radiation)	Scintillators
Ionoluminescence	Ion or α -particles beam	Polar auroras
Sonoluminescence	Ultrasound	Cr(CO) ₆

1.3.2. Photoluminescence

The processes that occur during an excitation cycle are commonly elucidated using a Jablonski diagram, an illustrative depiction of a molecule's diverse energy levels, **Figure 1.9**. Upon absorption of a photon, a molecule becomes electronically excited and assumes higher energy states such as S₁, S₂, and so forth. However, these excited states are transient, and molecules expeditiously undergo relaxation to reach the lowest vibrational level via a phenomenon known as vibrational relaxation (VR).

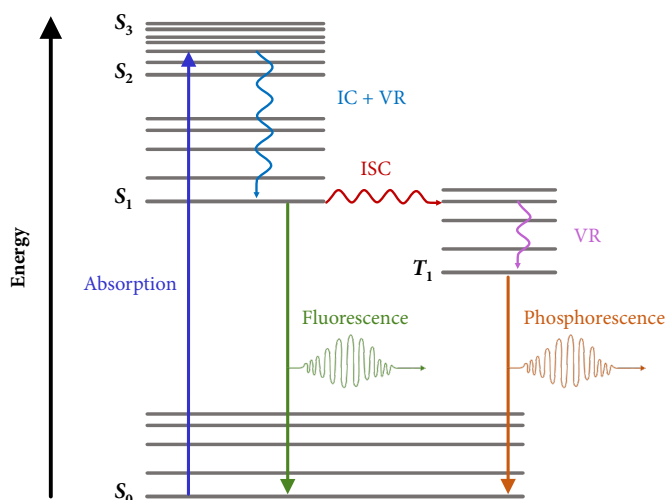


Figure 1.9. Jablonski diagram illustrating different energy levels and photophysical processes. IC: internal conversion, ISC: intersystem crossing, VR: vibrational relaxation.

Subsequently, molecules may undergo decay to the lowest electronic state through radiative or non-radiative processes. Non-radiative processes encompass internal conversion (IC) and intersystem crossing (ISC). IC refers to the relaxation of molecules between states characterized by the same spin multiplicity (referred to as S). Conversely, ISC takes place when the conversion is between states of differing spin multiplicities, involving both singlet (S) and triplet (T) states.

Concerning radiative processes, fluorescence and phosphorescence are salient phenomena. Fluorescence pertains to the emission of light from singlet-excited states (S_1), wherein the electron in the excited orbital manifests a distinct spin orientation relative to the electron in the ground state (S_0). As a result, the transition is spin-allowed and occurs promptly. On the other hand, phosphorescence corresponds to the emission of light from triplet-excited states (T_1), wherein the electron in the excited orbital exhibits the same spin orientation as the electron in the ground state (S_0). Therefore, the transition to the ground state is spin forbidden, resulting in

emission rates slower than those observed in fluorescence.

To summarize, fluorescence is characterized by the swift emission of light while the excitation source remains active, whereas phosphorescence entails a more gradual release of light that can continue even after the excitation source has been turned off.

1.3.2.1. Excitation and emission spectra

Apart from the acquisition of the absorption spectra, the most common photoluminescent measurements imply the obtention of the excitation and emission spectra, particularly when working with lanthanide ions.

The excitation spectrum reveals the specific wavelengths or energies at which the material efficiently absorbs light, leading to excitation and subsequent emission. This spectrum helps identify the optimal excitation conditions for maximizing the photoluminescent response of the material. To perform this type of measurement, a specific emission wavelength is fixed.

Prior to further discussion about the emission spectrum, it is important to recall some differences between absorption and excitation spectra. Both spectra are obtained by measuring the interaction of light with the material, but they serve different purposes and reveal distinct aspects of the material's properties that arise from the nature of the luminescent process and the measurements involved. As previously mentioned, the excitation spectrum can provide insights into the electronic structure and energy levels of the luminescent species, as well as any dependence on the excitation wavelength. The absorption spectrum, on the other hand, reveals the wavelengths of light that are absorbed by the sample and sheds light on the electronic transitions and absorptivity of the luminescent species.

Namely, the absorption spectrum shows the wavelengths of light that the material

absorbs, indicating the allowed energy transitions of the electrons within the material, while the excitation spectrum shows the wavelengths of light that efficiently induce luminescence in the material, providing information about the electronic transitions responsible for luminescence. See, as an example, **Figure 1.10** [75].

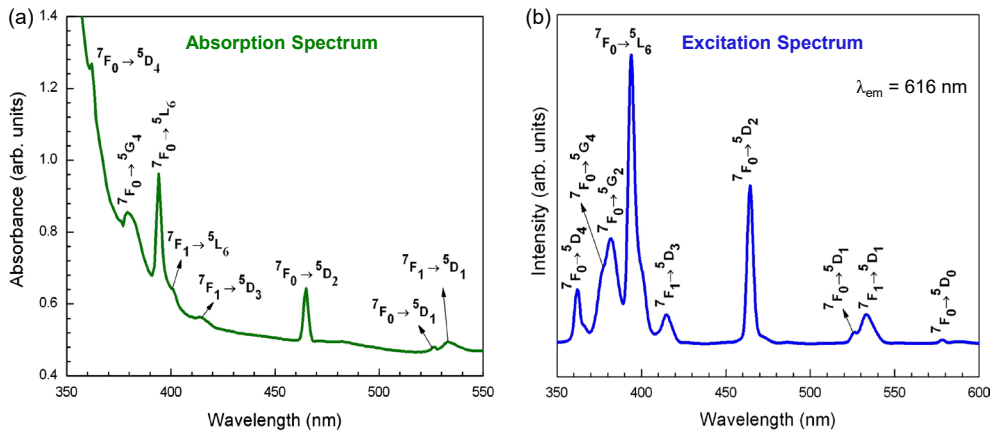


Figure 1.10. (a) Absorption and (b) excitation spectra of a Eu^{3+} -doped niobium oxyfluorosilicate glass. Adapted with permission from reference [75].

Regarding the emission spectrum, it refers to the range of wavelengths or energies of light that is emitted by a material after it has been excited by incident light (with a fixed value). This type of spectrum is essential for understanding the photoluminescent properties of a material. It can provide insights into the nature of electronic states, band structure, and energy transfer mechanisms. By analyzing the emission spectrum, it is possible to characterize the photoluminescent behavior of materials, such as the color or range of emitted light, the efficiency of emission, and the presence of any spectral shifts or broadening effects. A classical excitation and emission spectra for a Eu^{3+} -doped compound is presented in **Figure 1.11** [76]. As can be appreciated, the excitation spectrum also shows the presence of charge transfer bands (CTBs) that correspond to specific wavelengths or energy levels at which

electrons are transferred between different species within the material. When these charge transfer transitions occur, they can result in the absorption of light at distinct wavelengths, which becomes evident in the excitation spectrum generally as broad bands.

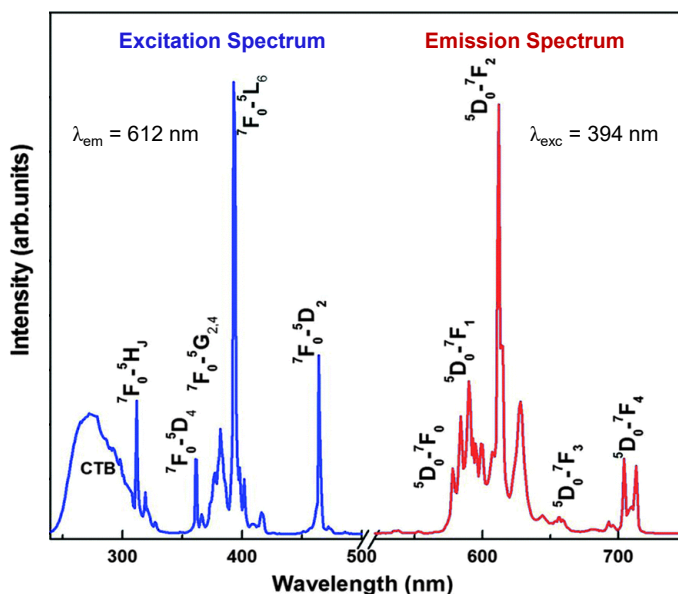


Figure 1.11. Excitation spectrum (in blue) recorded for an emission at 612 nm, and emission spectrum (in red) under 394 nm excitation of a $\text{Gd}_{2.85}\text{TaO}_7:0.15\text{Eu}^{3+}$ sample. CTB: charge transfer band. Adapted with permission from reference [76].

1.3.2.2. Time-resolved fluorescence spectroscopy

Time-resolved fluorescence (TRF) is a spectroscopy technique performed with pulsed excitation and is distinguished from steady-state luminescence measurements, in which a constant illumination and observation is used (e.g. common excitation and emission spectra).

TRF is used to study the decay kinetics of fluorescent molecules or fluorophores. It provides information about the excited-state lifetime of the fluorophore and can be

used to investigate various phenomena, such as molecular/ion interactions, energy transfer processes, and environmental changes [77].

In TRF, a sample containing fluorescent molecules/ions is excited with a short pulse of light which promotes the molecules/ions to higher energy levels. As the excited species return to their ground state, they emit fluorescence light. The time-resolved aspect of the technique involves measuring the decay of the fluorescence signal over time.

By correlating the arrival times of the detected photons with the timing of the excitation pulses, the decay profile of the fluorescence can be determined. The decay profile of the luminescent response is typically analyzed using exponential functions, and the decay kinetics are characterized by the fluorescence decay or lifetime. The fluorescence lifetime represents the average time the fluorophore spends in its excited state before returning to the ground state through various relaxation pathways [78].

Upon excitation of a sample containing a fluorophore using a light pulse, an initial population (N_0) of fluorophores in the excited state is generated. Over time, this population undergoes decay as a result of fluorescence emission and non-radiative processes. The decay process can be mathematically described by a differential equation:

$$\frac{dN(t)}{dt} = -(k_r + k_{nr}) N(t) \quad (1.1)$$

where $N(t)$ is the number of species in the excited state at time t . k_r and k_{nr} refer to the radiative and non-radiative constants, respectively, associated with the different existing physical phenomena that a sample undergoes after being excited [79]. The above equation can be reorganized and integrated as follows:

$$\int_{N_0}^{N(t)} \frac{1}{N(t)} dN(t) = -(k_r + k_{nr}) \int_0^t dt \quad (1.2)$$

$$\ln\left(\frac{N(t)}{N_0}\right) = -(k_r + k_{nr}) t \quad (1.3)$$

$$N(t) = N_0 \exp(-(k_r + k_{nr}) t) = N_0 \exp\left(\frac{-t}{\tau}\right) \quad (1.4)$$

where the lifetime is represented by τ .

In practice, it is only possible to observe luminescence intensity, I , rather than having a value for the excited/deexcited population. But as $I(t) \propto N(t)$, **equation 1.4** can also be written in terms of intensity, yielding the usual equation for a single exponential decay:

$$I(t) = I_0 \exp\left(\frac{-t}{\tau}\right) \quad (1.5)$$

Sometimes, it might be necessary to fit the decay curve to a multi-exponential model with the following expression:

$$I(t) = \sum_i I_i \exp\left(\frac{-t}{\tau_i}\right) \quad (1.6)$$

As previously noted, fluorescence phenomena occur fast (usually in a few ns), while phosphorescence materials have longer lifetimes (from μ s to ms). The diagram presented in **Figure 1.12** illustrates the contrasting decay behaviors of fluorescence and phosphorescence over time when the radiation source is deactivated. To differentiate between these phenomena, a pulsed source is utilized. This type of source is briefly activated and subsequently deactivated. In many fluorescent spectrophotometers, a pulsed source is employed, allowing the electronic components of the detector to synchronize with the pulsing of the source.

During fluorescence measurements, the detector registers signals only when the pulse is active. Conversely, in the case of phosphorescence measurements, a delay period (known as delay time) follows the termination of the pulse, during which the detector remains inactive. Subsequently, the detector is activated for a defined duration known as the gate time. In **Figure 1.12**, the diagram also indicates the potential settings for the delay and gate times, specific to the sample represented by the decay curves [80]. The appropriate gate time is determined, in part, by the rate at which the phosphorescence decays.

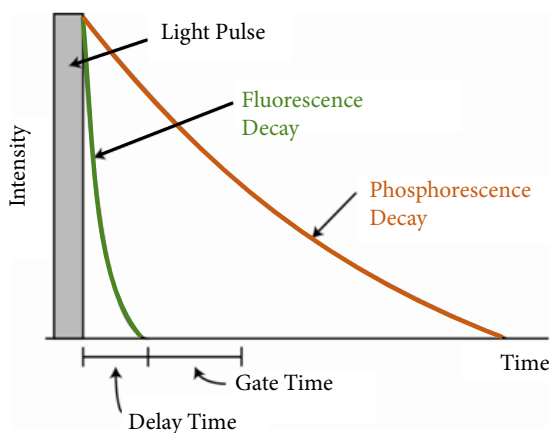


Figure 1.12. Fluorescence and phosphorescence decay profiles after a pulse of light [80].

1.3.2.3. Quantum yield

Luminescent materials transform excitation energy into photons, but this conversion is typically not completely efficient due to different losses that occur through alternative deactivation routes (non-radiative processes). Consequently, it becomes necessary to establish two extra parameters: the quantum yield (QY) and the quantum (energy) efficiency.

The QY, Φ , is a measure of the efficiency of light emission or luminescence in a

material. It is defined as the ratio of the number of photons emitted to the number of photons absorbed by the material:

$$\Phi = \frac{N_{\text{em}}}{N_{\text{abs}}} = \frac{k_r}{k_r + k_{nr}} \quad (1.7)$$

On the other hand, quantum efficiency (η) refers to energy and not to the number of photons:

$$\eta = \frac{E_{\text{output}}}{E_{\text{input}}} \quad (1.8)$$

The equality between QY and quantum efficiency ($\Phi = \eta$) is applicable only in the case of a primary photochemical process, such as resonant luminescence from a two-level system. A good example of the connection between Φ and η can be appreciated in **Figure 1.13** for different photoluminescence processes [81].

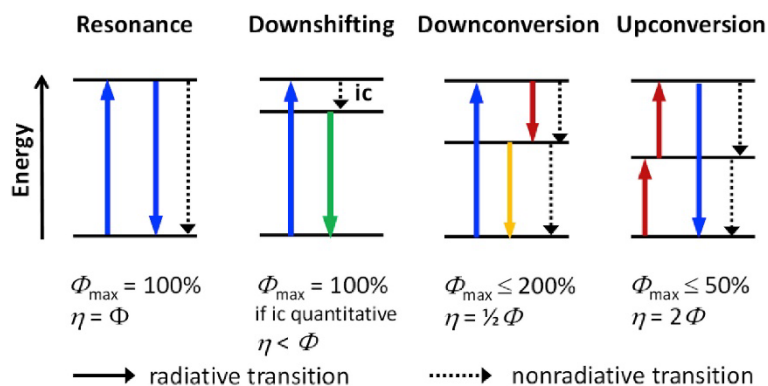


Figure 1.13. Simplified diagram illustrating resonant emission, downshifting, downconversion, and upconversion processes (ic = internal conversion). Adapted with permission from reference [81].

However, when a material exhibits energy transfers from the host-lattice, ligands, or different luminescent centers, the relationship between Φ and η can vary. For example, compounds exhibiting quantum cutting (QC) can have $\eta > 100\%$ [82–84].

QC refers to the conversion of a single high-energy photon into multiple lower-energy photons, although it should not be confused with downconversion since the latter one encompasses a broader range of processes that involve the conversion of photons to lower energies.

When the emitting entity is not directly excited to one of its energy levels (resonant emission), it becomes necessary to define two distinct QYs: the intrinsic QY (or quantum efficiency) and the overall (or absolute) QY. However, it must be noted that these parameters can have varying interpretations in different fields of study.

The overall QY concept and expression is the same as the one previously described, see **equation 1.7**. It can be obtained by measuring N_{em} and N_{abs} absolutely with an integrating sphere setup, which effectively bypasses the uncertainties associated with the use of inherent fluorescence standards [85].

The quantum efficiency η (intrinsic QY) adopts a similar expression but with the proviso that in this case the number of photons excited and emitted exclusively refers to the excited state from which the emission occurs ($N_{abs} = N_{excited\ state}$). The quantum efficiency of the luminescence material can be evaluated considering the calculated radiative lifetimes, τ_{rad} , and the observed (experimental) lifetimes, τ_{obs} , of the relevant state:

$$\eta = \frac{N_{em}}{N_{abs}} = \frac{k_r}{k_r + k_{nr}} = \frac{\tau_{obs}}{\tau_{rad}} \quad (1.9)$$

There are several ways of determining τ_{rad} depending on the fluorophore, but for the Eu^{3+} ion (which is the lanthanide ion used in this Doctoral Thesis), it can be directly calculated from the emission spectra [86–88], as will be outlined in the following Chapters.

1.4. Lanthanides

Lanthanides (Ln) are a group of chemical elements that belong to the *f*-block in the periodic table. They are located in period 6 and are positioned below the transition metals. The lanthanide series consists of 15 elements, starting with atomic number 57 (lanthanum, La) and ending with atomic number 71 (lutetium, Lu).

Lanthanides are also often referred to as rare earth (RE) elements, although not all rare earth elements are lanthanides. In fact, RE elements include the 15 lanthanides, scandium (Sc), and yttrium (Y). The term “rare earth” comes from their initial discovery when they were challenging to isolate and purify, leading to the misconception that they were scarce. However, in reality, some of these elements are relatively abundant in the Earth’s crust [89].

They are generally soft, malleable, and have relatively high densities. These elements have unique magnetic and optical properties, making them essential components in various applications, such as magnets, catalysts, lasers, and phosphors used in lighting and displays. Despite being utilized in small quantities, these elements have become indispensable to nearly every facet of modern life [90].

1.4.1. Electronic structure

The electron configuration of lanthanides follows the general pattern of $[\text{Xe}]4f^N 5d^0 6s^2$, where Xe represents the noble gas core (the electron configuration of xenon), and *N* is a number that varies from 0 to 14 depending on the specific lanthanide element.

Lanthanides typically exhibit a common oxidation state of +3 in their compounds. This is because they tend to lose three valence electrons from their $6s^2$ and $4f^N$ orbitals to attain a stable electronic configuration. The loss of three electrons results in the formation of a Ln^{3+} cation, which is the most stable and common oxidation state for

these elements. Some lanthanides can exhibit other oxidation states as well (+2 and +4), though they are less common but can find other interesting applications since the spectroscopic properties are very different in comparison to their trivalent counterparts [91]. For example, Eu^{2+} presents strong broad excitation and emission bands [92], while Tb^{4+} does not exhibit any emission, and when it is present within any host material, it functions as a quenching center [93]. **Table 1.2** shows the electron configurations of the lanthanides and their (di/tri/tetra)valent ions [94].

Table 1.2. Electron configurations of the lanthanides and their (di/tri/tetra)valent ions.

Element	Atom	Ln^{3+}	Ln^{4+}	Ln^{2+}
La	$[\text{Xe}]5d^1 6s^2$	$[\text{Xe}]$	–	–
Ce	$[\text{Xe}]4f^1 5d^1 6s^2$	$[\text{Xe}]4f^1$	$[\text{Xe}]$	–
Pr	$[\text{Xe}]4f^3 6s^2$	$[\text{Xe}]4f^2$	$[\text{Xe}]4f^1$	–
Nd	$[\text{Xe}]4f^4 6s^2$	$[\text{Xe}]4f^3$	$[\text{Xe}]4f^2$	$[\text{Xe}]4f^1$
Pm	$[\text{Xe}]4f^6 6s^2$	$[\text{Xe}]4f^4$	–	–
Sm	$[\text{Xe}]4f^6 6s^2$	$[\text{Xe}]4f^5$	–	$[\text{Xe}]4f^6$
Eu	$[\text{Xe}]4f^7 6s^2$	$[\text{Xe}]4f^6$	–	$[\text{Xe}]4f^7$
Gd	$[\text{Xe}]4f^7 5d^1 6s^2$	$[\text{Xe}]4f^7$	–	–
Tb	$[\text{Xe}]4f^9 6s^2$	$[\text{Xe}]4f^8$	$[\text{Xe}]4f^7$	–
Dy	$[\text{Xe}]4f^{10} 6s^2$	$[\text{Xe}]4f^9$	$[\text{Xe}]4f^8$	$[\text{Xe}]4f^{10}$
Ho	$[\text{Xe}]4f^{11} 6s^2$	$[\text{Xe}]4f^{10}$	–	–
Er	$[\text{Xe}]4f^{12} 6s^2$	$[\text{Xe}]4f^{11}$	–	–
Tm	$[\text{Xe}]4f^{13} 6s^2$	$[\text{Xe}]4f^{12}$	–	$[\text{Xe}]4f^{13}$
Yb	$[\text{Xe}]4f^{14} 6s^2$	$[\text{Xe}]4f^{13}$	–	$[\text{Xe}]4f^{14}$
Lu	$[\text{Xe}]4f^{14} 5d^1 6s^2$	$[\text{Xe}]4f^{14}$	–	–

The versatility of these elements arises from the distinct electronic and magnetic interactions facilitated by the $4f$ orbitals, which make them valuable components in

modern materials and technologies. The nature of the $4f$ orbitals, whose shape can be appreciated in **Figure 1.14**, results in weak interactions between the $4f$ electrons and the surrounding environment, primarily due to the shielding effect caused by the electrons in the $5s$ and $5p$ orbitals, as outlined in **Figure 1.15** [95,96].

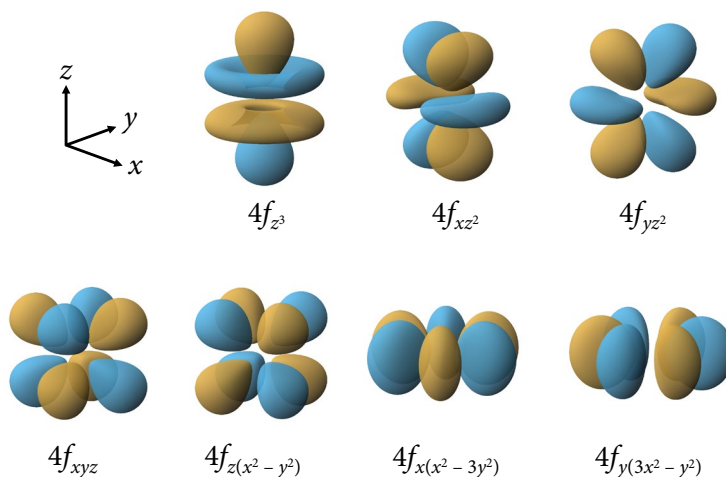


Figure 1.14. Shape of the hydrogenoid $4f$ orbitals. Yellow zones represent regions where the wavefunction Ψ_n is positive, while the blue regions denote negative values.

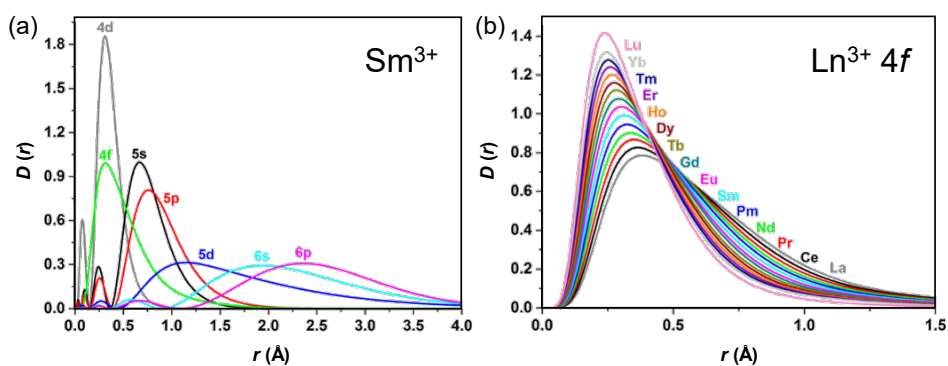


Figure 1.15. (a) Radial densities $D(r) = r^2 R(r)^2$ for $4d$, $5s$, $5p$, $4f$, $5d$, and $6s$ orbitals of Sm^{3+} . (b) Radial densities $D(r)$ of $4f$ orbitals from La^{3+} to Lu^{3+} . Adapted with permission from reference [96].

Considering the inherent character of the $4f$ wavefunctions and their limited extent of interaction with the outer orbitals, the resulting crystal field splitting is of minor magnitude, typically on the order of a few hundreds of cm^{-1} , in contrast with the common CF splitting of d orbitals observed in transition metals (several thousands of cm^{-1}). Furthermore, it is this shielding effect that accounts for the characteristic narrow lines observed in the electronic spectra of compounds based on Ln^{3+} ions [97]. The optical properties of Ln^{3+} ions are mainly related with intraconfigurational $4f-4f$ transitions. The energy levels in the $4f$ subshell are influenced by various factors, including the effective nuclear charge experienced by the $4f$ electrons, the shielding effect from inner electron shells, and the interactions between the electrons themselves. **Figure 1.16** depicts the energy levels scheme of the $4f^N$ configurations of Ln^{3+} free-ions in the energy range up to $40,000 \text{ cm}^{-1}$ [98].

The energy levels of the $4f$ electrons in Ln^{3+} ions are affected by the surrounding CF. When lanthanide ions are incorporated into different host material, the CF splits the degenerate $4f$ orbitals into distinct energy levels. This splitting is responsible for the characteristic luminescence and absorption spectra observed in lanthanide-based materials. The extent of energy level splitting depends on several factors, including the nature and arrangement of ligands, the coordination geometry, and the specific lanthanide ion involved [99]. Different ligands and crystal field environments can lead to varying magnitudes and patterns of energy level splitting [100]. However, as previously noted, this resulting crystal field splitting is of minor magnitude, typically on the order of a few hundreds of cm^{-1} . More information regarding the lanthanide photophysics can be found in Appendix 2.

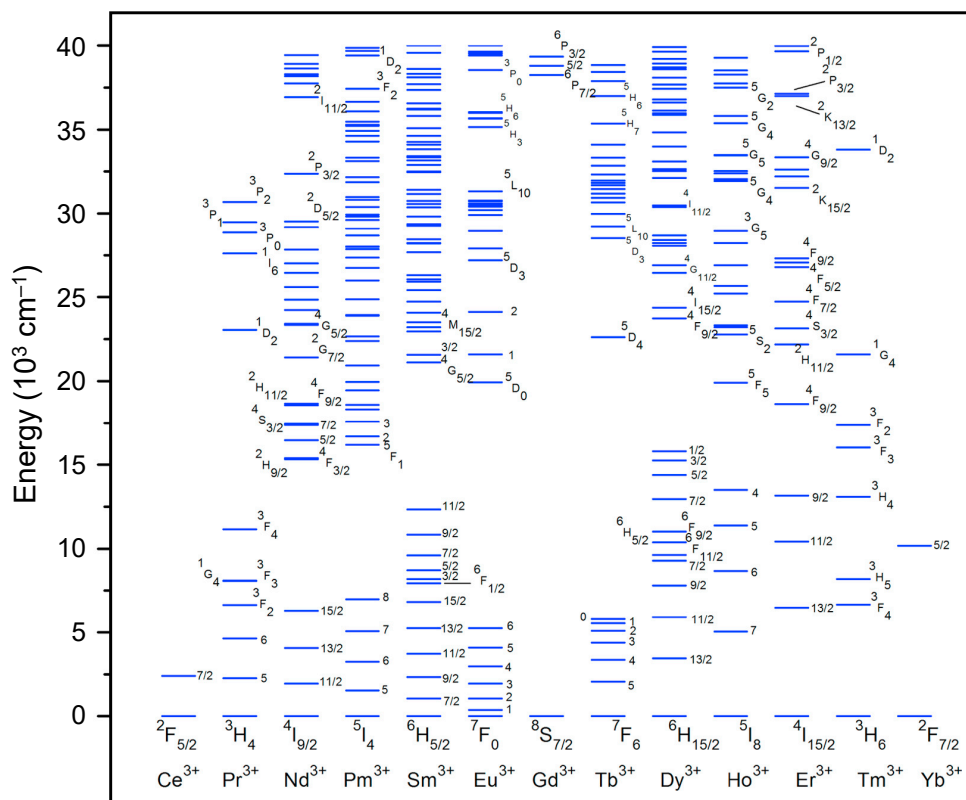


Figure 1.16. Energy levels scheme of the $4f^N$ configurations of Ln^{3+} free-ions in the energy range up to $40,000 \text{ cm}^{-1}$. Adapted with permission from reference [98].

1.4.2. Luminescent applications of lanthanides

Lanthanides have been integral to numerous groundbreaking inventions that have become indispensable in shaping our modern society. These rare earth elements possess unique properties that make them invaluable across a wide range of applications, revolutionizing various industries [101]. The adaptability of lanthanide-based luminescent materials, with their ability to be excited by diverse sources and emit light at different wavelengths, lifetimes, and band characteristics, makes them highly sought-after in numerous fields reliant on light-based technologies [102,103].

Some common applications of Ln^{3+} -doped materials encompass emitting diodes,

solar cells, lasers, or catalysts [104–106]. In addition, their excellent photostability and low cytotoxicity make them excellent candidates for being applied in bioanalytics and biomedics, for example as biomarkers for *in vivo* imaging [107–109]. The following subsections explore with further detail some of the main important applications.

1.4.2.1. Lanthanides in lighting and displays

Lanthanide-based phosphors have played a significant role in various display technologies, such as cathode-ray tube (CRT) televisions and monitors. These phosphors are crucial in converting high-energy electrons to visible light, enabling the creation of realistic and vibrant images on screens [110,111]. The golden age of lanthanide phosphors in the 1960s marked their commercialization, and they have been widely used in CRT displays for their ability to provide high color purity. Lanthanide phosphors come in different host materials, with specific lanthanides like Eu^{3+} , Tb^{3+} , and Eu^{2+} used for red, green, and blue emissions (RGB), respectively [112,113]. **Figure 1.17** depicts an illustrative scheme of a CRT where the use of phosphors with different colors (RGB) can be appreciated [114]. Although CRT displays are now niche products due to their bulkiness, lanthanide phosphors are still used in specialized applications like avionics and marine radar displays [115].

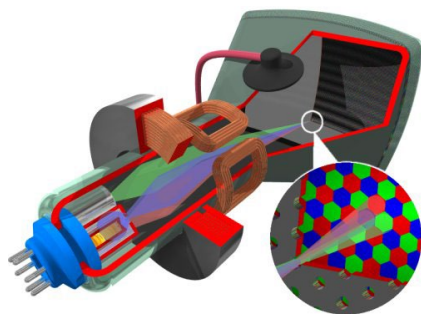


Figure 1.17. Illustrative scheme of a CRT where the use of phosphors with different colors (RGB) can be appreciated [114].

Light-emitting devices, such as LEDs and displays, rely on electrical pumping into semiconductor materials to convert electric energy into luminescence. Lanthanides are used in LEDs either by doping the semiconductor active layer to transform its emission wavelength or by coating the layers with lanthanide-based phosphors that can emit desired visible wavelengths [116]. The most efficient LEDs on the market are based on lanthanide luminophores, which have enabled high-efficiency light emission. In displays, Eu^{3+} -based red LEDs have gained much interest, and research is focused on improving lanthanide luminescence through different strategies [117]. **Figure 1.18(a)** shows the main components of a phosphor-based LED [118], while **Figure 1.18(b,c)** depicts the experimental setup of a LED using a Eu^{3+} -doped material as a phosphor [119].

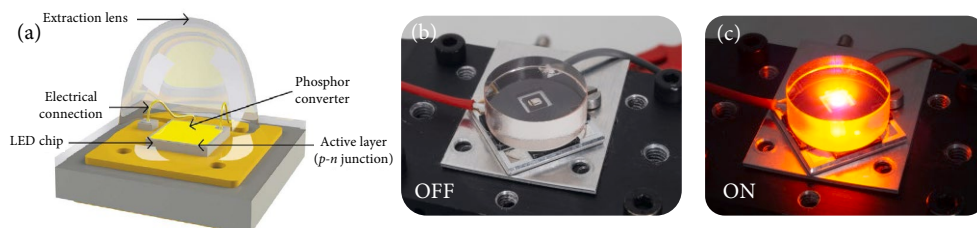


Figure 1.18. (a) Main components of a phosphor-based LED [118]. (b,c) experimental setup of a LED (OFF/ON) using a Eu^{3+} -doped material as a phosphor. Adapted with permission from reference [119].

On the other hand, hybrid organic-LEDs (OLEDs) based on lanthanides show great promise for applications in lighting and displays. OLEDs are currently replacing LEDs due to their higher performance in resolution and color rendering. Despite the strong electroluminescence efficiency of many lanthanide compounds, they are not yet widely employed in current OLED products, possibly due to supply chain issues.

1.4.2.2. Lanthanides in lasers

Lanthanide ions are crucial for the continuous development and applications of lasers on Earth and in space for communications. Lanthanides emitting in the near-infrared (NIR) range are highly efficient activators for lasers, with Nd:YAG being widely used, especially in spectroscopy [120]. Recent innovations, such as optical fibers and pumping diodes, have led to smaller and more powerful laser devices, benefiting material ablation in industries [121].

In the medical surgical sector, lasers with short pulses are used to deliver high-power densities in a single pulse, avoiding prolonged invasive treatments. Laser ablation, ranging from UV to NIR wavelengths, is a significant advancement in surgery. Femtosecond lasers based on Yb^{3+} dominate ophthalmic surgeries [122], while Nd^{3+} and Er^{3+} NIR lasers effectively treat deep tissues, including tumor removal [123]. Laser treatments are also applied in cosmetic surgeries for tattoo removal, cellulite or aging [124,125]. Aesthetic laser procedures, including dentistry and hair removal, are available as well and have found widespread attention among people [126,127].

1.4.2.3. Lanthanides for anti-counterfeiting

Counterfeiting is a significant global issue, with approximately \$500 billion USD of counterfeit goods sold each year, impacting various industries like footwear, textiles, jewelry, electronics, and pharmaceuticals. To combat counterfeiting, manufacturers use unique markers called taggants, which can be physical, chemical, or spectroscopic [128]. Spectroscopic taggants, especially phosphors containing lanthanide ions like europium and cerium, are preferred for their robust and bright emission spectra. Several companies offer anti-counterfeiting solutions using lanthanide-doped phosphors, with applications in banknotes, government documents, healthcare, food

packaging, and automotive industries. Lanthanide-doped phosphors are employed as spectroscopic taggants in banknotes and various documents by certain countries. When exposed to ultraviolet excitation, these luminescent features become visible on currencies and passports worldwide, as depicted in **Figure 1.19** [115]. While the exact composition of these phosphors is undisclosed, their use demonstrates the practicality of using lanthanide-doped phosphors to prevent counterfeiting.

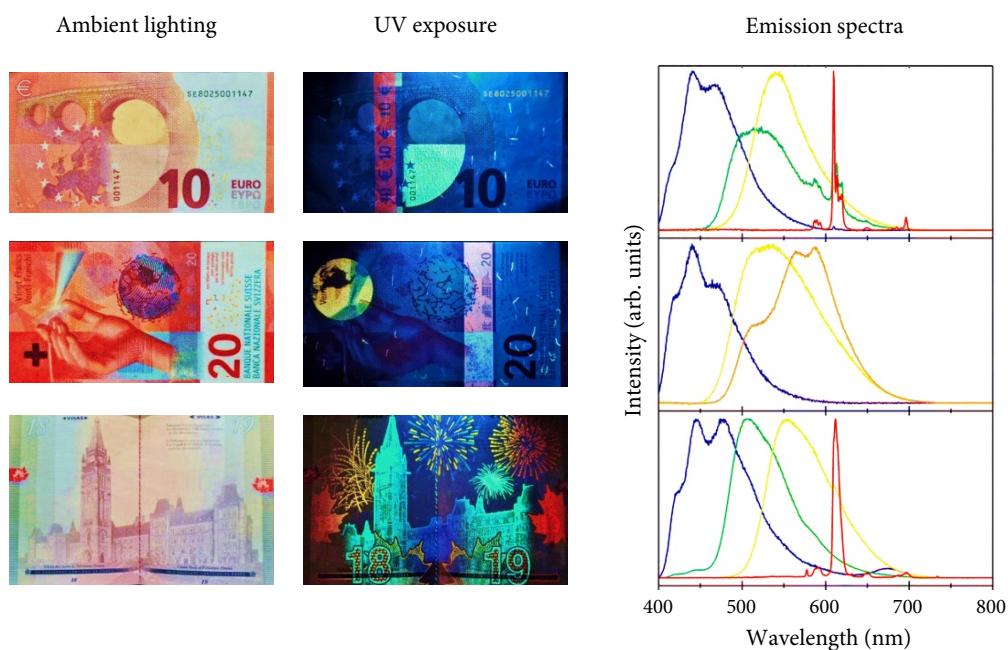


Figure 1.19. Banknotes and documents photographed under different lighting conditions for analysis. The selected documents, arranged from top to bottom, include a 10 € note, 20 Swiss francs note, and a visa page from a Canadian passport. Adapted with permission from reference [115].

1.4.3. The Eu^{3+} ion

In this Doctoral Thesis, the Eu^{3+} ion has been chosen among all the lanthanides due to its particular optical behavior. In the subsequent chapters, particularly Chapter 9 which focuses on the Eu^{3+} luminescence in solid-state hosts, very detailed information

regarding specific aspects will be provided. For the sake of brevity, a concise overview of the key features is presented here.

Europium, with an atomic number of 63, stands out as one of the most intriguing elements within the lanthanide series, particularly in its +3 oxidation state (Eu^{3+} , with a $[\text{Xe}]4f^6$ electronic configuration). Compounds containing europium typically exhibit a red emission, see **Figure 1.20** [129], ascribed to the $^5\text{D}_0 \rightarrow ^7\text{F}_j$ transitions. An example of the excitation and emission spectra have been shown previously in **Figure 1.11**.

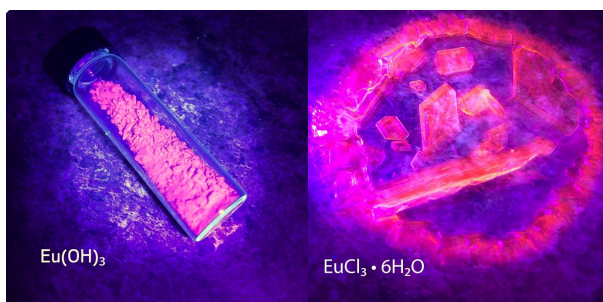


Figure 1.20. Red emission of $\text{Eu}(\text{OH})_3$ and $\text{EuCl}_3 \cdot 6\text{H}_2\text{O}$ compounds under exposure to UV light [129].

The Eu^{3+} -doped compounds have numerous significant properties and find diverse applications in solid-state lighting, display devices, solar cells, optical detectors, medical imaging, and tumor detection, among others [130–132].

The emission spectra lines are typically sharp and influenced by the crystal field surrounding the europium ions [133]. This characteristic proves valuable in determining the symmetry and geometry of complex species, where europium can act as a site-sensitive structural probe [134–136], which can be beneficial for examining the optical behavior of the materials and properly understanding the structure-property relationship. Indeed, it is reasonable to infer the site-selective symmetries of

Eu³⁺ ions by analyzing the emission profile and the number of Starks components for each $^5D_0 \rightarrow ^7F_j$ transition.

Some examples of absorption, excitation, and emission spectra of different Eu³⁺-doped compounds can be found in the previous **Figures 1.10** and **1.11**.

1.5. Synthesis methods

This Section provides a comprehensive overview of the key synthetic methods employed in this Doctoral Thesis for the synthesis of the materials. The main techniques utilized are succinctly presented, highlighting their significance in the research.

1.5.1. Coprecipitation method

The coprecipitation method is highly advantageous for incorporating doping lanthanides ions into nanophosphors, leading to the formation of solid solutions with a narrow size distribution. Unlike other methods, coprecipitation offers convenience without the need for expensive equipment, stringent reaction conditions, or complex procedures [137].

In synthetic methodologies employing the coprecipitation process, metallic precursors are dissolved, and subsequently, a precipitating agent is introduced to induce the formation of a solid precipitate. Generally, bases such as NaOH, KOH, NH₄OH, among others, are utilized as precipitating agents. The addition of the precipitating agent initiates the nucleation and subsequent growth of the solid phase. The resulting precipitate can either be allowed to mature for a defined period to enhance its crystallinity or undergo a post-treatment step, such as calcination, to further modify its properties [138]. The coprecipitation technique offers a versatile

and straightforward approach to obtaining desired solid materials with a homogeneous size distribution, making it a widely employed method in various fields of material synthesis. Therefore, it has also been a good strategy to obtain complex fluorides [139–141].

1.5.2. Sonochemical synthesis

Sonochemistry has revolutionized the field of inorganic material synthesis, providing a cost-effective and environmentally friendly route to produce materials with desired properties and functionalities, including novel fluoride-based compounds [142–144]. One notable advantage is the ability to achieve controlled structures, shapes, and crystallinity of chemical compounds at room temperature. This is particularly significant as it eliminates the need for high-pressure or high-temperature conditions. In addition, ultrasound-induced reactions have significantly reduced reaction times, particularly when water is used as a solvent, and improved product yields [145].

Sonochemical reactions are initiated by the application of ultrasonic radiations (with frequencies in the range of 20 kHz to 1 MHz), which generate localized regions of high energy known as hot spots. These hot spots can reach extraordinary temperatures above 5000 K, pressures exceeding 1000 atm, and heating and cooling rates higher than 10^{10} K/s [146,147].

The localized hot spots generated by ultrasound waves create intense cavitation phenomena [148]. Cavitation refers to the formation, growth, and collapse of small gas bubbles in a liquid medium, as can be appreciated in **Figure 1.21**. This phenomenon leads to a range of chemical and physical effects, such as the breaking of chemical bonds, enhanced mass transfer, and the generation of highly reactive species [147].

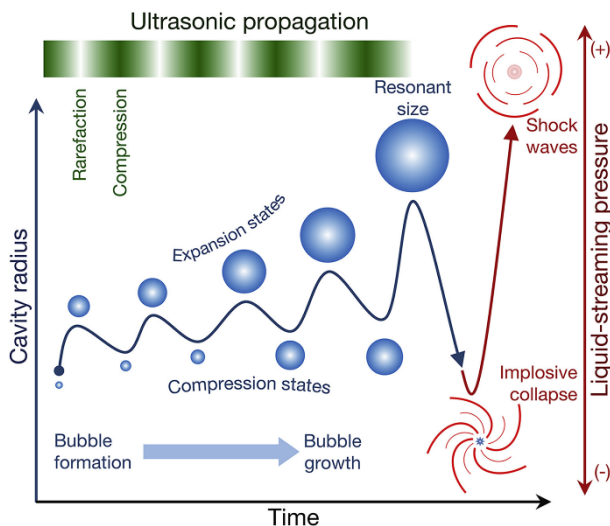


Figure 1.21. Illustration of acoustic cavitation occurring during external ultrasonic propagation, as well as the subsequent rebounding shock waves following the implosive collapse. Reprinted with permission from reference [148].

1.5.3. Hydrothermal synthesis

The hydrothermal method has found widespread application in creating advanced inorganic materials that are challenging or unattainable through high-temperature solid-state reactions. Numerous innovative hydrothermal reactions have been devised specifically for synthesizing complex fluorides [68,149–153]. Hydrothermal synthesis offers several advantages, including the use of relatively gentle conditions, and a streamlined single-step process [154]. Particularly, the hydrothermal method has proven to be highly effective in controlling the morphologies, sizes, and crystal phases of inorganic materials [155,156]. See **Figure 1.22** as an example of the tunable morphology of (α/β) - NaYF_4 fluorides [157].

The hydrothermal method involves employing an aqueous solution within a Teflon-lined vessel (which is put inside a sealed autoclave, as shown in **Figure 1.23**) to establish a high-temperature, high-pressure reaction environment through the

application of heat and pressure (or the generation of vapor pressure as a consequence of heating the medium above the boiling point of water) that induces the formation of the desired product [158].

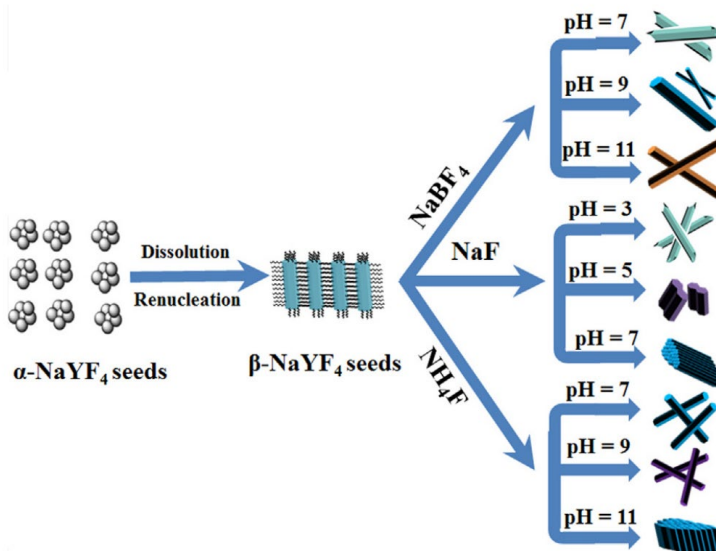


Figure 1.22. Scheme for the effects of pH values and fluoride sources in the crystal growth and morphology of $(\alpha/\beta)\text{-NaYF}_4$ fluorides prepared under hydrothermal conditions. Reprinted with permission from reference [157].



Figure 1.23. Autoclave with a Teflon-lined vessel to carry out hydrothermal reactions.

In hydrothermal reactions, the mechanism primarily follows a liquid nucleation model [159], which distinguishes it from solid-state reactions where atom or ion

diffusion at the reactant interface plays a key role. The steps involved in crystalline growth under hydrothermal conditions can be summarized as follows [160]:

- 1) Dissolution: Reactants dissolve as ions or molecular groups in a hydrothermal medium.
- 2) Separation and transport: temperature gradients separate and move ions/molecules to a cooler region, enabling seed crystal growth and supersaturated solution formation.
- 3) Adsorption, decomposition, and movement: species adsorb, decompose, and desorb at the growth interface, with the adsorbed material moving along the interface.
- 4) Crystallization of the dissolved species to form the final compound.

However, it is also important to note that sometimes an incipient and amorphous precipitate is treated hydrothermally to yield the desired crystal phase. Thus, the incipient solid may suffer from redissolution-crystallization processes.

References

- [1] M. Itoh, T. Akatsu, M. Azuma, K. Kamata, T. Kamiya, *Sci. Technol. Adv. Mater.* 16 (2015) 020302.
- [2] A.K. Cheetham, *Science*. 264 (1994) 794–795.
- [3] T. Ayode Otitoju, P. Ugochukwu Okoye, G. Chen, Y. Li, M. Onyeka Okoye, S. Li, *J. Ind. Eng. Chem.* 85 (2020) 34–65.
- [4] A.D. Terna, E.E. Elemike, J.I. Mbonu, O.E. Osafire, R.O. Ezeani, *Mater. Sci.*

- Eng. B.* 272 (2021) 115363.
- [5] M.S. Ramkumar, R. Priya, R.F. Rajakumari, P. Valsalan, M.K. Chakravarthi, G.C.P. Latha, S. Mathupriya, K. Rajan, *J. Nanomater.* 2022 (2022) 8648284.
- [6] C. Yao, Y. Ma, *iScience.* 24 (2021) 102541.
- [7] A. Blázquez-Castro, A. García-Cabañes, M. Carrascosa, *Appl. Phys. Rev.* 5 (2018) 041101.
- [8] A. Jain, Y.G. Wang, L.N. Shi, *J. Alloys Compd.* 928 (2022) 167066.
- [9] X. Wang, X. Zhong, J. Li, Z. Liu, L. Cheng, *Chem. Soc. Rev.* 50 (2021) 8669–8742.
- [10] S.A. Mazari, E. Ali, R. Abro, F.S.A. Khan, I. Ahmed, M. Ahmed, S. Nizamuddin, T.H. Siddiqui, N. Hossain, N.M. Mubarak, A. Shah, *J. Environ. Chem. Eng.* 9 (2021) 105028.
- [11] H. Suo, X. Zhao, Z. Zhang, Y. Wang, J. Sun, M. Jin, C. Guo, *Laser Photonics Rev.* 15 (2021) 2000319.
- [12] S. Yuan, J. Wang, Y. Xiang, S. Zheng, Y. Wu, J. Liu, X. Zhu, Y. Zhang, *Small.* 18 (2022) 2200020.
- [13] L. Huang, S. Cao, Y. Liang, J. Chen, T. Yang, J. Zhao, B. Zou, *J. Mater. Chem. C.* 11 (2023) 10107–10120.
- [14] G.C. Righini, C. Armellini, M. Ferrari, A. Carlotto, A. Carpentiero, A. Chiappini, A. Chiasera, A. Lukowiak, T.N.L. Tran, S. Varas, *Materials.* 16 (2023) 2724.
- [15] J. Liu, A.M. Kaczmarek, F. Artizzu, R. Van Deun, *ACS Photonics.* 6 (2019) 659–

666.

- [16] J. del-Castillo, J. Méndez-Ramos, P. Acosta-Mora, A.C. Yanes, *J. Lumin.* 241 (2022) 118490.
- [17] Y. Zhang, W. Ying, J. He, X. Fan, S. Xu, J. Gu, S. Liu, *Dalt. Trans.* 52 (2023) 2948–2955.
- [18] F.E. Maturi, A. Gaddam, C.D.S. Brites, J.M.M. Souza, H. Eckert, S.J.L. Ribeiro, L.D. Carlos, D. Manzani, *Chem. Mater.* 35 (2023) 7229–7238.
- [19] F. Wang, X. Liu, Rare-earth doped upconversion nanophosphors, in: D.L. Andrews, G.D. Scholes, G.P. Wiederrecht (Eds.), *Comprehensive Nanoscience and Nanotechnology*, Elsevier, 2011: pp. 607–635.
- [20] A. Gulzar, J. Xu, P. Yang, F. He, L. Xu, *Nanoscale.* 9 (2017) 12248–12282.
- [21] P. Serna-Gallén, H. Beltrán-Mir, E. Cordoncillo, *Opt. Laser Technol.* 136 (2021) 106734.
- [22] A. Jain, S.P. Ong, G. Hautier, W. Chen, W.D. Richards, S. Dacek, S. Cholia, D. Gunter, D. Skinner, G. Ceder, K.A. Persson, *APL Mater.* 1 (2013) 0011002.
- [23] A.J. Stevenson, H. Serier-Brault, P. Gredin, M. Mortier, *J. Fluor. Chem.* 132 (2011) 1165–1173.
- [24] C. Li, J. Lin, *J. Mater. Chem.* 20 (2010) 6831–6847.
- [25] F. Pellé, F. Auzel, *J. Alloys Compd.* 300–301 (2000) 131–140.
- [26] R.K. Sharma, A.V. Mudring, P. Ghosh, *J. Lumin.* 189 (2017) 44–63.
- [27] M. Mortier, Y.D. Huang, F. Auzel, *J. Alloys Compd.* 300–301 (2000) 407–413.

- [28] V.B. Pawade, N.R. Pawar, S.J. Dhoble, *Infrared Phys. Technol.* 123 (2022) 104148.
- [29] C. Sun, M. Schäferling, U. Resch-Genger, M. Gradzielski, *ChemNanoMat.* 7 (2021) 174–183.
- [30] R.K. Sharma, A.V. Mudring, P. Ghosh, *J. Lumin.* 189 (2017) 44–63.
- [31] X.F. Huang, X. Bin Yang, D. Zhao, L.P. Ma, Y.Z. Bao, *Opt. Mater. (Amst).* 126 (2022) 112134.
- [32] N. Pawlik, B. Szpikowska-Sroka, T. Goryczka, E. Pietrasik, W.A. Pisarski, *Nanomaterials.* 12 (2022) 259.
- [33] L. Zhang, T. Guo, Y. Ren, Y. Cai, M.D. Mackenzie, A.K. Kar, Y. Yao, *Opt. Commun.* 441 (2019) 8–13.
- [34] W. Wang, J. Tian, N. Li, J. Dong, Q. Wang, Y. Xue, X. Xu, H. Tang, H. Lin, D. Li, J. Xu, *J. Alloys Compd.* 887 (2021) 161327.
- [35] A. Pant, X. Xia, E.J. Davis, P.J. Pauzauskie, *Nat. Commun.* 11 (2020) 3235.
- [36] F. Carl, L. Birk, B. Grauel, M. Pons, C. Würth, U. Resch-Genger, M. Haase, *Nano Res.* 14 (2021) 797–806.
- [37] Y. Zhuang, D. Chen, W. Chen, W. Zhang, X. Su, R. Deng, Z. An, H. Chen, R.J. Xie, *Light Sci. Appl.* 10 (2021) 132.
- [38] M.F. Torresan, A. Wolosiuk, *ACS Appl. Bio Mater.* 4 (2021) 1191–1210.
- [39] B.M. Cruz, T.S. Lilge, A.B. Andrade, R.P.R. Moura, M.A.R.C. Alencar, J.J. Rodrigues, M.E.G. Valerio, Z.S. Macedo, *Opt. Mater. (Amst).* 131 (2022) 112661.

- [40] R. Bajaj, A.S. Rao, G.V. Prakash, *J. Alloys Compd.* 885 (2021) 160893.
- [41] C. Cressoni, F. Vurro, E. Milan, M. Muccilli, F. Mazzer, M. Gerosa, F. Boschi, A.E. Spinelli, D. Badocco, P. Pastore, N.F. Delgado, M.H. Collado, P. Marzola, A. Speghini, *ACS Appl. Mater. Interfaces.* 15 (2023) 12171–12188.
- [42] X. Wang, G. De, Y. Liu, *Mater. Res. Bull.* 110 (2019) 181–189.
- [43] E.N. Silva, A.P. Ayala, J.Y. Gesland, R.L. Moreira, *Vib. Spectrosc.* 37 (2005) 21–26.
- [44] R.D. Shannon, *Acta Crystallogr.* A32 (1976) 751–767.
- [45] G. Chen, H. Qiu, R. Fan, S. Hao, S. Tan, C. Yang, G. Han, *J. Mater. Chem.* 22 (2012) 20190–20196.
- [46] G. Murali, B.H. Lee, R.K. Mishra, J.M. Lee, S.H. Nam, Y.D. Suh, D.K. Lim, J.H. Lee, S.H. Lee, *J. Mater. Chem. C.* 3 (2015) 10107–10113.
- [47] Z. Gao, Z. Lai, K. Lu, S. Guo, L. Liu, F. He, P. Yang, J. Ren, J. Zhang, J. Yang, *Opt. Lett.* 44 (2019) 4674.
- [48] L. Zhu, Y. Liu, X. Fan, D. Yang, X. Cao, *J. Lumin.* 131 (2011) 1380–1385.
- [49] S. Goderski, M. Runowski, S. Lis, *J. Rare Earths.* 34 (2016) 808–813.
- [50] L. Zhu, J. Meng, X. Cao, *Mater. Lett.* 62 (2008) 3007–3009.
- [51] C. Cao, *J. Mater. Res. Soc.* 27 (2012) 2988–2995.
- [52] M. Runowski, *J. Lumin.* 186 (2017) 199–204.
- [53] M. Runowski, S. Goderski, J. Paczesny, M. Ksiezopolska-Gocalska, A. Ekner-Grzyb, T. Grzyb, J.D. Rybka, M. Giersig, S. Lis, *J. Phys. Chem. C.* 120 (2016)

- 23788–23798.
- [54] L. Gomes, H.M. Linhares, R.U. Ichikawa, L.G. Martinez, S.L. Baldochi, *Opt. Mater. (Amst)*. 54 (2016) 57–66.
- [55] A. Grzechnik, K. Friese, *Solid State Sci.* 30 (2014) 61–67.
- [56] M. Chen, P. Loiko, J.M. Serres, S. Veronesi, M. Tonelli, M. Aguiló, F. Díaz, S.Y. Choi, J.E. Bae, F. Rotermund, S. Dai, Z. Chen, U. Griebner, V. Petrov, X. Mateos, *J. Alloys Compd.* 813 (2020) 152176.
- [57] F. Le Berre, E. Boucher, M. Allain, G. Courbion, *J. Mater. Chem.* 10 (2000) 2578–2586.
- [58] P. Villars, K. Cenzual, eds., KY_3F_{10} Crystal Structure: Datasheet from “PAULING FILE Multinaries Edition – 2012” in Springer Materials (https://materials.springer.com/isp/crystallographic/docs/sd_0552093).
- [59] A. Grzechnik, J. Nuss, K. Friese, J.-Y. Gesland, M. Jansen, *Z. Krist. NCS.* 217 (2002) 460.
- [60] R.U. Ichikawa, H.M.S.M.D. Linhares, I. Peral, S.L. Baldochi, I.M. Ranieri, X. Turrillas, L.G. Martinez, *ACS Omega.* 2 (2017) 5128–5136.
- [61] P. Serna-Gallén, H. Beltrán-Mir, E. Cordoncillo, *J. Mater. Res. Technol.* 15 (2021) 6940–6946.
- [62] N.F. Stephens, P. Lightfoot, *J. Solid State Chem.* 180 (2007) 260–264.
- [63] B.E.G. Lucier, K.E. Johnston, D.C. Arnold, J.L. Lemyre, A. Beaupré, M. Blanchette, A.M. Ritcey, R.W. Schurko, *J. Phys. Chem. C.* 118 (2014) 1213–1228.

- [64] P. Villars, K. Cenzual, eds., YF_3 Crystal Structure: Datasheet from “PAULING FILE Multinaries Edition – 2012” in Springer Materials (https://materials.springer.com/isp/crystallographic/docs/sd_1802348)
- [65] H.-G. Liu, W.-C. Zheng, *Phys. B Condens. Matter.* 496 (2016) 15–19.
- [66] P. Villars, K. Cenzual, eds., $\text{Y(OH)}_{1.57}\text{F}_{1.43}$ ($\text{Y(OH)}_2\text{F}$) Crystal Structure: Datasheet from “PAULING FILE Multinaries Edition – 2012” in Springer_Materials_ (https://materials.springer.com/isp/crystallographic/docs/sd_1900591).
- [67] T.Y. Sun, D.Q. Zhang, X.F. Yu, Y. Xiang, M. Luo, J.H. Wang, G.L. Tan, Q.Q. Wang, P.K. Chu, *Nanoscale.* 5 (2013) 1629–1637.
- [68] J. Li, X. Wang, Q. Zhu, B.N. Kim, X. Sun, J.G. Li, *RSC Adv.* 7 (2017) 53032–53042.
- [69] B. Valeur, M.N. Berberan-Santos, *J. Chem. Educ.* 88 (2011) 731–738.
- [70] J.W. Verhoeven, *Pure Appl. Chem.* 68 (1996) 2223–2286.
- [71] G. Blasse, B.C. Grabmaier, *Luminescent Materials*, Springer-Verlag Berlin Heidelberg, Germany, 1994.
- [72] M. Testa-Anta, M.A. Ramos-Docampo, M. Comesaña-Hermo, B. Rivas-Murias, V. Salgueiriño, *Nanoscale Adv.* 1 (2019) 2086–2103.
- [73] <https://www.cyberphysics.co.uk/topics/light/emspect.htm>. (Accessed June 22, 2023)
- [74] P.C. De Sousa Filho, J.F. Lima, O.A. Serra, *J. Braz. Chem. Soc.* 26 (2015) 2471–2495.

- [75] D. Ramachari, L. Rama Moorthy, C.K. Jayasankar, *J. Lumin.* 143 (2013) 674–679.
- [76] L.T. Francis, P. Prabhakar Rao, M. Thomas, S.K. Mahesh, V.R. Reshmi, T.S. Sreena, *Phys. Chem. Chem. Phys.* 16 (2014) 17108–17115.
- [77] J.R. Lakowicz, Introduction to Fluorescence, in: *Principles of Fluorescence Spectroscopy*, Springer, 2006: pp. 1–26.
- [78] J.R. Lakowicz, Time-Domain Lifetime Measurements, in: *Principles of Fluorescence Spectroscopy*, Springer, 2006: pp. 97–155.
- [79] A. Jain, C. Blum, V. Subramaniam, Fluorescence Lifetime Spectroscopy and Imaging of Visible Fluorescent Proteins, in: *Advances in Biomedical Engineering*, Elsevier, 2008: pp. 147–176.
- [80] T. Wenzel, Molecular and atomic spectroscopy, LibreTexts Chemistry, Bates College, 2023.
- [81] K.L. Wong, J.C.G. Bünzli, P.A. Tanner, *J. Lumin.* 224 (2020) 117256.
- [82] X. Chen, J. Wu, X. Xu, Y. Zhang, N. Sawanobori, C. Zhang, Q. Pan, G.J. Salamo, *Opt. Lett.* 34 (2009) 887.
- [83] X. Chen, G.J. Salamo, S. Li, J. Wang, Y. Guo, Y. Gao, L. He, H. Ma, J. Tao, P. Sun, W. Lin, Q. Liu, *Phys. B Condens. Matter.* 479 (2015) 159–164.
- [84] Y. Liu, J. Zhang, C. Zhang, J. Jiang, H. Jiang, *J. Phys. Chem. C.* 120 (2016) 2362–2370.
- [85] J. Hu, C.Y. Zhang, *Anal. Chem.* 85 (2013) 2000–2004.
- [86] P. Ghosh, A. Patra, *J. Phys. Chem. C.* 112 (2008) 19283–19292.

- [87] X.-N. Tian, G.-C. Jiang, X.-T. Wei, L.-Y. Wu, S. Li, K.-M. Deng, Y.H. Chen, M. Yin, *J. Nanosci. Nanotechnol.* 14 (2014) 4490–4494.
- [88] M.H.V. Werts, R.T.F. Jukes, J.W. Verhoeven, *Phys. Chem. Chem. Phys.* 4 (2002) 1542–1548.
- [89] S.H. Shin, H.O. Kim, K.T. Rim, *Saf. Health Work.* 10 (2019) 409–419.
- [90] J.-C.G. Bünzli, Lanthanides, in: *Kirk-Othmer Encyclopedia of Chemical Technology*, Wiley Blackwell, 2004.
- [91] M. Suta, C. Wickleder, *J. Lumin.* 210 (2019) 210–238.
- [92] Y. Zhang, X. Li, K. Li, H. Lian, M. Shang, J. Lin, *ACS Appl. Mater. Interfaces.* 7 (2015) 2715–2725.
- [93] R.K. Verma, K. Kumar, S.B. Rai, *Solid State Sci.* 12 (2010) 1146–1151.
- [94] S. Cotton, *Lanthanide and Actinide Chemistry*, John Wiley & Sons Ltd, 2006.
- [95] A.N. Carneiro Neto, R.T. Moura, *Chem. Phys. Lett.* 757 (2020) 137884.
- [96] J.B. Lu, D.C. Cantu, M.T. Nguyen, J. Li, V.A. Glezakou, R. Rousseau, *J. Chem. Theory Comput.* 15 (2019) 5987–5997.
- [97] J.-C.G. Bünzli, S. V. Eliseeva, Basics of Lanthanide Photophysics, in: P. Hänninen, H. Härmä (Eds.), *Lanthanide Luminescence: Photophysical, Analytical and Biological Aspects*, Springer, 2010.
- [98] C.G. Ma, M.G. Brik, D.X. Liu, B. Feng, Y. Tian, A. Suchocki, *J. Lumin.* 170 (2016) 369–374.
- [99] G.H. Dieke, H.M. Crosswhite, *Appl. Opt.* 2 (1963) 675–686.

- [100] K. Binnemans, *Chem. Rev.* 109 (2009) 4283–4374.
- [101] J.A. Cotruvo, *ACS Cent. Sci.* 5 (2019) 1496–1506.
- [102] J.C.G. Bünzli, C. Piguet, *Chem. Soc. Rev.* 34 (2005) 1048–1077.
- [103] C. Ronda, *Prog. Electromagn. Res.* 147 (2014) 81–93.
- [104] J. Wu, J. Wang, J. Lin, Y. Xiao, G. Yue, M. Huang, Z. Lan, Y. Huang, L. Fan, S. Yin, T. Sato, *Sci. Rep.* 3 (2013) 1–5.
- [105] B.M. Tissue, *Chem. Mater.* 10 (1998) 2837–2845.
- [106] T. Grzyb, M. Węclawiak, T. Pędziński, S. Lis, *Opt. Mater. (Amst).* 35 (2013) 2226–2233.
- [107] M. Deng, Y. Ma, S. Huang, G. Hu, L. Wang, *Nano Res.* 4 (2011) 685–694.
- [108] A. Podhorodecki, A. Noculak, M. Banski, B. Sojka, A. Zelazo, J. Misiewicz, J. Cichos, M. Karbowski, B. Zasonska, D. Horak, B. Sikora, D. Elbaum, T. Dumych, R. Bilyy, M. Szewczyk, *ECS Trans.* 61 (2014) 115–125.
- [109] A. Jain, P.G.J. Fournier, V. Mendoza-Lavaniegos, P. Sengar, F.M. Guerra-Olvera, E. Iñiguez, T.G. Kretschmar, G.A. Hirata, P. Juárez, *J. Nanobiotechnology.* 16 (2018) 1–18.
- [110] N. Katoh, T. Deguchi, R.S. Berns, *Opt. Rev.* 8 (2001) 305–314.
- [111] L. Ozawa, M. Itoh, *Chem. Rev.* 103 (2003) 3835–3855.
- [112] M. Pham-Thi, *J. Alloys Compd.* 225 (1995) 547–551.
- [113] P.N. Yocom, *J. Soc. Inf. Disp.* 4 (1996) 149–152.
- [114] <https://www.pctechguide.com/crt-monitors/the-anatomy-of-a-crt-monitor->

- and-crt-tvs (Accessed July 19, 2023).
- [115] G. Tessitore, G.A. Mandl, S.L. Maurizio, M. Kaur, J.A. Capobianco, *RSC Adv.* 13 (2023) 17787–17811.
- [116] R. Marin, D. Jaque, *Chem. Rev.* 121 (2021) 1425–1462.
- [117] Y. Zhang, J. Xu, Q. Cui, B. Yang, *Sci. Rep.* 7 (2017) 42464.
- [118] <https://www.led-professional.com/resources-1/articles/optimization-of-ssl-led-devices-by-osram-opto-semiconductors> (Accessed July 21, 2023).
- [119] J. Steinbrück, P.W. Nolte, S. Schweizer, *Opt. Mater. X.* 5 (2020) 100046.
- [120] V. Lupei, A. Lupei, *J. Lumin.* 169 (2016) 426–439.
- [121] M. Malinauskas, A. Žukauskas, S. Hasegawa, Y. Hayasaki, V. Mizeikis, R. Buividas, S. Juodkazis, *Light Sci. Appl.* 5 (2016) 16133.
- [122] X. Chen, J. Xu, X. Chen, K. Yao, *Adv. Ophthalmol. Pract. Res.* 1 (2021) 100008.
- [123] M. Chu, Y. Shao, J. Peng, X. Dai, H. Li, Q. Wu, D. Shi, *Biomaterials.* 34 (2013) 4078–4088.
- [124] G. Cannarozzo, F. Negosanti, M. Sannino, M. Santoli, L. Bennardo, N. Banzola, L. Negosanti, S.P. Nisticò, *Dermatol. Ther.* 32 (2019) e13042.
- [125] Y.T. Yeh, J.H. Peng, P. Peng, *J. Cosmet. Laser Ther.* 22 (2020) 43–47.
- [126] Y. Saydjari, T. Kuypers, N. Gutknecht, *Biomed Res. Int.* 2016 (2016) 8421656.
- [127] S.D. Gan, E.M. Graber, *Dermatologic Surg.* 39 (2013) 823–838.
- [128] X. Yu, H. Zhang, J. Yu, *Aggregate.* 2 (2021) 20–34.
- [129] <https://cen.acs.org/synthesis/Chemistry-Pictures-Fluorescent->

- europium/99/web/2021/06 (Accessed July 17, 2023).
- [130] J. Song, C. Zhang, C. Xu, Y. Qiang, A. Lu, L. Han, *Appl. Phys. A Mater. Sci. Process.* 128 (2022) 1–10.
- [131] H. Groult, J. Ruiz-Cabello, J. Pellico, A. V. Lechuga-Vieco, R. Bhavesh, M. Zamai, E. Almarza, I. Martín-Padura, E. Cantelar, M.P. Martínez-Alcázar, F. Herranz, *Bioconjug. Chem.* 26 (2015) 153–160.
- [132] B. Song, M. Li, J. Ren, Q. Liu, X. Wen, W. Zhang, J. Yuan, *New J. Chem.* 46 (2022) 9658–9665.
- [133] G. Vicentini, L.B. Zinner, J. Zukerman-Schpector, K. Zinner, *Coord. Chem. Rev.* 196 (2000) 353–382.
- [134] C. Cascales, R. Balda, V. Jubera, J.P. Chaminade, J. Fernández, *Opt. Express.* 16 (2008) 2653–2662.
- [135] C. Cascales, P. Porcher, J. Fernández, A. Oleaga, R. Balda, E. Diéguez, *J. Alloys Compd.* 323–324 (2001) 260–266.
- [136] C. Cascales, J. Fernández, R. Balda, *Opt. Express.* 13 (2005) 2141–2152.
- [137] F. Wang, X. Liu, Rare-earth doped upconversion nanophosphors, in: D.L. Andrews, G.D. Scholes, G.P. Wiederrecht (Eds.), *Comprehensive Nanoscience and Nanotechnology*, Elsevier, 2011: pp. 607–635.
- [138] I.M. Kolthoff, *J. Phys. Chem.* 36 (1932) 860–881.
- [139] P.P. Fedorov, M.N. Mayakova, S. V. Kuznetsov, V. V. Voronov, R.P. Ermakov, K.S. Samarina, A.I. Popov, V. V. Osiko, *Mater. Res. Bull.* 47 (2012) 1794–1799.
- [140] L.L. Wei, C.C. Lin, M.H. Fang, M.G. Brik, S.F. Hu, H. Jiao, R.S. Liu, *J. Mater.*

- Chem. C.* 3 (2015) 1655–1660.
- [141] T.T. Deng, E.H. Song, Y.Y. Zhou, J.Y. Chen, Y.F. Cheng, J. Yuan, T. Fan, *Dalt. Trans.* 49 (2020) 5823–5831.
- [142] J. Lellouche, A. Friedman, A. Gedanken, E. Banin, *Int. J. Nanomedicine.* 7 (2012) 5611–5624.
- [143] L. Zhu, C. Fan, W. Fan, J. Yang, W. Huang, J. Zeng, Y. Zhang, X. Cao, *Ceram. Int.* 41 (2015) 5032–5040.
- [144] M. Vukovic, I. Dinic, P. Jardim, S. Marković, L. Veselinović, M. Nikolić, L. Mancic, *Adv. Powder Technol.* 33 (2022).
- [145] S. Głowniak, B. Szczęśniak, J. Choma, M. Jaroniec, *Molecules.* 28 (2023) 2639.
- [146] K.S. Suslick, *Science.* 247 (1990) 1439–1445.
- [147] X. Hangxun, B.W. Zeiger, K.S. Suslick, *Chem. Soc. Rev.* 42 (2013) 2555–2567.
- [148] T.Q. Bui, H.T.M. Ngo, H.T. Tran, *J. Sci. Adv. Mater. Devices.* 3 (2018) 323–330.
- [149] M.M. Taheri, M.R. Abdul Kadir, T. Shokuhfar, A. Hamlekhan, M. Assadian, M.R. Shirdar, A. Mirjalili, *Ceram. Int.* 41 (2015) 9867–9872.
- [150] T. Zhou, X. Jiang, C. Zhong, X. Tang, S. Ren, Y. Zhao, M. Liu, X. Lai, J. Bi, D. Gao, *J. Lumin.* 175 (2016) 1–8.
- [151] P. Fedorov, M. Mayakova, A. Alexandrov, V. Voronov, S. Kuznetsov, A. Baranchikov, V. Ivanov, *Inorganics.* 6 (2018) 1–17.
- [152] L. Han, S. Xie, M. Wang, T. Sun, Q. Liu, G. Jiang, Y. Shi, Y. Tang, *Mater. Lett.* 234 (2019) 241–244.

- [153] A.B. Bard, X. Zhou, X. Xia, G. Zhu, M.B. Lim, S.M. Kim, M.C. Johnson, J.M. Kollman, M.A. Marcus, S.R. Spurgeon, D.E. Perea, A. Devaraj, J. Chun, J.J. De Yoreo, P.J. Pauzauskie, *Chem. Mater.* 32 (2020) 2753–2763.
- [154] S. Feng, R. Xu, *Acc. Chem. Res.* 34 (2001) 239–247.
- [155] W. Xia, J. Xiong, L. Jiang, R. Ye, Y. Mao, S. Hu, J. Yang, *CrystEngComm.* 21 (2019) 3939–3947.
- [156] H. Guan, Y. Sheng, Y. Song, C. Xu, X. Zhou, K. Zheng, Z. Shi, H. Zou, *J. Phys. Chem. C.* 121 (2017) 23080–23095.
- [157] M. Ding, S. Yin, D. Chen, J. Zhong, Y. Ni, C. Lu, Z. Xu, Z. Ji, *Appl. Surf. Sci.* 333 (2015) 23–33.
- [158] R. Zanella, *Mundo Nano.* 5 (2012) 69–81.
- [159] Y. Wang, Q. Yang, Y. Zhao, S. Du, C. Zhi, *Adv. Mater. Technol.* 4 (2019) 1–17.
- [160] G. Yang, S.J. Park, *Materials.* 12 (2019) 1177.

Chapter 2

Objectives

As mentioned in the Introduction section, the incorporation of luminescent lanthanide ions into fluorides has been widely recognized as a highly appealing approach in the area of inorganic materials, finding extensive utility across a diverse spectrum of applications. Driven by a profound interest in conducting research that integrates both fundamental and applied scientific principles, the primary objective of this Doctoral Thesis is to formulate solid-state hosts based on yttrium complex fluorides, with a specific focus on their application in photoluminescence. Within this context, the research undertaken is intricately framed at the confluence of several distinct but interrelated disciplines, namely Materials Science, Crystallography, and Physics.

One of the central aims of this endeavor is to comprehensively investigate innovative and enhanced synthesis procedures. These methodologies are intended to provide precise control over the crystal structure, and consequently, the optical properties of Eu^{3+} ions, which have been selected as dopants due to their distinctive and highly esteemed characteristics within the field of photonics. Through a profound characterization of these novel materials, it is intended to elucidate the luminescence mechanisms that underlie the optical response, bearing in mind the relationship that must be established between the structure of the compounds (both at the macroscopic and atomic levels) and the final properties.

The specific objectives addressed in each chapter are as follows:

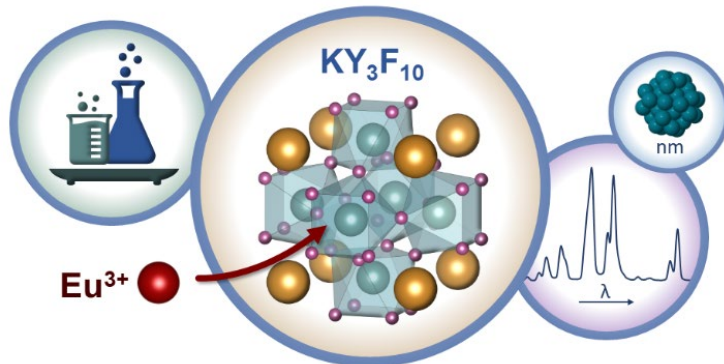
- **Chapter 3 (Article 1).** To study the structural, morphological, and luminescence properties of Eu^{3+} -doped $\alpha\text{-KY}_3\text{F}_{10}$ materials prepared by different synthetic routes (sonochemical, coprecipitation, and continuous stirring; combined with a successive hydrothermal treatment of the as-obtained compounds). It is also pretended to analyze the energy transfers from a photophysical point of view.

- **Chapter 4 (Article 2).** To prove the usefulness of dicarboxylic acids (oxalic and tartaric acid) to modulate the evolution of the surface and crystal phases in the KF-YF₃ system. Another important goal is to unveil the effect of the pH in the reaction medium and follow all the structural changes by the tunable optical response of europium.
- **Chapter 5 (Article 3).** To report a new, simple, and high-yield method based on a sonochemical process for obtaining the δ -KY₃F₁₀·xH₂O compound, a material that has been completely neglected in the literature since it was first discovered. The objective is also to elucidate the growth mechanism of this material and its adequacy for optical applications.
- **Chapter 6 (Article 4).** To reveal the significance of sonochemistry in the design of Eu³⁺-doped fluorides with intriguing morphologies and modulated crystal structures (α -KY₃F₁₀, δ -KY₃F₁₀·xH₂O, and Y(OH)_{3-x}F_x). Moreover, it is pursued to explain how the different pH-dependent reactions govern the formation mechanisms of these compounds.
- **Chapter 7 (Article 5).** To propose another alternative and low-time-consuming method to obtain nanospheres of the δ -phase of KY₃F₁₀. Employing time-resolved fluorescence line-narrowing, it is also intended to describe the site-selective symmetries of Eu³⁺ ions embedded in α -KY₃F₁₀ and δ -KY₃F₁₀·xH₂O.
- **Chapter 8 (Article 6).** To demonstrate the interplay between thermodynamics and kinetics in the synthesis of α and δ -phases of KY₃F₁₀ as well as follow the transition-phase pathway. In addition, it is aimed to establish a direct connection between the phase fractions and the europium luminescence.

- **Chapter 9 (Article 7).** To review and offer easy guidance with helpful advice on how to interpret measurements of the Eu^{3+} emission spectra in solid-state hosts. It is also purposed to present the most useful tools for saving time and give a focused and practical explanation of the theoretical concepts involved.

Chapter 3

Tuning the optical and photoluminescence properties of high efficient Eu^{3+} -doped KY_3F_{10} phosphors by different synthetic approaches



Article 1

Optics & Laser Technology, 136 (2021) 106734

Tuning the optical and photoluminescence properties of high efficient Eu^{3+} -doped KY_3F_{10} phosphors by different synthetic approaches

Pablo Serna-Gallén, Héctor Beltrán-Mir, Eloísa Cordoncillo

Departamento de Química Inorgánica y Orgánica, Universitat Jaume I, Av. Vicent Sos Baynat s/n 12071, Castelló de la Plana, Spain

Journal Impact Factor: 4.939

Quartile: Q1

Category: Optics

Position: 20/101

Abstract

Eu³⁺-doped KY₃F₁₀ materials with a dopant content between 0 and 5 mol% were prepared based on the nominal composition K(Y_{3-x}Eu_x)F₁₀ using different synthetic routes. The reaction conditions have been proven to be critical factors for the characteristics of the final products: morphology, size and crystallinity. As a result, noticeable changes in their photoluminescence spectra and lifetimes were observed. Quantum cutting processes or similar energy transfers between Eu³⁺ ions allowed obtaining high quantum efficiencies, while the analysis of the Ω_2 Judd-Ofelt parameter suggested that the crystal field of Eu³⁺ was very similar in all the compositions. A well-designed synthesis of Ln³⁺-doped fluorides can provide a full range of opportunities to explore new phenomena. Thus, this study highlights the complexity of the fluoride-based systems, which are exceptional candidates for doping with luminescent lanthanide ions and have very important characteristics for their future application in bioanalytics, biomedics or photonics. Indeed, the color-tunable emissions of the phosphors, which vary from orangish to yellow, could be interesting for their application in white light-emitting diodes through their combination with blue chips.

Keywords: Fluorides; Europium; Optical Spectroscopy; Luminescence; Morphology; Structure

3.1. Introduction

Over the last few decades, materials doped with luminescent lanthanide ions (Ln^{3+}) have been widely studied because of their application in emitting diodes, solar cells, lasers, and catalysts, among others [1–3]. Fluorides are better host candidates than their respective oxides for optical applications due to the high ionicity of the metal–fluorine bonds, which provides low phonon energy of the crystal lattice (associated with atomic vibrations) [4]. As a result, the quantum efficiencies of the photoluminescent processes are higher and the lifetimes of Ln^{3+} are longer, varying from a few microseconds to several milliseconds [5].

In addition, fluorides have also been used as upconversion (UC) phosphors [6–8]. Indeed, lanthanide-doped phosphors are of great interest for UC because their electronic configuration makes them more suitable for the absorption of a second photon [9]. For instance, upconverting fluorides have been reported to be promising materials for bioanalytical and biomedical applications, such as bio-imaging [10,11]. Novel multifunctional materials have also been designed combining the luminescence properties of Ln^{3+} -doped fluorides with the plasmonic activity of metallic nanoparticles (NPs) [12–14]. Therefore, spectroscopic techniques based on plasmonic interactions, such as the well-known Surface Enhanced Raman Spectroscopy (SERS), allow us to detect and quantify different analytes with great sensitivity [15].

On the other hand, white light-emitting diodes (w-LEDs) have lately received attention because of their good stability in their physical and chemical properties. One of the most common strategies to generate these devices is the combination of orange-yellow-emitting phosphors (such as the well-known yellow-emitting $\text{Y}_3\text{Al}_5\text{O}_{12}:\text{Ce}^{3+}$) with blue InGaN chips [16]. Nevertheless, the main drawback of this combination is the modest color-rendering index. Additionally, it is also possible to combine near-

ultraviolet LED chips with tricolor (red, green, blue) phosphors [17]. Thus, it is still important to develop and optimize the luminescence properties of new orangish-yellow-emitting phosphors. For this reason, many studies have used phosphors based on oxides, phosphates or nitrides matrices [18–21], although fluorides have also been proved recently to be good candidates for w-LEDs [22]. Indeed, the high quantum efficiencies and long lifetimes of fluoride-based structures (due to the low phonon interaction of the host lattice) open up new strategies to the design of materials with interesting properties for their applications in such devices.

Fluoride crystals supporting trivalent lattice cations (such as Y^{3+}) are especially attractive for luminescence because they allow their isovalent substitution for a lanthanide ion [23]. The potassium-yttrium-fluorine system has been studied and has yielded many phases: KYF_4 , KY_2F_7 , KY_3F_{10} , KY_7F_{22} , K_2YF_5 and K_3YF_6 [24–29]. Of these, KY_3F_{10} has attracted a lot of attention because of its spectroscopic properties over a wide range of temperatures [4,30]. Moreover, KY_3F_{10} crystal melts congruently and is a suitable host for Ln^{3+} ions, which can easily substitute Y^{3+} ions in a non-center-symmetrical site (C_{4v} symmetry) [31,32].

Under ambient conditions, KY_3F_{10} crystallizes in a face-centered cubic structure (fluorite-type structure) belonging to the $Fm\bar{3}m (O_h^5)$ space group, with lattice parameter $a = 11.536 \text{ \AA}$, cell volume $V = 1535.20 \text{ \AA}^3$, and 8 formula units per unit cell ($Z = 8$) [33]. The crystallographic parameters are detailed in **Table 3.1**, while the crystal structure is depicted in **Figure 3.1**.

The structure can be described as square antiprisms composed of YF_8 units. A central cation of yttrium is linked to two squares of non-equivalent fluorine anions. One square contains four anions in $32f$ sites (F1), while the other is composed of four anions in $48i$ sites (F2) [34], **Figure 3.1(a)**. The union of six antiprisms generates a

cluster-type assemblage, whose edges are shared, leaving an empty cuboctahedron in the center formed by ions in position $48i$, **Figure 3.1(b)**. The empty cuboctahedra are situated at the center of the unit cell and in the middle of its edges, **Figure 3.1(c)**. The potassium cations are distributed along channels running parallel to the a , b and c crystallographic axes [35]. Structures were drawn with VESTA software [36].

Table 3.1. Distribution of KY_3F_{10} atoms in space group $Fm\bar{3}m$ (no. 225) [33].

Name	Species	Wyckoff Position	Local Symmetry	Atomic Coordinates		
				x	y	z
K	K^+	$8c$	$T_d (-43m)$	1/4	1/4	1/4
Y	Y^{3+}	$24e$	$C_{4v} (4m.m)$	0.2401	0	0
F1	F^-	$32f$	$C_{2v} (.3m)$	0.1081	0.1081	0.1081
F2	F^-	$48i$	$C_{3v} (m.m2)$	1/2	0.1647	0.1647

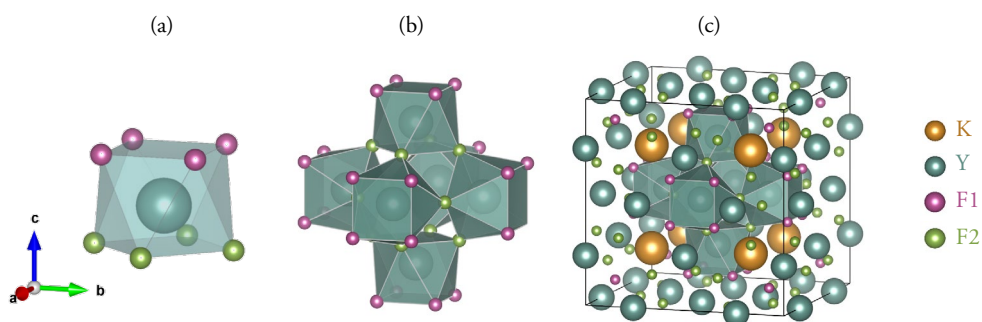


Figure 3.1. Structure of cubic KY_3F_{10} : (a) basic unit composed of YF_8 square antiprisms, (b) cluster assemblage of six antiprisms, and (c) unit cell.

KY_3F_{10} compounds have been synthesized via different methods, including the hydrothermal method, coprecipitation or sonochemical processes, giving rise to nano/micron-sized materials with different morphologies (spherical, semi-spherical, rodlike, etc.) [12,13,32,37–40]. However, these preparation methods are frequently

problematic to use because of the complexity and difficulties involved in the reproducibility of the product [38].

The structural and optical properties of KY_3F_{10} have also been reported in the literature. Nevertheless, to the best of our knowledge, no accurate attempts have been made to provide a full analysis of different synthetic procedures that studies their influence on the luminescence features of these materials. Among all the lanthanides, we have chosen Eu^{3+} as a dopant ion in view of its adequacy as a site-sensitive structural probe [41–43], which can be useful to discuss the optical response of the materials. In addition, the ionic radius for Y^{3+} (coordination number, CN = 8) is 1.019 Å and for Eu^{3+} (CN = 8), it is 1.066 Å [44]. Therefore, these similar values ensure a good incorporation of the Eu^{3+} ions in KY_3F_{10} .

The luminescence properties of the materials are highly dependent on their size, shape, and structure. A well-designed and controlled synthesis of Ln^{3+} -doped fluorides can provide a full range of opportunities to explore new phenomena [45,46]. In view of this, the present paper is focused on the study of the structural, morphological, and luminescence properties of Eu^{3+} -doped KY_3F_{10} materials. This study enriches the literature and also reveals the effects of post-hydrothermal treatments on the as-synthesized materials. In addition, we show that quantum cutting processes or similar energy transfers between Eu^{3+} ions allow yielding quantum efficiencies higher than 100%. For all of this, the materials investigated (with highly tunable properties) offer different possibilities depending on the synthesis process used, which can be a keystone for future optical, bioanalytical or biomedical applications. Indeed, the color-tunable emissions of the phosphors could be very interesting for their applications in w-LEDs through their combination with blue chips.

3.2. Experimental section

3.2.1. Materials

Reagents used were yttrium(III) nitrate hexahydrate [$\text{Y}(\text{NO}_3)_3 \cdot 6\text{H}_2\text{O}$ 99.9%, Alfa Aesar], europium(III) nitrate hexahydrate [$\text{Eu}(\text{NO}_3)_3 \cdot 6\text{H}_2\text{O}$ 99.9%, Strem Chemicals], potassium hydroxide [KOH 85%, Labkem], and potassium tetrafluoroborate [KBF_4 96%, Sigma-Aldrich].

3.2.2. Synthesis of Eu^{3+} -doped KY_3F_{10} compounds

Different synthetic routes were addressed to prepare KY_3F_{10} . On the one hand, the synthesis of KY_3F_{10} was studied by means of the following methods: sonochemical, coprecipitation, and a continuous stirring process. On the other hand, these methods were also combined with a successive hydrothermal treatment in both acidic and basic medium conditions. Calculations were performed to obtain 0.25 g of the final product, giving yields higher than 90%. In all cases, the final volume of the aqueous solution was adjusted to 50 mL. For the sonochemical processes, a *Bandelin Sonorex* ultrasonic bath with a frequency of 35 kHz was used. For the hydrothermal treatments, the temperature was set to 180 °C for 24 h, and the Teflon-lined vessel used had a total volume of 125 mL.

Samples of KY_3F_{10} with a content of 0, 1, 3 and 5 mol% Eu^{3+} were synthesized according to the nominal formula $\text{K}(\text{Y}_{3-x}\text{Eu}_x)\text{F}_{10}$, where $x = 0, 0.01, 0.03$ and 0.05 , respectively. The molar ratio of reagents was $1\text{Ln}(\text{NO}_3)_3 : 2\text{KBF}_4$ ($\text{Ln} = \text{Eu}, \text{Y}$); this ratio has been previously reported to be efficient for the synthesis of KY_3F_{10} compounds with good homogeneity [39].

The undoped KY_3F_{10} sample ($x = 0$) was first prepared following the experimental procedures detailed below. In view of the structural and morphological

characterization (see the following section) some synthetic routes were repeated incorporating Eu^{3+} into the crystal structure, which allowed us to study the optical properties of the materials. **Table 3.2** summarizes the different synthetic routes evaluated and the abbreviation used for the samples.

Table 3.2. Nomenclature of the different routes and the compounds synthesized in each one, where n indicates the molar percentage of Eu^{3+} in the sample.

Synthetic route	Reference
1) Ultrasonication	$n\%$ -R1
2) Ultrasonication + Basic Hydrothermal	$n\%$ -R2
3) Ultrasonication + Acidic Hydrothermal	$n\%$ -R3
4) Stirring	$n\%$ -R4
5) Stirring + Basic Hydrothermal	$n\%$ -R5
6) Stirring + Acidic Hydrothermal	$n\%$ -R6
7) Coprecipitation	$n\%$ -R7
8) Coprecipitation + Basic Hydrothermal	$n\%$ -R8

3.2.2.1. Synthetic Routes with an Ultrasonication Common Step (Routes 1–3)

The general scheme of the experimental procedure is depicted in **Figure 3.2**. In Route 1 (*Ultrasonication*), $\text{Ln}(\text{NO}_3)_3 \cdot 6\text{H}_2\text{O}$ ($\text{Ln} = \text{Eu}, \text{Y}$) was dissolved in water with the appropriate amount of KBF_4 , with a resulting pH of 4. Next, this solution was introduced into an ultrasonic bath at room temperature for 24 h, which led to the formation of a white precipitate and a decrease in the pH to 1. The precipitate was then centrifuged, rinsed several times with water, and dried under an infrared lamp.

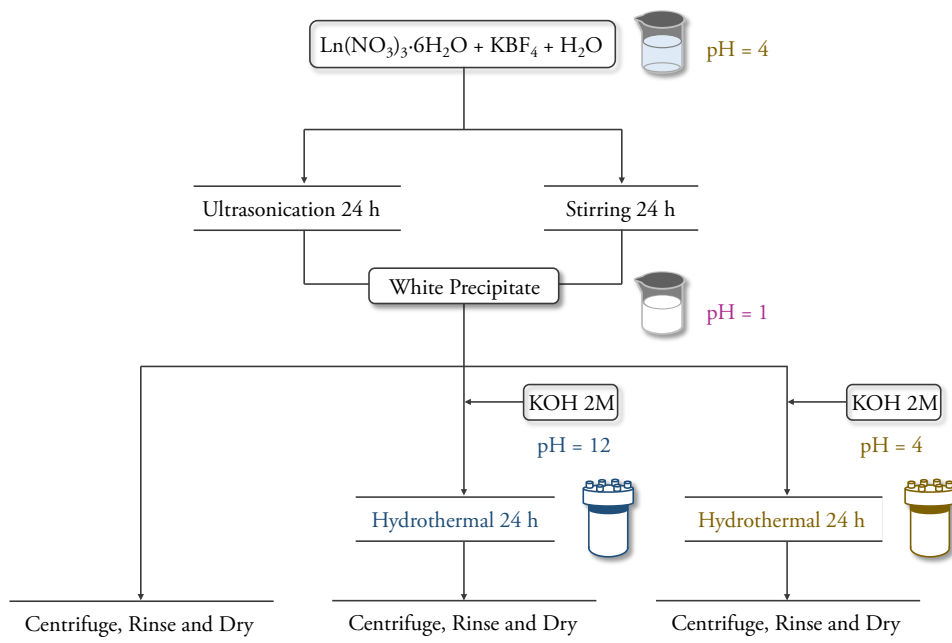


Figure 3.2. General scheme for the synthetic routes with an ultrasonication common step (Routes 1–3) and with a continuous stirring common step (Routes 4–6).

With the aim of studying the effect of a hydrothermal treatment over the as-obtained precipitate, two more routes were addressed. In Route 2 (*Ultrasonication + Basic Hydrothermal*), the pH of the dispersion obtained after the ultrasonication process was readjusted to 12 by adding KOH 2M. The whole system was transferred into a Teflon-lined vessel and treated hydrothermally for 24 h in a thermally heated autoclave at 180 °C. After that, the precipitate was centrifuged, rinsed, and dried. Alternatively, in Route 3 (*Ultrasonication + Acidic Hydrothermal*), the pH of the dispersion obtained after the ultrasonication process was increased to 4 with KOH 2M. The as-formed precipitate was then treated hydrothermally, centrifuged, rinsed, and dried.

3.2.2.2. Synthetic Routes with a Continuous Stirring Common Step (Routes 4–6)

The experimental procedure is the same as for Routes 1–3 (see **Figure 3.2**), but with the proviso that instead of ultrasonicing the solution of the reagents, continuous stirring is maintained for 24 h at room temperature. After this time, the presence of a white precipitate was also observed.

3.2.2.3. Synthetic Routes with a Coprecipitation Common Step (Routes 7–8)

Figure 3.3 shows the general scheme for the synthesis of the materials following Routes 7–8, with a coprecipitation common step. In Route 7 (*Coprecipitation*), after dissolving the reagents, KOH 2M was added dropwise until a pH of 12 was reached. While doing this, the solution became whitish, indicating the formation of a precipitate.

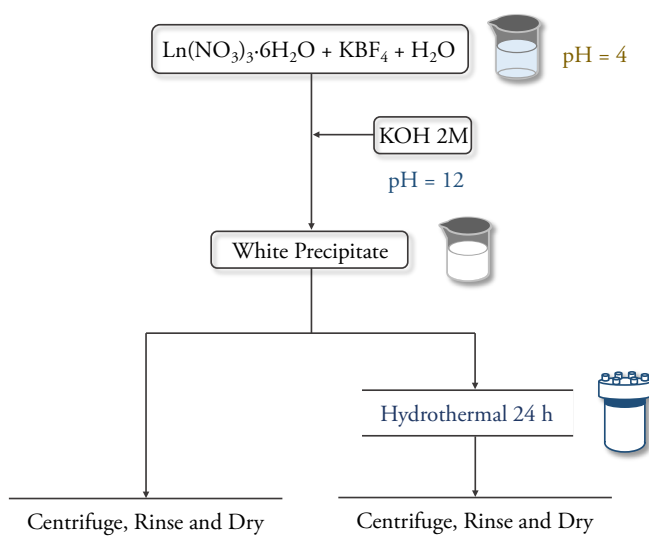


Figure 3.3. General scheme for the synthetic routes with a coprecipitation common step (Routes 7–8).

Moreover, in Route 8 (*Coprecipitation + Basic Hydrothermal*), the as-formed precipitate was treated hydrothermally for 24 h as previously described for the other routes. Finally, the precipitates were centrifuged, rinsed, and dried.

3.2.3. Characterization

All the characterization was carried out at room temperature. Powder X-ray diffraction (XRD) was performed using a Bruker-AX D8-Advance X-ray diffractometer with $\text{CuK}_{\alpha 1}$ radiation at a scan speed of $0.36^\circ/\text{min}$. All data were collected between $20 \leq 2\theta \leq 90$. Unit cell parameters were refined using WinX^{POW} 1.06 software version. The microstructure of samples was observed using a JEOL 7001F scanning electron microscope (SEM). The operation parameters were: acceleration voltage 15 kV, measuring time 20 s, and working distance 10 mm.

Different optical properties were studied for Eu^{3+} -doped KY_3F_{10} samples with an Eclipse Fluorescence Spectrophotometer (Varian). Excitation spectra were recorded in the range 250–550 nm with an emission wavelength of 593 nm. Emission spectra were performed upon excitation at 395 nm in the range 500–750 nm and normalized to the magnetic dipole $^5\text{D}_0 \rightarrow ^7\text{F}_1$ transition. From the spectra, the asymmetry ratio R and the Ω_2 Judd-Ofelt parameter were calculated. In addition, the CIE coordinates of the corresponding materials doped with Eu^{3+} were calculated from the emission spectra using the GoCIE software. Time-resolved luminescence measurements were also performed at different emission wavelengths, with the excitation wavelength set to 395 nm. Lifetime values were extracted from decay profiles.

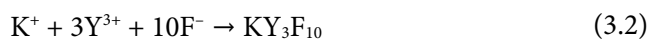
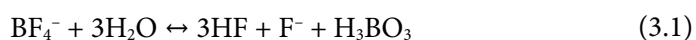
Furthermore, IR spectra were recorded using an Agilent Cary 630 FTIR spectrometer in transmission mode and Raman measurements were performed with a Jasco NRS-3100 Raman spectrometer. The excitation source for the Raman

measurements was a 633 nm diode laser with a power of 80 mW at the sample.

3.3. Results and discussion

3.3.1. Structural characterization

Figure 3.4 shows the XRD patterns of the undoped KY_3F_{10} (0% Eu^{3+}) obtained by the different synthetic routes. **Figure 3.4(a)** corresponds to the samples of routes with an ultrasonication common step (Routes 1–3). The XRD patterns show all the peaks corresponding to the cubic phase of KY_3F_{10} (ICSD card 00-040-9643). Samples 0%-R1 and 0%-R2 have broad, low-intensity peaks, meaning that the materials may not be so much crystalline or are nano-sized. However, the peaks of sample 0%-R3 are very well defined and, therefore, a higher crystallinity is expected. It is therefore clearly demonstrated that the acidity of the medium in the hydrothermal treatment after the ultrasonication process plays an important role in the final properties of the material. The reactions that take place to form this crystalline phase considering the reagents used are:



In view of that, it might be possible that some redissolution processes occurred during the high conditions of pressure in the hydrothermal treatment of the as-formed KY_3F_{10} . In the acidic treatment, the system may evolve through partial redissolution-nucleation-growth processes to particles of larger size, which would explain the narrow peaks found in the XRD pattern of sample 0%-R3. However, with the basic treatment, the as-formed KY_3F_{10} would be stabilized and no changes are

found in sample 0%-R2 with respect to 0%-R1. Further work to investigate these possibilities is in progress.

Regarding the XRD results for the routes with a continuous stirring common step (**Figure 3.4(b)**, Routes 4–6), noticeable changes seem to take place. The diffractogram of the sample 0%-R4 (without hydrothermal treatment) presents the main reflections of cubic KY_3F_{10} together with other more intense peaks associated with a secondary phase (red stars in **Figure 3.4(b)**). However, when the as-obtained precipitate is thermally heated in the autoclave (Routes 5 and 6), the secondary phase disappears and we achieve the stabilization of the crystalline KY_3F_{10} phase. In addition, it is also worth noting that in these routes, the acidic or basic conditions of the medium in the hydrothermal treatment do not have so much influence over the crystallinity, since the diffraction patterns are quite similar. As per the above behavior, we consider that the secondary phase plays an important role when the as-formed precipitate is hydrothermally treated. Possibly, for the thermodynamics of the system in the presence of the secondary phase, the redissolution-nucleation-growth processes are not affected by the pH level in the hydrothermal treatment, which allows the formation of crystalline KY_3F_{10} with very similar characteristics regardless of the medium acidity.

With regard to **Figure 3.4(c)**, we must emphasize the absence of any diffraction peak in sample 0%-R7, thereby indicating that the solid obtained following Route 7 is mainly amorphous. Despite this, when this solid is treated under hydrothermal conditions (Route 8), the crystalline phase of cubic KY_3F_{10} is formed. It is important to note that coprecipitation synthesis often results in amorphous products as a first phase, generally composed of hydroxide-type compounds. During the hydrothermal treatment, the reactivity of the as-formed precipitate is highly enhanced due to the

high pressure achieved in the system. As a result, the amorphous precipitates can undergo several phase transformations which lead them to a crystalline structure.

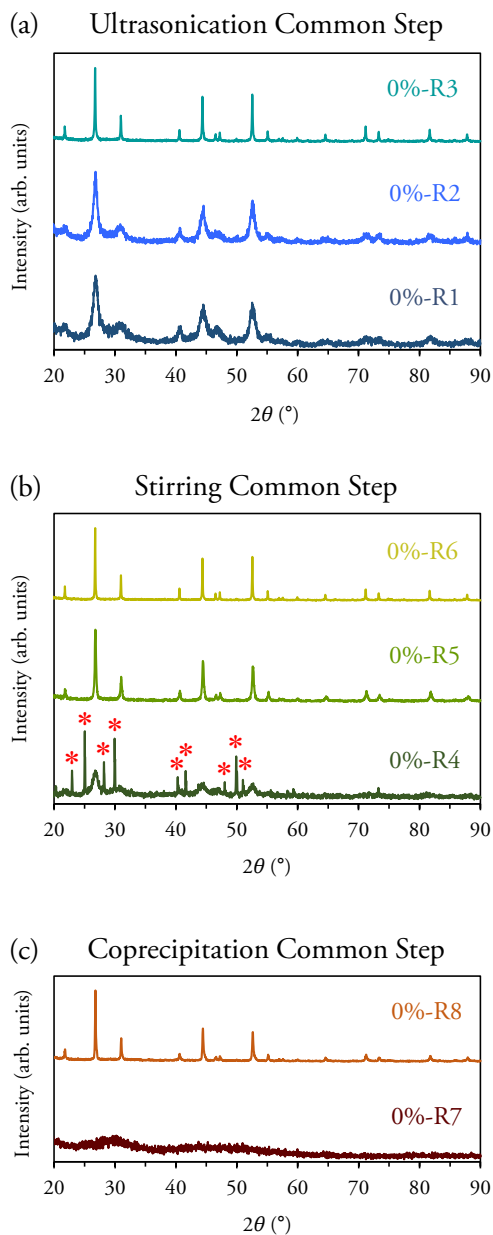


Figure 3.4. XRD patterns for the different 0% Eu^{3+} samples of the synthetic routes with a common step of (a) ultrasonication, Routes 1–3; (b) continuous stirring, Routes 4–6; and (c) coprecipitation, Routes 7–8. Red stars in (b) highlight the presence of a secondary phase.

As a conclusion, the XRD results reveal that the hydrothermal treatments and the acidity of the medium can have a great impact on the crystallinity of the samples depending on the synthetic route. Additionally, the unit cell parameters of the undoped samples having single phase were refined. The results were in good agreement with the reported values for cubic KY_3F_{10} , although no remarkable differences can be found between samples of different synthetic routes (see Supporting Information, **Table S3.1**).

3.3.2. Morphological characterization

Figure 3.5 shows the SEM images of the undoped KY_3F_{10} (0% Eu^{3+}) obtained by the different synthetic procedures. **Figure 3.5(a-c)** corresponds to the samples of routes with an ultrasonication common step (Routes 1–3). The morphologies observed are in good agreement with the XRD results, since the samples with the same XRD profile (0%-R1 and 0%-R2) also have a very similar microstructure, **Figure 3.5(a-b)**. These materials are formed by spherical particles with a diameter range from 100 to 400 nm. In addition, they are self-assembled from nanoparticles with a diameter of about 10 nm, which would explain the XRD broad peaks. These results are also in agreement with the ones obtained by L. Zhu *et al.* [39] following a similar synthesis to obtain KY_3F_{10} compounds. Regarding the 0%-R3 sample, **Figure 3.5(c)**, there is a clear evolution of the spherical morphology. There are particles of about 400 nm (whose geometry is less defined) around which nanoparticles of 50 nm have been distributed. This morphological change is attributed to the acidic hydrothermal treatment after the ultrasonication process, as was commented in the previous section.

The morphologies of samples with a continuous stirring common process (Routes 4–6) were also studied by SEM, **Figure 3.5(d-f)**. Sample 0%-R4, **Figure 3.5(d)**, is composed of particles of two completely different shapes (octahedrons and spheres).

Most of the octahedral particles have sizes closer to 1 μm and could be associated with the highly crystalline secondary phase observed by XRD. In contrast, when the subsequent hydrothermal treatment is carried out, both Routes 5 and 6 lead to the same particle morphology, with no presence of octahedral shapes, **Figure 3.5(e-f)**. The greater particles might be formed from the respective octahedrons during the hydrothermal conditions. Moreover, this microstructure is very similar to that of sample 0%-R3.

Finally, the amorphous character of sample 0%-R7 is also evident with its heterogeneous morphology, **Figure 3.5(g)**. There are particle aggregates for which neither the geometry nor the size is defined. However, when this precipitate is subsequently treated hydrothermally (Route 8), the microstructure evolves toward a system composed of particles that are far more crystalline and defined, although some microstructural disorder still exists, **Figure 3.5(h)**.

Taking everything into consideration, SEM micrographs of the undoped KY_3F_{10} materials reveal that samples of Routes 1 and 2 have similar morphologies, as well as samples of Routes 3, 5 and 6. In contrast, Route 4 yields a solid with the presence of a secondary phase and, following Route 7, we obtain an amorphous material. Therefore, three synthetic routes were strategically chosen with the aim of studying the possible influence of different morphologies over the luminescent response of Eu^{3+} . To carry out the study of the optical properties, samples of KY_3F_{10} with a content of 1, 3 and 5 mol% Eu^{3+} were synthesized following the experimental procedure of Routes 1, 3 and 8. The other synthetic routes were disregarded for similitude in the morphology of the materials, the presence of secondary phases, or the absence of crystallinity. It must be noted that Eu^{3+} -doped KY_3F_{10} materials presented the same XRD patterns and morphologies as their respective undoped compounds.

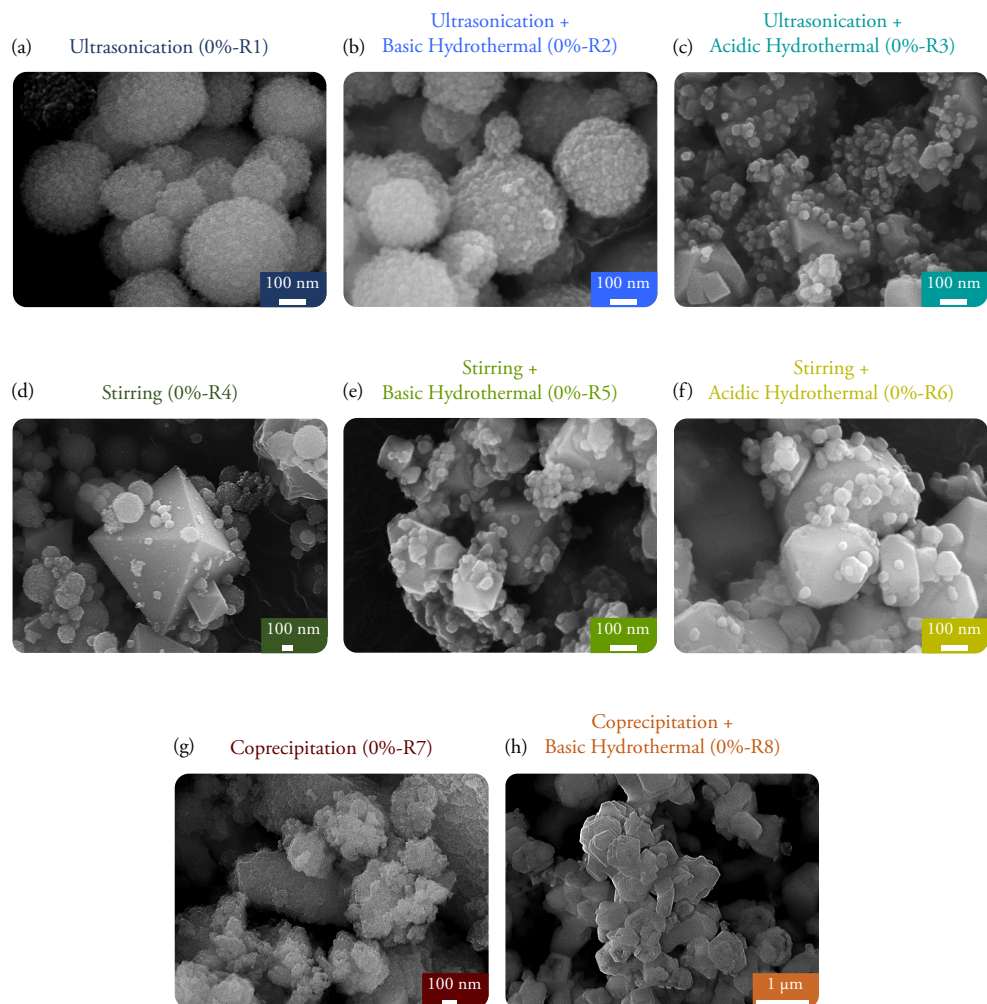


Figure 3.5. SEM images for the different 0% Eu^{3+} samples of the synthetic routes with a common step of (a-c) ultrasonication, Routes 1–3; (d-f) continuous stirring, Routes 4–6; and (g-h) coprecipitation, Routes 7–8.

3.3.3. Photoluminescence studies

3.3.3.1. Emission spectra

All the excitation spectra were very similar (see Supporting Information, **Figure S3.1**). Different bands associated with the Eu^{3+} transitions were observed from the ground level ${}^7\text{F}_0$ to the different excited levels. Among all of them, the most intense was the

${}^7F_0 \rightarrow {}^5L_6$ transition, with a maximum at 395 nm. Therefore, emission spectra were recorded using this value as the excitation wavelength and were normalized to the magnetic dipole ${}^5D_0 \rightarrow {}^7F_1$ transition.

Figure 3.6 shows the emission spectra corresponding to the samples of Routes 1, 3 and 8 with different Eu^{3+} concentrations (1, 3 and 5%) obtained with a delay time (DT) of 0.2 ms. The spectra show a complex behavior due the mixing of some ${}^5D_{1-3} \rightarrow {}^7F_j$ transitions. The emission bands are assigned to the following transitions [47]: ${}^5D_3 \rightarrow {}^7F_1$ (417 nm), ${}^5D_3 \rightarrow {}^7F_2$ (429 nm), ${}^5D_3 \rightarrow {}^7F_3$ (445 nm), ${}^5D_2 \rightarrow {}^7F_3$ (511 nm), ${}^5D_1 \rightarrow {}^7F_0$ (526 nm), ${}^5D_1 \rightarrow {}^7F_2$ (554 nm), ${}^5D_1 \rightarrow {}^7F_3$ (586 nm), ${}^5D_0 \rightarrow {}^7F_1$ (593 nm), ${}^5D_0 \rightarrow {}^7F_2$ (600–635 nm, with the most intense peak at 621 nm), ${}^5D_0 \rightarrow {}^7F_3$ (650–670 nm) and ${}^5D_0 \rightarrow {}^7F_4$ (690–710 nm). Those emission bands arising from possible mixing of different transitions (see **Figure 3.6**) have not been considered to avoid misleading interpretations. Luminescence measurements of samples 0%-R1, 0%-R3 and 0%-R8 were also performed in order to check if there were any optical response to consider apart from the $4f-4f$ transitions of Eu^{3+} that appear in the doped samples. However, the undoped samples showed a total absence of optical response.

From the emission spectra in **Figure 3.6** (DT = 0.2 ms), attention must be drawn to the presence of bands associated with transitions occurring from the higher excited levels ${}^5D_{1-3}$. For the Eu^{3+} ion, whether the emission can occur from higher excited levels or not depends critically upon the doping concentration of Eu^{3+} and the dominant vibration frequencies available in the host lattice [48]. As it has been commented previously in the introductory section, the phonon energy of fluorides is low, allowing these transitions to occur.

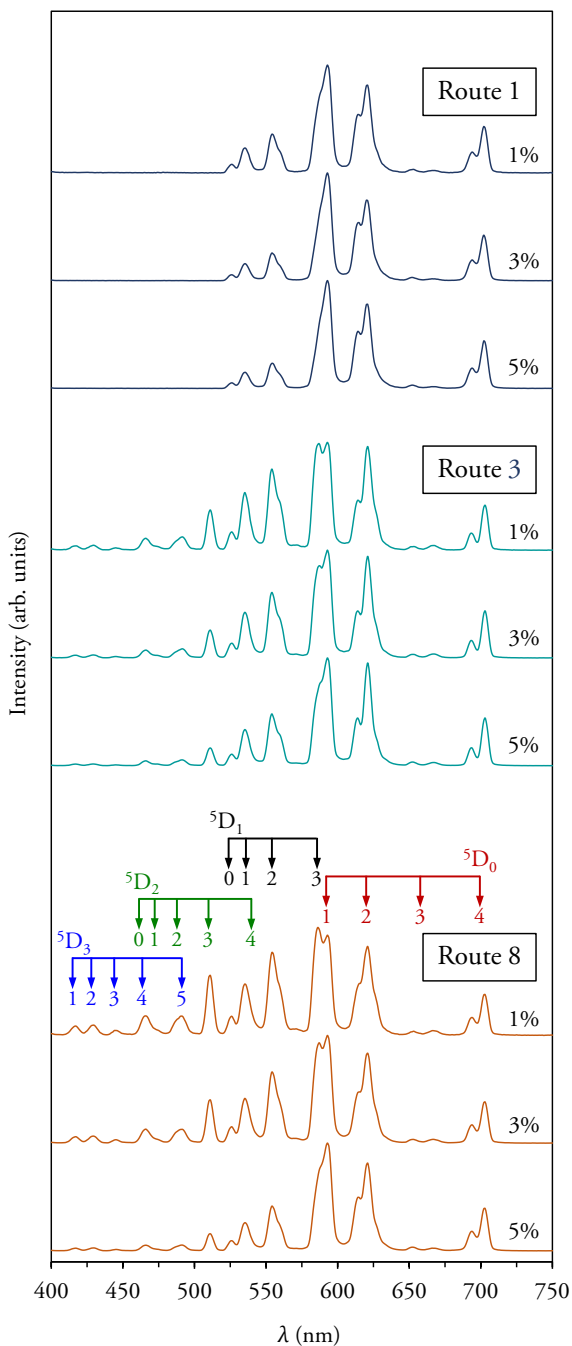


Figure 3.6. Room temperature emission spectra obtained with a delay time of 0.2 ms upon excitation at 395 nm for samples of Routes 1, 3 and 8 with different molar percentage of Eu³⁺ (1, 3 and 5%). The numbers down the rows indicate the value of J associated with the respective transition ⁵D_i→⁷F_J.

Samples of Routes 3 and 8 present similar spectral profiles. Nevertheless, the samples of Route 1 deserve some specific comments. The most interesting fact is the absence of the ${}^5D_{2,3} \rightarrow {}^7F_j$ transitions. As a result, it can be expected that the phonon energy associated with the lattice is higher in these samples in comparison to those of Routes 3 and 8, where these transitions exist. This is also consistent with a lower intensity of the ${}^5D_1 \rightarrow {}^7F_j$ transitions. In fact, the ${}^5D_1 \rightarrow {}^7F_3$ transition appears almost totally convoluted with the ${}^5D_0 \rightarrow {}^7F_1$ transition. There is not a splitting of the most intense peak (593 nm) as in the samples prepared by other routes, although the presence of the ${}^5D_1 \rightarrow {}^7F_3$ transition can be inferred in the band from the shoulder at its high-energy side (compare sample 1%-R1 with 5%-R3 and 5%-R8). As the dopant concentration increases, the shoulder tends to disappear as well. A reasonable explanation may be found if we consider the particle size of the samples. The spherical particles, **Figure 3.5(a,b)**, are self-assembled from nanoparticles with a diameter of about 10 nm. Therefore, due to possible quantum confinement effects, the Ln^{3+} ions may be closer in the host lattice, resulting in higher phonon energy and making the system relaxation from 5D_3 , 5D_2 and 5D_1 levels to the 5D_0 more likely, quenching the ${}^5D_{2,3} \rightarrow {}^7F_j$ transitions.

Another aspect to highlight is that the intensity of ${}^5D_{1-3} \rightarrow {}^7F_j$ transitions decreases as the Eu^{3+} concentration becomes higher. Therefore, the emission from higher excited levels is partially quenched by cross-relaxation occurring between two neighboring Eu^{3+} ions in the lattice. In this non-radiative process, the higher energy emission is quenched in favor of the lower energy level emission according to [49].

Special attention might be paid to the relative intensity of the ${}^5D_0 \rightarrow {}^7F_1$ transition (the magnetic dipole one) and ${}^5D_1 \rightarrow {}^7F_3$. Apart from the absence of the splitting for samples of Route 1 (explained above), with the increase in the dopant concentration,

the peak corresponding to the ${}^5D_0 \rightarrow {}^7F_1$ transition becomes more intense at the expense of the ${}^5D_1 \rightarrow {}^7F_3$, thus implying that the cross-relaxation process is taking place. This behavior agrees well with the established assignment for the two-component band. If the peak at 586 nm had not corresponded to the ${}^5D_1 \rightarrow {}^7F_3$ transition, no noticeable decrease in its intensity would probably have been observed when increasing the cross-relaxation process.

Referring to the previous emission bands assignment, at first glance some misunderstanding may occur regarding the two-component bands that appear between 575–600 and 600–635 nm. Indeed, the peak at 586 nm could either fit the ${}^5D_1 \rightarrow {}^7F_3$ transition or be part of the ${}^5D_0 \rightarrow {}^7F_1$. A similar question may also arise for the peak at 621 nm, which could either fit the ${}^5D_1 \rightarrow {}^7F_4$ transition or be part of the ${}^5D_0 \rightarrow {}^7F_2$. Further experiments were carried out in order to confirm the previous assignments, as outlined in the following.

The Eu^{3+} lifetimes associated with the transitions occurring from the ${}^5D_{1,2,3}$ higher energy levels are expected to be lower than the lifetimes associated with transitions from the 5D_0 ground level. If the detector delay time (DT) is changed, we can observe the evolution of these transitions and ensure that the assignment of some of the previous two-component bands is accurate. **Figure 3.7** displays the emission spectra of sample 1%-R8 recorded at different delay times. As the DT increases, the intensity of ${}^5D_{1-3} \rightarrow {}^7F_j$ transitions diminishes gradually, and only the transitions from the 5D_0 ground level at a DT of 10 ms are observable. The peak at 586 nm disappears at 10 ms, indicating that it corresponds to the ${}^5D_1 \rightarrow {}^7F_3$ transition rather than being a component of the ${}^5D_0 \rightarrow {}^7F_1$. However, the two peaks at 616 and 621 nm remain at 10 ms, proving that both of them are associated with the ${}^5D_0 \rightarrow {}^7F_2$ transition. In addition, at this DT the long tail of the ${}^5D_0 \rightarrow {}^7F_2$ transition becomes narrower and the

splitting of the band is also more prominent. This result could be associated with the presence of an additional component as a result of a small contribution from the ${}^5D_1 \rightarrow {}^7F_4$ transition at a DT of 0.2 ms. The ${}^5D_0 \rightarrow {}^7F_0$ transition was not observed, although it could have been overlapped with the ${}^5D_0 \rightarrow {}^7F_1$ band due to its typical low intensity. Similar behavior was observed for samples 1%-R1 and 1%-R3 (see Supporting Information, **Figure S3.2**).

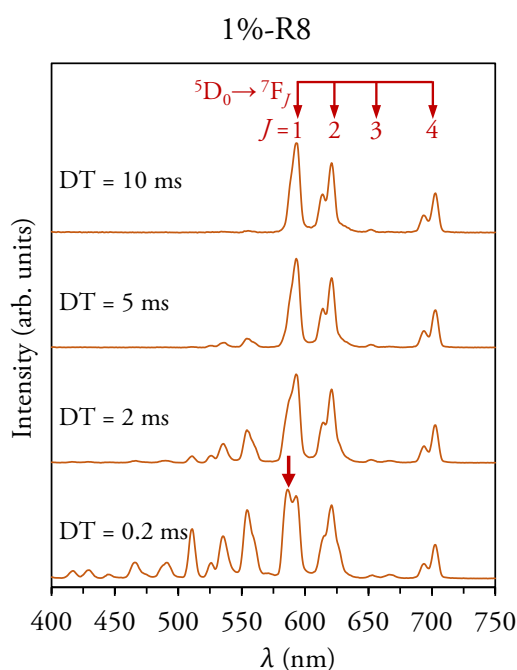


Figure 3.7. Room temperature emission spectra obtained at different delay times for sample 1%-R8 upon excitation at 395 nm.

The evaluation of the cut-off phonon energy (the highest-energy vibrational mode) for KY_3F_{10} has been ambiguous in the literature, with values obtained in the range 400–600 cm^{-1} [23,50,51]. In order to have a deeper knowledge of the phonon energy and get a general idea on how the lattice vibrations may vary depending on the

morphology of samples, IR and Raman spectroscopy was performed for the undoped KY_3F_{10} samples of Routes 1, 3 and 8, as presented in **Figure 3.8**.

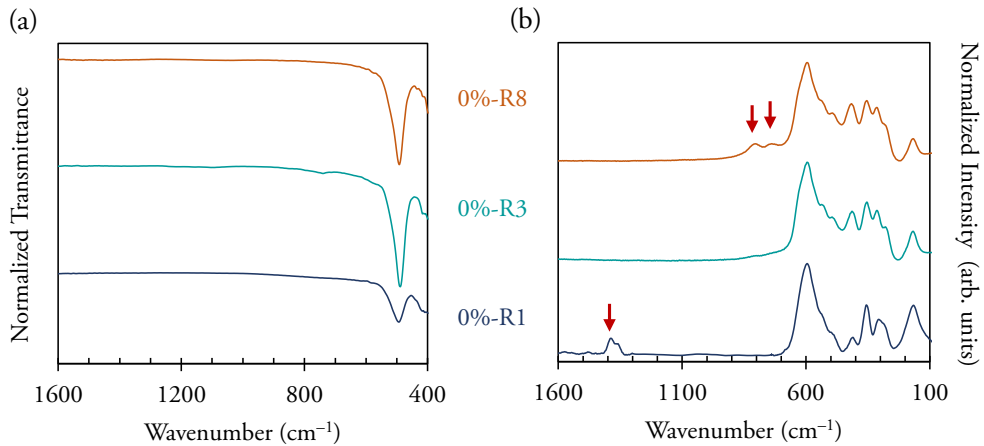


Figure 3.8. Room temperature (a) IR, and (b) Raman spectra for the undoped KY_3F_{10} samples of Routes 1, 3 and 8.

Regarding the IR spectra, there are no differences among all the samples, which present a unique band centered at 492 cm^{-1} . In the low-frequency region of the Raman spectra (below 700 cm^{-1}), all samples display the same bands with very similar positions and relative intensities, the main dominant peak occurring at 592 cm^{-1} . However, substantial changes appear at higher frequencies depending on the sample. Therefore, the compounds exhibit different cut-off phonon energies, which can be directly related to the photoluminescence behavior of the materials. The sample of Route 8 presents two additional peaks at 731 and 810 cm^{-1} , but the higher cut-off energy is observed for the sample of Route 1, whose Raman spectrum displays two peaks at 1361 and 1391 cm^{-1} . These results are in total agreement with the previous discussion of the changes observed in the transitions occurring from higher excited levels. The differences between samples may arise from the particle size and

morphology. Particularly, from the analysis of the Raman spectra it is clear that the sample synthesized following Route 1 has the highest phonon energy. Probably, the small size of the particles (self-assembled nanoparticles with a diameter of about 10 nm) enhances the presence of quantum confinement effects making that the Ln^{3+} ions are closer in the host lattice and, thus, increasing the cut-off energy of it. A thorough description of the assignment of Raman bands can be found in Section S4 of Supporting Information.

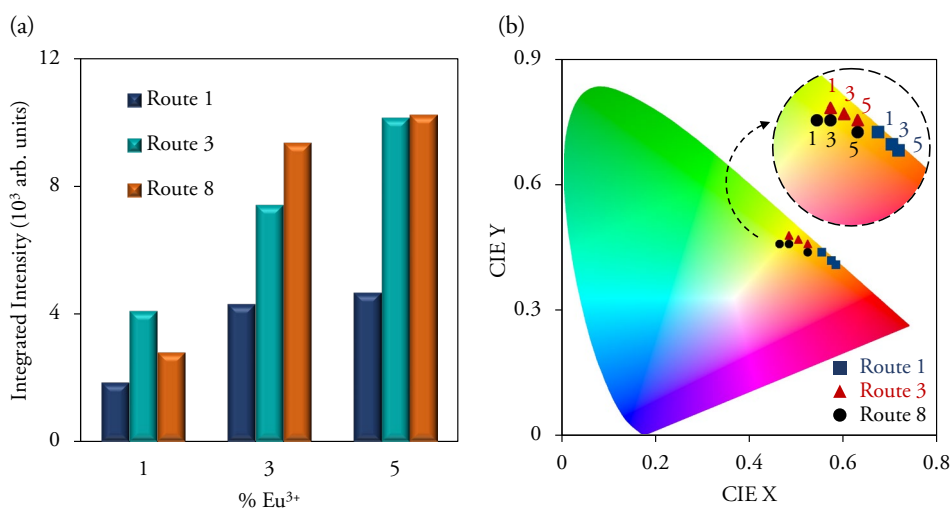


Figure 3.9. (a) Integrated luminescence intensity and (b) CIE chromaticity diagram for Eu^{3+} -doped samples of Routes 1, 3 and 8 excited by 395 nm. The numbers in the inset indicate the molar percentage of Eu^{3+} (1, 3 and 5%).

Furthermore, the bar chart in **Figure 3.9(a)** presents the values of the total integrated luminescence intensity for the different Eu^{3+} -doped phosphors. It can be seen that the emission intensity depends strongly on both the synthetic route and the dopant concentration. The lowest values correspond to samples of Route 1. Following with the previous line of reasoning, a higher phonon interaction with the luminescent ions could be the critical factor responsible for the intensity quenching. On the other

hand, when increasing the dopant content from 3 to 5 mol%, minor changes are appreciated in the emission intensity of samples from Routes 3 and 8.

In addition, the CIE coordinates of the corresponding materials doped with Eu^{3+} were calculated from the emission spectra using the GoCIE software [52] and are shown in **Figure 3.9(b)**. It is worthy of praise emphasizing that the choice of the synthetic route and dopant content allowed strategically to obtain color-tunable emissions of the phosphors, which vary from orangish to yellow colors and are, therefore, potential candidates for their application in solid state lighting devices, such as blue-InGaN chips based w-LEDs.

3.3.3.2. *Judd-Ofelt and Asymmetry Ratio Calculations*

The Judd-Ofelt theory describes the transition intensities for lanthanides and actinides in solids and solutions. According to this theory, the central ion is affected by the surrounding host ions, which produce a static electric field (the crystal field) [53]. The Ω_2 Judd-Ofelt parameter correlates with the polarizable and covalent character of the lanthanide ion in the lattice [54,55]. Thus, the analysis of this parameter can be useful to describe the Eu^{3+} surroundings in the host lattice. Moreover, the intensity of the magnetic dipole ${}^5\text{D}_0 \rightarrow {}^7\text{F}_1$ transition is considered to be independent of the host matrix, while the electric dipole ${}^5\text{D}_0 \rightarrow {}^7\text{F}_2$ is known as a hypersensitive transition because it is highly influenced by the local symmetry of the Eu^{3+} ion [56]. Therefore, the asymmetry ratio R provides information about the local symmetry of the dopant and is defined as the ratio between the intensities of the ${}^5\text{D}_0 \rightarrow {}^7\text{F}_2$ and ${}^5\text{D}_0 \rightarrow {}^7\text{F}_1$ transitions:

$$R = \frac{I_{02}}{I_{01}} \quad (3.3)$$

where I_{0j} is the intensity associated with the transition ${}^5D_0 \rightarrow {}^7F_j$ that takes place at a λ_{0j} wavelength. For Eu^{3+} , the asymmetry ratio is proportional to the Judd-Ofelt parameter Ω_2 , which can be calculated from the experimental emission spectra according to the following expression [57]:

$$\Omega_2 = A_{01} \cdot R \cdot \frac{\lambda_{02}^4}{\lambda_{01}} \cdot \frac{3h}{64e^2\pi^4 \chi \|U^2\|} \quad (3.4)$$

where A_{01} is the magnetic dipole transition rate, which is assumed to be constant and equal to 50 s^{-1} ; h is the Planck constant; e denotes the elementary charge; χ is the Lorentz local field correction term (which is equal to $\frac{n(n^2+2)^2}{9}$, n is the refractive index at λ_{02}); and $\|U^2\|$ corresponds to the reduced matrix element of the unit tensor operator connecting levels 0–2 [58].

The value reported in the literature for $\|U^2\|$ is 0.0032 [59]. The maximum wavelength value obtained for samples is 593 nm for λ_{01} (${}^5D_0 \rightarrow {}^7F_1$ transition) and 621 nm for λ_{02} (${}^5D_0 \rightarrow {}^7F_2$ transition). The refractive index of KY_3F_{10} at 621 nm is 1.490 and can be considered as a constant in the spectrum range 470–700 nm [60,61]. Expressing λ_{0j} in cm, taking $h = 6.6261 \cdot 10^{-27} \text{ erg}\cdot\text{s}$, $e = 4.803 \cdot 10^{-10} \text{ esu}$, and substituting the rest of the values [62], Ω_2 results in:

$$\Omega_2 = (1.837 R) \cdot 10^{-20} \text{ cm}^2 \quad (3.5)$$

The calculation of the asymmetry ratio R was performed using the integrated intensities corresponding to the respective emission bands. To avoid the contributions from higher excited levels (${}^5D_{1-3}$), which could lead to non-accurate results, the intensity values were extracted from the emission spectra recorded with a DT of 10 ms, **Figure 3.7**. All the R and Ω_2 values, summarized in **Table 3.3**, are very similar regardless of the synthetic route or the europium concentration. In short, there are no

noticeable changes in the polarizability environment of the ion, suggesting that the crystal field of Eu^{3+} must be quite similar in all the samples.

Table 3.3. R and Ω_2 values obtained from the emission spectra with a DT of 10 ms ($\lambda_{\text{exc}} = 395$ nm).

Eu ³⁺ mol %	R			Ω_2 (10^{-20} cm ²)		
	Route 1	Route 3	Route 8	Route 1	Route 3	Route 8
1	1.03	1.05	0.95	1.89(2)	1.93(2)	1.75(1)
3	1.01	1.04	0.96	1.86(2)	1.91(3)	1.76(1)
5	1.06	1.09	1.00	1.95(3)	2.00(3)	1.84(2)

3.3.3.3. Lifetimes and Quantum Efficiencies Analysis

In addition to the previous experiments, useful information about the photoluminescence properties can also be obtained from the fluorescence kinetics. In order to study the decay curves for the different ${}^5\text{D}_{0-3} \rightarrow {}^7\text{F}_j$ emissions and evaluate the observed lifetime (τ_{obs}) of the different excited levels, time-resolved luminescence measurements were performed with an excitation wavelength of 395 nm. The experiments were carried out setting a DT of 0.2 ms to collect ${}^5\text{D}_{1,2,3} \rightarrow {}^7\text{F}_j$ emissions and a DT of 10 ms to collect ${}^5\text{D}_0 \rightarrow {}^7\text{F}_j$ transitions and avoid the contribution from higher excited levels that could lead to misleading results. Different emission wavelengths were used according to the respective ${}^5\text{D}_{0-3} \rightarrow {}^7\text{F}_j$ transitions. The decay profiles of the ${}^5\text{D}_{0,1} \rightarrow {}^7\text{F}_j$ transitions were fitted by the following single exponential function:

$$I(t) = I_0 \exp\left(\frac{-t}{\tau_{\text{obs}}}\right) \quad (3.6)$$

where I refers to the intensity as a function of time (t). On the other hand, the decay

curves of the ${}^5D_{2,3} \rightarrow {}^7F_j$ transitions were best fitted to a double exponential model:

$$I(t) = I_1 \exp\left(\frac{-t}{\tau_{\text{obs } 1}}\right) + I_2 \exp\left(\frac{-t}{\tau_{\text{obs } 2}}\right) \quad (3.7)$$

This fact could be related to some energy transfer or cross-relaxation processes that quench the luminescence from the higher excited states. When the double exponential model was used, an effective lifetime (τ_{eff}) was calculated:

$$\tau_{\text{eff}} = \frac{I_1(\tau_{\text{obs } 1})^2 + I_2(\tau_{\text{obs } 2})^2}{I_1(\tau_{\text{obs } 1}) + I_2(\tau_{\text{obs } 2})} \quad (3.8)$$

Some examples of the decay profiles can be found in the Supporting Information, **Figure S3.4**. In order to evaluate the quantum efficiencies (the intrinsic quantum yields, η) of the phosphors, the radiative lifetimes (τ_{rad}) of Eu^{3+} can be calculated from the emission spectra directly using the following expression [63–65]:

$$\tau_{\text{rad}} = \frac{I_{01}}{n^3 \cdot I_{\text{total}} \cdot (A_{01})_{\text{vac}}} \quad (3.9)$$

where I_{01} is the integrated intensity associated with the transition ${}^5D_0 \rightarrow {}^7F_j$; I_{total} is the integrated intensity of all the spectra corresponding to ${}^5D_0 \rightarrow {}^7F_j$ transitions; n denotes the refractive of the material (which can be considered equal to 1.490); and $(A_{01})_{\text{vac}}$ is the magnetic dipole transition rate in the vacuum (14.65 s^{-1}). The quantum efficiency of the luminescence material can be evaluated considering the calculated radiative lifetimes and the observed lifetimes for the 5D_0 level as follows:

$$\eta = \frac{\tau_{\text{obs}}}{\tau_{\text{rad}}} \quad (3.10)$$

Table 3.4. Average observed lifetimes for the different excited levels (${}^5D_{0-3}$) of the Eu^{3+} - KY_3F_{10} phosphors, calculated radiative lifetimes and quantum efficiencies for the 5D_0 level.

Sample	$\langle \tau_{\text{obs}} \rangle$ (ms)				τ_{rad} (ms)	η (%)
	5D_3	5D_2	5D_1	5D_0		
1%-R1	-	-	1.68(6)	8.02(6)	8.32(4)	96
3%-R1	-	-	1.53(6)	8.09(7)	8.27(4)	98
5%-R1	-	-	1.50(8)	8.15(6)	8.07(3)	101
1%-R3	0.45(2)	0.71(1)	2.06(3)	8.98(2)	8.14(4)	110
3%-R3	0.38(1)	0.66(1)	1.94(1)	8.99(7)	8.00(3)	112
5%-R3	0.29(1)	0.56(1)	1.79(1)	9.16(3)	7.84(3)	117
1%-R8	0.61(2)	0.92(4)	2.05(1)	7.93(7)	8.56(4)	93
3%-R8	0.50(2)	0.85(5)	1.97(5)	8.17(7)	8.55(4)	96
5%-R8	0.43(2)	0.73(4)	1.78(1)	8.78(4)	8.35(4)	105

Table 3.4 summarizes the average observed lifetimes, $\langle \tau_{\text{obs}} \rangle$, for the different excited levels (${}^5D_{0-3}$) of the Eu^{3+} - KY_3F_{10} phosphors. Different transitions of each level were used for the calculation of the average value (a detailed description can be found in **Table S3.3** of the Supporting Information). All the correlation coefficients of the fits (R^2) were ≥ 0.999 and when the decay profiles were fitted to a double exponential model, the lifetime shown refers to τ_{eff} . The calculated radiative lifetimes and quantum efficiencies for the 5D_0 level are also listed in **Table 3.4**.

From the analysis of the lifetimes, interesting conclusions can be drawn. Firstly, the discussion of the lifetimes associated with the 5D_3 , 5D_2 and 5D_1 emissions will be addressed. From the experimental data, it is clearly shown that they are shorter than those of the low-energy 5D_0 emission, as previously suggested. This is because the Eu^{3+} population in higher excited levels relaxes non-radiatively to the metastable 5D_0 level

by cross-relaxation processes [48]. In addition, when the Eu^{3+} content is increased, the lifetime value for ${}^5\text{D}_{1-3}$ levels becomes shorter. This fact can be well explained considering the cross-relaxation processes too. Furthermore, there are also differences when comparing samples of different routes. Among all the samples with the same mol% Eu^{3+} , samples of Route 1 present the lowest lifetimes for the ${}^5\text{D}_1$ level. This result is consistent with the previous phonon energy comments (indeed, the emission from ${}^5\text{D}_{2,3}$ levels is totally suppressed). However, while for the ${}^5\text{D}_1$ level there are no differences between samples of Routes 3 and 8, different values are obtained for higher excited levels (${}^5\text{D}_2$ and ${}^5\text{D}_3$), showing the longer lifetimes samples of Route 8. Considering the cut-off phonon energy results, it was expected the inverse situation. Nonetheless, as described below, the phonon energy mainly affects the ${}^5\text{D}_0$ lifetimes for these samples.

Regarding the ${}^5\text{D}_0$ level, all the lifetimes were determined to be about 8–9 ms, collecting the longest lifetime for the sample 5%-R3. When increasing the dopant content in samples of the same route, the lifetime becomes longer as a general tendency. This is due to the more probable relaxation occurring from the higher excited levels that allow increasing the population of the ${}^5\text{D}_0$ level. As it has been shown before, the Raman spectrum of the sample of Route 8 presented two additional peaks at 731 and 810 cm^{-1} , thus increasing the cut-off phonon energy (in comparison with the sample of Route 3). As a result, it was expected that slightly higher lifetimes would be obtained for samples of Route 3, which is now confirmed. Then, it is easy to notice that the phonon energy differences in these samples mainly affects the ${}^5\text{D}_0$ lifetimes while those of higher excited levels are very similar.

Finally, the quantum efficiencies calculations deserve some particular comments. The values obtained were in the range of 93–117%. Though high quantum efficiencies

were expected due to the low phonon energy of the crystal lattice, the obtained values higher than 100% suggest that other processes may take place. The quantum cutting (QC) process allows obtaining luminescent materials with more than 100% efficiency, which can be very interesting for their application in light-emitting diodes. Theoretically, the QC for a single Ln^{3+} is possible. However, competing emissions in the infrared and ultraviolet could prevent efficient visible QC on a single ion [66]. As an alternative, many studies have reported the use of Ln^{3+} ions pairs (Gd^{3+} - Eu^{3+} , Yb^{3+} - Tb^{3+} , Yb^{3+} - Pr^{3+} ...) which lead to quantum efficiencies up to 200%. Nevertheless, a few studies have focused on the possibility of obtaining materials with efficient QC processes using only a single luminescent ion. The studies developed by X. Chen *et al.* showed that QC was observable using only Er^{3+} ions, or in the host matrix YNbO_4 using Tm^{3+} as activator ions [67,68].

To the best of our knowledge, no efficient QC processes have been addressed for the Eu^{3+} ion as a single luminescent center. However, the study developed by Y. Liu *et al.* [69] demonstrated that QC processes can efficiently occur in $\text{Ba}_9\text{Lu}_2\text{Si}_6\text{O}_{24}:\text{Tb}^{3+}$ via cross-relaxation energy transfers between Tb^{3+} ions. They also observed that the lifetimes speeded up by increasing the Tb^{3+} concentration because the cross-relaxation effects were strengthened. Relating these findings with our results, a plausible explanation for the high quantum efficiencies yielded is that QC or similar energy transfers may also occur via cross-relaxation energy processes in our materials. Further work to investigate this possibility is in progress.

3.4. Conclusions

The structure, morphologies and luminescence properties of Eu^{3+} -doped KY_3F_{10} materials have been investigated in detail. The compounds with the nominal formula

$K(Y_{3-x}Eu_x)F_{10}$ were prepared according to different synthetic routes. The synthesis was performed via the sonochemical, coprecipitation and continuous stirring methods. Moreover, a combination of these methods with a successive hydrothermal treatment was also addressed. The results obtained allow us to draw the following conclusions:

- The synthetic methodology and the reaction conditions are critical factors for the characteristics of the final products. The synthetic routes provide solids with very different types of morphology, size, and crystallinity.
- The Eu^{3+} -doped KY_3F_{10} samples show the characteristic emission lines corresponding to the ${}^5D_{0-3} \rightarrow {}^7F_j$ transitions. The various morphologies and sizes lead to differences in the phonon energy associated with the lattice vibrations, implying noticeable changes in the luminescence spectra. In particular, a total quenching of the ${}^5D_{2,3} \rightarrow {}^7F_j$ transitions was observed for the samples obtained by an ultrasonication process (with a higher cut-off energy than the others). As a result, color-tunable emissions were obtained, which varied from orangish to yellow colors.
- The calculations of the asymmetry ratio R and the Ω_2 Judd-Ofelt parameter report very similar values regardless of the synthetic route or the europium concentration. Bearing in mind the adequacy of the dopant ion as a structural probe, these results suggest that the crystal field of Eu^{3+} must be quite similar.
- Different lifetime values are obtained for the samples depending on the synthetic route and a plausible relation with the cut-off phonon energy of the compounds can be established. Moreover, quantum cutting processes or similar energy transfers between Eu^{3+} ions allow yielding quantum efficiencies higher than 100%.

For the reasons commented above, this study enriches the literature and shows that the investigated Eu^{3+} -doped KY_3F_{10} phosphors offer different possibilities depending on the synthetic strategy used, which can be a keystone for future optical, bioanalytical or biomedical applications. In fact, the orange-yellow emissions of the phosphors could be interesting for their application in w-LEDs through their combination with blue chips.

Acknowledgments

P. S-G, H. B-M, and E. C. thank the Universitat Jaume I (Project UJI-B2019-41) and Ministerio de Economía y Competitividad (Project MAT2016-80410-P) for financial support. P. S.-G. also thanks the Spanish Ministerio de Ciencia, Innovación y Universidades for an FPU predoctoral contract.

References

- [1] J. Wu, J. Wang, J. Lin, Y. Xiao, G. Yue, M. Huang, Z. Lan, Y. Huang, L. Fan, S. Yin, T. Sato, *Scientific Reports*. 3 (2013) 1–5.
- [2] B.M. Tissue, *Chemistry of Materials*. 10 (1998) 2837–2845.
- [3] T. Grzyb, M. Węclawiak, T. Pędziński, S. Lis, *Optical Materials*. 35 (2013) 2226–2233.
- [4] C. Sassoie, G. Patriarche, M. Mortier, *Optical Materials*. 31 (2009) 1177–1183.
- [5] F. Auzel, *Chemical Reviews*. 104 (2004) 139–173.
- [6] L. Tao, W. Xu, Y. Zhu, L. Xu, H. Zhu, Y. Liu, S. Xu, P. Zhou, H. Song, *Journal of Materials Chemistry C*. 2 (2014) 4186–4195.

- [7] Y. Zhang, X. Li, D. Geng, M. Shang, H. Lian, Z. Cheng, J. Lin, *CrystEngComm*. 16 (2014) 2196–2204.
- [8] G. Yi, H. Lu, S. Zhao, Y. Ge, W. Yang, D. Chen, L.H. Guo, *Nano Letters*. (2004).
- [9] K.K. Markose, R. Anjana, A. Antony, M.K. Jayaraj, *Journal of Luminescence*. 204 (2018) 448–456.
- [10] M. Deng, Y. Ma, S. Huang, G. Hu, L. Wang, *Nano Research*. 4 (2011) 685–694.
- [11] A. Podhorodecki, A. Noculak, M. Banski, B. Sojka, A. Zelazo, J. Misiewicz, J. Cichos, M. Karbowski, B. Zasonska, D. Horak, B. Sikora, D. Elbaum, T. Dumych, R. Bilyy, M. Szewczyk, *ECS Transactions*. 61 (2014) 115–125.
- [12] M. Runowski, *Journal of Luminescence*. 186 (2017) 199–204.
- [13] M. Runowski, S. Goderski, J. Paczesny, M. Ksiezopolska-Gocalska, A. Ekner-Grzyb, T. Grzyb, J.D. Rybka, M. Giersig, S. Lis, *Journal of Physical Chemistry C*. 120 (2016) 23788–23798.
- [14] M. Runowski, N. Stopikowska, S. Goderski, S. Lis, *Journal of Alloys and Compounds*. 762 (2018) 621–630.
- [15] B. Sharma, R.R. Frontiera, A. Henry, E. Ringe, R.P. Van Duyne, *Materials Today*. 15 (2012) 16–25.
- [16] H. Wu, H. Li, L. Jiang, R. Pang, S. Zhang, D. Li, G. Liu, C. Li, J. Feng, H. Zhang, *Journal of Materials Chemistry C*. (2020).
- [17] Y. Zhang, J. Xu, Q. Cui, B. Yang, *Scientific Reports*. 7 (2017) 1–12.
- [18] Y. Zhou, W. Zhuang, Y. Hu, R. Liu, Z. Jiang, Y. Liu, Y. Li, Y. Zheng, L. Chen, J. Zhong, *RSC Advances*. 7 (2017) 46713–46720.

- [19] T. Wanjun, Z. Fen, *Journal of the American Ceramic Society*. 102 (2019) 4632–4639.
- [20] W. Sun, Y. Jia, R. Pang, H. Li, T. Ma, D. Li, J. Fu, S. Zhang, L. Jiang, C. Li, *ACS Applied Materials and Interfaces*. 7 (2015) 25219–25226.
- [21] L. Liu, R.J. Xie, W. Li, N. Hirosaki, Y. Yamamoto, X. Sun, *Journal of the American Ceramic Society*. 96 (2013) 1688–1690.
- [22] L.Y. Wang, E.H. Song, T.T. Deng, Y.Y. Zhou, Z.F. Liao, W.R. Zhao, B. Zhou, Q.Y. Zhang, *Dalton Transactions*. 46 (2017) 9925–9933.
- [23] E.N. Silva, A.P. Ayala, J.Y. Gesland, R.L. Moreira, *Vibrational Spectroscopy*. 37 (2005) 21–26.
- [24] S. Guo, C. Cao, R. Cao, *Journal of Nanoscience and Nanotechnology*. 16 (2016) 3857–3860.
- [25] P. Caro, P. Porcher, *Journal of Luminescence*. 18–19 (1979) 257–261.
- [26] K. Friese, H. Krüger, V. Kahlenberg, T. Balić-Zunić, H. Emerich, J.Y. Gesland, A. Grzechnik, *Journal of Physics Condensed Matter*. 18 (2006) 2677–2687.
- [27] L. Aigouy, A. Cazé, P. Gredin, M. Mortier, R. Carminati, *Physical Review Letters*. 113 (2014) 1–5.
- [28] P.A. Loiko, N.M. Khaidukov, J. Méndez-Ramos, E. V. Vilejshikova, N.A. Skoptsov, K. V. Yumashev, *Journal of Luminescence*. 170 (2016) 1–7.
- [29] M.A. Gusowski, A. Gagor, M. Trzebiatowska-Gusowska, W. Ryba-Romanowski, *Journal of Solid State Chemistry*. 179 (2006) 3145–3150.
- [30] A. Bensalah, M. Ito, Y. Guyot, C. Goutaudier, A. Jouini, A. Brenier, H. Sato, T.

- Fukuda, G. Boulon, *Journal of Luminescence*. 122–123 (2007) 444–446.
- [31] B. Petrovich Sobolev, *The Rare Earth Trifluorides: The high temperature chemistry of the rare earth trifluorides*, Barcelona, Spain, 2000.
- [32] L. Gomes, H.M.D.S.M.D. Linhares, R.U. Ichikawa, L.G. Martinez, S.L. Baldochi, *Optical Materials*. 54 (2016) 57–66.
- [33] P. Villars, K. Cenzual, eds., KY_3F_{10} Crystal Structure: Datasheet from “PAULING FILE Multinaries Edition – 2012” in Springer Materials (https://materials.springer.com/isp/crystallographic/docs/sd_0552093)
- [34] A. Grzechnik, J. Nuss, K. Friese, J.-Y. Gesland, M. Jansen, *Z. Kristallographic NCS*. 217 (2002) 460.
- [35] R.U. Ichikawa, H.M.S.M.D. Linhares, I. Peral, S.L. Baldochi, I.M. Ranieri, X. Turrillas, L.G. Martinez, *ACS Omega*. 2 (2017) 5128–5136.
- [36] K. Momma, F. Izumi, *Journal of Applied Crystallography*. 44 (2011) 1272–1276.
- [37] L. Zhu, Y. Liu, X. Fan, D. Yang, X. Cao, *Journal of Luminescence*. 131 (2011) 1380–1385.
- [38] S. Goderski, M. Runowski, S. Lis, *Journal of Rare Earths*. 34 (2016) 808–813.
- [39] L. Zhu, J. Meng, X. Cao, *Materials Letters*. 62 (2008) 3007–3009.
- [40] C. Cao, *Journal of Materials Research Society*. 27 (2012) 2988–2995.
- [41] C. Cascales, R. Balda, V. Jubera, J.P. Chaminade, J. Fernández, *Optics Express*. 16 (2008) 2653–2662.
- [42] C. Cascales, P. Porcher, J. Fernández, A. Oleaga, R. Balda, E. Diéguez, *Journal of Alloys and Compounds*. 323–324 (2001) 260–266.

- [43] C. Cascales, J. Fernández, R. Balda, *Optics Express*. 13 (2005) 2141–2152.
- [44] R.D. Shannon, *Acta Crystallogr.* A32 (1976) 751–767.
- [45] I.E. Kolesnikov, A. V. Povolotskiy, D. V. Mamonova, E. Lähderanta, A.A. Manshina, M.D. Mikhailov, *RSC Advances*. 6 (2016) 76533–76541.
- [46] G.A. Sotiriou, M. Schneider, S.E. Pratsinis, *Journal of Physical Chemistry C*. 116 (2012) 4493–4499.
- [47] K. Binnemans, *Coordination Chemistry Reviews*. 295 (2015) 1–45.
- [48] X. Liu, L. Yan, J. Lin, *Journal of the Electrochemical Society*. 156 (2009) 1–6.
- [49] T. Yamase, T. Kobayashi, M. Sugeta, H. Naruke, *Journal of Physical Chemistry A*. 101 (1997) 5046–5053.
- [50] M. Mortier, J.Y. Gesland, M. Rousseau, M.A. Pimenta, L.O. Ladeira, J.C. Machado da Silva, G.A. Barbosa, *Journal of Raman Spectroscopy*. 22 (1991) 393–396.
- [51] I.R. Martín, Y. Guyot, M.F. Joubert, R.Y. Abdulsabirov, S.L. Korableva, V. V. Semashko, *Journal of Alloys and Compounds*. 323–324 (2001) 763–767.
- [52] K. R. Justin Thomas, GoCIE V2 software (2009), downloaded from <http://faculty.iitr.ac.in/~krjt8fcy/index.html>
- [53] B.M. Walsh, Judd-Ofelt theory: principles and practices, in: B. Di Bartolo, O. Forte (Eds.), *Advances in Spectroscopy for Lasers and Sensing*, Springer, Dordrecht, 2006; pp. 403–433.
- [54] D.K. Patel, B. Vishwanadh, V. Sudarsan, S.K. Kulshreshtha, *Journal of the American Ceramic Society*. 96 (2013) 3857–3861.

- [55] C. de Mello Donegá, S.A. Junior, G.F. de Sá, *Journal of Alloys and Compounds*. 250 (1997) 422–426.
- [56] K. Vuković, M. Medić, M. Sekulić, M.D. Dramićanin, *Advances in Condensed Matter Physics*. 2015 (2015) 1–7.
- [57] P. Serna-Gallén, H. Beltrán-Mir, E. Cordoncillo, A.R. West, R. Balda, J. Fernández, *J. Mater. Chem C*. 7 (2019) 13976–13985.
- [58] B. Julián, J. Planelles, E. Cordoncillo, P. Escribano, P. Aschehoug, C. Sanchez, B. Viana, F. Pellé, *Journal of Materials Chemistry*. 16 (2006) 4612–4618.
- [59] S. Constantin, M.L. Stanciu, *Annals of West University of Timisoara - Physics*. 56 (2012) 127–131.
- [60] P. Porcher, P. Caro, *The Journal of Chemical Physics*. 68 (1978) 4176–4182.
- [61] J. Zhang, Z. Hao, X. Zhang, Y. Luo, X. Ren, X.J. Wang, J. Zhang, *Journal of Applied Physics*. 106 (2009) 034915.
- [62] Y.H. Elbashar, D.A. Rayan, *International Journal of Applied Chemistry*. 12 (2016) 59–66.
- [63] P. Ghosh, A. Patra, *Journal of Physical Chemistry C*. 112 (2008) 19283–19292.
- [64] X.-N. Tian, G.-C. Jiang, X.-T. Wei, L.-Y. Wu, S. Li, K.-M. Deng, Y.H. Chen, M. Yin, *Journal of Nanoscience and Nanotechnology*. 14 (2014) 4490–4494.
- [65] M.H.V. Werts, R.T.F. Jukes, J.W. Verhoeven, *Physical Chemistry Chemical Physics*. 4 (2002) 1542–1548.
- [66] R.T. Wegh, H. Donker, E. V.D. Van Loef, K.D. Oskam, A. Meijerink, *Journal of Luminescence*. 87 (2000) 1017–1019.

- [67] X. Chen, J. Wu, X. Xu, Y. Zhang, N. Sawanobori, C. Zhang, Q. Pan, G.J. Salamo, *Optics Letters*. 34 (2009) 887.
- [68] X. Chen, G.J. Salamo, S. Li, J. Wang, Y. Guo, Y. Gao, L. He, H. Ma, J. Tao, P. Sun, W. Lin, Q. Liu, *Physica B: Condensed Matter*. 479 (2015) 159–164.
- [69] Y. Liu, J. Zhang, C. Zhang, J. Jiang, H. Jiang, *Journal of Physical Chemistry C*. 120 (2016) 2362–2370.

S3. Supporting Information

S3.1. Unit cell parameters

Unit cell parameters (a and V) were refined using WinX^{POW} 1.06 software version and are summarized in **Table S3.1**. The results are in good agreement with the reported values for cubic KY₃F₁₀ ($a = 11.536 \text{ \AA}$, $V = 1535.20 \text{ \AA}^3$) [S1], but no remarkable differences can be found between samples of different synthetic routes.

Table S3.1. Unit cell parameters of the undoped samples of the different synthetic routes.

Synthetic Route	a (Å)	V (Å ³)
1	11.5306(11)	1533.0(3)
2	11.5349(11)	1534.7(3)
3	11.5416(3)	1537.45(7)
5	11.5210(8)	1529.23(19)
6	11.5410(4)	1537.20(9)
8	11.5317(9)	1533.49(22)

S3.2. Excitation spectra

All the excitation spectra were very similar, **Figure S3.1**. Neither the Eu³⁺ concentration nor the experimental route seemed to show much influence. Different bands associated with the Eu³⁺ transitions were observed from the ground level ⁷F₀ to the different excited levels. Among all of them, the most intense was the ⁷F₀→⁵L₆ transition, with a maximum at 395 nm.

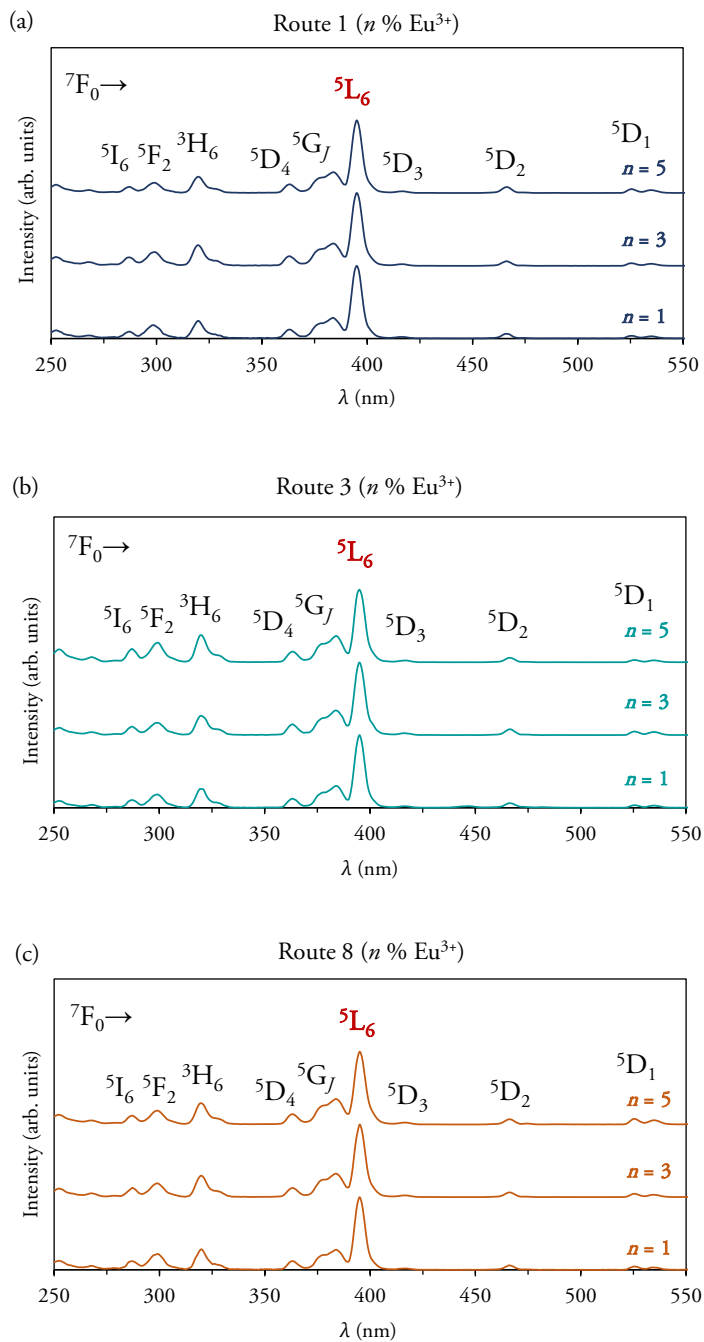


Figure S3.1. Room temperature excitation spectra obtained with a delay time of 0.2 ms for samples of (a) Route 1, (b) Route 3, and (c) Route 8, recorded with an emission wavelength of 593 nm.

S3.3. Emission spectra recorded with a DT = 10 ms

Figure S3.2 displays the emission spectra of samples 1%-R1 and 1%-R3. The same spectral behavior as the corresponding sample of Route 8 is observed (**Figure 3.7**, Article). As the DT increases, the intensity of the ${}^5D_{1,2,3} \rightarrow {}^7F_j$ transitions diminishes, being only observable the transitions from the 5D_0 ground level at a DT of 10 ms.

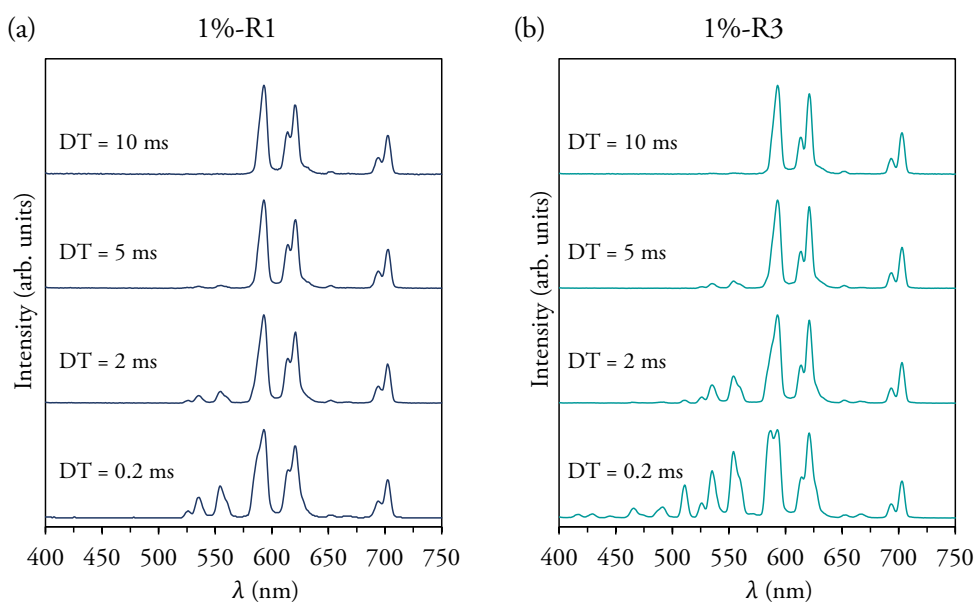


Figure S3.2. Room temperature emission spectra obtained at different delay times for samples 1%-R1 and 1%-R3 upon excitation at 395 nm.

S3.4. Interpretation of the Raman spectra

According to the group theory and irreducible representations of the O_h point group for cubic KY_3F_{10} , the irreducible representation for the Raman-active modes is $\Gamma_{Raman} = 3A_{1g} \oplus 4E_g \oplus 6T_{2g}$, while for the IR-active modes it is $\Gamma_{IR} = 7T_{1u}$ [S2]. The different vibration modes have been well distinguished in the literature by taking advantage of the polarization dependence of the Raman scattered light [S3]. However,

conventional Raman spectroscopy can also be useful to obtain important information about the prepared KY_3F_{10} compounds. **Figure S3.3** depicts, as an example, a deconvolution of the Raman spectrum obtained for the undoped KY_3F_{10} sample of Route 8 (**Figure 3.8** in the Article). In addition to the bands corresponding to Raman-active vibrational modes, the Raman spectra of samples present additional bands above the one-phonon frequency range ($\approx 500 \text{ cm}^{-1}$), which can emerge from combination bands and second-order overtones. On the other hand, **Table S3.2** summarizes the frequencies and the proposed assignment of vibrational modes. For combination bands and second-order overtones, the respective one-phonon vibrational modes are indicated in brackets.

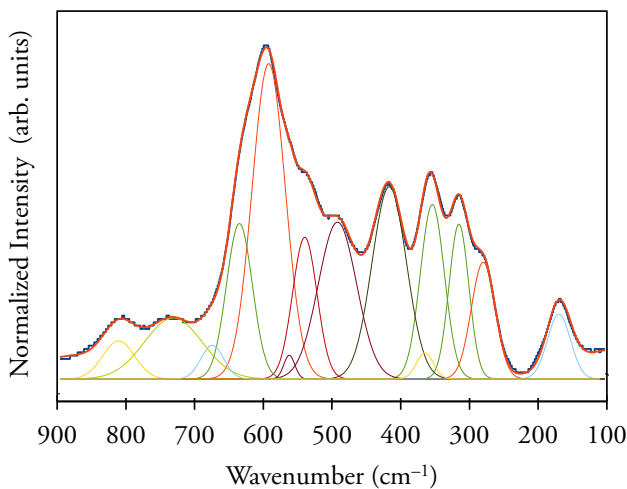


Figure S3.3. Deconvolution of the Raman spectrum for the 0%- Eu^{3+} KY_3F_{10} sample of Route 8.

Overtones are always Raman-allowed [S4] and all the combination bands proposed in **Table S3.2** are Raman-active according to the direct product of the irreducible representations associated with the respective phonon vibration modes: $A_{1g} \otimes A_{1g} = A_{1g}$, $A_{1g} \otimes E_g = E_g$, $A_{1g} \otimes T_{2g} = T_{2g}$ and $T_{2g} \otimes T_{2g} = A_{1g} \oplus E_g \oplus T_{1g} \oplus T_{2g}$. Thus, different possible assignments have been addressed for some bands.

Regarding the 0%-Eu³⁺ sample of Route 1, the 1361 cm⁻¹ band could fit the combination of A_{1g}(279) ⊕ A_{1g}(353) + overtone T_{2g}(364); or overtone A_{1g}(314) ⊕ overtone T_{2g}(364). On the other hand, the 1391 cm⁻¹ band could be well fitted to the sum of the following contributions: T_{2g}(167) ⊕ E_g(492) ⊕ overtone T_{2g}(364).

Table S3.2. Frequencies and assignment of vibrational modes obtained from the deconvolution of the Raman spectrum for the 0%-Eu³⁺ KY₃F₁₀ sample of Route 8.

ν_{obs} (cm ⁻¹)	Mode	ν_{obs} (cm ⁻¹)	Mode
167	T _{2g}	539	T _{2g} (167) ⊕ T _{2g} (364)
279	A _{1g}	561	overtone A _{1g} (279)
315	A _{1g}	592	A _{1g} (279) ⊕ A _{1g} (315)
353	A _{1g}	634 ^b	A _{1g} (279) ⊕ A _{1g} (353)
364	T _{2g}	674 ^c	A _{1g} (315) ⊕ A _{1g} (353)
416 ^a	E _g (142) ⊕ A _{1g} (279)	731	overtone T _{2g} (364)
492	E _g	810	A _{1g} (315) ⊕ E _g (810)

^a The E_g(142) mode has not been observed in the spectrum but has been reported in the literature [S3].

^{b, c} These values could also fit with the overtone A_{1g}(315) and the combination band A_{1g}(315) ⊕ T_{2g}(364), respectively.

S3.5. Eu³⁺ lifetimes

Time-resolved luminescence measurements were performed with an excitation wavelength of 395 nm. The experiments were carried out setting a DT of 0.2 ms to collect ⁵D_{1,2,3}→⁷F₇ emissions and a DT of 10 ms to collect ⁵D₀→⁷F₇ transitions and avoid the contribution from higher excited levels that could lead to misleading results. For each ⁵D_{*i*} excited level, the decay profiles were collected at two different emission wavelengths in order to check if there were some differences. For the ⁵D₂ level, the experiments were carried out only using the 511 nm emission wavelength (⁵D₂→⁷F₃)

since the rest of ${}^5D_2 \rightarrow {}^7F_j$ transitions can be mixed with others arising from different excited levels (see **Figure 3.6**, Article). As can be seen in **Table S3.3**, the experimental lifetimes were very similar for those ${}^5D_i \rightarrow {}^7F_j$ transitions with the same 5D_i excited level. **Figure S3.4** presents, as an example, the decay profiles for different excited levels of sample 1%-R3.

Table S3.3. Observed lifetimes for the different transitions of the $\text{Eu}^{3+}\text{-KY}_3\text{F}_{10}$ phosphors. When a double exponential model has been used (λ_{em}^*), the value corresponds to the effective lifetime (τ_{eff}). All the correlation coefficients of the fits (R^2) were ≥ 0.999 .

λ_{em} (nm)	Transition	τ_{obs} (ms)											
		Route 1				Route 3				Route 8			
		1%	3%	5%		1%	3%	5%		1%	3%	5%	
417*	${}^5D_3 \rightarrow {}^7F_1$	-	-	-	-	0.45(4)	0.37(3)	0.29(2)		0.62(4)	0.49(2)	0.43(2)	
429*	${}^5D_3 \rightarrow {}^7F_2$	-	-	-	-	0.44(3)	0.38(2)	0.28(2)		0.60(3)	0.50(2)	0.43(2)	
511*	${}^5D_2 \rightarrow {}^7F_3$	-	-	-	-	0.76(5)	0.66(1)	0.56(1)		0.92(4)	0.85(5)	0.73(4)	
526	${}^5D_1 \rightarrow {}^7F_0$	1.72(2)	1.58(1)	1.55(2)		2.043(5)	1.945(9)	1.799(6)		2.047(4)	2.01(1)	1.788(5)	
554	${}^5D_1 \rightarrow {}^7F_2$	1.64(5)	1.49(1)	1.44(1)		2.086(6)	1.928(9)	1.779(4)		2.053(4)	1.929(7)	1.771(3)	
593	${}^5D_0 \rightarrow {}^7F_1$	8.761(9)	8.086(9)	8.152(7)		8.970(6)	8.988(6)	9.134(7)		7.986(7)	8.227(4)	8.784(5)	
621	${}^5D_0 \rightarrow {}^7F_2$	8.874(8)	8.089(8)	8.153(7)		8.996(7)	8.996(9)	9.181(7)		7.882(9)	8.122(5)	8.778(5)	

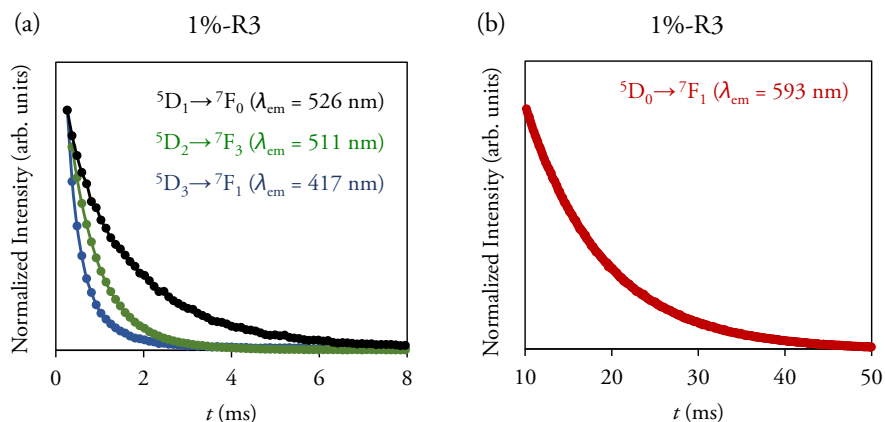


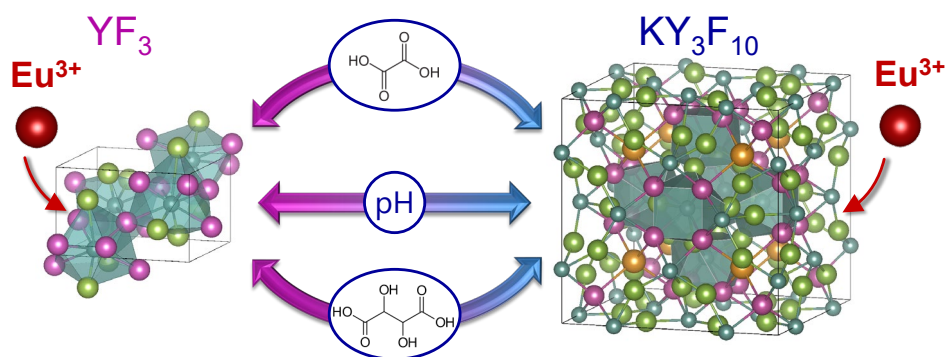
Figure S3.4. Decay profiles collected using $\lambda_{\text{exc}} = 395$ nm with (a) $\text{DT} = 0.2$ ms, $\lambda_{\text{em}} = 526, 511, 417$ nm; and (b) $\text{DT} = 10$ ms, $\lambda_{\text{em}} = 593$.

S3.6. References for the Supporting Information

- [S1] P. Villars, K. Cenzual, KY_3F_{10} Crystal Structure: Datasheet from “PAULING FILE Multinaries Edition – 2012” in SpringerMaterials (https://materials.springer.com/isp/crystallographic/docs/sd_0552093).
- [S2] E.N. Silva, A.P. Ayala, J.Y. Gesland, R.L. Moreira, *Vibrational Spectroscopy*. 37 (2005) 21–26.
- [S3] M. Mortier, J.Y. Gesland, M. Rousseau, M.A. Pimenta, L.O. Ladeira, J.C. Machado da Silva, G.A. Barbosa, *Journal of Raman Spectroscopy*. 22 (1991) 393–396.
- [S4] C. Toulouse, D. Amoroso, C. Xin, P. Veber, M.C. Hatnean, G. Balakrishnan, M. Maglione, P. Ghosez, J. Kreisel, M. Guennou, *Physical Review B*. 100 (2019) 134102.

Chapter 4

Unraveling the superior role of dicarboxylic acids as surface chelators in Eu^{3+} -doped yttrium fluorides: a systematic modulation of the crystal phases and morphologies for highly tuned optical performance



Article 2

Journal of Alloys and Compounds, 883 (2021) 160847

Unraveling the superior role of dicarboxylic acids as surface chelators in Eu³⁺-doped yttrium fluorides: a systematic modulation of the crystal phases and morphologies for highly tuned optical performance

Pablo Serna-Gallén, Héctor Beltrán-Mir, Eloísa Cordoncillo

Departamento de Química Inorgánica y Orgánica, Universitat Jaume I, Av. Vicent Sos Baynat s/n 12071, Castelló de la Plana, Spain

Journal Impact Factor: 6.371

Quartile: Q1

Category: Metallurgy & Metallurgical Engineering

Position: 5/79

Abstract

Eu³⁺-doped YF₃ and KY₃F₁₀ phosphors have been prepared hydrothermally in a wide range of pH values without the use of surface chelators and adding oxalic or tartaric acid. We have proved, for the first time, the usefulness of dicarboxylic acids to modulate the evolution of the surface and crystal phases in the KF-YF₃ system. The morphologies and crystal structures of the materials displayed a critical dependence on the pH and the chelator employed, and a plausible mechanism to explain the differences among the distinct series of samples is proposed. As a result, the fluorides exhibited outstanding and tunable photoluminescence, with extremely high quantum efficiencies and very long lifetimes. The asymmetry ratio and Judd-Ofelt parameters calculations allowed us to establish a relationship between the optical performance of the compounds and their physicochemical properties. We feel that this study can arouse widespread interest within the materials engineering community, since similar procedures could be implemented to the extended family of complex yttrium/lanthanide fluorides for advanced applications in important fields such as bioanalytics, biomedics, or photonics. Indeed, the materials in the present work, with orangish-yellow colored emissions, could be very interesting for application in white light emitting diodes through their combination with blue chips.

Keywords: Fluoride; Europium; Optical Spectroscopy; Luminescence; Surface Chelator; Structure

4.1. Introduction

Over the last few years, there has been an increasing interest in materials doped with luminescent lanthanide ions (Ln^{3+}) because of their wide-ranging potential applications in various fields, such as emitting diodes, solar cells, lasers, or catalysts [1–3]. Among many inorganic materials, fluorides are the most appealing candidates for optical applications because of their low phonon energy associated with the crystal lattice [4]. Consequently, fluoride-based materials present high quantum efficiencies with long lifetimes of Ln^{3+} ions that vary from a few microseconds to several milliseconds [5]. Due to their electronic features arising from the $4f$ electrons and the possibility of energy transfers, many studies have used fluoride phosphors as up/down-converters for efficient spectral conversion [6–8]. Additionally, Ln^{3+} -doped fluorides are of great interest for bioanalytical and biomedical applications. Besides the above-mentioned characteristics, the excellent photostability, low cytotoxicity, and narrow emission lines of these materials make them potential biomarkers for *in vivo* imaging [9–11].

Fluoride hosts with trivalent lattice cations such as Y^{3+} are considered of paramount importance for photoluminescence because Y^{3+} ions can easily be replaced by isovalent lanthanide ions [12]. Among them, both YF_3 and the crystalline compounds of the related $\text{KF}-\text{YF}_3$ system (KYF_4 , KY_3F_{10} , K_2YF_5 , etc.) doped with Ln^{3+} ions have shown outstanding optical response. In particular, YF_3 is considered one of the most significant host lattices for achieving efficient up/down-conversion emissions, and KY_3F_{10} has recently been drawing special interest [13–15]. Commonly, NaYF_4 has been coined as the best fluoride matrix. Nevertheless, some studies have demonstrated the usefulness of YF_3 over NaYF_4 to realize high up-conversion efficiency [16,17]. On the other hand, the thermodynamic stability of KY_3F_{10} is higher

than that of NaYF_4 , which often suffers phase transitions with temperature that can affect the repeatability of fluorescence-intensity-ratio-based optical thermometry measurements [18]. All these remarks emphasize the relevance of YF_3 and KY_3F_{10} , although they are both still subject to advanced research over a wide range of applications.

Under ambient conditions, KY_3F_{10} crystallizes in a cubic structure belonging to the $Fm\bar{3}m$ (O_h^5) space group, with 8 formula units per unit cell ($Z = 8$) [19], while YF_3 crystallizes in an orthorhombic structure with the $Pnma$ (D_{2h}^{16}) space group, and $Z = 4$ [20]. The unit cell structure of KY_3F_{10} and YF_3 crystals, the coordination polyhedra of Y^{3+} and K^+ , and their local symmetry plotted with VESTA software [21] are depicted in **Figure 4.1**.

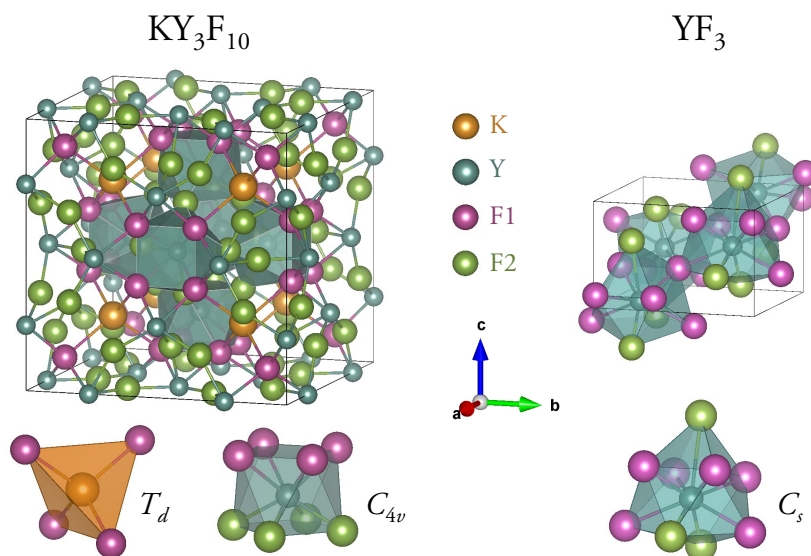


Figure 4.1. Structure of cubic KY_3F_{10} and orthorhombic YF_3 highlighting the coordination polyhedra of Y^{3+} and K^+ ions along with their local symmetry. The labels F1 and F2 refer to fluoride anions situated at different Wyckoff positions.

The luminescence properties of the materials depend to a great extent on their chemical reaction engineering, which opens up new strategies for the design and surface control of materials. To date, different methods have been used to synthesize nano/micron-sized fluorides [22–24]. Particularly, the hydrothermal method has been shown to be the most effective technique to control the morphologies, sizes, crystal phases, and color emissions of inorganic materials [25,26].

Although Ln^{3+} -doped fluorides with several shapes and sizes have been prepared in the literature with different capping agents that allow their surface modification, the vast majority have been synthesized by using hydrophobic organic molecules such as oleic acid, which results in hydrophobic surfaces [27,28]. As a consequence, the hydrophobicity prevents these materials from being used directly for bioapplications since neither good stability in water nor effective bioconjugation can be achieved without further surface modifications.

In light of this, different hydrophilic organic molecules can be used to replace the oleic acid ligand in the synthesis of these materials. Polydentate carboxylic ligands are regarded as excellent candidates because of the direct carboxylic-to-metal coordination [29], citric acid and ethylenediaminetetraacetic acid (EDTA) being the most common [30–33]. Nevertheless, the role of dicarboxylic acids (such as oxalic, tartaric, or malonic acid, to name but a few) has been almost entirely neglected in the literature and studies that report their use in the synthesis of the extended family of yttrium/lanthanide fluorides are scarce. Besides, the few that do use dicarboxylic acids have focused primarily only on NaLnF_4 compounds ($\text{Ln} = \text{Y, La to Lu}$) disregarding other types of fluorides [34–37]. Indeed, to the best of our knowledge, no attempts have been made to prove whether the use of dicarboxylic ligands in the KF-YF_3 system can be successful or not. Therefore, from a chemical engineering point of view, the

need to explore the usefulness of these capping agents in such materials is a matter of importance because they could also be applied to a vast gamut of compounds.

Based on the remarks made in the foregoing paragraphs, in this paper we further investigate Eu^{3+} -doped YF_3 and KY_3F_{10} materials prepared by a hydrothermal method using KBF_4 as the fluoride source. We have chosen Eu^{3+} as a dopant ion because of its unique luminescent properties and its adequacy as a site-sensitive structural probe [38], which is a keystone to describe the optical response of the materials and relate it to their chemical structure. Moreover, the similarity between the ionic radius of Y^{3+} (1.019 Å for a coordination number, CN, = 8; 1.075 Å for a CN = 9) and Eu^{3+} (1.066 Å for a CN = 8; 1.120 Å for a CN = 9) [39] ensures good incorporation of the Eu^{3+} ions in the $\text{YF}_3/\text{KY}_3\text{F}_{10}$ host lattices.

Here, we report for the first time the effective use of dicarboxylic acids (oxalic and tartaric acid) as chelating agents to control the surface and thus the evolution of the crystal phase between YF_3 and KY_3F_{10} . We show that the pH is also crucial to obtain the crystal phase with different morphologies and we propose a plausible mechanism to explain the results obtained. All these parameters make it possible to achieve materials with tunable optical properties.

4.2. Experimental section

4.2.1. Materials

The reagents used were yttrium(III) nitrate hexahydrate [$\text{Y}(\text{NO}_3)_3 \cdot 6\text{H}_2\text{O}$ 99.9%, Alfa Aesar], europium(III) nitrate hexahydrate [$\text{Eu}(\text{NO}_3)_3 \cdot 6\text{H}_2\text{O}$ 99.9%, Strem Chemicals], potassium hydroxide [KOH 85%, Labkem], potassium tetrafluoroborate [KBF_4 96%, Sigma-Aldrich], nitric acid [HNO_3 65%, Labkem], oxalic acid dihydrate [$\text{C}_2\text{H}_2\text{O}_4 \cdot 2\text{H}_2\text{O}$ 99.5%, Panreac], and DL-tartaric acid [$\text{C}_4\text{H}_6\text{O}_6$ 99%, Sigma-Aldrich].

4.2.2. Synthesis of Eu³⁺-doped compounds

In a typical synthesis procedure, 1.5 mmol Ln(NO₃)₃·6H₂O were dissolved in 30 mL of water (Ln = Y, Eu; 1 mol% Eu³⁺) with a resulting pH of 4. Then 3.0 mmol of KBF₄ were added to this solution and the pH was adjusted to the desired value (pH = 4, 6, 7, 8, and 10) using 0.1 or 2 M KOH aqueous solutions (for pH values higher than 7, a whitish precipitate appeared). The mixture was kept under vigorous stirring for 10 min and the final volume was adjusted to 50 mL with water. The whole system was transferred into a Teflon-lined vessel (with a total volume of 125 mL) and treated hydrothermally for 24 h in a thermally heated autoclave at 180°C. After cooling to room temperature, the product was collected by centrifugation, washed several times with water, and dried under an infrared lamp. The as-obtained powders were ground in an agate mortar to obtain a fine powder and break up any large aggregates.

To investigate the effect of the incorporation of dicarboxylic acids acting as chelating agents (oxalic and tartaric acid, OA and TA, respectively), the synthesis was performed in a similar manner. After obtaining the Ln³⁺ solution and before adding KBF₄, 3.0 mmol of oxalic/tartaric acid were dissolved in 10 mL of water. The pH of this solution was adjusted to 6.5 using 2 M KOH aqueous solution, and it was stirred for 10 min. It was then added to the previous Ln³⁺ solution dropwise with stirring, and the mixture was stirred for another 10 min. After that, 3.0 mmol of KBF₄ were added and it was performed in the same way as in the typical reaction. **Table 4.1** summarizes the abbreviations of the different samples according to the pH value and the chelator used in each synthesis. Some considerations about the experimental procedure when using chelating agents can be found in the Supporting Information (Section S4.1).

Table 4.1. Nomenclature of the different Eu^{3+} -doped compounds prepared by a hydrothermal process with different pH values and chelating agents.

pH	No Chelator	Oxalic Acid	Tartaric Acid
4	H4	H4-OA	H4-TA
6	H6	H6-OA	H6-TA
7	H7	H7-OA	H7-TA
8	H8	H8-OA	H8-TA
10	H10	H10-OA	H10-TA

4.2.3. Characterization

All the characterization was performed at room temperature. Powder X-ray diffraction (XRD) was performed using a Bruker-AX D8-Advance X-ray diffractometer with $\text{CuK}_{\alpha 1}$ radiation from $2\theta = 20$ to 90° and at a scan speed of $2.25^\circ/\text{min}$. The unit cell parameters were refined using the WinX^{POW} software package, version 1.06. The microstructure of samples was observed using a JEOL 7001F scanning electron microscope (SEM) operating with an acceleration voltage of 15 kV, a measuring time of 20 s, and a working distance of 10 mm. For microstructural characterization, the powders were deposited on carbon double-sided stickers (previously adhered to the surface of aluminum stubs) and were sputtered with platinum.

The optical properties were studied with an Eclipse Fluorescence Spectrophotometer (Varian). All the photoluminescence measurements were performed in a standard way by placing the powders in a solid sample holder provided by Agilent Technologies. Excitation spectra were recorded in the 250–500 nm range with an emission wavelength of 593 nm. Emission spectra were performed upon excitation at 395 nm in the 500–750 nm range and normalized to the magnetic dipole

$^5D_0 \rightarrow ^7F_1$ transition. The asymmetry ratio R , the branching ratios (β_i), and the Judd-Ofelt parameters (Ω_2 and Ω_4) were calculated from the spectra. The integrated emission intensities of the samples were obtained from the integrated area under the corresponding emission spectra. Besides, the CIE coordinates of the Eu^{3+} -doped materials were calculated from the emission spectra using the GoCIE software package. Time-resolved luminescence measurements were also performed at different emission wavelengths, with the excitation wavelength monitored at 395 nm. Lifetime values were extracted from decay profiles.

4.3. Results and discussion

4.3.1. Structural characterization

The XRD patterns of the Eu^{3+} -doped powders obtained at different pH values following a hydrothermal synthesis are depicted in **Figure 4.2**. **Figure 4.2(a)** corresponds to the samples synthesized without the incorporation of chelating agents. In this series of samples, interesting changes appear depending on the pH of the medium. The XRD patterns of samples H4, H6, and H7 (with a pH of 4, 6, and 7, respectively) exhibit all the peaks corresponding to the orthorhombic phase of YF_3 (JCPDS-ICDD card 321431). However, H4 and H6 present broad, low-intensity peaks, whereas H7 presents narrow, high-intensity peaks. These changes in the shape and intensity of the XRD peaks are attributed to differences in the crystallinity and size of the materials (micro/nano-sized) as will be discussed later. Another interesting detail is that the relative intensities of the peaks with Miller indices (101), (020), (111), and (301) in the XRD patterns of YF_3 samples vary according to the structure of the particles, thereby indicating that the morphologies have different crystalline planes as their dominant surfaces [40]. On the other hand, remarkable results are found in

samples synthesized with a pH equal to or higher than 7 (H7, H8, H10). The crystal structure of these samples evolves towards the formation of cubic KY_3F_{10} (ICSD card 00-040-9643). Thus, the acidity of the medium in the hydrothermal treatment without the addition of chelators plays an important role in the crystal structure and final properties of the materials.

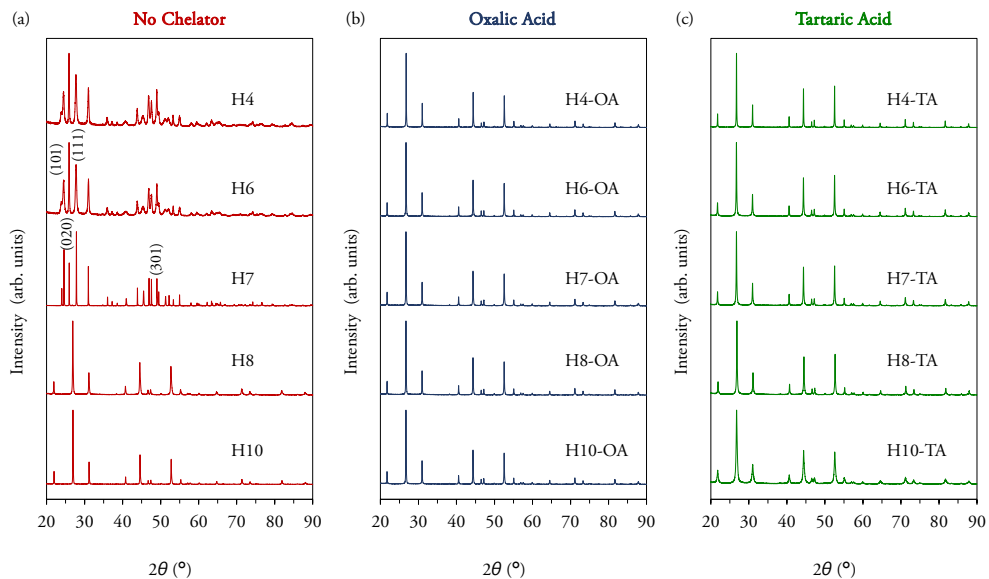


Figure 4.2. XRD patterns for the Eu^{3+} -doped compounds prepared at different pH values by a hydrothermal process (a) with no chelators, (b) using oxalic acid, and (c) adding tartaric acid as a chelating agent.

Figures 4.2(b) and **4.2(c)** present the XRD patterns of powders synthesized following the hydrothermal route with the incorporation of oxalic and tartaric acid as chelating agents, respectively. All the samples exhibited the cubic single-phase KY_3F_{10} in the total range of pH, in contrast to samples prepared without capping agents. The XRD profiles are quite similar with the proviso that the XRD peaks of samples prepared using tartaric acid become slightly broader with increased pH. As per the

above comments, these results highlight the important chelating effect of oxalic and tartaric acid that allows us to control the crystal phase formation at different pH levels.

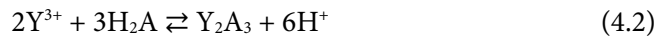
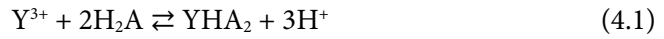
Additionally, the unit cell parameters of all the samples were refined and are indicated in **Table 4.2**. The values obtained were in good agreement with those reported for cubic KY_3F_{10} and orthorhombic YF_3 , although no notable differences could be found between samples with the same crystal structure.

Table 4.2. Crystal phases and unit cell parameter a for the different Eu^{3+} -doped phosphors.

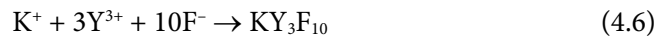
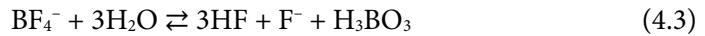
Sample	Crystal Phase	a (Å) ¹
H4	YF_3	6.3718(7)
H6	YF_3	6.3666(3)
H7	YF_3	6.3651(9)
H8	KY_3F_{10}	11.5348(2)
H10	KY_3F_{10}	11.5344(3)
H4-OA	KY_3F_{10}	11.5371(7)
H6-OA	KY_3F_{10}	11.5367(3)
H7-OA	KY_3F_{10}	11.5362(1)
H8-OA	KY_3F_{10}	11.5363(6)
H10-OA	KY_3F_{10}	11.5366(2)
H4-TA	KY_3F_{10}	11.5412(9)
H6-TA	KY_3F_{10}	11.5374(3)
H7-TA	KY_3F_{10}	11.5364(4)
H8-TA	KY_3F_{10}	11.5368(9)
H10-TA	KY_3F_{10}	11.5358(5)

¹ For the orthorhombic YF_3 compounds, the other unit cell parameters were: [H4: $b = 6.8939(6)$, $c = 4.4416(3)$], [H6: $b = 6.8862(4)$, $c = 4.4353(7)$], and [H7: $b = 6.8711(5)$, $c = 4.4089(4)$].

A plausible explanation of the reaction mechanism that leads the system towards the formation of YF_3 or KY_3F_{10} is discussed in the following. The reaction of Y^{3+} with oxalic and tartaric acid (H_2A) has been reported as producing two main products, namely YHA_2 and Y_2A_3 , as shown in equations (4.1) and (4.2) [41,42].

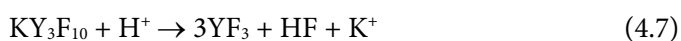


However, depending on the pH of the solution, other more complex species could also be formed, such as $[YA_2(OH)]^{2-}$ or $YA(OH)$, among others [43]. Hence, in order to simplify the mechanistic explanations, the complex formed between Y^{3+} ions and the (de)protonated species of oxalic/tartaric acid is denoted by Y-complex. Without the addition of any chelating agents, the reactions leading to the formation of YF_3 or KY_3F_{10} would follow the steps (4.3)–(4.6).



As the XRD results reveal, the pH of the initial solution is crucial to obtain the final YF_3 or KY_3F_{10} crystal phase. Under acidic conditions, the slow hydrolysis of KBF_4 ensures a small concentration of F^- anions with respect to Y^{3+} cations, which yields the YF_3 phase. If the pH of the initial solution is increased, however, so are the release rate

and concentration of F⁻ anions because the equilibrium is displaced towards the right. Additionally, a basic media of the initial solution can lead to the precipitation of a mixture of hydroxide complexes that help to prevent Y³⁺ from the attack of other ions. Higher pH values therefore allow stabilization of the KY₃F₁₀ phase rather than YF₃. Moreover, some researchers have also postulated that an acid medium can stabilize the YF₃ phase in detriment of KY₃F₁₀ according to expression (4.7), although they obtained a mixture of the two phases [44].



On the other hand, with the introduction of a chelating agent (oxalic or tartaric acid in this study), the reaction takes place primarily through the Y-complex, instead of the solvated Y³⁺ ions, partially preventing the attack of other ions and thus slowing down the reaction rate to form the desired crystal phase. Nevertheless, the chelating ability of the Y-complex is weakened under hydrothermal conditions so that Y³⁺ ions can be released gradually and react with K⁺ and F⁻ ions [45]. Therefore, the incorporation of dicarboxylic acids provides a higher concentration ratio between F⁻ and Y³⁺ ions, allowing the formation of the KY₃F₁₀ phase at much lower pH values.

4.3.2. Morphological characterization

The morphology evolution of Eu³⁺-doped YF₃/KY₃F₁₀ nano/microcrystals obtained by increasing the pH in the different series of samples (with and without chelating agents) is presented in **Figure 4.3**. As shown, interesting differences appear when comparing the samples. The incorporation of surface chelators and the pH of the medium have a profound influence on the sizes and morphologies of the as-synthesized powders.

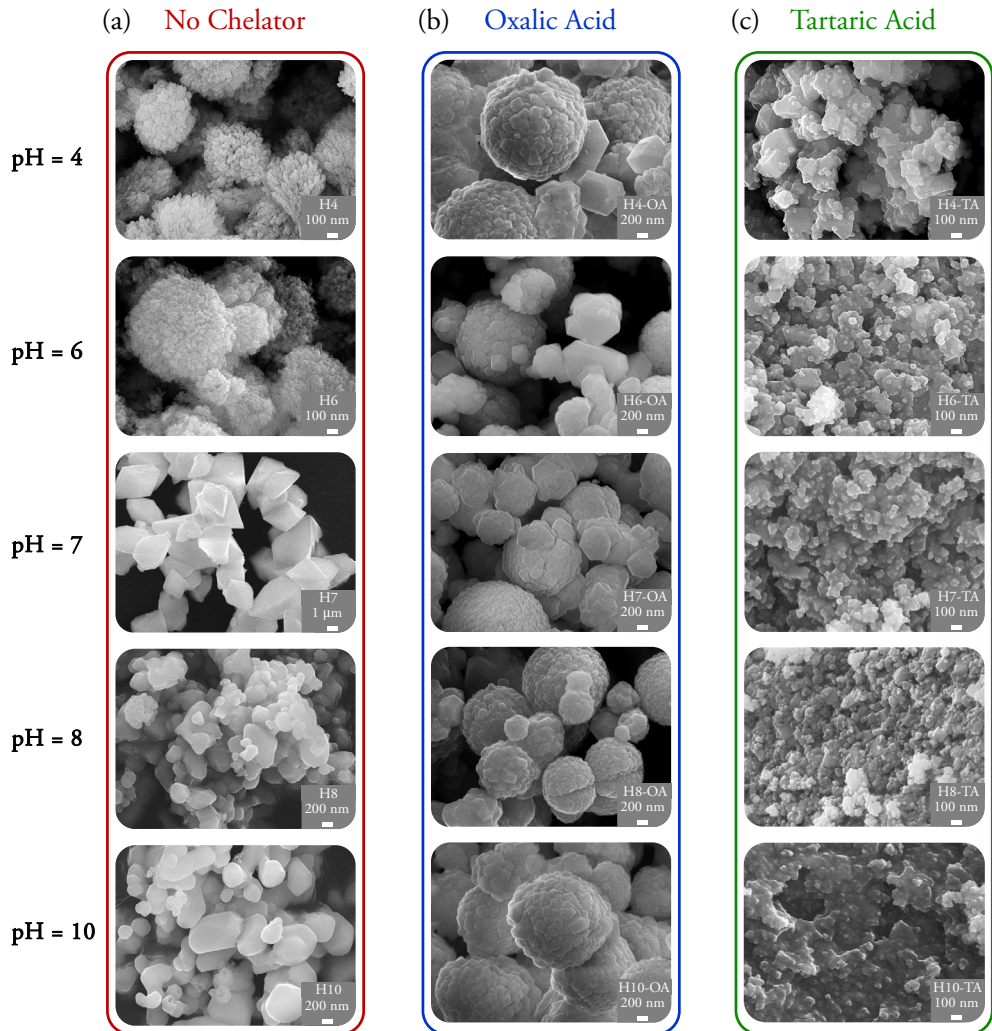


Figure 4.3. SEM images for the Eu^{3+} -doped samples prepared at different pH values by a hydrothermal process (a) with no chelator, (b) using oxalic acid, and (c) adding tartaric acid as a chelating agent.

4.3.2.1. Samples prepared without the incorporation of surface chelators

Figure 4.3(a) shows the SEM images of the materials prepared by the hydrothermal method without the incorporation of chelating agents. Samples H4 and H6 (YF_3 crystal structure) present very similar morphologies that can be described as self-assembled nanoparticles with an average size of 100 nm that form spheres with

diameters of about 0.6 and 1.1 μm , respectively. Interestingly, when the pH of the medium is increased to 7 (sample H7), although the crystal structure is still YF_3 , the shape of the particles changes dramatically evolving toward the formation of higher crystalline ones. The as-prepared product consists of a great deal of truncated/distorted octahedra with well-defined crystallographic facets and a size that varies from 4.0 to 6.0 μm . It is also consistent with the XRD pattern of H7, which revealed a narrowing of the peaks and a change in the relative intensity of some of them in comparison to samples H4 and H6.

With regard to samples H8 and H10 (KY_3F_{10} crystal structure), their microstructure can be described as particles characterized by irregular shapes whose size increases with the pH. We found particles with a size of 0.2–0.8 μm in sample H8, while the size was slightly larger in sample H10 (0.5–1.2 μm).

4.3.2.2. *Samples prepared with the incorporation of surface chelators*

Figure 4.3(b) shows the SEM images of the materials prepared by the hydrothermal method with the incorporation of oxalic acid as a chelating agent. As previously mentioned in the XRD section, the introduction of OA allowed single-phase KY_3F_{10} to be obtained over the whole range of pH. In contrast to **Figure 4.3(a)**, the microstructure of all the samples was very similar regardless of the acidity of the medium. Generally, the materials are composed of self-assembled nanoparticles with an average size of 200 nm that form spheres with a diameter between 1.5 and 2.0 μm . In contrast to the irregular shapes obtained without the addition of the chelating agent (samples H8 and H10), the formation of regular spheres can be attributed to the gradual and controlled release of Y^{3+} ions due to weakening of the chelating ability of the Y-complex under hydrothermal conditions, as explained previously.

On the other hand, **Figure 4.3(c)** presents the SEM images of the samples prepared by the hydrothermal method with the incorporation of tartaric acid as a surface chelator. At first glance, the change in the surface chelator produces noticeable microstructural effects. As with the use of OA, all the samples presented the KY_3F_{10} crystal structure irrespective of the pH. The microstructure of the materials can be described as agglomerated nanospheres (50–100 nm); however, when the pH increases, so does the degree of agglomeration and sintering of the particles. The differences found between the use of OA and TA may well be explained by taking into account the synthetic experimental details described in the Supporting Information.

Despite the fact of using chelating agents, we noted that some degree of agglomeration exists (in particular, for samples with tartaric acid). From the literature, we have found several factors that might have contributed to this phenomenon: the type of chelating agent and its chemical behavior, the molar ratio of the chelating agent to Ln^{3+} , the pH of the medium, the temperature and reaction time during the hydrothermal treatment that could favor that particles aggregate to reduce their surface energy, and the fluoride source [46–49]. All these remarks could lead to future more in-depth studies.

4.3.3. Photoluminescence studies

4.3.3.1. Excitation spectra

As per the XRD and morphological results, the optical properties were studied for samples synthesized at pH values of 4, 7, and 10 for comparison purposes. All the excitation spectra were similar. Different bands associated with the Eu^{3+} transitions were observed from the ground level ${}^7\text{F}_0$ to different excited levels. The relative intensities of the bands varied slightly depending on the crystal structure (YF_3 or KY_3F_{10}), see **Figure 4.4**. Among all the transitions, the most intense was ${}^7\text{F}_0 \rightarrow {}^5\text{L}_6$, with

a maximum at 395 nm. Therefore, the emission spectra were recorded using this value as the excitation wavelength and were normalized to the magnetic dipole ${}^5D_0 \rightarrow {}^7F_1$ transition.

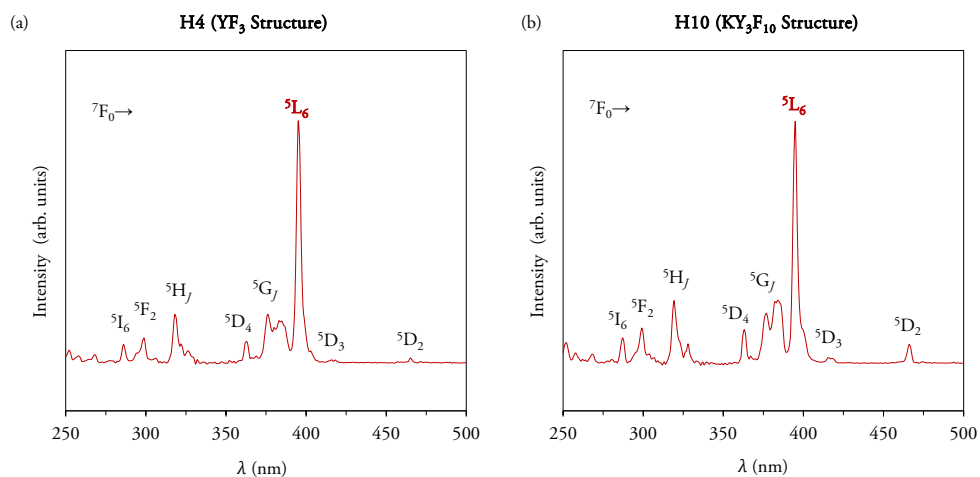


Figure 4.4. Room temperature excitation spectra obtained with a delay time of 0.2 ms and an emission wavelength of 593 nm for samples H4 and H10 as representatives of YF₃ and KY₃F₁₀ structures, respectively.

4.3.3.2. Emission spectra

Figure 4.5 shows the room temperature emission spectra obtained with a delay time (DT) of 0.2 and 10 ms upon excitation at 395 nm for samples H4 and H10, as representatives of YF₃ and KY₃F₁₀ structures, respectively. With a DT = 0.2 ms, the spectra showed a complex behavior due to the mixing of ${}^5D_{0-3} \rightarrow {}^7F_j$ transitions. It is worth noting that the Eu³⁺ lifetimes associated with the transitions occurring from the ${}^5D_{1,2,3}$ higher energy levels are expected to be lower than the lifetimes associated with transitions from the 5D_0 ground level. Therefore, if the detector delay time is increased to 10 ms, we can observe only the contribution of ${}^5D_0 \rightarrow {}^7F_j$ transitions and ensure that the assignment of bands is accurate.

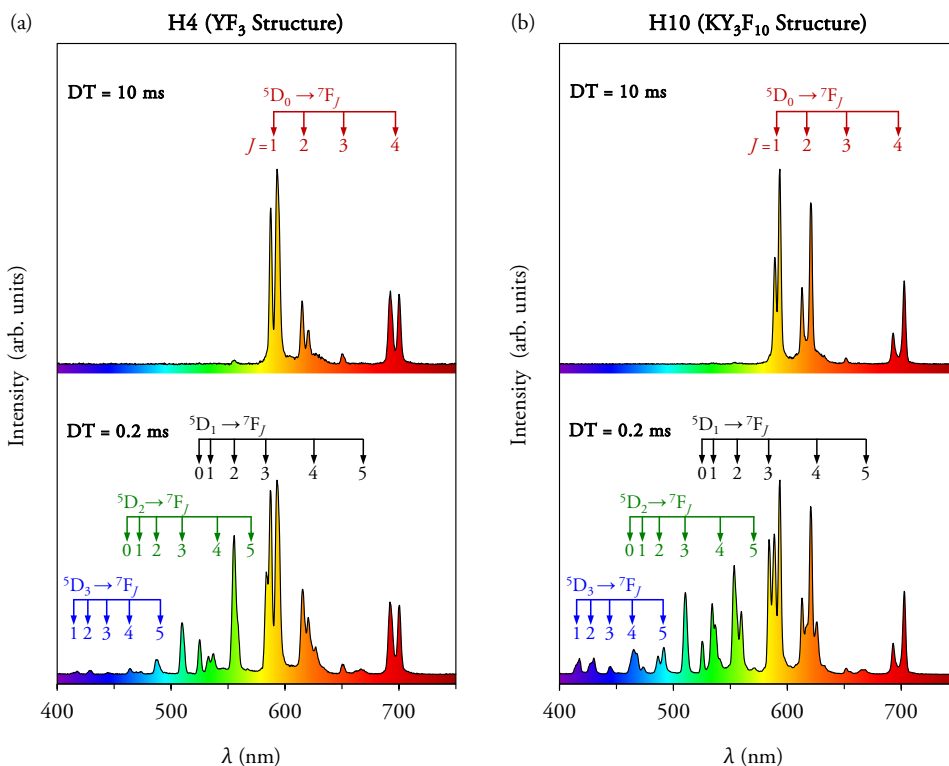


Figure 4.5. Room temperature emission spectra obtained with a delay time (DT) of 0.2 and 10 ms upon excitation at 395 nm for samples H4 and H10 as representatives of YF₃ and KY₃F₁₀ structures, respectively. The numbers under the rows indicate the value of J associated with the respective transition ${}^5D_i \rightarrow {}^7F_j$.

The presence of bands associated with transitions occurring from the higher excited levels (${}^5D_{1-3}$) is in accordance with the typical low dominant vibration frequencies available in the host lattice of fluorides [50]. As we can see from the colored plots in **Figure 4.5**, the emission lines of the Eu³⁺-doped materials cover the whole visible spectral region: 5D_3 (blue), 5D_2 (blue-green), 5D_1 (green-yellow), and 5D_0 (orange-red). Further information about the assignation of the emission bands to their respective transitions can be found in the Supporting Information (Section S4.2).

On comparing **Figure 4.5(a)** with **Figure 4.5(b)**, we observe notable differences

regarding the relative intensity and the splitting of the emission bands. The variation in the splitting arises from the incorporation of the Eu^{3+} ion in different symmetry sites of the host lattice when they replace the Y^{3+} ions: C_s symmetry in the YF_3 structure, and C_{4v} in the KY_3F_{10} structure (see **Figure 4.1** for the interpretation of the coordination polyhedra). The differences found in the relative intensity of the bands are related to the change in the crystal structure and their associated phonon energy. Therefore, it is fairly clearly demonstrated that the optical response of Eu^{3+} can be tuned by modulating the different crystal phases.

To further investigate the optical properties and analyze the variations among the different series of samples, in **Figure 4.6(a-c)** we present the emission spectra of the phosphors prepared at different pH values without the incorporation of chelating agents, using oxalic acid, or adding tartaric acid as a chelator, respectively. In general terms, all the emission spectra of samples with the same crystal structure, i.e., YF_3 or KY_3F_{10} , are similar, but some appreciations need to be considered.

In **Figure 4.6(a)**, the photoluminescence modulation of the phosphors prepared with no chelators is clearly observed on comparing samples H4 and H7 (YF_3 structure) with H10 (KY_3F_{10} structure). Another important detail to note is the similitude in the emission profiles of H4 and H7, despite having a morphology and crystallinity that are extremely different, as discussed in the previous section. Referring to the oxalic acid series, **Figure 4.6(b)**, no remarkable changes seem to take place when the pH is modified. However, on comparing these samples with H10, a higher degree of suppression of the $^5\text{D}_3 \rightarrow ^7\text{F}_j$ transitions is observed. On the other hand, particular differences are found in the powders prepared using tartaric acid, see **Figure 4.6(c)**. With the increase in the pH, the intensity of the emission bands associated with transitions from the higher excited levels diminishes, a fact that can be especially

apparent if we focus on the decrease in the emission line appearing at 584 nm ($^5D_1 \rightarrow ^7F_3$), marked with red arrows in **Figure 4.6(c)**. All the above-commented differences affect the resulting emission coloration, as discussed in the following.

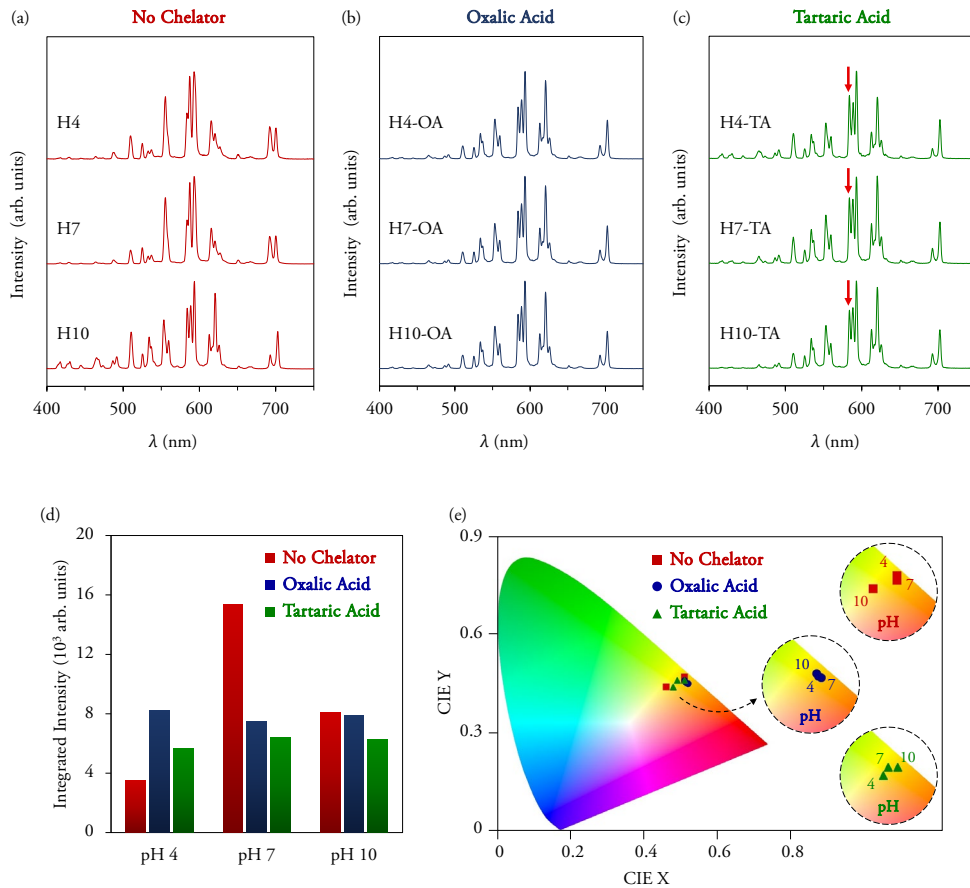


Figure 4.6. Room temperature emission spectra obtained with $DT = 0.2$ ms upon excitation at 395 nm for samples prepared at different pH values (a) with no chelators, (b) using oxalic acid, and (c) adding tartaric acid as a chelating agent. (d) Integrated luminescence intensity of the phosphors, and (e) CIE chromaticity diagram for Eu³⁺-doped samples. The numbers in the insets indicate the pH value (4, 7, and 10).

Additionally, the bar chart in **Figure 4.6(d)** presents the values of the total integrated luminescence intensity for the different Eu³⁺-doped phosphors. First, it is

important to note that the luminescence intensity depends on several factors, such as the existence of non-radiative processes (intrinsic properties of the materials and the different crystal structures), or the scattering rate (influenced by the size and shape of particles), as noted by G. Dantelle *et al.* [51]. On this basis, the high intensity observed in sample H7 in comparison to H4 (both with YF_3 structure) can be ascribed to a higher scattering rate, which is related to the high crystallinity and well-defined geometry of its particles [52]. In contrast, the phosphors prepared with oxalic acid have the same crystal structure (KY_3F_{10}) and particles with very similar morphologies and sizes, therefore minor changes are appreciated in the emission intensities. Similar conclusions can be drawn for the compounds prepared with tartaric acid.

Lastly, the CIE coordinates of the corresponding materials doped with Eu^{3+} were calculated from the emission spectra using the GoCIE software package [53] and are depicted in **Figure 4.6(e)**. Different color emissions of the phosphors, which vary from orangish to yellow, were obtained depending on the pH and the chelating agent used. The main point is that there is a direct connection between the chromaticity and the features of the emission profiles, which can be corroborated with the insets in **Figure 4.6(e)**, which corresponds to the color emission for each series of samples. For the phosphors prepared without chelators, the change in the color emission depends on the crystal phase. H4 and H7 (YF_3 structure) have a more orangish component while H10 (KY_3F_{10} structure) leads to a yellow color of the emission, closer to the white zone in the CIE diagram. As occurred with the emission spectra, no significant results are found in the series “Oxalic Acid”, while a progressive evolution from yellow to orangish hues is observed for samples prepared with tartaric acid as the pH increases. This result is in perfect agreement with the onward suppression of the ${}^5\text{D}_{1-3} \rightarrow {}^7\text{F}_j$ transitions (blue-green region of the visible spectra). Consequently, the different tunable emissions of these compounds can be appealing for advanced applications.

The technology of white light emitting diodes (w-LEDs) is nowadays attracting a lot of attention, the combination of orange-yellow-emitting phosphors with blue InGaN chips being a common strategy to generate them [54]. Recently, fluorides have been proposed as good candidates for w-LEDs due to the high quantum efficiencies and long lifetimes of fluoride-based structures in comparison to oxide matrices [55]. Therefore, the materials synthesized in the present work could also find very interesting applications in solid-state lighting devices.

4.3.3.3. Judd-Ofelt and Asymmetry Ratio Calculations

According to the Judd-Ofelt theory, the transition intensities for lanthanides and actinides in solids and solutions can be explained through the calculation of different physical parameters [56]. On the one hand, the branching ratios can be used to predict the relative intensities of the emission lines originating from a given excited level and evaluate important differences among different Eu^{3+} crystal environments [57]. The experimental branching ratios for the ${}^5\text{D}_0 \rightarrow {}^7\text{F}_j$ transitions (β_j) can be found from the relative areas of the emission lines:

$$\beta_j(\text{experimental}) = \frac{I_{0j}}{\sum I_{0j}} \quad (4.8)$$

where I_{0j} is the intensity associated with the transition ${}^5\text{D}_0 \rightarrow {}^7\text{F}_j$ that takes place at a λ_{0j} average wavelength.

On the other hand, the intensity of the magnetic dipole ${}^5\text{D}_0 \rightarrow {}^7\text{F}_1$ transition is considered to be independent of the host matrix, while the electric dipole ${}^5\text{D}_0 \rightarrow {}^7\text{F}_2$ is known as a hypersensitive transition because it is highly influenced by the local symmetry of the Eu^{3+} ion [58]. The asymmetry ratio R is useful to analyze the local symmetry of the dopant and is defined as the ratio between the intensities of the

${}^5D_0 \rightarrow {}^7F_2$ and ${}^5D_0 \rightarrow {}^7F_1$ transitions, which can also be related to the corresponding branching ratios:

$$R = \frac{I_{02}}{I_{01}} = \frac{\beta_2}{\beta_1} \quad (4.9)$$

The Judd-Ofelt parameters Ω_λ ($\lambda = 2, 4, 6$) characterize the local structure and bonding in the vicinity of lanthanide ions. For the Eu^{3+} ion, the Judd-Ofelt parameters can be determined directly from the analysis of the emission spectra. The Ω_2 parameter correlates with the polarizable and covalent character of the lanthanide ion in the lattice (larger values of Ω_2 imply a stronger covalence) [59,60], while the Ω_4 parameter is sensitive to the viscosity and rigidity of the host lattice, which is a long-range effect. The Ω_6 parameter cannot usually be obtained from the emission spectrum due to instrumental limitations for recording the ${}^5D_0 \rightarrow {}^7F_6$ transition. However, the value of Ω_6 is unnecessary to predict the dynamics of the 5D_0 emitting manifold because its contribution to the overall transition probability is negligible [61]. The formula derived for the calculation of Ω_2 and Ω_4 Judd-Ofelt parameters is expressed as [62]:

$$\Omega_\lambda (\lambda = 2, 4) = A_{01} \cdot \frac{I_{0J}}{I_{01}} \cdot \frac{\lambda_{0J}^4}{\lambda_{01}} \cdot \frac{3h}{64e^2\pi^4 \chi \|U^\lambda\|} \quad (4.10)$$

where A_{01} is the magnetic dipole transition rate, which is assumed to be constant and equal to 50 s^{-1} ; h is the Planck constant; e denotes the elementary charge; χ is the Lorentz local field correction term (which is equal to $\frac{n(n^2+2)^2}{9}$, where n is the refractive index at λ_{0J}); and $\|U^\lambda\|$ corresponds to the reduced matrix element of the unit tensor operator connecting levels $0-\lambda$ [63]. The value reported in the literature for $\|U^2\|$ is 0.0032 and for $\|U^4\|$ it is 0.0023 [64]. The average wavelength value obtained for the samples is 593 nm for λ_{01} (${}^5D_0 \rightarrow {}^7F_1$ transition), 616 nm for λ_{02} (${}^5D_0 \rightarrow {}^7F_2$ transition),

and 695 nm for λ_{04} (${}^5D_0 \rightarrow {}^7F_4$ transition). The refractive index of YF_3 and KY_3F_{10} is 1.49 and can be considered a constant in the spectrum range 470–700 nm [65–67]. All the calculations were performed using the data extracted from the emission spectra recorded with a DT of 10 ms to avoid the contributions from higher excited levels (${}^5D_{1,3}$), which could lead to inaccurate values. The experimental branching ratios are listed in **Table S4.1** of the Supporting Information and the rest of the parameters are presented in **Table 4.3**.

Table 4.3. Asymmetry ratio values and Judd-Ofelt parameters for Eu^{3+} -doped phosphors. All the data were obtained from the emission spectra recorded with a DT of 10 ms and monitoring the excitation at 395 nm.

Sample	R	Ω_2 (10^{-20} cm ²)	Ω_4 (10^{-20} cm ²)	Ω_2/Ω_4
H4	0.33	0.60(1)	1.70(1)	0.35
H7	0.33	0.59(1)	1.56(1)	0.38
H10	1.00	1.79(2)	1.72(1)	1.04
H4-OA	1.00	1.80(2)	1.75(1)	1.03
H7-OA	1.02	1.83(2)	1.75(1)	1.05
H10-OA	1.01	1.80(2)	1.77(2)	1.02
H4-TA	1.08	1.95(3)	1.92(3)	1.02
H7-TA	1.11	2.03(3)	1.88(2)	1.08
H10-TA	1.10	1.98(3)	1.91(3)	1.04

The symmetry of the crystal site at which the dopant ions are located determines the relative intensity of the magnetic and electric dipole transitions. Lower values of the asymmetry ratio R are therefore expected for compounds in which Eu^{3+} occupies a site with an inversion center. Following the same line of reasoning, higher Ω_2 values are associated with more covalent and polarizable environments of the dopant ion, that is to say, with lower symmetric crystal sites. If we consider the replacement of Y^{3+}

by Eu^{3+} in the crystal matrices studied in this work, the site symmetry of Eu^{3+} would be C_s in the YF_3 structure and C_{4v} in the KY_3F_{10} structure. At first glance, an important change in the previous parameters can be appreciated depending on the crystal structure. Notwithstanding, the low values obtained for the asymmetry ratio ($R = 0.33$ for YF_3 compounds, and $R \approx 1$ for KY_3F_{10}) would not be a priori in agreement with the previous reasoning, since neither the low-symmetric point group C_s nor the C_{4v} possesses an inversion center. Nevertheless, this anomalous tendency of R has been reported to be characteristic in fluoride matrices. The higher intensity of the magnetic dipole transition ${}^5\text{D}_0 \rightarrow {}^7\text{F}_1$ over the electric dipole transition ${}^5\text{D}_0 \rightarrow {}^7\text{F}_2$ in fluorides is a result of the high ionicity of the $\text{Eu}-\text{F}$ bonds, which allows only a little admixture of opposite parity states to the Eu^{3+} f -states. Thus, the ${}^5\text{D}_0 \rightarrow {}^7\text{F}_2$ transition becomes far less favorable as compared to, for example, the oxides [68]. On this basis, the differences found between the two crystal structures may arise from the different coordination numbers of Eu^{3+} ions and their respective changes in the ionicity of the $\text{Eu}-\text{F}$ bonds. Indeed, the higher Ω_2 parameter for KY_3F_{10} indicates a higher degree of covalence and thus lower ionicity. Similar conclusions can be extracted from the analysis of the Judd-Ofelt parameters Ω_2 (the short-range parameter) and Ω_4 (the large-range parameter). In fact, the Ω_2/Ω_4 ratio follows the same tendency as the asymmetry ratio R .

Moreover, it is important to note that samples prepared using the same chelating agent (oxalic or tartaric acid) present similar values of R , Ω_2 and Ω_4 regardless of the pH. We can therefore assume that there are no noticeable changes in the polarizability environment of the ion, and the crystal field of Eu^{3+} must be quite similar. However, slightly higher values of these parameters are obtained for the compounds prepared using tartaric acid. A reasonable explanation may be found taking into account the different morphology and size of the particles.

4.3.3.4. Lifetimes and Quantum Efficiencies Analysis

The decay curves for the different ${}^5D_{0-3} \rightarrow {}^7F_J$ emissions of Eu^{3+} were measured to give further information about the photoluminescence properties of the materials that were prepared. In order to analyze the observed lifetime (τ_{obs}) of the different excited levels, time-resolved luminescence measurements were performed with an excitation wavelength of 395 nm, setting a DT of 0.2 ms, and monitoring different emission wavelengths according to the respective ${}^5D_{0-3} \rightarrow {}^7F_J$ transitions.

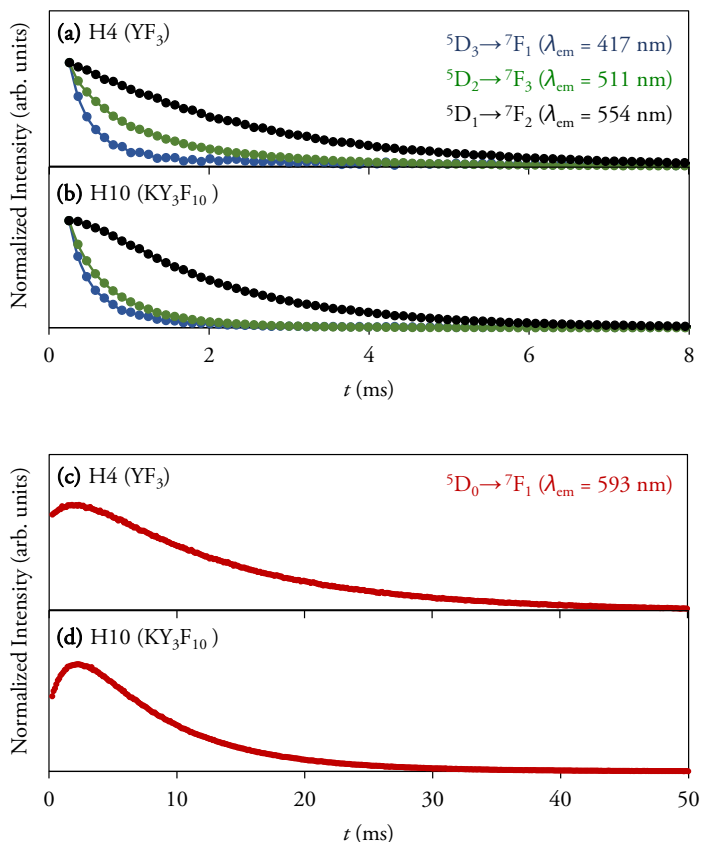


Figure 4.7. Normalized decay curves acquired at room temperature with a DT of 0.2 ms under the excitation of 395 nm monitoring the emission at 417 nm (${}^5D_3 \rightarrow {}^7F_1$), 511 nm (${}^5D_2 \rightarrow {}^7F_3$), 554 nm (${}^5D_1 \rightarrow {}^7F_2$), and 593 nm (${}^5D_0 \rightarrow {}^7F_1$). (a), (c) Exhibit the decay curves for sample H4; (b), (d) exhibit the decay profiles for sample H10.

Figure 4.7 shows examples of the decay measurements for transitions originating from the different excited levels corresponding to samples H4 and H10 as representatives of YF₃ and KY₃F₁₀ structures, respectively. An interesting feature is the presence of a rising part at the beginning of the decay profiles of the ⁵D₀ and ⁵D₁ emissions due to the Eu³⁺ population feeding from upper excited levels. The rising phenomenon is more notable for the ⁵D₀ emissions, since the emission from higher excited levels is partially quenched by cross-relaxation occurring between neighboring Eu³⁺ ions in the lattice. In this non-radiative process, the higher energy emission is quenched in favor of the lower energy level emission according to [69]. Thus, the ⁵D_{0,1}→⁷F₇ decay profiles were fitted using the following equation:

$$I(t) = \left[I_0 + I_1 \left(1 - \exp\left(\frac{-t}{\tau_{\text{rise}}}\right) \right) \right] \exp\left(\frac{-t}{\tau_{\text{obs}}}\right) \quad (4.11)$$

where I refers to the intensity as a function of time (t) and τ_{rise} is the rising time. In terms of physics, this mathematical expression can be considered a single exponential model with a modified pre-exponential factor that modulates the population of Eu³⁺ ions [70].

However, the decay curves of the ⁵D_{2,3}→⁷F₇ transitions were best fitted to a double exponential model without the presence of a rising part:

$$I(t) = I_1 \exp\left(\frac{-t}{\tau_{\text{obs } 1}}\right) + I_2 \exp\left(\frac{-t}{\tau_{\text{obs } 2}}\right) \quad (4.12)$$

The presence of these two lifetimes in the higher excited levels of the materials has been attributed to a different distribution of lanthanide ions in the crystal lattice: Eu³⁺ ions occupying the expected local symmetry and Eu³⁺ ions situated in the vicinity of a defect or impurity group in the surface of the materials [71]. When the double exponential model was used, an effective lifetime (τ_{eff}) was calculated according to:

$$\tau_{\text{eff}} = \frac{I_1(\tau_{\text{obs } 1})^2 + I_2(\tau_{\text{obs } 2})^2}{I_1(\tau_{\text{obs } 1}) + I_2(\tau_{\text{obs } 2})} \quad (4.13)$$

In order to evaluate the quantum efficiencies (the intrinsic quantum yields, η) of the materials, the radiative lifetimes (τ_{rad}) of Eu^{3+} ions for the ${}^5\text{D}_0$ level were calculated from the emission spectra recorded at a DT of 10 ms using the following expression, which is also related to the branching ratios [72–74]:

$$\tau_{\text{rad}} = \frac{I_{01}}{n^3 \cdot I_{\text{total}} \cdot (A_{01})_{\text{vac}}} = \frac{\beta_1}{n^3 \cdot (A_{01})_{\text{vac}}} \quad (4.14)$$

where n denotes the refractive index of the material and $(A_{01})_{\text{vac}}$ is the magnetic dipole transition rate in a vacuum (14.65 s^{-1}). The quantum efficiency of the luminescence material can be evaluated considering the calculated radiative lifetimes and the observed lifetimes for the ${}^5\text{D}_0$ level as follows:

$$\eta = \frac{\tau_{\text{obs}}}{\tau_{\text{rad}}} \quad (4.15)$$

Table 4.4 summarizes the lifetimes for the different excited levels (${}^5\text{D}_{0-3}$) of the Eu^{3+} -doped phosphors. All the correlation coefficients of the fits (R^2) were ≥ 0.999 . The calculated radiative lifetimes and quantum efficiencies for the ${}^5\text{D}_0$ level are also listed in **Table 4.4**. As can be appreciated, the pH and the choice of the surface chelator have a strong impact on the time-resolved luminescence of the materials, with the most remarkable effects in the lifetimes and quantum yields associated with the ${}^5\text{D}_0$ level.

From the experimental data, it is shown quite clearly that the lifetimes associated with the ${}^5\text{D}_3$, ${}^5\text{D}_2$, and ${}^5\text{D}_1$ emissions are shorter than those of the low-energy ${}^5\text{D}_0$ emission due to the cross-relaxation of the Eu^{3+} population at higher excited levels to the metastable ${}^5\text{D}_0$ level [50]. Besides, the lifetimes of the higher excited levels (${}^5\text{D}_{1-3}$)

slightly decrease as the pH of the medium becomes more basic.

Table 4.4. $^5D_{0-3}$ lifetimes and 5D_0 quantum efficiencies for Eu^{3+} -doped phosphors. All the correlation coefficients of the fits (R^2) were ≥ 0.999 .

Sample	5D_3 (417 nm)	5D_2 (511 nm)	5D_1 (554 nm)	5D_0 (593 nm)		η (%)
	τ_{eff} (ms)	τ_{eff} (ms)	τ_{obs} (ms)	τ_{obs} (ms)	τ_{rad} (ms)	
H4	0.95(4)	1.19(3)	2.23(1)	12.03(5)	11.53(6)	104
H7	0.76(5)	1.08(3)	1.95(1)	7.68(1)	11.83(6)	65
H10	0.64(3)	0.84(1)	1.87(1)	7.93(1)	8.45(4)	94
H4-OA	0.49(6)	0.60(1)	1.69(1)	7.18(1)	8.40(4)	85
H7-OA	0.47(4)	0.59(2)	1.71(4)	7.21(1)	8.40(4)	86
H10-OA	0.44(4)	0.57(1)	1.70(1)	7.47(1)	8.35(4)	89
H4-TA	0.58(3)	0.89(1)	1.92(1)	8.73(2)	8.02(3)	109
H7-TA	0.44(6)	0.74(6)	1.87(1)	10.11(1)	7.93(3)	127
H10-TA	0.40(3)	0.60(6)	1.85(1)	10.59(2)	7.96(3)	133

Regarding the 5D_0 level, it should be noted that the longest lifetime (12 ms) was collected for sample H4. This sample presented the YF_3 structure and was formed by self-assembled nanoparticles. In contrast, an important decrease (from 12 to 7.7 ms) is observed in sample H7, which also had the YF_3 structure and presented the highest crystallinity among all the samples studied. Another point to consider is that sample H7 also had the most intense emission, **Figure 4.6(d)**.

For the samples synthesized using oxalic acid, the lifetimes were about 7.2–7.5 ms, while a notable rise (up to 10.6 ms) was observed for the powders obtained using tartaric acid as a surface chelator. Powders synthesized using the same chelator (OA or TA) had very similar integrated emission intensities, as previously noted. However,

the differences in the lifetimes may be ascribed to the change in the size and morphology of the particles that can affect the electron microstructure of the samples, hence resulting in different luminescence kinetics that do not alter the emission intensity. A plausible explanation could be found considering different cross-relaxation processes of Eu^{3+} ions at higher excited levels, which could increase the ${}^5\text{D}_0$ population with an enhancement of the corresponding lifetime. Indeed, for samples with OA, the ${}^5\text{D}_3$ lifetimes do not vary so much with the increase of pH (0.49–0.44 ms) and similar values are obtained for the ${}^5\text{D}_0$ lifetimes.

Interestingly, apart from the H7 sample (whose behavior has been commented on above), the lifetimes of the ${}^5\text{D}_0$ level follow the opposite tendency with the pH in comparison to the rest of the excited levels. In this case, the lifetimes become longer as the basicity of the medium increases.

In direct connection with this, we demonstrate that the pH and the chelating agents allow us to tune the quantum efficiency of the materials to a high degree, with values in the range of 65–133%. The use of tartaric acid and the basicity of the medium enhanced the quantum efficiency of the samples. Although high values were expected due to the low phonon energy of the crystal lattices, the values higher than 100% suggest the existence of quantum cutting (QC) processes or similar energy transfers between Eu^{3+} ions that occur via cross-relaxation, as we previously noted in a recent study of Eu^{3+} -doped KY_3F_{10} materials [75]. The QC process is an interesting optical phenomenon that enables a luminescent material to convert one high-energy photon into two low-energy photons through energy transfers between ions. Thereby, the quantum efficiency of phosphors can be enhanced and reach values up to 200% [76]. The most common strategy to obtain materials with efficient QC processes involves the use of Ln^{3+} ions pairs, such as Eu^{3+} - Gd^{3+} . Efficient QC processes using only a single

luminescent ion are more challenging but also possible [77–79], as evidenced in this work.

All the results lead us to confirm the extreme importance of dicarboxylic acids as surface chelators to obtain materials with different crystal phases and morphologies in a wide range of pH values. We feel that the novel use of these hydrophilic capping agents in the preparation of compounds of the KF-YF₃ system (with high relevance in photonics), instead of the commonly hydrophobic chelators, can be vital for their possible use for bioapplications. Besides, the different fluorides prepared have shown an outstanding and tunable optical response, yielding samples with very high quantum efficiencies (more than 100%) and very long lifetimes (up to 12 milliseconds). These values are totally superior in comparison to the typical oxides that are used for the fabrication of LEDs, whose efficiencies tend to be much lower and the lifetimes are usually on the microsecond scale. Therefore, the synthesized materials in the present work might have very interesting applications in solid-state lighting devices.

4.4. Conclusions

We prove for the first time the effective use of dicarboxylic ligands as chelating agents to modulate the surface and thus the crystal phase evolution in the KF-YF₃ system. The major conclusions that can be extracted from this study are the following:

- The crystal phase and the morphology of the Eu³⁺-doped YF₃ and KY₃F₁₀ materials prepared by a hydrothermal procedure depend critically on the pH and the chelator used. A plausible chemical mechanism to explain the differences among the distinct series of samples has also been proposed.

- The choice of Eu^{3+} as a dopant ion and site-sensitive structural probe has allowed us to describe the optical performance of the materials properly and to establish a relationship with their chemical structure, as has been observed with the calculations of the asymmetry ratio and the Judd-Ofelt physical parameters.
- The photoluminescence of Eu^{3+} can be tuned through the different series of samples, resulting in emissions that vary from orangish to yellow hues.
- Time-resolved luminescence experiments outlined the long lifetimes of the materials (up to 12 ms). Along with that, the high quantum of these materials also showed a strong dependence on the chelator and the pH.

Based on the remarks made above, we feel that the novel use of these capping agents in such materials could arouse widespread interest, since they could also be applied to a vast gamut of compounds from the extended family of yttrium/lanthanide fluorides and find very interesting applications in bioanalytics, biomedics or photonics. Additionally, the synthesized materials in the present work, with orangish-yellow emissions, could be interesting for application in white light emitting diodes through their combination with blue chips.

Acknowledgments

The authors thank the Universitat Jaume I (Project UJI-B2019-41) and Ministerio de Economía y Competitividad (Project MAT2016-80410-P) for financial support. P. Serna also thanks the Spanish Ministerio de Ciencia, Innovación y Universidades for an FPU predoctoral contract.

References

- [1] J. Wu, J. Wang, J. Lin, Y. Xiao, G. Yue, M. Huang, Z. Lan, Y. Huang, L. Fan, S. Yin, T. Sato, *Scientific Reports*. 3 (2013) 1–5.
- [2] B.M. Tissue, *Chemistry of Materials*. 10 (1998) 2837–2845.
- [3] T. Grzyb, M. Węclawiak, T. Pędziński, S. Lis, *Optical Materials*. 35 (2013) 2226–2233.
- [4] C. Sassoie, G. Patriarche, M. Mortier, *Optical Materials*. 31 (2009) 1177–1183.
- [5] F. Auzel, *Chemical Reviews*. 104 (2004) 139–173.
- [6] L. Tao, W. Xu, Y. Zhu, L. Xu, H. Zhu, Y. Liu, S. Xu, P. Zhou, H. Song, *Journal of Materials Chemistry C*. 2 (2014) 4186–4195.
- [7] Y. Zhang, X. Li, D. Geng, M. Shang, H. Lian, Z. Cheng, J. Lin, *CrystEngComm*. 16 (2014) 2196–2204.
- [8] G. Yi, H. Lu, S. Zhao, Y. Ge, W. Yang, D. Chen, L.H. Guo, *Nano Letters*. (2004).
- [9] M. Deng, Y. Ma, S. Huang, G. Hu, L. Wang, *Nano Research*. 4 (2011) 685–694.
- [10] A. Podhorodecki, A. Noculak, M. Banski, B. Sojka, A. Zelazo, J. Misiewicz, J. Cichos, M. Karbowski, B. Zasonska, D. Horak, B. Sikora, D. Elbaum, T. Dumych, R. Bilyy, M. Szewczyk, *ECS Transactions*. 61 (2014) 115–125.
- [11] A. Jain, P.G.J. Fournier, V. Mendoza-Lavaniegos, P. Sengar, F.M. Guerra-Olvera, E. Iñiguez, T.G. Kretschmar, G.A. Hirata, P. Juárez, *Journal of Nanobiotechnology*. 16 (2018) 1–18.
- [12] E.N. Silva, A.P. Ayala, J.Y. Gesland, R.L. Moreira, *Vibrational Spectroscopy*. 37 (2005) 21–26.

- [13] J. Xi, M. Ding, M. Zhang, H. Zhang, D. Chen, Z. Ji, *Journal of Materials Science: Materials in Electronics*. 28 (2017) 9489–9494.
- [14] J. Dabachi, M. Body, J. Dittmer, A. Rakhmatullin, F. Fayon, C. Legein, *Dalton Transactions*. 48 (2019) 587–601.
- [15] M. Chen, P. Loiko, J.M. Serres, S. Veronesi, M. Tonelli, M. Aguiló, F. Díaz, S.Y. Choi, J.E. Bae, F. Rotermund, S. Dai, Z. Chen, U. Griebner, V. Petrov, X. Mateos, *Journal of Alloys and Compounds*. 813 (2020) 152176.
- [16] G. Chen, H. Qiu, R. Fan, S. Hao, S. Tan, C. Yang, G. Han, *Journal of Materials Chemistry*. 22 (2012) 20190–20196.
- [17] G. Murali, B.H. Lee, R.K. Mishra, J.M. Lee, S.H. Nam, Y.D. Suh, D.K. Lim, J.H. Lee, S.H. Lee, *Journal of Materials Chemistry C*. 3 (2015) 10107–10113.
- [18] Z. Gao, Z. Lai, K. Lu, S. Guo, L. Liu, F. He, P. Yang, J. Ren, J. Zhang, J. Yang, *Optics Letters*. 44 (2019) 4674.
- [19] P. Villars, K. Cenzual, eds., KY_3F_{10} Crystal Structure: Datasheet from “PAULING FILE Multinaries Edition – 2012” in Springer Materials (https://materials.springer.com/isp/crystallographic/docs/sd_0552093)
- [20] P. Villars, K. Cenzual, eds., YF_3 Crystal Structure: Datasheet from “PAULING FILE Multinaries Edition – 2012” in Springer Materials (https://materials.springer.com/isp/crystallographic/docs/sd_1802348)
- [21] K. Momma, F. Izumi, *Journal of Applied Crystallography*. 44 (2011) 1272–1276.
- [22] L. Zhu, Y. Liu, X. Fan, D. Yang, X. Cao, *Journal of Luminescence*. 131 (2011) 1380–1385.
- [23] L. Zhu, J. Meng, X. Cao, *Materials Letters*. 62 (2008) 3007–3009.

- [24] C. Cao, *Journal of Materials Research Society*. 27 (2012) 2988–2995.
- [25] W. Xia, J. Xiong, L. Jiang, R. Ye, Y. Mao, S. Hu, J. Yang, *CrystEngComm*. 21 (2019) 3939–3947.
- [26] H. Guan, Y. Sheng, Y. Song, C. Xu, X. Zhou, K. Zheng, Z. Shi, H. Zou, *Journal of Physical Chemistry C*. 121 (2017) 23080–23095.
- [27] L. Rao, W. Lu, H. Wang, Z. Yi, S. Zeng, Z. Li, *Materials Research Bulletin*. 64 (2015) 27–32.
- [28] X. Wang, J. Zhuang, Q. Peng, Y. Li, *Inorganic Chemistry*. 45 (2006) 6661–6665.
- [29] J. Martínez-Esaín, J. Faraudo, T. Puig, X. Obradors, J. Ros, S. Ricart, R. Yáñez, *Journal of the American Chemical Society*. 140 (2018) 2127–2134.
- [30] C. Li, J. Yang, P. Yang, H. Lian, J. Lin, *Chemistry of Materials*. 20 (2008) 4317–4326.
- [31] H. Lin, D. Xu, A. Li, L. Yao, Z. Qiu, S. Yang, Y. Zhang, *Scientific Reports*. 7 (2017) 13762.
- [32] Y. Guo, J. Wei, Y. Liu, T. Yang, Z. Xu, *Journal of Materials Science: Materials in Electronics*. 29 (2018) 2463–2470.
- [33] T. Pang, M. Cai, Q. Chen, J. Xie, R. Jian, W. Lu, *Journal of Alloys and Compounds*. 789 (2019) 904–909.
- [34] J. Yang, D. Shen, X. Li, W. Li, Y. Fang, Y. Wei, C. Yao, B. Tu, F. Zhang, D. Zhao, *Chemistry: A European Journal*. 18 (2012) 13642–13650.
- [35] P. Qiu, R. Sun, G. Gao, B. Chen, C. Zhang, T. Yin, J. Zhang, S. Fang, D. Cui, *ChemNanoMat*. 1 (2015) 128–134.

- [36] F. Tao, Z. Shen, Z. Wang, D. Shu, Q. Liu, Y. Sun, *Journal of Nanomaterials*. 2017 (2017) 5320989.
- [37] F. Tao, Z. Zhang, J. Chen, Z. Wang, Y. Sun, *CrystEngComm*. 20 (2018) 512–519.
- [38] C. Cascales, J. Fernández, R. Balda, *Optics Express*. 13 (2005) 2141–2152.
- [39] R.D. Shannon, *Acta Crystallographica*. A32 (1976) 751–767.
- [40] G. Murali, S. Kaur, Y.C. Chae, M. Ramesh, J. Kim, Y.D. Suh, D.K. Lim, S.H. Lee, *RSC Advances*. 7 (2017) 24255–24262.
- [41] E. Combes, C. Sella, D. Bauer, J.L. Sabot, *Hydrometallurgy*. 46 (1997) 137–148.
- [42] E. Combes, C. Sella, D. Bauer, J.L. Sabot, *Hydrometallurgy*. 46 (1997) 1–12.
- [43] M. Zabiszak, M. Nowak, Z. Hnatejko, J. Grajewski, K. Ogawa, M.T. Kaczmarek, R. Jastrzab, *Molecules*. 25 (2020) 1121.
- [44] L. He, L. Xia, Y. Yang, Q. Zheng, N. Jiang, C. Xu, Y. Liu, D. Lin, *Materials Research Bulletin*. 95 (2017) 483–490.
- [45] M. Ding, D. Chen, S. Yin, Z. Ji, J. Zhong, Y. Ni, C. Lu, Z. Xu, *Scientific Reports*. 5 (2015) 12745.
- [46] Z. Wang, W. Han, H. Liu, *CrystEngComm*. 21 (2019) 1691–1700.
- [47] Z. Yang, C.F. Guo, Y.Q. Chen, L. Li, T. Li, J.H. Jeong, *Chinese Physics B*. 23 (2014) 1–7.
- [48] Q. Cui, J. Xu, *Journal of Materials Science: Materials in Electronics*. 27 (2016) 4372–4377.

- [49] S. Duhan, K. Sahoo, A. Imteyaz, S. Singh, M. Kumar, *Processing and Application of Ceramics*. 15 (2021) 69–78.
- [50] X. Liu, L. Yan, J. Lin, *Journal of the Electrochemical Society*. 156 (2009) 1–6.
- [51] G. Dantelle, B. Fleury, J.P. Boilot, T. Gacoin, *ACS Applied Materials and Interfaces*. 5 (2013) 11315–11320.
- [52] J. Adam, W. Metzger, M. Koch, P. Rogin, T. Coenen, J.S. Atchison, P. König, *Nanomaterials*. 7 (2017) 1–17.
- [53] K. R. Justin Thomas, GoCIE V2 software (2009), downloaded from <http://faculty.iitr.ac.in/~krjt8fcy/index.html>
- [54] H. Wu, H. Li, L. Jiang, R. Pang, S. Zhang, D. Li, G. Liu, C. Li, J. Feng, H. Zhang, *Journal of Materials Chemistry C*. (2020).
- [55] L.Y. Wang, E.H. Song, T.T. Deng, Y.Y. Zhou, Z.F. Liao, W.R. Zhao, B. Zhou, Q.Y. Zhang, *Dalton Transactions*. 46 (2017) 9925–9933.
- [56] B.M. Walsh, Judd-Ofelt theory: principles and practices, in: B. Di Bartolo, O. Forte (Eds.), *Advances in Spectroscopy for Lasers and Sensing*, Springer, Dordrecht, 2006: pp. 403–433.
- [57] P. Babu, C.K. Jayasankar, *Physica B: Condensed Matter*. 279 (2000) 262–281.
- [58] K. Vuković, M. Medić, M. Sekulić, M.D. Dramićanin, *Advances in Condensed Matter Physics*. 2015 (2015) 1–7.
- [59] D.K. Patel, B. Vishwanadh, V. Sudarsan, S.K. Kulshreshtha, *Journal of the American Ceramic Society*. 96 (2013) 3857–3861.
- [60] C. de Mello Donegá, S.A. Junior, G.F. de Sá, *Journal of Alloys and Compounds*.

- 250 (1997) 422–426.
- [61] E. Cantelar, J.A. Sanz-García, A. Sanz-Martín, J.E. Muñoz Santiuste, F. Cussó, *Journal of Alloys and Compounds*. 813 (2020) 152194.
- [62] P. Serna-Gallén, H. Beltrán-Mir, E. Cordoncillo, A.R. West, R. Balda, J. Fernández, *J. Mater. Chem C*. 7 (2019) 13976–13985.
- [63] B. Julián, J. Planelles, E. Cordoncillo, P. Escribano, P. Aschehoug, C. Sanchez, B. Viana, F. Pellé, *Journal of Materials Chemistry*. 16 (2006) 4612–4618.
- [64] S. Constantin, M.L. Stanciu, *Annals of West University of Timisoara - Physics*. 56 (2012) 127–131.
- [65] P. Porcher, P. Caro, *The Journal of Chemical Physics*. 68 (1978) 4176–4182.
- [66] J. Zhang, Z. Hao, X. Zhang, Y. Luo, X. Ren, X.J. Wang, J. Zhang, *Journal of Applied Physics*. 106 (2009) 034915.
- [67] D.F. Bezuidenhout, K.D. Clarke, R. Pretorius, *Thin Solid Films*. 155 (1987) 17–30.
- [68] M.M. Lezhnina, T. Jüstel, H. Kätker, D.U. Wiechert, U.H. Kynast, *Advanced Functional Materials*. 16 (2006) 935–942.
- [69] T. Yamase, T. Kobayashi, M. Sugeta, H. Naruke, *Journal of Physical Chemistry A*. 101 (1997) 5046–5053.
- [70] M.L. Debasu, D. Ananias, A.G. Macedo, J. Rocha, L.D. Carlos, *Journal of Physical Chemistry C*. 115 (2011) 15297–15303.
- [71] L.J.B. Erasmus, H.C. Swart, J.J. Terblans, *Applied Surface Science*. 487 (2019) 41–51.

- [72] P. Ghosh, A. Patra, *Journal of Physical Chemistry C*. 112 (2008) 19283–19292.
- [73] X.-N. Tian, G.-C. Jiang, X.-T. Wei, L.-Y. Wu, S. Li, K.-M. Deng, Y.H. Chen, M. Yin, *Journal of Nanoscience and Nanotechnology*. 14 (2014) 4490–4494.
- [74] M.H.V. Werts, R.T.F. Jukes, J.W. Verhoeven, *Physical Chemistry Chemical Physics*. 4 (2002) 1542–1548.
- [75] P. Serna-Gallén, H. Beltrán-Mir, E. Cordoncillo, *Optics and Laser Technology*. 136 (2021) 106734.
- [76] Z. Zou, L. Feng, C. Cao, J. Zhang, Y. Wang, *Scientific Reports*. 6 (2016) 1–7.
- [77] X. Chen, J. Wu, X. Xu, Y. Zhang, N. Sawanobori, C. Zhang, Q. Pan, G.J. Salamo, *Optics Letters*. 34 (2009) 887.
- [78] X. Chen, G.J. Salamo, S. Li, J. Wang, Y. Guo, Y. Gao, L. He, H. Ma, J. Tao, P. Sun, W. Lin, Q. Liu, *Physica B: Condensed Matter*. 479 (2015) 159–164.
- [79] Y. Liu, J. Zhang, C. Zhang, J. Jiang, H. Jiang, *Journal of Physical Chemistry C*. 120 (2016) 2362–2370.

S4. Supporting Information

S4.1. Insights into the experimental procedure

The initial solutions of oxalic and tartaric acid were adjusted to a pH of 6.5 for comparison purposes. It is important to note that both the oxalic and tartaric acid are diprotic acids with the general formula H_2A that have approximately the same pK_{a2} value, 4.3. Thus, a pH of 6.5 ensures the presence of the A^{2-} deprotonated species in the medium before its addition to the Ln^{3+} solution [S1]. Indeed, when the solution of tartaric acid was basified with 2M KOH aqueous solution, a white solid started to form at pH 3.0 (indicating the presence of HA^-) and was not redissolved until the value of 6.5 was reached (all the HA^- was converted to A^{2-}) [S1]. The precipitate corresponded to the formation of potassium hydrogen tartrate, which has a bad solubility (0.006 g/mL in water at 25 °C). However, in the case of oxalic acid no precipitate was formed probably because potassium hydrogen oxalate has a higher solubility (0.053 g/mL in water at 25 °C).

When the above solutions (pH = 6.5) were added to the previous Ln^{3+} solution (pH = 4.0), the pH of the mixture decreased to approximately 5.5 for OA- Ln^{3+} mixture, and 4.5 for TA- Ln^{3+} mixture. While doing so, a whitish precipitate appeared, indicating the formation of the Ln-complex. After the addition of KBF_4 , the pH was adjusted to the desired value although to achieve the value of pH 4, it was added 2 M HNO_3 aqueous solution. The precipitate in the OA- Ln^{3+} mixture was maintained in all the pH range. However, it was redissolved in the TA- Ln^{3+} mixture for $pH \geq 6$. This result implies that tartaric acid has a different behavior than oxalic acid concerning the formation/precipitation of chelating species, though it is also effective since it prevents the formation of hydroxide-type solids when the pH is increased (which would have occurred if tartaric acid had not acted as a surface chelator).

S4.2. Emission bands assignation and branching ratios

The emission bands have been assigned to their respective transitions according to [S2]: $^5D_3 \rightarrow ^7F_1$ (417 nm), $^5D_3 \rightarrow ^7F_2$ (429 nm), $^5D_3 \rightarrow ^7F_3$ (445 nm), $^5D_3 \rightarrow ^7F_4$ (460–476 nm), $^5D_3 \rightarrow ^7F_5$ (482–496 nm), $^5D_2 \rightarrow ^7F_{0,1}$ (460–476 nm), $^5D_2 \rightarrow ^7F_2$ (482–496 nm), $^5D_2 \rightarrow ^7F_3$ (511 nm), $^5D_2 \rightarrow ^7F_4$ (540 nm), $^5D_2 \rightarrow ^7F_5$ (571 nm), $^5D_1 \rightarrow ^7F_0$ (526 nm), $^5D_1 \rightarrow ^7F_1$ (534 nm), $^5D_1 \rightarrow ^7F_2$ (550–562 nm, with the most intense peak at 554 nm), $^5D_1 \rightarrow ^7F_3$ (584 nm), $^5D_1 \rightarrow ^7F_4$ (625 nm), $^5D_1 \rightarrow ^7F_5$ (667 nm), $^5D_0 \rightarrow ^7F_1$ (586–599, with the most intense peak at 593 nm), $^5D_0 \rightarrow ^7F_2$ (610–624 nm, with the most intense peak at 616 nm for sample H4, and 621 nm for H10), $^5D_0 \rightarrow ^7F_3$ (650 nm) and $^5D_0 \rightarrow ^7F_4$ (690–710 nm).

Table S4.1. Experimental branching ratios (β_i) for Eu^{3+} -doped phosphors. All the data were obtained from the emission spectra recorded with a DT of 10 ms and monitoring the excitation at 395 nm.

Sample	β_1	β_2	β_3	β_4
H4	0.56	0.19	0.01	0.24
H7	0.57	0.19	0.02	0.22
H10	0.41	0.41	0.01	0.17
H4-OA	0.40	0.41	0.01	0.18
H7-OA	0.40	0.41	0.02	0.17
H10-OA	0.40	0.41	0.01	0.18
H4-TA	0.39	0.42	0.01	0.18
H7-TA	0.38	0.43	0.01	0.18
H10-TA	0.39	0.43	0.01	0.17

For Eu^{3+} -doped YF_3 compounds (samples H4, H7), the branching ratio β_1 has the greatest value (0.56 and 0.57, respectively), indicating that the magnetic dipole

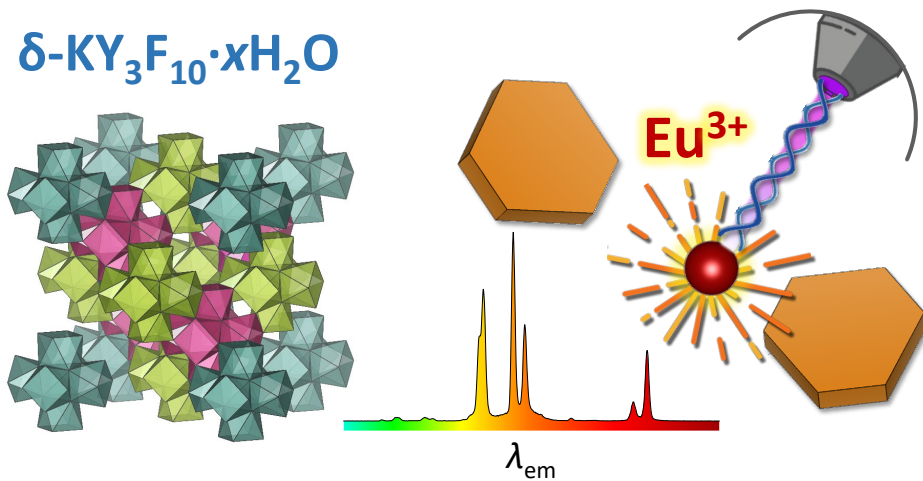
transition ${}^5D_0 \rightarrow {}^7F_1$ dominates the spectra. However, for samples with the KY_3F_{10} structure both β_1 and β_2 have virtually the same value (about 0.40), highlighting an equal contribution of the magnetic and the electric dipole transition (${}^5D_0 \rightarrow {}^7F_2$).

S4.3. References for the Supporting Information

- [S1] T. Yanai, K. Furutani, T. Masaki, T. Ohgai, M. Nakano, H. Fukunaga, *AIP Advances*. 6 (2016) 056014.
- [S2] K. Binnemans, *Coordination Chemistry Reviews*. 295 (2015) 1–45.

Chapter 5

The unexplored δ -phase of KY_3F_{10} : Toward novel Eu^{3+} -doped nanoplates with a 'super-diamond' structure for optical applications



Article 3

Journal of Materials Research and Technology, 15 (2021) 6940–6946

The unexplored δ -phase of KY_3F_{10} : Toward novel Eu^{3+} -doped nanoplates with a ‘super-diamond’ structure for optical applications

Pablo Serna-Gallén, Héctor Beltrán-Mir, Eloísa Cordoncillo

Departamento de Química Inorgánica y Orgánica, Universitat Jaume I, Av. Vicent Sos Baynat s/n 12071, Castelló de la Plana, Spain

Journal Impact Factor: 6.267

Quartile: Q1

Category: Metallurgy & Metallurgical Engineering

Position: 8/79

Abstract

This article describes a new, simple, and high-yield method based on a sonochemical process for obtaining the δ - $\text{KY}_3\text{F}_{10} \cdot x\text{H}_2\text{O}$ compound with a 'super-diamond' structure, a material that has been completely neglected in the literature since it was first discovered. We explore the mechanism underlying the formation of the synthesized nanomaterials and show their connection with the pH of the medium. Additionally, we demonstrate for the first time the adequacy of the δ -phase of KY_3F_{10} for optical applications through the novel Eu^{3+} -doped nanoplates, which exhibit long lifetimes and high quantum efficiencies. The results reveal that this material, which also has zeolitic characteristics, can have a strong impact on future photonic and associated applications.

Keywords: Crystal Phase; Europium; Luminescent Materials; Fluoride; Nanoplates; Sonochemistry

5.1. Introduction

Fluorides doped with luminescent lanthanide ions (Ln^{3+}) are one of the most attractive inorganic materials used for a vast gamut of applications: emitting diodes, up/down-converter phosphors, lasers, catalysts, or biomarkers for in vivo imaging, to name but a few [1–7]. Over the last decade, the KY_3F_{10} structure has received an increasingly large amount of attention due to its photoluminescence features and their associated applications in many fields of materials chemistry [8–12]. Unfortunately, the studies in the literature have only focused on the common α -phase of KY_3F_{10} , a cubic structure with space group (SG) $Fm\bar{3}m$, 8 formula units (Z) per unit cell, and lattice parameter $a = 11.536 \text{ \AA}$ [13].

It was not until the year 2000 when a new family of fluorides was discovered by Le Berre *et al.* [14], who described the structural and crystallographic parameters of the isotypic hydrated δ -phases of $(\text{H}_3\text{O})\text{Y}_3\text{F}_{10}$ and KY_3F_{10} , among others. According to those authors, the compounds were synthesized by adding $\text{Y}_2(\text{C}_2\text{O}_4)_3 \cdot x\text{H}_2\text{O}$ (0.7 g) to a heated solution of HF (20 mL of HF 40%) and KF (different $[\text{KF}]/[\text{Y}^{3+}]$ ratios were used to synthesize the required compound). One aspect that stands out is the amount of hydrofluoric acid (HF) used. It is common knowledge that HF has an acute toxicity because of its harmful effects and the ability to be readily absorbed through the skin and attack bones [15]. Consequently, the use and handling of HF in the laboratory must be a hazard of concern, and alternative procedures that reduce or eliminate the use of reagents that are harmful to health are a matter of importance.

Since then, little research addressing the δ - $(\text{H}_3\text{O})\text{Y}_3\text{F}_{10} \cdot x\text{H}_2\text{O}$ structure has appeared in the literature [16–20], the study reported by Caron *et al.* [18] being the only one that focuses on the properties of this compound for optical applications. Surprisingly, as far as we know, since it was first discovered in 2000, no other

additional research has been conducted on the unexplored δ -KY₃F₁₀·xH₂O structure. Moreover, the aforementioned paper of Le Berre *et al.* did not include any kind of characterization regarding the morphology or size of the material.

δ -KY₃F₁₀·xH₂O has a cubic structure with SG = $Fd\bar{3}m$, $Z = 16$, and $a = 15.4917(2)$ Å [14]. The crystal structure can be described as an association of six YF₈ square antiprisms, called unit of octahedral antiprism (UOA), **Figure 5.1(a,b)**. Edge- and corner-shared UOAs are linked to form a three-dimensional cage-like structure with cavities occupied by potassium ions and water molecules, **Figure 5.1(c)**. The water molecules can move through the tunnels, conferring a zeolitic behavior on this unique phase. The three-dimensional network can be described as a diamond-type stacking of UOAs, where the central vacancy within each UOA is at the position of a carbon atom in the diamond structure [17,21], **Figure 5.1(d,e)**. For comparison purposes, the color of the UOAs in the ‘super-diamond’ structure view of δ -KY₃F₁₀·xH₂O has been maintained to indicate their respective C atoms.

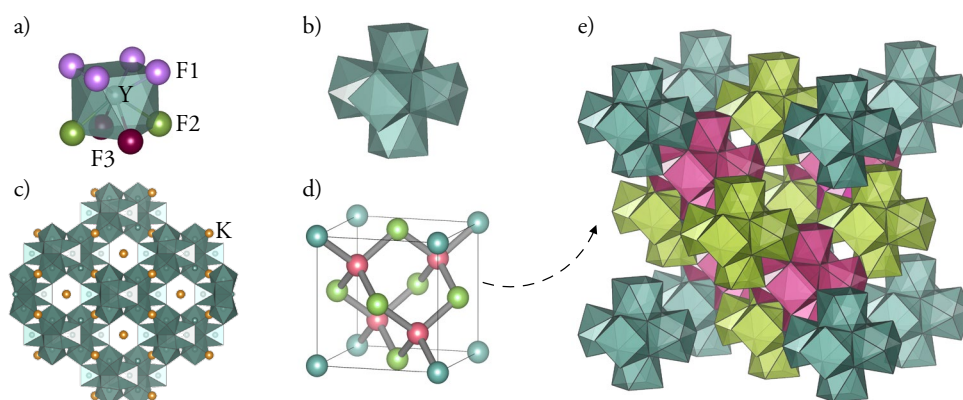


Figure 5.1. (a) YF₈ square antiprism where the F-labels indicate fluoride ions in different Wyckoff positions. (b) Schematic representation of the unit of octahedral antiprism. (c) Three-dimensional cage-like structure with cavities and channels. (d) Corresponding view of the diamond structure with C atoms represented as spheres. (e) ‘Super-diamond’ structure view of δ -KY₃F₁₀·xH₂O.

As per the above considerations, the scope of this publication is to report a simple and high-yield method to obtain the δ - $\text{KY}_3\text{F}_{10}\cdot x\text{H}_2\text{O}$ compound. In addition, we study for the first time the growth mechanism of this structure and its perfect adequacy for important optical applications through the novel Eu^{3+} -doped nanoplates. To the best of our knowledge, this is the only research to have contemplated the study of the δ - $\text{KY}_3\text{F}_{10}\cdot x\text{H}_2\text{O}$ structure since its original discovery more than twenty years ago. Besides, the alternative method that we present does not require the use of HF and minimizes the safety hazards.

5.2. Experimental

The novel synthesis of the δ -phase of KY_3F_{10} powders was performed following a sonochemistry approach. Calculations were performed so as to obtain approximately 0.25 g of the final product. In a typical synthesis procedure, 1.5 mmol of $\text{Y}(\text{NO}_3)_3\cdot 6\text{H}_2\text{O}$ were dissolved in 30 mL of water with a resulting pH of 4.0. Then, 3.0 mmol of KBF_4 were added to the above solution and the pH of the medium was adjusted to 7.0 by adding dropwise 2 M KOH aqueous solution. The mixture was stirred vigorously for 5 min and the final volume was adjusted to 50 mL with water. The whole system was transferred into a *Bandelin Sonorex* ultrasonic bath operating with a frequency of 35 kHz. After some time, the formation of a white precipitate was observed, while a progressive decrease in the pH was also noted, as will be discussed below. The precipitate was then centrifuged, washed three times with water, and dried under an infrared lamp. The choice of the pH values and their effect on the material is currently under study and will be discussed in a forthcoming publication. The reaction that controls the formation of KY_3F_{10} is highly influenced by the ultrasound-assisted processes that affect the hydrolysis degree of tetrafluoroborate ion. The slow

hydrolysis of BF_4^- also depends on the pH (it is favored in basic medium) and implies a large set of reactions that involve complex mechanisms of reaction. Thus, F^- ions are successively released to the medium and react with Y^{3+} and K^+ cations following different pathways to form the corresponding crystal phase. Nevertheless, a comprehensive and accurate approach to fully understand the reaction mechanisms that govern the formation of materials with different structures and morphologies is required and will be the scope of a new study.

Several samples of the material were prepared according to different reaction times: denoted T2, T4, T6, and T24, with a reaction time of $t = 2, 4, 6,$ and 24 hours, respectively. Moreover, in order to study the photoluminescence properties of the δ -phase of KY_3F_{10} for future photonic applications, we also incorporated the Eu^{3+} ion into the crystal structure ($\text{KLn}_3\text{F}_{10}$, $\text{Ln} = \text{Y, Eu}$; 1 mol% Eu^{3+}). The nomenclature of this sample was denoted as T6Eu, since the reaction time was 6 hours. Further details about the materials and the characterization of the samples can be found in Section S5.1 of the Supporting Information.

5.3. Results and discussion

5.3.1. Crystal structure and growth mechanism

Figure 5.2 shows the SEM images and their respective XRD patterns for samples (a) T2, (b) T4, and (c) T6, which correspond to samples synthesized at different reaction times. The reaction yields are also indicated as an inset in the XRD patterns. The Eu^{3+} -doped sample (T6Eu, not shown) presented the same structural and morphological characteristics as T6. Sample T24 has been omitted throughout the paper because no improvement in the reaction yield nor any noticeable changes in the morphology/size and XRD pattern were appreciated, suggesting that the reaction is already completed

within 6 hours. Thus, the crystal and thermal analyses were performed with sample T6, which reached the maximum reaction yield (94%).

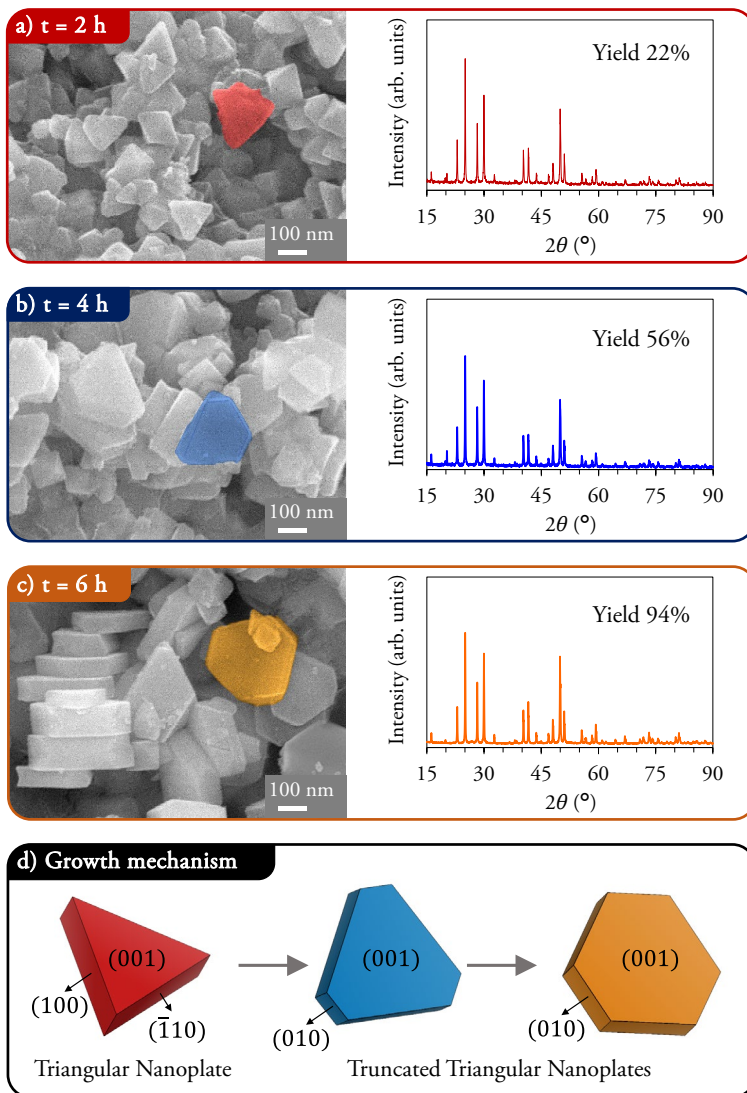


Figure 5.2. SEM images and their respective XRD patterns for samples (a) T2, (b) T4, and T6 (c), which correspond to samples synthesized at different reaction times. For clarity, the ideal morphology has been highlighted in each micrograph. The reaction yields are also indicated as an inset in the XRD patterns. (d) Description of the general growth mechanism along with the evolution of the crystal planes.

The XRD patterns show all the peaks corresponding to δ -KY₃F₁₀·xH₂O (ICDD card 04-016-7073) [22]. All samples exhibit narrow, high-intensity peaks, meaning that the materials are fairly crystalline. The refined crystal parameters of sample T6 ($a = 15.4934(5) \text{ \AA}$, $V = 3719.12(21) \text{ \AA}^3$) are also in good agreement with those reported for the structure.

For the interpretation of the growth mechanism, **Figure 5.2(d)**, the ideal morphology of the majority of the particles was computer-simulated indicating the corresponding crystal planes of the different facets. The proposed mechanism can be well explained through the evolution of triangular nanoplates with time toward the formation of truncated triangular nanoplates by the gradual growth of (010) planes. We also noted that the aggregation of some particles occurred in order to reduce their surface energy. The mechanism is fairly correlated with the pH of the reaction medium, as highlighted in **Figure 5.3(a)**. At ≈ 1.5 hours (which coincides with the inflection point of the curve) the formation of an incipient precipitate was observed. With the evolution of the reaction time, the amount of precipitate increased (see the reaction yields) and the morphology of samples changed while a progressive decrease in the pH was observed until a value of 1.1 was reached.

To further confirm the formation of the desired compound instead of the δ -(H₃O)Y₃F₁₀·xH₂O structure, the potassium-yttrium proportion was measured by ICP-MS, an approximate atomic ratio of (0.9)K:(3.0)Y being obtained, which is in perfect agreement with the stoichiometry of the crystal structure. Moreover, the FT-IR spectrum, **Figure 5.3(b)**, shows the common stretching and bending vibrational modes of the crystalline water molecules, as well as the Y–F host lattice vibrations below 600 cm^{-1} .

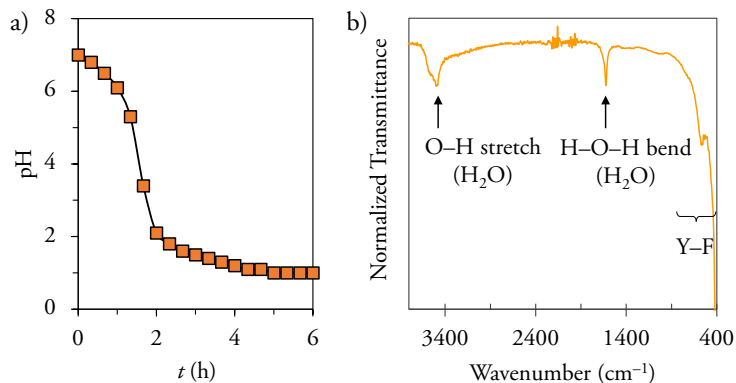


Figure 5.3. (a) Evolution of the pH of the reaction medium with time. (b) FT-IR spectrum of sample T6.

5.3.2. Thermal analysis

TG/DSC experiments of sample T6 allowed us to study the thermal behavior of the nanomaterials, **Figure 5.4**. The compound exhibits a progressive loss of mass (6.65%), which is associated with the crystalline water present in the δ -KY₃F₁₀·xH₂O structure. According to these data, the number of water molecules was established to be $x = 1.96$ (≈ 2). Thus, to obtain the reaction yields (see the previous section), the compound was considered to be δ -KY₃F₁₀·2H₂O. The absence of multiple or notable (endo/exo)thermic peaks in the temperature range 25–300 °C also highlights the fact that there are no apparent traces of a possible δ -(H₃O)Y₃F₁₀·xH₂O phase. The exothermic peak found at 439.2 °C is associated with the δ -KY₃F₁₀ → α -KY₃F₁₀ transition [14].

The enthalpy corresponding to this transition ($\Delta H = -25.5$ KJ/mol) was calculated from the experimental data taking into account the area of the exothermic peak, the heat flow, and considering the δ -KY₃F₁₀·2H₂O stoichiometry for the initial mass of the sample. The exothermic process has been expressed with a negative ΔH value by the usual convention in thermodynamics.

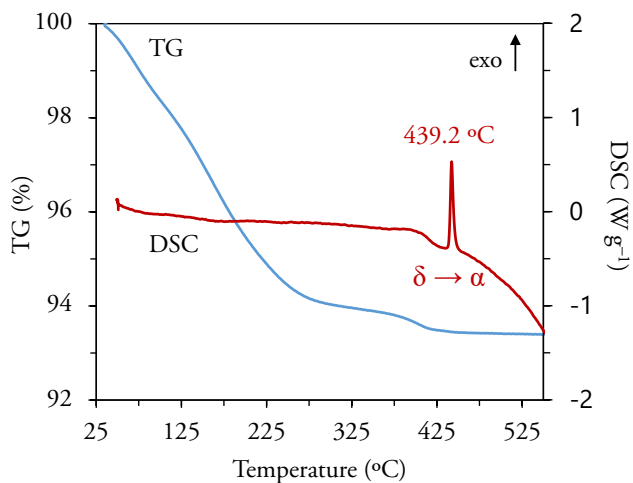


Figure 5.4. TG/DSC curves for sample T6.

5.3.3. Photoluminescence studies

The photoluminescence studies were conducted on the Eu^{3+} -doped sample (T6Eu), which incorporates the Eu^{3+} ion into the crystal structure of the material ($\text{KLn}_3\text{F}_{10}$, Ln = Y, Eu; 1 mol% Eu^{3+}). The similarity between the ionic radius of Y^{3+} (1.019 Å for a coordination number, CN, = 8) and Eu^{3+} (1.066 Å for a CN = 8) [23] ensures perfect incorporation of the Eu^{3+} ions in the host lattice. See Figure 5.1(a) for a better comprehension of the CN.

Regarding the excitation spectrum of sample T6Eu, Figure 5.5(a), different bands associated with the Eu^{3+} transitions were observed from the ground level ${}^7\text{F}_0$ to the different excited levels. Among all the transitions, the most intense was ${}^7\text{F}_0 \rightarrow {}^5\text{L}_6$, with a maximum at 395 nm. Therefore, the emission spectrum of this powder was recorded using this value as the excitation wavelength.

Figure 5.5(b) shows the emission spectrum obtained with a delay time (DT) of 0.2 ms and the typical bands corresponding to the ${}^5\text{D}_0 \rightarrow {}^7\text{F}_j$ transitions of Eu^{3+} . The blue stars are associated with a small contribution of ${}^5\text{D}_1 \rightarrow {}^7\text{F}_j$ transitions. With the

aim of suppressing the contribution of the latter transitions to subsequent calculations of some optical parameters, the emission spectrum was also recorded with a DT = 10 ms. A comparison between the emission spectrum of sample T6Eu recorded at DT = 0.2 and 10 ms can be found in **Figure S5.1**.

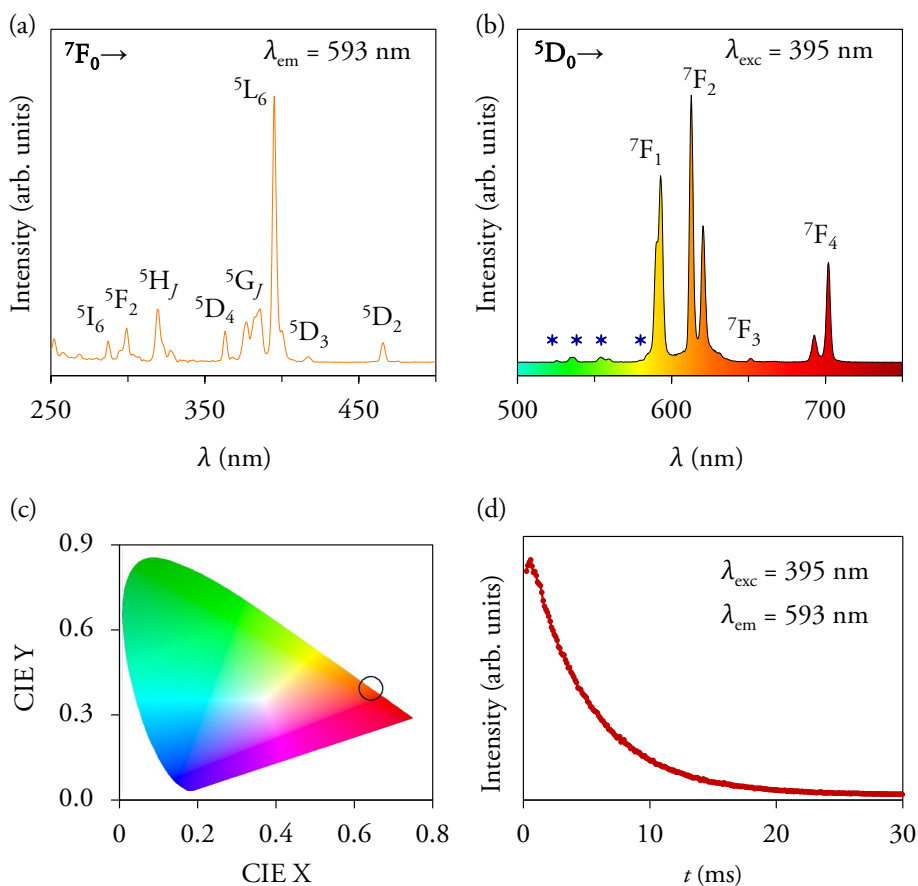


Figure 5.5. Room temperature photoluminescent studies of sample T6Eu obtained with a DT of 0.2 ms: (a) excitation and (b) emission spectra, (c) CIE chromaticity diagram, and (d) decay curve. The blue stars in (b) correspond to a small contribution of ${}^5D_1 \rightarrow {}^7F_1$ transitions.

The CIE chromaticity diagram is depicted in **Figure 5.5(c)**, highlighting the orange-reddish color emission of the nanoplates. Additionally, the Eu^{3+} -doped

powders were studied by time-resolved phosphorescence spectroscopy. The observed lifetime (τ_{obs}) of the $^5\text{D}_0$ excited level was extracted from the decay curve corresponding to the $^5\text{D}_0 \rightarrow ^7\text{F}_1$ transition, **Figure 5.5(d)**, and the quantum efficiency (the intrinsic quantum yield, η) of the material was also calculated.

On the other hand, for the particular case of the Eu^{3+} ion, several physicochemical parameters can be determined directly from the analysis of the emission spectra. The asymmetry ratio R is useful to analyze the local symmetry of the dopant and is defined as the ratio between the intensities of the $^5\text{D}_0 \rightarrow ^7\text{F}_2$ (electric dipole) and $^5\text{D}_0 \rightarrow ^7\text{F}_1$ (magnetic dipole) transitions. The Ω_2 Judd-Ofelt parameter is related to the polarizable and covalent character of the lanthanide ion in the lattice associated with the crystal environment, while the Ω_4 Judd-Ofelt parameter is sensitive to the rigidity of the crystal lattice, which is a long-range effect [24,25]. **Table 5.1** lists the values of R , Ω_2 , Ω_4 , τ_{obs} , and η for sample T6Eu ($\delta\text{-KY}_3\text{F}_{10} \cdot x\text{H}_2\text{O}$ structure). For further explanations about the calculations of the previous parameters, see Section S5.3 of the Supporting Information.

Table 5.1. Photoluminescent parameters for the Eu^{3+} -doped $\delta\text{-KY}_3\text{F}_{10} \cdot x\text{H}_2\text{O}$ crystal structure.

R	Ω_2 (10^{-20} cm ²)	Ω_4 (10^{-20} cm ²)	Ω_2/Ω_4	τ_{obs} (ms)	η (%)
1.46	2.57(3)	1.94(2)	1.32	4.96(1)	70

The value of R is in agreement with the dominance of the electric dipole transition in the emission spectrum and evidences the existence of some asymmetry around Eu^{3+} ions. The Ω_2/Ω_4 ratio also suggests that Eu^{3+} ions are mostly localized in symmetry sites with some degree of distortion [26]. In addition, the nanoparticles exhibit long lifetimes (≈ 5 ms) and high quantum efficiencies (70%).

As stated earlier, Caron *et al.* studied the optical properties of Eu^{3+} -doped $\delta\text{-(H}_3\text{O)Y}_3\text{F}_{10}\cdot x\text{H}_2\text{O}$ compounds [18]. Although the values of R and the Judd-Ofelt parameters were not reported in their study, a qualitative interpretation can be made from the emission spectra (Figure 7 of their publication) because these parameters are directly related to the intensity of ${}^5\text{D}_0\rightarrow{}^7\text{F}_j$ transitions (see equations S5.1 and S5.2 of the Supporting Information). In comparison with the emission spectrum of sample T6Eu (this work), the relative intensities of ${}^5\text{D}_0\rightarrow{}^7\text{F}_1$ and ${}^5\text{D}_0\rightarrow{}^7\text{F}_2$ transitions seem to be similar, while the intensity of the ${}^5\text{D}_0\rightarrow{}^7\text{F}_4$ transition is clearly higher. Thus, similar values of R and Ω_2 , and a higher value of Ω_4 are expected for Eu^{3+} -doped $\delta\text{-(H}_3\text{O)Y}_3\text{F}_{10}\cdot x\text{H}_2\text{O}$ compounds. These remarks lead us to believe that europium has comparable crystal environments when doping $\delta\text{-KY}_3\text{F}_{10}\cdot x\text{H}_2\text{O}$ and $\delta\text{-(H}_3\text{O)Y}_3\text{F}_{10}\cdot x\text{H}_2\text{O}$ structures, since in both cases Eu^{3+} occupies the crystallographic position of Y^{3+} . The differences expected in Ω_4 can be attributed to the different host lattices, as it is a long-range parameter.

In any case, the nanoparticles of this work exhibit longer lifetimes (≈ 5 ms) than those of Caron *et al.* [18], which obtained a lifetime of 3.20(9) ms with a similar Eu^{3+} concentration for the $\delta\text{-(H}_3\text{O)Y}_3\text{F}_{10}\cdot x\text{H}_2\text{O}$ structure. This improvement might be well attributed to the presence of K^+ ions in the host lattice instead of hydroniums, which could partially quench the luminescence. Therefore, the novel nanomaterials could find interesting applications in photonics.

5.4. Conclusions

This work presents a new, simple, and high-yield method to synthesize the δ -phase of KY_3F_{10} . In order to shed some light on the formation of the truncated triangular nanoplates, the growth mechanism has been studied, the results showing a strong

dependence on the pH of the medium. We have also explored for the first time the photoluminescence features of the Eu^{3+} -doped nanomaterials of this structure. The electric dipole transition domination over the emission spectrum results in an orangish emission of the powders. The zeolitic character of this structure and the unique site-sensitive properties of Eu^{3+} make these materials potentially useful candidates as probes in detection or imaging applications. At the same time, the optical analysis underscores their good suitability for photonics, which could arouse widespread interest among the scientific community.

Acknowledgments

The authors thank the Universitat Jaume I (Project UJI-B2019-41) for financial support. P. Serna also thanks the Spanish Ministerio de Ciencia, Innovación y Universidades for an FPU predoctoral contract.

References

- [1] C. Sassoze, G. Patriarche, M. Mortier, *Optical Materials*. 31 (2009) 1177–1183.
- [2] J. Wu, J. Wang, J. Lin, Y. Xiao, G. Yue, M. Huang, Z. Lan, Y. Huang, L. Fan, S. Yin, T. Sato, *Scientific Reports*. 3 (2013) 1–5.
- [3] B.M. Tissue, *Chemistry of Materials*. 10 (1998) 2837–2845.
- [4] T. Grzyb, M. Węclawiak, T. Pędziński, S. Lis, *Optical Materials*. 35 (2013) 2226–2233.
- [5] M. Deng, Y. Ma, S. Huang, G. Hu, L. Wang, *Nano Research*. 4 (2011) 685–694.
- [6] A. Podhorodecki, A. Noculak, M. Banski, B. Sojka, A. Zelazo, J. Misiewicz, J.

- Cichos, M. Karbowski, B. Zasonska, D. Horak, B. Sikora, D. Elbaum, T. Dumych, R. Bilyy, M. Szewczyk, *ECS Transactions*. 61 (2014) 115–125.
- [7] A. Jain, P.G.J. Fournier, V. Mendoza-Lavaniegos, P. Sengar, F.M. Guerra-Olvera, E. Iñiguez, T.G. Kretzschmar, G.A. Hirata, P. Juárez, *Journal of Nanobiotechnology*. 16 (2018) 1–18.
- [8] L. Zhu, J. Meng, X. Cao, *Materials Letters*. 62 (2008) 3007–3009.
- [9] C. Cao, *Journal of Materials Research Society*. 27 (2012) 2988–2995.
- [10] S. Goderski, M. Runowski, S. Lis, *Journal of Rare Earths*. 34 (2016) 808–813.
- [11] M. Runowski, *Journal of Luminescence*. 186 (2017) 199–204.
- [12] M. Chen, P. Loiko, J.M. Serres, S. Veronesi, M. Tonelli, M. Aguiló, F. Díaz, S.Y. Choi, J.E. Bae, F. Rotermund, S. Dai, Z. Chen, U. Griebner, V. Petrov, X. Mateos, *Journal of Alloys and Compounds*. 813 (2020) 152176.
- [13] P. Villars, K. Cenzual, eds., KY_3F_{10} Crystal Structure: Datasheet from “PAULING FILE Multinaries Edition – 2012” in SpringerMaterials (https://materials.springer.com/isp/crystallographic/docs/sd_0552093)
- [14] F. Le Berre, E. Boucher, M. Allain, G. Courbion, *Journal of Materials Chemistry*. 10 (2000) 2578–2586.
- [15] J. Harris, P. Minor, N. Chawla, S. Singh, *ACS Chemical Health & Safety*. 27 (2020) 183–189.
- [16] P.P. Fedorov, M.N. Mayakova, S. V. Kuznetsov, V. V. Voronov, R.P. Ermakov, K.S. Samarina, A.I. Popov, V. V. Osiko, *Materials Research Bulletin*. 47 (2012) 1794–1799.

- [17] B.E.G. Lucier, K.E. Johnston, D.C. Arnold, J.L. Lemyre, A. Beaupré, M. Blanchette, A.M. Ritcey, R.W. Schurko, *Journal of Physical Chemistry C*. 118 (2014) 1213–1228.
- [18] C. Caron, D. Boudreau, A.M. Ritcey, *Journal of Materials Chemistry C*. 3 (2015) 9955–9963.
- [19] B. Richard, J.L. Lemyre, A.M. Ritcey, *Langmuir*. 33 (2017) 4748–4757.
- [20] O. V. Andreev, I.A. Razumkova, A.N. Boiko, *Journal of Fluorine Chemistry*. 207 (2018) 77–83.
- [21] N.F. Stephens, P. Lightfoot, *Journal of Solid State Chemistry*. 180 (2007) 260–264.
- [22] P. Villars, K. Cenzual, eds., δ - $\text{KY}_3\text{F}_{10}\cdot x\text{H}_2\text{O}$ ($\text{KY}_3\text{F}_{10}[\text{H}_2\text{O}]$) Crystal Structure: Datasheet from “PAULING FILE Multinaries Edition – 2012” in Springer Materials (https://materials.springer.com/isp/crystallographic/docs/sd_1004004).
- [23] R.D. Shannon, *Acta Crystallographica*. A32 (1976) 751–767.
- [24] D.K. Patel, B. Vishwanadh, V. Sudarsan, S.K. Kulshreshtha, *Journal of the American Ceramic Society*. 96 (2013) 3857–3861.
- [25] C. de Mello Donegá, S.A. Junior, G.F. de Sá, *Journal of Alloys and Compounds*. 250 (1997) 422–426.
- [26] E. Cantelar, J.A. Sanz-García, A. Sanz-Martín, J.E. Muñoz Santiuste, F. Cussó, *Journal of Alloys and Compounds*. 813 (2020) 152194.

S5. Supporting Information

S5.1. Experimental Details

S5.1.1. Materials

Reagents used were yttrium(III) nitrate hexahydrate [$\text{Y}(\text{NO}_3)_3 \cdot 6\text{H}_2\text{O}$ 99.9%, Alfa Aesar], europium(III) nitrate hexahydrate [$\text{Eu}(\text{NO}_3)_3 \cdot 6\text{H}_2\text{O}$ 99.9%, Strem Chemicals], potassium hydroxide [KOH 85%, Labkerm], and potassium tetrafluoroborate [KBF_4 96%, Sigma-Aldrich].

S5.1.2. Sample characterization

All the characterization was carried out at room temperature. Powder X-ray diffraction (XRD) was performed using a Bruker-AX D8-Advance X-ray diffractometer with $\text{CuK}_{\alpha 1}$ radiation at a scan speed of $0.36^\circ/\text{min}$. All data were collected between $15 \leq 2\theta \leq 90$. Unit cell parameters were refined using WinX^{POW} 1.06 software version. The microstructure of samples was observed using a JEOL 7001F scanning electron microscope (SEM). The operation parameters were: acceleration voltage 15 kV, measuring time 20 s, and working distance 10 mm. For microstructural characterization, the powders were deposited on carbon double-sided stickers (previously adhered to the surface of aluminum stubs) and were sputtered with platinum.

Different optical properties were studied for sample T6Eu with an Eclipse Fluorescence Spectrophotometer (Varian). The excitation spectrum was recorded in the range 250–500 nm with an emission wavelength of 593 nm, while the emission spectrum was performed upon excitation at 395 nm in the range 500–750 nm. The asymmetry ratio R and the Judd-Ofelt parameters Ω_2 and Ω_4 were calculated from the spectra. Besides, the CIE coordinates were calculated using the GoCIE software [S1].

Time-resolved luminescence measurements were also performed monitoring the excitation at 395 nm and setting the emission wavelength to 593 nm. Lifetime values were extracted from decay profiles.

Furthermore, the FT-IR spectrum was recorded using an Agilent Cary 630 FTIR spectrometer in transmission mode. Thermal analysis was carried out by a simultaneous thermogravimetric analysis (TG) and differential scanning calorimetry (DSC) using a Mettler Toledo TGA/DSC3 equipment (Al_2O_3 crucible, argon atmosphere, 5 °C/min heating rate, 25–550 °C). The potassium-yttrium ratio was measured by inductively coupled plasma mass spectrometry (ICP-MS) on an ICP-MS iCAP RQ Thermo Fisher.

S5.2. Emission profiles and bands assignment

The emission bands have been assigned to their respective transitions according to [S2]: $^5\text{D}_1 \rightarrow ^7\text{F}_0$ (526 nm), $^5\text{D}_1 \rightarrow ^7\text{F}_1$ (534 nm), $^5\text{D}_1 \rightarrow ^7\text{F}_2$ (550–562 nm, with the most intense peak at 554 nm), $^5\text{D}_1 \rightarrow ^7\text{F}_3$ (584 nm), $^5\text{D}_0 \rightarrow ^7\text{F}_1$ (593 nm), $^5\text{D}_0 \rightarrow ^7\text{F}_2$ (610–624 nm, with the most intense peak at 613 nm), $^5\text{D}_0 \rightarrow ^7\text{F}_3$ (650 nm) and $^5\text{D}_0 \rightarrow ^7\text{F}_4$ (690–710 nm).

The Eu^{3+} lifetimes of the transitions occurring from the higher energy levels ($^5\text{D}_{1,2,3}$) are lower than the lifetimes associated with transitions from the $^5\text{D}_0$ ground level. Therefore, increasing the detector delay time (DT), we can observe only the transitions from the $^5\text{D}_0$ ground level [S3], as can be appreciated in **Figure S5.1**, where the contribution of $^5\text{D}_1 \rightarrow ^7\text{F}_j$ transitions is suppressed when $\text{DT} = 10$ ms.

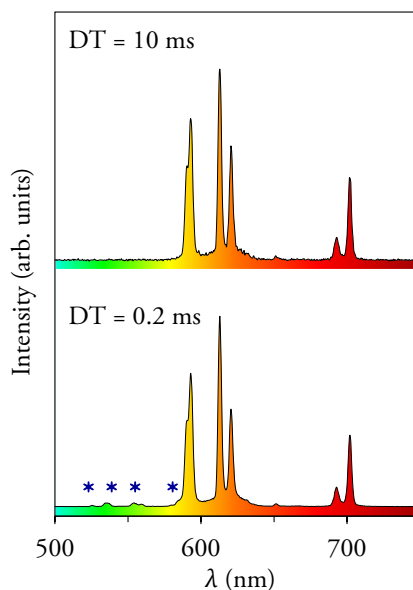


Figure S5.1. Room temperature emission spectra obtained with a DT of 0.2 and 10 ms upon excitation at 395 nm for sample T6Eu. The blue stars correspond to a small contribution of ${}^5D_1 \rightarrow {}^7F_7$ transitions.

S5.3. On the calculations of the photoluminescent parameters

S5.3.1. Asymmetry ratio and Judd-Ofelt parameters

The intensity of the magnetic dipole ${}^5D_0 \rightarrow {}^7F_1$ transition is considered to be independent of the host matrix, while the electric dipole ${}^5D_0 \rightarrow {}^7F_2$ is known as a hypersensitive transition because it is highly influenced by the local symmetry of the Eu^{3+} ion [S4]. The asymmetry ratio has been calculated according to:

$$R = \frac{I_{02}}{I_{01}} \quad (\text{S1})$$

where I_{0j} is the intensity associated with the transition ${}^5D_0 \rightarrow {}^7F_j$ that takes place at a λ_{0j} average wavelength.

The formula derived for the calculation of Ω_2 and Ω_4 Judd-Ofelt parameters is expressed as [S5]:

$$\Omega_\lambda (\lambda = 2, 4) = A_{01} \cdot \frac{I_{0J}}{I_{01}} \cdot \frac{\lambda_{0J}^4}{\lambda_{01}} \cdot \frac{3h}{64e^2\pi^4 \chi \|U^\lambda\|} \quad (S2)$$

where h is the Planck constant; e denotes the elementary charge; χ is the Lorentz local field correction term (which is equal to $\frac{n(n^2+2)^2}{9}$, n is the refractive index at λ_{0J}); $\|U^\lambda\|$ corresponds to the reduced matrix element of the unit tensor operator connecting levels $0-\lambda$ [S6]. The value reported in the literature for $\|U^2\|$ is 0.0032 and for $\|U^4\|$ is 0.0023 [S7]. A_{01} is the magnetic dipole transition rate, which is defined as $A_{01} = n^3 \cdot (A_{01})_{\text{vac}}$, where n denotes the refractive index of the material and $(A_{01})_{\text{vac}}$ is the magnetic dipole transition rate in the vacuum (14.65 s^{-1}). The average wavelength value obtained for samples is 593 nm for λ_{01} (${}^5\text{D}_0 \rightarrow {}^7\text{F}_1$ transition), 616 nm for λ_{02} (${}^5\text{D}_0 \rightarrow {}^7\text{F}_2$ transition), and 695 nm for λ_{04} (${}^5\text{D}_0 \rightarrow {}^7\text{F}_4$ transition). The refractive index of $\alpha\text{-KY}_3\text{F}_{10}$ and YF_3 is 1.49 and can be considered as a constant in the spectrum range 470–700 nm [S8–S10]. Since yttrium fluorides present very similar values of the refractive index, the value 1.49 was used as an approximation for $\delta\text{-KY}_3\text{F}_{10} \cdot x\text{H}_2\text{O}$ as well.

All the calculations were performed using the data extracted from the emission spectrum recorded with a DT = 10 ms to avoid the small contributions from the ${}^5\text{D}_1$ level, which could lead to non-accurate values.

S5.3.2. Lifetime and Quantum Efficiency

The ${}^5\text{D}_0 \rightarrow {}^7\text{F}_1$ decay profile of sample T6Eu presents a small rising part at the beginning of the curve. Therefore, it was fitted using the following equation:

$$I(t) = \left[I_0 + I_1 \left(1 - \exp\left(\frac{-t}{\tau_{\text{rise}}}\right) \right) \right] \exp\left(\frac{-t}{\tau_{\text{obs}}}\right) \quad (\text{S3})$$

where I refers to the intensity as a function of time (t) and τ_{rise} is the rising time associated with Eu^{3+} population feeding from the upper ${}^5\text{D}_1$ excited level. This mathematical expression can be considered as a single exponential model with a modified pre-exponential factor that modulates the population of Eu^{3+} ions [S11]. The correlation coefficient of the fit (R^2) was ≥ 0.999 .

The radiative lifetime (τ_{rad}) of Eu^{3+} ions for the ${}^5\text{D}_0$ level was calculated from the emission spectrum recorded at a DT of 10 ms using the following expression [S12–S14]:

$$\tau_{\text{rad}} = \frac{I_{01}}{n^3 \cdot I_{\text{total}} \cdot (A_{01})_{\text{vac}}} \quad (\text{S4})$$

where n denotes the refractive index of the material and $(A_{01})_{\text{vac}}$ is the magnetic dipole transition rate in the vacuum (14.65 s^{-1}). The quantum efficiency of the luminescence material can be evaluated considering the calculated radiative lifetimes and the observed lifetimes for the ${}^5\text{D}_0$ level as follows:

$$\eta = \frac{\tau_{\text{obs}}}{\tau_{\text{rad}}} \quad (\text{S5})$$

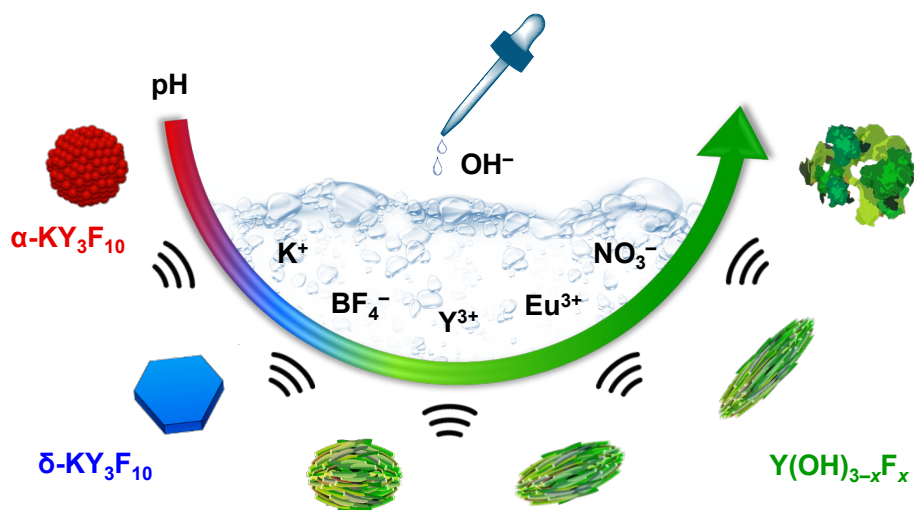
S5.4. References for the Supporting Information

- [S1] K. R. Justin Thomas, GoCIE V2 software (2009), downloaded from <http://faculty.iitr.ac.in/~krjt8fcy/index.html>
- [S2] K. Binnemans, *Coordination Chemistry Reviews*. 295 (2015) 1–45.

- [S3] P. Serna-Gallén, H. Beltrán-Mir, E. Cordoncillo, *Optics and Laser Technology*. 136 (2021) 106734.
- [S4] K. Vuković, M. Medić, M. Sekulić, M.D. Dramićanin, *Advances in Condensed Matter Physics*. 2015 (2015) 1–7.
- [S5] P. Serna-Gallén, H. Beltrán-Mir, E. Cordoncillo, A.R. West, R. Balda, J. Fernández, *Journal of Materials Chemistry C*. 7 (2019) 13976–13985.
- [S6] B. Julián, J. Planelles, E. Cordoncillo, P. Escribano, P. Aschehoug, C. Sanchez, B. Viana, F. Pellé, *Journal of Materials Chemistry*. 16 (2006) 4612–4618.
- [S7] S. Constantin, M.L. Stanciu, *Annals of West University of Timisoara - Physics*. 56 (2012) 127–131.
- [S8] P. Porcher, P. Caro, *The Journal of Chemical Physics*. 68 (1978) 4176–4182.
- [S9] J. Zhang, Z. Hao, X. Zhang, Y. Luo, X. Ren, X.J. Wang, J. Zhang, *Journal of Applied Physics*. 106 (2009) 034915.
- [S10] D.F. Bezuidenhout, K.D. Clarke, R. Pretorius, *Thin Solid Films*. 155 (1987) 17–30.
- [S11] M.L. Debasu, D. Ananias, A.G. Macedo, J. Rocha, L.D. Carlos, *Journal of Physical Chemistry C*. 115 (2011) 15297–15303.
- [S12] P. Ghosh, A. Patra, *Journal of Physical Chemistry C*. 112 (2008) 19283–19292.
- [S13] X.-N. Tian, G.-C. Jiang, X.-T. Wei, L.-Y. Wu, S. Li, K.-M. Deng, Y.H. Chen, M. Yin, *Journal of Nanoscience and Nanotechnology*. 14 (2014) 4490–4494.
- [S14] M.H.V. Werts, R.T.F. Jukes, J.W. Verhoeven, *Physical Chemistry Chemical Physics*. 4 (2002) 1542–1548

Chapter 6

The pH-dependent reactions in the sonochemical synthesis of luminescent fluorides: the quest for the formation of KY_3F_{10} crystal phases



Article 4

Ultrasonics Sonochemistry, 87 (2022) 106059

The pH-dependent reactions in the sonochemical synthesis of luminescent fluorides: the quest for the formation of KY_3F_{10} crystal phases

Pablo Serna-Gallén, Héctor Beltrán-Mir, Eloísa Cordoncillo

Departamento de Química Inorgánica y Orgánica, Universitat Jaume I, Av. Vicent Sos Baynat s/n 12071, Castelló de la Plana, Spain

Journal Impact Factor: 8.4

Quartile: Q1

Category: Acoustics

Position: 1/31

Abstract

In this study Eu^{3+} -doped yttrium fluorides were designed by ultrasound-assisted processes at different pH values (4.0–9.0). This novel strategy has enabled to obtain materials with intriguing morphologies and modulated crystal structures: $\alpha\text{-KY}_3\text{F}_{10}$, $\delta\text{-KY}_3\text{F}_{10}\cdot x\text{H}_2\text{O}$, and $\text{Y}(\text{OH})_{3-x}\text{F}_x$. To date, the literature has primarily focused only on the α -phase of KY_3F_{10} . Yet, explaining the formation of the mostly uncharted δ -phase of KY_3F_{10} remains a challenge. Thus, this paper offers the key to synthesizing both the α and the δ -phases of KY_3F_{10} and also reports the first ultrasound-assisted process for the preparation of yttrium hydroxyfluorides. It is also unraveled the connection between the different pH-dependent reactions and the formation mechanisms of the compounds. In addition to this, the unique features of the Eu^{3+} ion have allowed to conduct a thorough study of the different materials and have endowed the compounds with photoluminescent properties. The results underscore a highly tunable optical response, with a wide gamut of color emissions (from orangish to red hues), lifetimes (from 7.9 ms to 1.1 ms) and quantum efficiencies (98–28%). The study unveils the importance of sonochemistry in obtaining luminescent fluorides with controlled crystal structures that can open up new avenues in the synthesis and design of inorganic materials.

Keywords: Fluoride; Europium; Sonochemistry; Luminescence; Crystal phase, pH

6.1. Introduction

Sonochemistry has emerged as a powerful strategy in the synthesis and design of novel inorganic materials by virtue of its unique features [1,2]. Sonochemical reactions are induced by ultrasound radiations that generate local hot spots which can reach temperatures above 5000 K, pressures exceeding 1000 atm, and heating and cooling rates higher than 10^{10} K/s [3]. These extreme, transient conditions allow the synthesis of chemical compounds with controllable structures, shapes, and crystallinity at room temperature, without the need to use high pressures or high temperatures that would entail an important economic cost. It comes as no surprise, therefore, that ultrasound-assisted processes to develop nano/micron-sized materials at the expense of other conventional methods have aroused a great deal of enthusiasm [4,5].

As a series of important luminescent materials, fluoride hosts doped with lanthanide ions (Ln^{3+}) are attracting a growing amount of attention owing to their remarkable applications in photonics, solar energy, medicine, bioanalytics, or environmental science [6–10]. The extraordinary optical response of these materials arises from their electronic characteristics: sharp f - f transitions, low phonon energy (usually below 600 cm^{-1}), and high viability of energy transfers with other ions [11,12]. Particularly, fluoride crystal lattices with trivalent yttrium cations are the most common due to the ease with which they replace Y^{3+} ions by isovalent Ln^{3+} ions [13]. Moreover, Eu^{3+} has been widely appreciated for its adequacy as a site-sensitive structural probe, while the great similarity of its ionic radius to that of Y^{3+} ensures a perfect incorporation of the Ln^{3+} ion into the host matrix [14].

To date, KY_3F_{10} and its Ln^{3+} -doped counterparts have gained much attention for their important applications in several fields of materials science [15–19]. However, the studies in the literature have only focused on the common α -phase of KY_3F_{10} in

detriment of the mostly unknown δ -phase, which was discovered in 2000 by Le Berre *et al.* [20]. These authors reported the crystallographic description of this new structure and performed a detailed analysis of its zeolitic and thermal behavior. As a drawback, it is important to note that a great amount of hydrofluoric acid (HF) was required during the synthesis process. Even so, as far as we are aware, no additional research about this material had been conducted until the results of a recent study by our laboratory were published [21]. It was reported a simple high-yield method based on a sonochemical approach to obtain the compound δ -KY₃F₁₀·*x*H₂O. For the first time, the growth mechanism of this structure and its perfect adequacy for optical applications were studied. Moreover, the alternative method did not require the use of HF, which greatly reduced the safety hazards.

Despite the aforementioned signs of progress, explaining the mechanism underlying the formation of such an uncharted and promising phase of KY₃F₁₀ remains a challenge. In addition, further studies to exploit the δ -phase as host lattice for luminescent ions are required. The zeolitic behavior of this compound could also be essential for different photonic applications since it could help to modulate the incorporation/substitution of different cations inside the structure. With this in mind, in this paper, the significance of sonochemistry in the design of Eu³⁺-doped fluorides is revealed. The ultrasound-assisted processes enabled to obtain materials with intriguing morphologies and modulated crystal structures: α -KY₃F₁₀, δ -KY₃F₁₀·*x*H₂O, and Y(OH)_{3-*x*}F_{*x*}. Hence, this study not only offers the key to synthesizing both the α - and δ -phases of KY₃F₁₀ but also reports a landmark methodology for the preparation of yttrium hydroxyfluorides. It also explains how the different pH-dependent reactions govern the formation mechanisms of the compounds. Further to this, the incorporation of Eu³⁺ into the host lattice endows the material with important optical properties that are also highly tunable, depending on the compound.

Therefore, this study can contribute to a further comprehension of the δ -phase of KY_3F_{10} , while at the same time opening up novel avenues in the synthesis and design of inorganic materials for important photonic and associated applications.

6.2. Experimental section

6.2.1. Materials

The reagents used were yttrium(III) nitrate hexahydrate [$\text{Y}(\text{NO}_3)_3 \cdot 6\text{H}_2\text{O}$ 99.9%, Alfa Aesar], europium(III) nitrate hexahydrate [$\text{Eu}(\text{NO}_3)_3 \cdot 6\text{H}_2\text{O}$ 99.9%, Strem Chemicals], potassium hydroxide [KOH 85%, Labkem], and potassium tetrafluoroborate [KBF_4 96%, Sigma-Aldrich]. All reagents were used without further purification.

6.2.2. Synthesis of Eu^{3+} -doped compounds

The powders were prepared following a sonochemical process based on some previous studies of our research group detailed in references [21,22]. Calculations were performed in order to obtain approximately 0.25 g of the α/δ -phase of KY_3F_{10} . In the synthesis procedure, 1.5 mmol of $\text{Ln}(\text{NO}_3)_3 \cdot 6\text{H}_2\text{O}$ were dissolved in 30 mL of water ($\text{Ln} = \text{Y}, \text{Eu}$; 1 mol% Eu^{3+}) with a resulting pH of 4.0. Then, 3.0 mmol of KBF_4 were added to the above solution and the pH of the medium was adjusted to the desired value (pH: 4.0, 6.0, 6.5, 7.0, 7.5, 8.0, 8.5, 9.0) by adding dropwise 0.1 or 2 M KOH aqueous solutions (for $\text{pH} > 7.0$, a whitish precipitate appeared and it underwent redissolution/precipitation processes with the reaction time). The mixture was stirred for 5 min and the final volume was adjusted to 50 mL with water. The whole system was transferred into a *Bandelin Sonorex* ultrasonic bath operating at a frequency of 35 kHz for 24h. The as-formed precipitate was then centrifuged, washed several times with water, and dried under an infrared lamp. For convenience, the abbreviations used

for the different samples were denoted as “S-*n*”, where *n* indicates the initial pH of the reaction medium. A general scheme of the experimental procedure can be found in **Figure S6.1** of the Supporting Information.

6.2.3. Characterization

All the characterization was performed at room temperature. Powder X-ray diffraction (XRD) was performed using a Bruker-AX D8-Advance X-ray diffractometer with $\text{CuK}\alpha_1$ radiation from $2\theta = 15^\circ$ to 90° at a scan speed of $2.25^\circ/\text{min}$. The microstructure of the samples was observed using a JEOL 7001F scanning electron microscope (SEM) operating with an acceleration voltage of 30 kV, a measuring time of 20 s, and a working distance of 10 mm. For the microstructural characterization, the powders were deposited on double-sided carbon stickers (previously adhered to the surface of aluminum stubs) and were sputtered with platinum. Moreover, the FT-IR spectra of the powders were recorded using an Agilent Cary 630 FT-IR spectrometer in transmission mode. Chemical equilibrium diagrams were generated with the Database-Spana software package, which is based on the SOLGASWATER and HALTAFALL algorithms [23,24].

The optical properties were studied with an Eclipse Fluorescence Spectrophotometer (Varian). Excitation spectra were recorded in the range 250–500 nm with an emission wavelength of 593 nm, while emission spectra were performed upon excitation at 395/397 nm (depending on the compound) in the 500–750 nm range. All the spectra were normalized to unity. The asymmetry ratio *R* and the Judd-Ofelt parameters (Ω_2 and Ω_4) were calculated from the emission spectra. In addition, the CIE coordinates of the Eu^{3+} -doped materials were calculated from the spectra using the GoCIE software package [25]. Time-resolved luminescence measurements were also performed to obtain the lifetimes and calculate the

corresponding quantum efficiencies. In these experiments, the emission wavelength was set to 593 nm and the excitation was monitored at 395/397 nm (depending on the compound).

6.3. Results and discussion

6.3.1. Structural characterization

Prior to the discussion on the structural characterization, a brief description of the different crystal structures is provided in order to properly understand some concepts that can be helpful in this and subsequent sections of the paper. The compound α - KY_3F_{10} crystallizes in a cubic structure belonging to the $Fm\bar{3}m (O_h^5)$ space group (SG) with 8 formula units per unit cell ($Z = 8$) [26], while δ - $\text{KY}_3\text{F}_{10}\cdot x\text{H}_2\text{O}$ presents a cubic crystal system with $\text{SG} = Fd\bar{3}m (O_h^7)$ and $Z = 16$ [27]. Conversely, $\text{Y}(\text{OH})_{3-x}\text{F}_x$ is a hexagonal structure with $\text{SG} = P6_3/m (C_{6h}^2)$ and $Z = 2$ [28]. The coordination polyhedra of Y^{3+} in the different crystal structures are depicted in **Figure 6.1**. All structures were plotted with VESTA software [29]. The coordination number (CN) and the local symmetry (LS) of Y^{3+} are also shown. For the sake of clarity, different colors have been assigned to the crystal structures and have been maintained throughout all the graphics in the article: red (α - KY_3F_{10}), blue (δ - $\text{KY}_3\text{F}_{10}\cdot x\text{H}_2\text{O}$), and green ($\text{Y}(\text{OH})_{3-x}\text{F}_x$). When a mixture of α - and δ -phases exists, the color purple is used.

It is important to mention that the ideal LS of Y^{3+} in $\text{Y}(\text{OH})_{3-x}\text{F}_x$ is C_{3h} . Yet, this symmetry would only be strictly true for the fluoride-free compound, i.e., $\text{Y}(\text{OH})_3$, since the partial substitution of OH^- by F^- generates some local distortions and a lack/descent in symmetry is expected. The C_{3h} point group is thus lowered to other subgroups of symmetry such as C_{3v} , C_s , or C_1 , depending on the local environment of Y^{3+} .

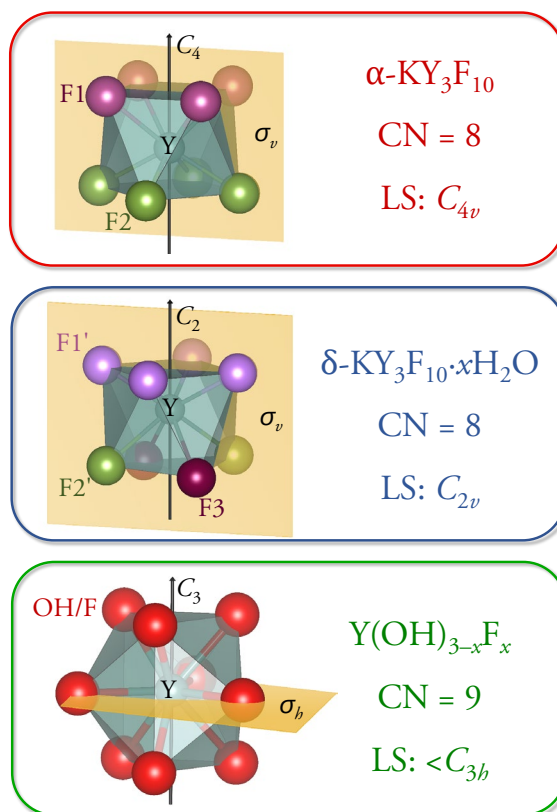


Figure 6.1. Coordination polyhedra of Y³⁺ in the different crystal structures together with the corresponding coordination numbers (CN) and local symmetries (LS). Some symmetry elements have been included for clarification purposes. The labels F1, F2, F3... refer to fluoride anions situated at different Wyckoff positions.

The XRD patterns of the Eu³⁺-doped powders prepared at different pH values following the sonochemical synthesis procedure are depicted in **Figure 6.2** and the results are summarized in **Table 6.1**. As can be appreciated, there is an extreme influence of the pH in the resulting crystal phase. Sample S-4.0 exhibits all the peaks corresponding to the single phase of cubic α -KY₃F₁₀ (ICSD card 00-040-9643). However, the increase in pH produces a coexistence between the α -KY₃F₁₀ and δ -KY₃F₁₀·xH₂O phases in samples S-6.0 and S-6.5. Indeed, the peaks corresponding to the cubic δ -phase of KY₃F₁₀ become more prominent as the pH increases (see the blue

stars in **Figure 6.2**). Surprisingly, as presented in a recent publication [21], when the initial pH of the synthesis is set to 7.0 (sample S-7.0) the XRD pattern exhibits only the peaks corresponding to δ -KY₃F₁₀·xH₂O (ICDD card 04-016-7073) [27], with no traces of α -KY₃F₁₀ secondary phase or other impurities.

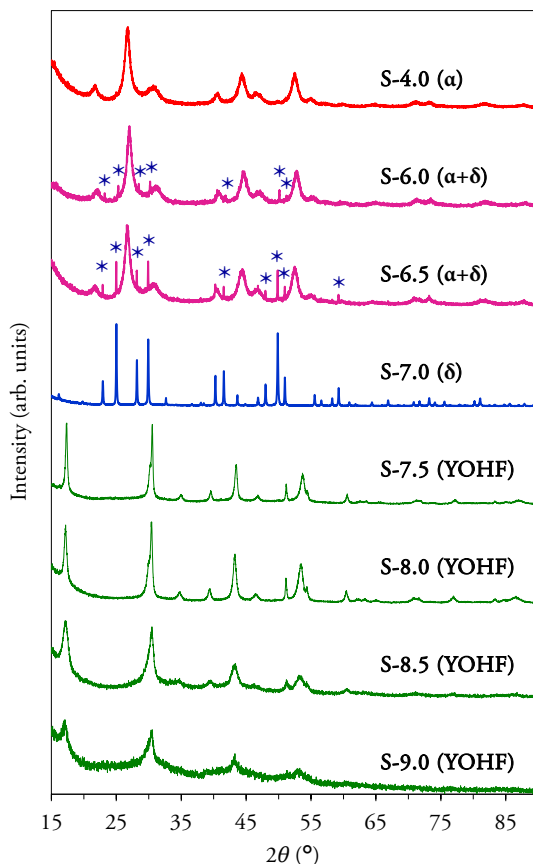


Figure 6.2. XRD patterns for the Eu³⁺-doped compounds prepared at different pH values by a sonochemical process. The blue stars in samples S-6.0 and S-6.5 highlight the presence of peaks corresponding to the δ -KY₃F₁₀·xH₂O structure. For the sake of greater clarity, the crystal phases of each powder have been indicated in brackets as abbreviations: α for α -KY₃F₁₀, δ for δ -KY₃F₁₀·xH₂O, and YOHF for Y(OH)_{3-x}F_x.

For the rest of the samples synthesized with a pH \geq 7.5, another substantial change occurs. At first glance, the most notable visual change is the absence of peaks between

20–25° 2θ (present in the previous samples), a fact that affirms that the crystal structure of these compounds is different and, probably, with a different spatial group and/or crystal system. The XRD patterns of samples S-(7.5–9.0) are in good agreement with the hexagonal structure $Y(OH)_{3-x}F_x$ (ICDD card 00-080-2008, $x = 1.43$). The reflection peaks of these powders are slightly shifted toward a higher angle relative to the JCPDS data (**Figure S6.2**, Supporting Information), a behavior previously noted in several studies [30–34]. In this series of samples, it is important to note that the increase in the pH produces a broadening and a decrease in the intensity of the peaks, resulting in a more amorphous character.

Table 6.1. Initial and final pH values of the reaction medium for the different Eu^{3+} -doped compounds. The crystal phase and the weight of the synthesized powders are also indicated.

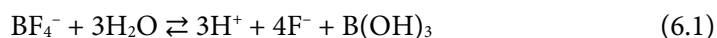
Sample	Initial pH	Final pH	Powder Weight (g)	Crystal Phase
S-4.0	4.0	1.0	0.24	α - KY_3F_{10}
S-6.0	6.0	1.0	0.24	α - KY_3F_{10} + δ - $KY_3F_{10} \cdot xH_2O$
S-6.5	6.5	1.1	0.25	α - KY_3F_{10} + δ - $KY_3F_{10} \cdot xH_2O$
S-7.0	7.0	1.1	0.25	δ - $KY_3F_{10} \cdot xH_2O$
S-7.5	7.5	6.4	0.22	$Y(OH)_{3-x}F_x$
S-8.0	8.0	6.5	0.14	$Y(OH)_{3-x}F_x$
S-8.5	8.5	6.6	0.06	$Y(OH)_{3-x}F_x$
S-9.0	9.0	7.2	0.05	$Y(OH)_{3-x}F_x$

In addition, the initial pH has an extreme influence not only on the crystal phase(s) obtained, but also on the weight of the final product and on the final pH of the reaction medium (measured at the end of the ultrasonic process, that is, 24 hours after the reaction started), which are summarized in **Table 6.1** as well. The results will be discussed in the following section because of their direct connection with the reaction

mechanisms. To further characterize the materials, the FT-IR spectra of some representative compounds were recorded (**Figure S6.3**, Supporting Information). All the spectra exhibited the characteristic bands associated with the internal vibrations of the different crystal structures. Besides, the presence of some absorbed water was noted.

6.3.2. Reaction mechanism

In order to elucidate the phenomena that govern the reaction mechanisms, some emphasis must first be placed on the equilibria that take place in the aqueous medium. Hence, it has been noted that one of the keystones is the hydrolysis of the tetrafluoroborate ion, which can be written as [35]:



In addition, the equilibrium reactions of hydrofluoric acid and the species formed with boric acid [36,37] also have to be considered:



Moreover, there is an equilibrium between the deprotonated $[\text{BF}_x(\text{OH})_{4-x}]^-$ species and their respective protonated forms $\text{HBF}_x(\text{OH})_{4-x}$, although the latter compounds dissociate very quickly and only $\text{HBF}_3(\text{OH})$ has a significant concentration in the system at $\text{pH} < 0$, so they can be neglected. The equilibrium constant for the reverse reaction of (6.1), i.e., the formation of BF_4^- , takes the value $K_f = 10^{19.21}$ at 25 °C. Consequently, the hydrolysis of BF_4^- is not favored due to the small value of the

equilibrium constant of the forward reaction (6.1), $K_h = 10^{-19.21}$, which has also been established to be very slow [35,38].

In order to properly understand the reaction mechanisms, the theoretical chemical equilibrium diagrams were generated with the Database-Spana software package and are presented in **Figure 6.3**. Default parameter values (temperature and total concentrations) were set according to the experimental procedure followed in the synthesis of the materials. It should be noted that these diagrams take into account the thermodynamic behavior of the species, while neither the kinetics nor the sonochemical effects are contemplated. Hence, the diagrams can be useful to discuss some aspects of the reactions but they are not representative of the final products. Bearing this in mind, yttrium was considered separately because its reactivity with fluoride anions depends on the degree of hydrolysis of BF_4^- .

Figure 6.3(a) depicts the speciation in the $\text{B}(\text{OH})_3$ -HF system as a function of pH, see reactions (6.1)–(6.3). At $\text{pH} \approx 7$, an inflection point in the F^- curve is observed with a plateau for $\text{pH} > 7$. By that stage BF_4^- hydrolysis should be completed. **Figure 6.3(b)** presents the fractions of the dominant species of yttrium as a function of pH. It is clear that in the pH range 6–7, $\text{Y}(\text{OH})_3$ starts to become the dominant species. In contrast to the hydrolysis and reactivity of BF_4^- (slow and requires activation by sonochemical processes), the solid formation of $\text{Y}(\text{OH})_3$ is immediate. This fact is in clear agreement with the experimental procedure since in the basic medium a whitish precipitate was formed, thus indicating the formation of yttrium hydroxide, which will be redissolved, as highlighted in the following. As per the above considerations, it can be distinguished different reaction pathways (addressed in the following sections) that determine the formation of the final product. Furthermore, for a better comprehension of the results, the evolution of the final pH and the weight of the

powders synthesized at different initial pH values are depicted in **Figure 6.4**. This will also be discussed below because of their direct connection with the reaction mechanisms.

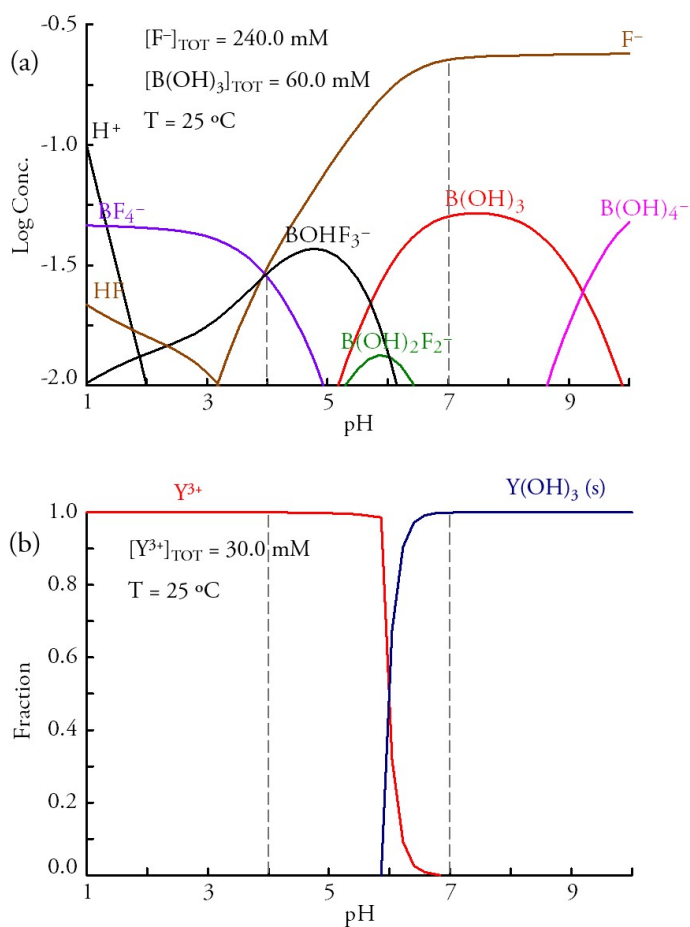


Figure 6.3. (a) Speciation in the boric acid–hydrofluoric acid system as a function of pH. (b) Fractions of the dominant species of yttrium as a function of pH.

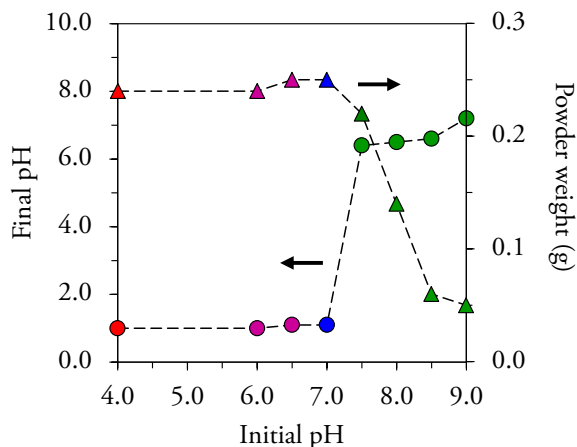
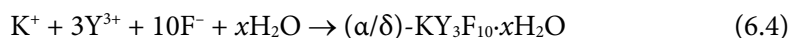


Figure 6.4. Evolution of the final pH and the weight of the powders at different initial pH values.

6.3.2.1. Formation of compounds with initial pH ≤ 7

As can be observed in **Figure 6.4**, all the samples synthesized with an initial pH ≤ 7 had a very similar behavior taking into account the weight of the powders (0.24/0.25 g) and the final pH of the reaction medium (1.0/1.1). The amounts of the powders produced indicate that the reactions have a high yield since the calculations were performed so as to obtain approximately 0.25 g. The final pH values agree with the protons released during the successive hydrolysis of BF_4^- , see reaction (6.1). These facts lead to feel that the general reaction for these compounds must be very similar and can be represented as:



The most intriguing issue to understand is perhaps the evolution from the α -phase of KY_3F_{10} toward the formation of the δ -phase as the initial pH is increased. It should be noted that both phases crystallize in a cubic system with very similar space groups ($Fm\bar{3}m$ for the α -phase, and $Fd\bar{3}m$ for the δ -phase). Therefore, these similarities may explain the possible coexistence of the two phases (as in samples S-6.0 and S-6.5) or

the tendency of the system to form only one crystal structure in detriment of the other one (samples S-4.0 and S-7.0).

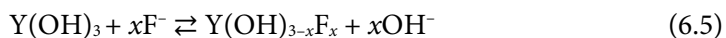
To explain the single-phase formation of $\delta\text{-KY}_3\text{F}_{10}\cdot x\text{H}_2\text{O}$ (sample S-7.0), more focus must be put again on **Figure 6.3(b)**. As mentioned earlier, yttrium hydroxide precipitates at $\text{pH} \approx 7$. Moreover, the equilibrium of reaction (6.1) is expected to be shifted to the right by the addition of OH^- , which partially neutralizes the H^+ . In fact, during the synthesis of this sample, when the pH value was initially set to 7.0, the solution became turbid, thereby indicating the precipitation of a whitish solid that corresponded to $\text{Y}(\text{OH})_3$. However, within a few minutes after putting the mixture in the ultrasonic bath, the pH of the medium decreased (which is in agreement with the successive hydrolysis of BF_4^-) and the precipitate was redissolved (see our previous publication for further details [21]). It also has to be noted that for samples synthesized with $\text{pH} \leq 6.5$, this effect was not observed and no precipitate was initially formed. Therefore, the incipient precipitation of $\text{Y}(\text{OH})_3$ and its posterior redissolution could be crucial to control the fluoride and yttrium concentrations that would lead the system toward the formation of $\delta\text{-KY}_3\text{F}_{10}\cdot x\text{H}_2\text{O}$.

Additionally, the formation of $[\text{BF}_x(\text{OH})_{4-x}]^-$ species might also play a pivotal role because they could affect the solvation shell of Y^{3+} ions and make the reaction advance through different pathways. Indeed, at $\text{pH} = 4$, in **Figure 6.3(a)** the confluence of curves corresponding to BF_4^- , $[\text{BF}_3(\text{OH})]^-$ and F^- can be appreciated.

6.3.2.2. *Formation of compounds with initial pH > 7*

The mechanistic explanations for these compounds are easier because all the samples present the same crystal structure: $\text{Y}(\text{OH})_{3-x}\text{F}_x$. According to **Figure 6.3(b)**, $\text{Y}(\text{OH})_3$ is the dominant species in a basic medium. During the synthesis procedure, the fast

precipitation of $Y(OH)_3$ yields an amorphous solid that can progressively react with fluoride anions released by BF_4^- hydrolysis. The reaction that takes place to form the final product may be understood by means of an anion-exchange process [39]:



For these samples, at the initial stage (before being ultrasonicated), two phases were clearly distinguished in the reaction medium: a solid phase at the bottom of the bottle containing mainly the as-formed $Y(OH)_3$, and a transparent aqueous phase at the top of it. As time went by, the distinction between the two phases started to disappear and only one phase was appreciated at the end of the reaction with the final product dispersed (as in the rest of the samples in this work).

Nonetheless, the amount of product decreased as the medium became more basic (see **Figure 6.4**). Hence, the sonochemical processes involved in the formation of crystalline yttrium hydroxyfluorides are not favored in highly basic media. A plausible account of it might be found considering that some redissolution processes can occur promoted by ultrasonication. Additionally, the decrease in the powder weight may also be explained considering the kinetics of reaction (5), which is influenced by the pH. Thus, further analysis about the formation of hydroxyfluorides at different reaction times could complement this work and be the scope of future studies. Be that as it may, it is important to note that, to the best of our knowledge, this is the first publication in which an ultrasound-assisted process is described for the fabrication of yttrium hydroxyfluorides. Particularly, these materials can be used as precursors to produce the greatly appreciated YOF compounds by topotactic transformations or thermal decompositions [40,41].

6.3.3. Morphological characterization

Figure 6.5 presents the SEM images of the different Eu^{3+} -doped materials and a schematic representation to illustrate the evolution of the morphology in a simple way. Table 6.2 summarizes the morphological results (shapes and approximate sizes of the particles and their respective subunits).

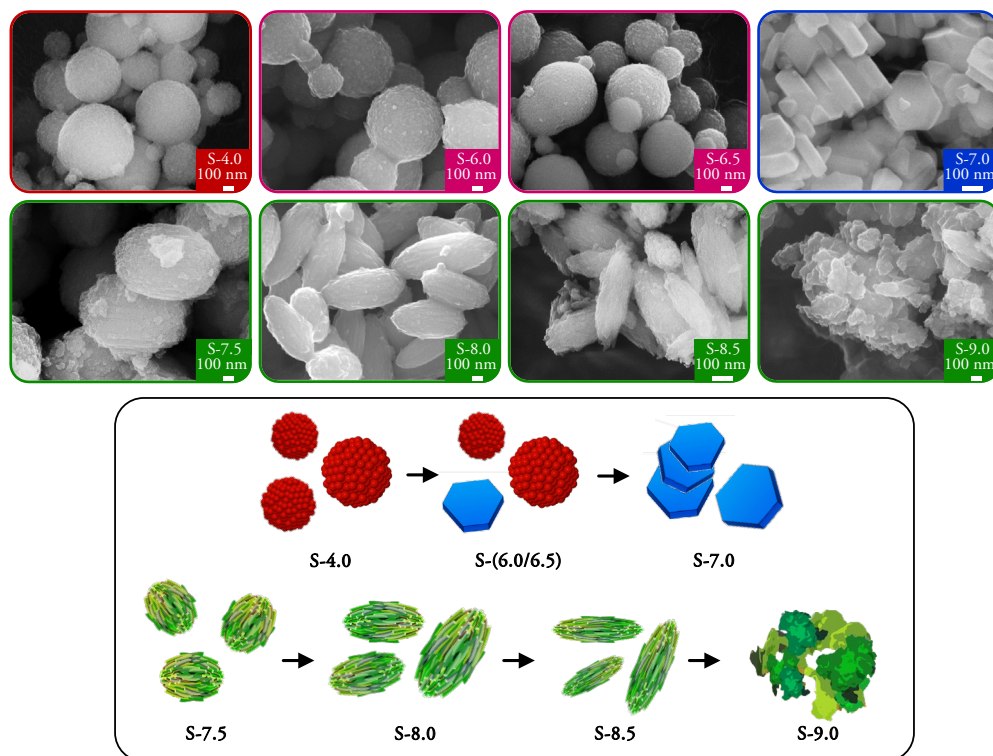


Figure 6.5. SEM images of the Eu^{3+} -doped samples prepared at different pH values by a sonochemical process, and schematic representation of the morphology of the particles.

Sample S-4.0 ($\alpha\text{-KY}_3\text{F}_{10}$ structure) consists of spherical particles. A close-up observation (Figure S6.4(a), Supporting Information) shows that these particles resulted from the self-assembly of nano-sized subunits around 20 nm in diameter (\varnothing). The same morphology is representative of samples S-6.0 and S-6.5 ($\alpha\text{-KY}_3\text{F}_{10}$ + $\delta\text{-KY}_3\text{F}_{10}\cdot x\text{H}_2\text{O}$ structures), although some truncated triangular nanoplates were also

observed in a very small proportion (**Figure S6.4(b)**, Supporting Information). The major particles (spherical) are attributed to the α -phase, while the minor ones (nanoplates) can be assigned to the δ -phase. These remarks suggest that the δ -phase is in the minority. In contrast, sample S-7.0 (δ - $\text{KY}_3\text{F}_{10}\cdot x\text{H}_2\text{O}$ structure) only exhibits truncated triangular nanoplates, which is consistent with the existence of a single-phase rather than a mixture as in samples S-6.0 and S-6.5. It was also noted that the aggregation of some nanoplates occurred in order to reduce their surface energy.

Table 6.2. Representative morphologies and approximate sizes of the different particles and subunits.

Sample	Morphology	Particle size (μm) ^a	Subunit	Subunit size (\AA nm) ^a
S-4.0	Spherical	0.2 – 0.7 (\AA)	Nanospheres	20
S-6.0	Spherical + Truncated Triangular Nanoplates	0.2 – 0.7 (\AA)	Nanospheres	20
S-6.5	Spherical + Truncated Triangular Nanoplates	0.2 – 0.7 (\AA)	Nanospheres	20
S-7.0	Truncated Triangular Nanoplates	0.1 (thickness), 0.2 (long edge)	–	–
S-7.5	Spheroidal	1.0 (long axis), 0.6 (short axis)	Nanorods	30
S-8.0	Spheroidal	0.8 (long axis), 0.3 (short axis)	Nanorods	40
S-8.5	Spheroidal	0.9 (long axis), 0.3 (short axis)	Nanorods	50
S-9.0	Amorphous	Aggregates	–	–

^a For samples S-6.0 and S-6.5, the particle/subunit size refers to the spherical particles.

As explained in the previous sections, substantial changes take place in materials with a $\text{Y}(\text{OH})_{3-x}\text{F}_x$ structure. The SEM micrographs show that samples S-(7.5–8.5) exhibit spheroidal particles that are composed of aligned nanorods as subunits (a magnification can be found in **Figure S6.4(c,d)** of the Supporting Information). These nanorods were observed both on the surface and in the interior of the architectures

and they aggregated side-by-side. Similar morphologies were obtained by Xianghong *et al.* [34] for $Y(OH)_{3-x}F_x$ compounds synthesized hydrothermally. Curiously, the spheroidal particles tend to elongate with an increase in the pH. Lastly, the particle aggregates of sample S-9.0 evidence its amorphous character, as observed in the XRD pattern. Hence, the evolution of the crystal phase is also linked to the evolution of the morphology of particles (from spherical to truncated triangular nanoplates and to spheroidal). This fact can be explained taking into account that the activation energy required to form each compound is different, so the ultrasound radiation affects the morphology in different manners as well.

6.3.4. Photoluminescence studies

6.3.4.1. Excitation and emission spectra

The room temperature excitation and emission spectra of the Eu^{3+} -doped samples recorded with a delay time (DT) of 0.2 ms are shown in **Figure 6.6**. All the excitation spectra present similar spectra profiles, exhibiting the common bands associated with the different transitions of Eu^{3+} from the ground 7F_0 level to higher excited levels with a clear dominance of the ${}^7F_0 \rightarrow {}^5L_6$ transition. For samples S-(4.0–7.0), with (α/δ) - $KY_3F_{10} \cdot xH_2O$ structures, the maximum of the band corresponding to the above transition is observed at 395 nm, while for samples S-(7.5–9.0), with a $Y(OH)_{3-x}F_x$ structure, the band is slightly shifted toward the low-energy side (397 nm). Therefore, the corresponding emission spectra were recorded upon excitation at 395/397 nm, depending on the sample.

The most significant differences are found in the emission spectra of the phosphors, the profiles of which depend on the crystal lattice of the materials and thus the resulting color emission is affected, as will be discussed later on. All the samples

present the typical ${}^5D_0 \rightarrow {}^7F_j$ transitions of Eu^{3+} but interesting changes occur, taking into account the presence of transitions from higher excited levels, the splitting and relative intensities of bands, and their broadening.

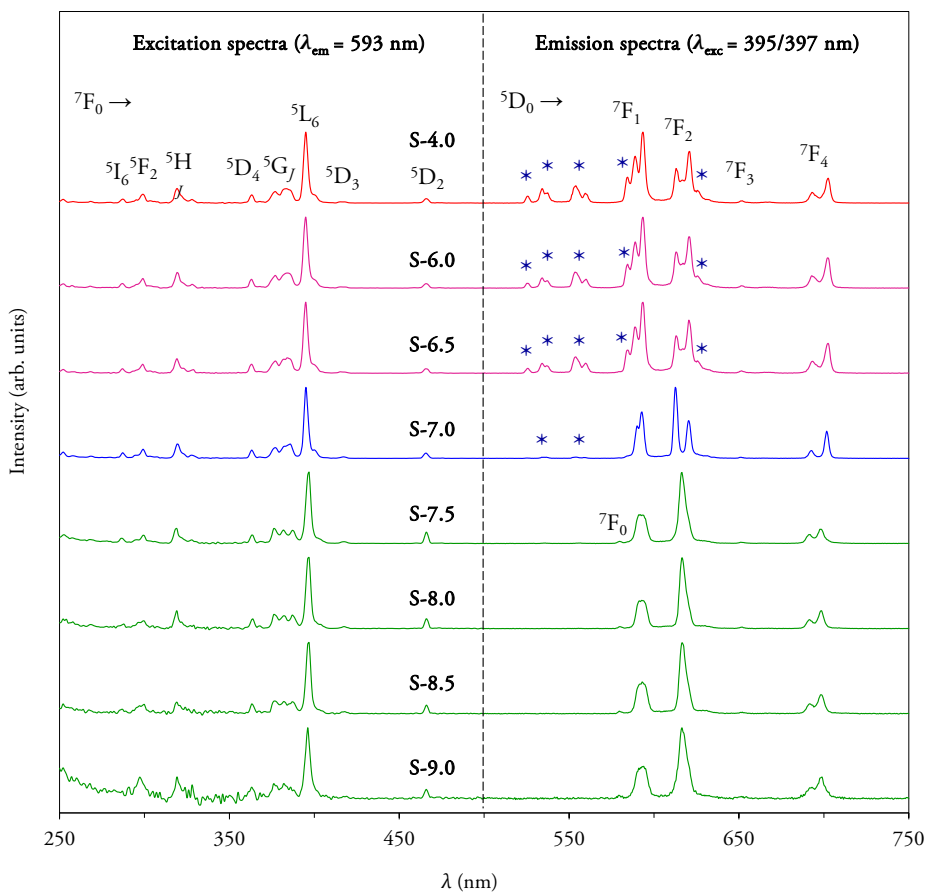


Figure 6.6. Room temperature excitation and emission spectra obtained with a DT = 0.2 ms for samples prepared at different pH values. The blue stars in the emission spectra indicate bands associated with ${}^5D_1 \rightarrow {}^7F_j$ transitions from the higher excited level 5D_1 .

Samples S-4.0 ($\alpha\text{-KY}_3\text{F}_{10}$ structure) and S-(6.0, 6.5), with a mixture of $\alpha\text{-KY}_3\text{F}_{10}$ + $\delta\text{-KY}_3\text{F}_{10} \cdot x\text{H}_2\text{O}$ structures, have the same emission profile. These results suggest that Eu^{3+} ions are mainly incorporated into the crystal lattice of $\alpha\text{-KY}_3\text{F}_{10}$ in samples where

the coexistence of α/δ -phases exists (S-6.0 and S-6.5). For these first samples, S-(4.0, 6.0, 6.5), the whole spectra are dominated by the $^5D_0 \rightarrow ^7F_1$ magnetic dipole transition and notable contributions from transitions that take place from the higher excited state 5D_1 are observed (highlighted with blue stars in **Figure 6.6**). The absence of the $^5D_0 \rightarrow ^7F_0$ transition is justified by its overlapping with the $^5D_0 \rightarrow ^7F_1$ band and because of its typical low intensity. The interpretation of the emission spectra recorded with a DT = 0.2 ms can be difficult due to the mixing of $^5D_{0,1} \rightarrow ^7F_j$ transitions. Therefore, the photoluminescence measurements of these samples were also carried out increasing the detector delay time to 10 ms, since the Eu^{3+} lifetimes associated with the transitions occurring from the 5D_1 higher energy level are lower than those corresponding to the 5D_0 ground level. As a result, these experiments allowed to observe only the contribution of $^5D_0 \rightarrow ^7F_j$ transitions and ensure that the assignment of bands was accurate (**Figure S6.5** of the Supporting Information). Further information about the assignment of the emission bands to their respective transitions can also be found in Section 3 of the Supporting Information.

A remarkable contrast is observed in sample S-7.0 (with a single δ - $\text{KY}_3\text{F}_{10} \cdot x\text{H}_2\text{O}$ phase). In this case, the spectrum is dominated by the $^5D_0 \rightarrow ^7F_2$ electric dipole transition, and $^5D_1 \rightarrow ^7F_j$ transitions (blue stars) are almost absent, probably quenched by the existence of crystalline water molecules in the host lattice. However, although this contribution was very small and may not be of substantial importance for the subsequent calculation of physical parameters, the emission spectrum of sample S-7.0 was also collected with a DT = 10 ms.

The last series of samples S-(7.5–9.0) presents the typical photoluminescence profile of Eu^{3+} -doped $\text{Y}(\text{OH})_{3-x}\text{F}_x$ compounds [34], and also exhibits broad bands and is dominated by the $^5D_0 \rightarrow ^7F_2$ electric dipole transition. For these samples, there is a

complete absence of transitions from higher excited levels due to the presence of hydroxyl groups in the crystalline matrix. Besides, the observation of the ${}^5D_0 \rightarrow {}^7F_0$ transition is clearer, albeit with low intensity.

Lastly, the CIE coordinates of the materials are plotted in **Figure 6.7**. Interestingly, the color emissions of the phosphors can be tuned from orangish to red hues through the different crystal structures (higher pH values imply an evolution toward reddish tonalities). However, it is important to note that samples with the same crystal phase have virtually the same color emission regardless of the pH.

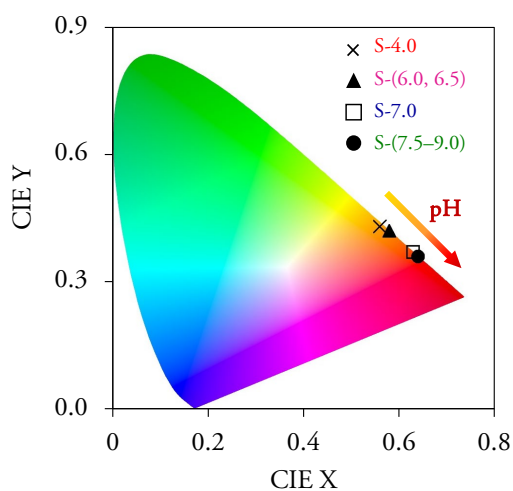


Figure 6.7. CIE chromaticity diagram of the Eu^{3+} -doped samples prepared at different pH values.

6.3.4.2. Asymmetry ratio and Judd-Ofelt parameters

The ${}^5D_0 \rightarrow {}^7F_1$ transition has a magnetic dipole character and is considered independent of the chemical surroundings of Eu^{3+} ions. Moreover, the ${}^5D_0 \rightarrow {}^7F_2$ transition of Eu^{3+} presents an electric dipole character, and is therefore hypersensitive to the local symmetry of the dopant [42,43]. As a consequence, the relative intensities

of these transitions are widely used to obtain information about the site symmetry of Eu^{3+} ions [44]. For that purpose, it is usual to define the asymmetry ratio R as the quotient between the integrated intensities of the ${}^5\text{D}_0 \rightarrow {}^7\text{F}_2$ and ${}^5\text{D}_0 \rightarrow {}^7\text{F}_1$ transitions.

On the other hand, the Judd-Ofelt (JO) parameters are extremely useful to characterize the local structure and bonding of lanthanide ions and, in the particular case of Eu^{3+} , they can be calculated directly from the emission spectra [45]. In the literature, it is well known that the short-range JO parameter (Ω_2) provides information about the polarizability and crystal environment of Eu^{3+} in the lattice, whereas the long-range JO parameter (Ω_4) is sensitive to macroscopic properties of the hosts such as viscosity and rigidity [46]. A direct relation between Ω_2 and the asymmetry ratio R can be established [47]. Hence, larger values of Ω_2 point to stronger polarizability and higher asymmetry of Eu^{3+} ions in the crystal lattice [48,49]. The physicochemical parameters mentioned above are listed in **Table 6.3**, while the equations employed to calculate them are described in Sections 4 and 5 of the Supporting Information.

The values of the asymmetry ratio are linked to the incorporation of Eu^{3+} ions in different crystal structures: $R \approx 1.0$ for $\alpha\text{-KY}_3\text{F}_{10}$ as the main phase ($\text{pH} \leq 6.5$), $R \approx 1.4$ for $\delta\text{-KY}_3\text{F}_{10} \cdot x\text{H}_2\text{O}$ ($\text{pH} = 7.0$), and $R \approx 1.8$ for $\text{Y}(\text{OH})_{3-x}\text{F}_x$ ($\text{pH} \geq 7.5$). The successive increase of R indicates the higher asymmetry of Eu^{3+} , which is in excellent agreement with the expected site symmetry for the dopant (see **Figure 6.1**). The asymmetry ratio and Ω_2 are directly related, and therefore the same reasoning can be applied to this JO parameter. It is also observed that Ω_4 increases as the pH rises, which can be attributed to the different host lattices and morphologies of the particles, since Ω_4 is ascribed to bulk properties.

Table 6.3. Asymmetry ratio (R) values, Judd-Ofelt parameters (Ω_2, Ω_4), 5D_0 lifetimes (τ_{obs}) and quantum efficiencies (η) for the different Eu^{3+} -doped phosphors. For samples S-(7.5–9.0), τ_{obs} corresponds to the effective lifetime.

Sample	R	Ω_2 (10^{-20} cm 2)	Ω_4 (10^{-20} cm 2)	τ_{obs} (ms)	τ_{rad} (ms)	η (%)
S-4.0	0.99	1.77(2)	1.65(1)	7.88(1)	8.07(4)	98
S-6.0	0.97	1.74(2)	1.77(2)	7.73(2)	8.10(4)	95
S-6.5	0.97	1.72(2)	1.80(2)	7.52(2)	7.99(4)	94
S-7.0	1.43	2.52(3)	1.93(3)	4.93(1)	6.80(3)	73
S-7.5	1.84	3.17(4)	1.96(3)	1.82(5)	4.25(3)	43
S-8.0	1.79	3.09(4)	2.16(3)	1.40(6)	4.23(3)	33
S-8.5	1.71	2.95(4)	2.30(3)	1.20(4)	4.28(4)	28
S-9.0	1.85	3.19(4)	2.56(3)	1.11(3)	3.99(2)	28

6.3.4.3. Time-resolved luminescence and quantum efficiencies

The decay curves for the $^5D_0 \rightarrow ^7F_1$ emission of Eu^{3+} were measured to allow further analysis of the luminescence properties of the samples (**Figure S6.7**, Supporting Information) and to extract the observed lifetimes (τ_{obs}). Interestingly, a small rising part at the beginning of the decay profiles was observed for samples synthesized with $\text{pH} \leq 7.0$ (samples with α/δ -phase of KY_3F_{10}). This effect is ascribed to the Eu^{3+} population feeding from the upper 5D_1 excited level. The rising phenomenon was more notable for samples S-(4.0–6.5), which also presented the most important contribution of $^5D_1 \rightarrow ^7F_7$ emissions (see the emission spectra in **Figure 6.6**). The decay curves were thus fitted using a single exponential model with a modified pre-exponential factor that modulates the population of Eu^{3+} ions [50,51]. However, the decay curves of samples synthesized with a $\text{pH} \geq 7.5$, $\text{Y}(\text{OH})_{3-x}\text{F}_x$ compounds, were best fitted with a double exponential model without the presence of a rising part. This

change in the fitting expression might well be attributed to different local environments of Eu^{3+} affected by the surrounding OH^- and F^- anions.

In order to evaluate the quantum efficiencies (the intrinsic quantum yields, η) of the materials, the theoretical radiative lifetimes (τ_{rad}) of Eu^{3+} ions for the $^5\text{D}_0$ level were also calculated from the emission spectra. Extra details about all the equations used can be found in Section 6 of the Supporting Information. The observed lifetimes, the calculated radiative lifetimes, and the quantum yields are presented in **Table 6.3**. All the parameters present a monotonic decrease with the rise in pH. Lifetimes vary from 7.9 ms to 1.1 ms, whereas extremely different quantum yields are also obtained (98–28%). The key point that allows these values to be obtained is the sequential evolution of the crystal phase. For instance, the crystalline water molecules in the host lattice of the δ -phase of KY_3F_{10} (sample S-7.0) can partially quench the radiative emission, thus yielding notably lower quantum efficiencies in comparison to the α -phase of KY_3F_{10} (sample S-4.0). Following the same line of reasoning, the presence of hydroxyls in $\text{Y}(\text{OH})_{3-x}\text{F}_x$ compounds has a strong impact on the quenching process. For this last series of samples, a higher degree of suppression also occurs while increasing the pH. This can be attributed to the increasing amorphous character of the particles (as noted in the lack of resolution in the photoluminescence spectra) and to the possible presence of residual hydroxyls in the surface of the particles.

By all accounts, the results underscore the highly tunable optical response of the materials, with a wide gamut of color emissions, lifetimes, and quantum efficiencies. These parameters have shown a direct connection with the modulated crystal structures and morphologies of the compounds. The detailed analysis of the photoluminescence properties has allowed to further confirm the formation of the different crystal structures due to the unique site-selective characteristics of the Eu^{3+}

ion. Hence, the optical study has also corroborated the postulated formation mechanisms of the materials.

6.4. Conclusions

In order to shed some light on the formation of the different crystal phases of KY_3F_{10} , Eu^{3+} -doped yttrium fluorides were designed by ultrasound-assisted processes at a wide range of pH values (4.0–9.0). The major conclusions that can be extracted are as follows:

- The crystal phase and the morphology of the materials are critically dependent upon the initial pH of the reaction medium.
- A description of plausible reaction mechanisms has underlined the fact that the hydrolysis of the tetrafluoroborate ion and the incipient precipitation of $Y(OH)_3$ and posterior redissolution/precipitation processes could play a crucial role.
- The unique site-selective characteristics of the Eu^{3+} ion have allowed to describe the optical performance of the materials and to establish a relationship with their chemical structure, as has been observed with the calculations of the asymmetry ratio and the Judd-Ofelt parameters.
- The emission profiles of the phosphors depend on the crystal lattice of the materials, which exhibit ${}^5D_i \rightarrow {}^7F_j$ transitions with different splitting, broadening, and relative intensities of bands. The resulting color can thus be tuned from orangish to red hues.
- The modulated optical response of the phosphors is also evidenced by the lifetime values (7.9–1.1 ms) and quantum efficiencies (98–28%).

Based on the aforementioned points, the present novel strategy can contribute to an in-depth comprehension of these materials, especially of the uncharted δ - $\text{KY}_3\text{F}_{10}\cdot x\text{H}_2\text{O}$ structure. Furthermore, the study unveils the importance of sonochemistry in obtaining luminescent fluorides with controlled crystal structures that can open up new avenues in the synthesis and design of inorganic materials for important photonic and associated applications.

Acknowledgments

This work was financially supported by the Spanish Ministerio de Ciencia e Innovación (Project PID2020-116149GB-I00) and the Universitat Jaume I (Project UJI-B2019-41). P. Serna also thanks the Spanish Ministerio de Ciencia, Innovación y Universidades for an FPU predoctoral contract.

References

- [1] A. Gedanken, *Ultrasonics Sonochemistry*. 11 (2004) 47–55.
- [2] N. Pokhrel, P.K. Vabbina, N. Pala, *Ultrasonics Sonochemistry*. 29 (2016) 104–128.
- [3] X. Hangxun, B.W. Zeiger, K.S. Suslick, *Chemical Society Reviews*. 42 (2013) 2555–2567.
- [4] L. Zhu, Y. Liu, X. Fan, D. Yang, X. Cao, *Materials Research Bulletin*. 46 (2011) 252–257.
- [5] Z. Li, T. Zhuang, J. Dong, L. Wang, J. Xia, H. Wang, X. Cui, Z. Wang, *Ultrasonics Sonochemistry*. 71 (2021) 105384.

- [6] J. Wu, J. Wang, J. Lin, Y. Xiao, G. Yue, M. Huang, Z. Lan, Y. Huang, L. Fan, S. Yin, T. Sato, *Scientific Reports*. 3 (2013) 1–5.
- [7] B.M. Tissue, *Chemistry of Materials*. 10 (1998) 2837–2845.
- [8] T. Grzyb, M. Węclawiak, T. Pędziński, S. Lis, *Optical Materials*. 35 (2013) 2226–2233.
- [9] A. Podhorodecki, A. Noculak, M. Banski, B. Sojka, A. Zelazo, J. Misiewicz, J. Cichos, M. Karbowski, B. Zasonska, D. Horak, B. Sikora, D. Elbaum, T. Dumych, R. Bilyy, M. Szewczyk, *ECS Transactions*. 61 (2014) 115–125.
- [10] A. Jain, P.G.J. Fournier, V. Mendoza-Lavaniegos, P. Sengar, F.M. Guerra-Olvera, E. Iñiguez, T.G. Kretzschmar, G.A. Hirata, P. Juárez, *Journal of Nanobiotechnology*. 16 (2018) 1–18.
- [11] C. Sassoie, G. Patriarche, M. Mortier, *Optical Materials*. 31 (2009) 1177–1183.
- [12] F. Auzel, *Chemical Reviews*. 104 (2004) 139–173.
- [13] E.N. Silva, A.P. Ayala, J.Y. Gesland, R.L. Moreira, *Vibrational Spectroscopy*. 37 (2005) 21–26.
- [14] C. Cascales, J. Fernández, R. Balda, *Optics Express*. 13 (2005) 2141–2152.
- [15] L. Zhu, J. Meng, X. Cao, *Materials Letters*. 62 (2008) 3007–3009.
- [16] C. Cao, *Journal of Materials Research Society*. 27 (2012) 2988–2995.
- [17] S. Goderski, M. Runowski, S. Lis, *Journal of Rare Earths*. 34 (2016) 808–813.
- [18] M. Runowski, *Journal of Luminescence*. 186 (2017) 199–204.
- [19] M. Chen, P. Loiko, J.M. Serres, S. Veronesi, M. Tonelli, M. Aguiló, F. Díaz, S.Y.

- Choi, J.E. Bae, F. Rotermund, S. Dai, Z. Chen, U. Griebner, V. Petrov, X. Mateos, *Journal of Alloys and Compounds*. 813 (2020) 152176.
- [20] F. Le Berre, E. Boucher, M. Allain, G. Courbion, *Journal of Materials Chemistry*. 10 (2000) 2578–2586.
- [21] P. Serna-Gallén, H. Beltrán-Mir, E. Cordoncillo, *Journal of Materials Research and Technology*. 15 (2021) 6940–6946.
- [22] P. Serna-Gallén, H. Beltrán-Mir, E. Cordoncillo, *Optics and Laser Technology*. 136 (2021) 106734.
- [23] G. Eriksson, *Analytica Chimica Acta*. 112 (1979) 375–383.
- [24] N. Ingri, W. Kakolowicz, L.G. Sillén, B. Warnqvist, *Talanta*. 14 (1967) 1261–1286.
- [25] K. R. Justin Thomas, GoCIE V2 software (2009), downloaded from <http://faculty.iitr.ac.in/~krjt8fcy/index.html>
- [26] P. Villars, K. Cenzual, eds., KY_3F_{10} Crystal Structure: Datasheet from “PAULING FILE Multinaries Edition – 2012” in Springer Materials (https://materials.springer.com/isp/crystallographic/docs/sd_0552093).
- [27] P. Villars, K. Cenzual, eds., $\delta\text{-KY}_3\text{F}_{10}\cdot x\text{H}_2\text{O}$ ($\text{KY}_3\text{F}_{10}[\text{H}_2\text{O}]$) Crystal Structure: Datasheet from “PAULING FILE Multinaries Edition – 2012” in Springer Materials (https://materials.springer.com/isp/crystallographic/docs/sd_1004004).
- [28] P. Villars, K. Cenzual, eds., $\text{Y}(\text{OH})_{1.57}\text{F}_{1.43}$ ($\text{Y}[\text{OH}]_2\text{F}$) Crystal Structure: Datasheet from “PAULING FILE Multinaries Edition – 2012” in Springer Materials (<https://materials.springer.com/isp/crystallographic/docs>

- /sd_1900591).
- [29] K. Momma, F. Izumi, *Journal of Applied Crystallography*. 44 (2011) 1272–1276.
- [30] B.-Q. Liu, K. Guo, J. Wang, Z.-J. Zhang, Y. Tao, Y. Huang, J.-T. Zhao, *Materials Letters*. 100 (2013) 245–247.
- [31] L. Guo, Y. Wang, L. Han, Q. Qiang, W. Zeng, Z. Zou, B. Wang, X. Guo, *Journal of Materials Chemistry C*. 1 (2013) 7952–7962.
- [32] L. Liu, H. Chen, B. Liu, H. Zhang, B. Tang, X. Feng, Z. Sun, J. Zhao, *Journal of Rare Earths*. 32 (2014) 686–690.
- [33] B. Shao, Q. Zhao, Y. Jia, W. Lv, M. Jiao, W. Lü, H. You, *Journal of Materials Chemistry C*. 2 (2014) 7666–7673.
- [34] X. He, B. Yan, *CrystEngComm*. 17 (2015) 621–627.
- [35] R.E. Zeebe, J.W.B. Rae, *Chemical Geology*. 550 (2020) 119693.
- [36] C.A. Wamser, *Journal of the American Chemical Society*. 73 (1951) 409–416.
- [37] R.E. Mesmer, K.M. Palen, C.F. Baes Jr., *Inorganic Chemistry*. 12 (1973) 89–95.
- [38] M. Anbar, S. Guttman, *Journal of Physical Chemistry*. 64 (1961) 1896–1899.
- [39] L. Tian, W. Jiang, Q. Sun, J. Liu, *Journal of Rare Earths*. 30 (2012) 378–382.
- [40] B. Shao, Q. Zhao, W. Lv, M. Jiao, W. Lü, H. You, *Advanced Optical Materials*. 3 (2015) 583–592.
- [41] J. Li, X. Wang, Q. Zhu, B.N. Kim, X. Sun, J.G. Li, *RSC Advances*. 7 (2017) 53032–53042.
- [42] K. Vuković, M. Medić, M. Sekulić, M.D. Dramićanin, *Advances in Condensed*

- Matter Physics*. 2015 (2015) 1–7.
- [43] E. Cantelar, J.A. Sanz-García, A. Sanz-Martín, J.E. Muñoz Santiuste, F. Cussó, *Journal of Alloys and Compounds*. 813 (2020) 152194.
- [44] M.A. Hassairi, A. Garrido Hernández, T. Kallel, M. Dammak, D. Zambon, G. Chadeyron, A. Potdevin, D. Boyer, R. Mahiou, *Journal of Luminescence*. 170 (2016) 200–206.
- [45] B.M. Walsh, Judd-Ofelt theory: principles and practices, in: B. Di Bartolo, O. Forte (Eds.), *Advances in Spectroscopy for Lasers and Sensing*, Springer, Dordrecht, 2006: pp. 403–433.
- [46] S.K. Gupta, M.A. Penilla Garcia, J.P. Zuniga, Y. Mao, *Journal of Luminescence*. 228 (2020) 117605.
- [47] P. Serna-Gallén, H. Beltrán-Mir, E. Cordoncillo, A.R. West, R. Balda, J. Fernández, *Journal of Materials Chemistry C*. 7 (2019) 13976–13985.
- [48] D.K. Patel, B. Vishwanadh, V. Sudarsan, S.K. Kulshreshtha, *Journal of the American Ceramic Society*. 96 (2013) 3857–3861.
- [49] C. de Mello Donegá, S.A. Junior, G.F. de Sá, *Journal of Alloys and Compounds*. 250 (1997) 422–426.
- [50] T. Yamase, T. Kobayashi, M. Sugeta, H. Naruke, *Journal of Physical Chemistry A*. 101 (1997) 5046–5053.
- [51] M.L. Debasu, D. Ananias, A.G. Macedo, J. Rocha, L.D. Carlos, *Journal of Physical Chemistry C*. 115 (2011) 15297–15303.

S6. Supporting Information

S6.1. Experimental procedure and structural characterization

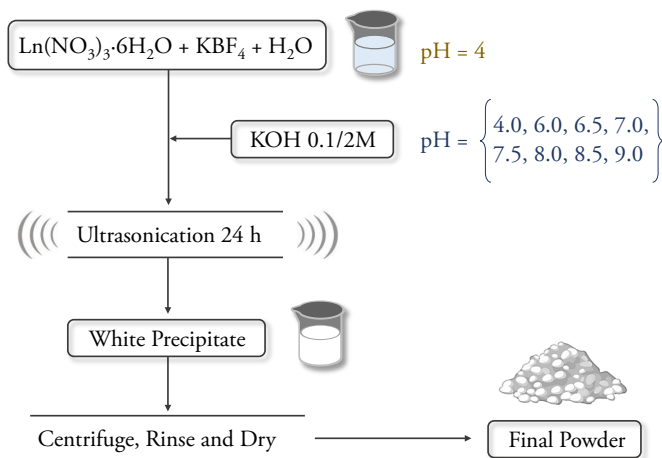


Figure S6.1. General scheme of the experimental procedure followed during the ultrasonic-assisted synthesis of the powders.

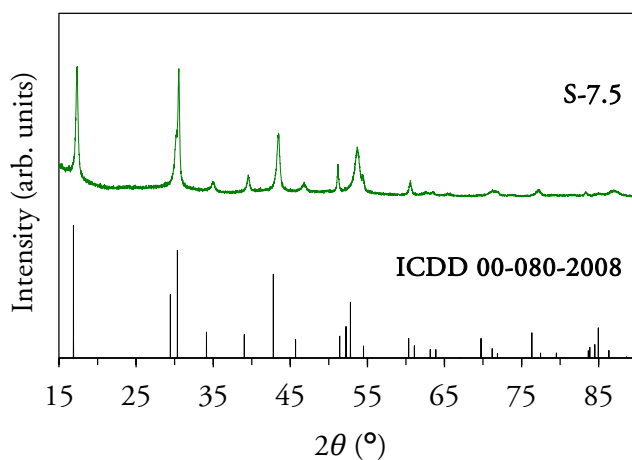


Figure S6.2. XRD pattern of sample S-7.5 and its respective ICDD card.

The peaks of the XRD patterns of samples S-(7.5–9.0) are in good agreement with those of $\text{Y}(\text{OH})_{3-x}\text{F}_x$ ($x = 1.43$, ICDD card 00-080-2008), although they are slightly

shifted towards a higher angle relative to the ICDD data, as appreciated in **Figure S6.2**.

Figure S6.3 shows the FT-IR spectra of samples S-4.0, S-7.0, and S-7.5 as an example of the different crystal structures.

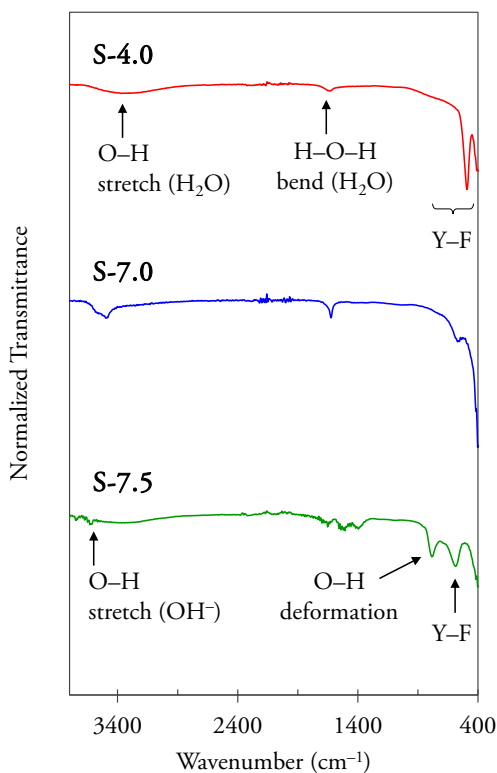


Figure S6.3. Room temperature FT-IR of the powders.

The broad and weak bands at $\approx 3100\text{--}3500\text{ cm}^{-1}$ and $\approx 1640\text{ cm}^{-1}$ are assigned to the O–H stretching vibrations and H–O–H bending mode of H₂O molecules, respectively. This indicates the presence of some absorbed water in the materials. For all the samples, the Y–F host lattice vibrations were observed below 600 cm^{-1} . In sample S-7.0, a notable difference is appreciated in the stretching and bending vibrational modes of H₂O molecules, since they are associated with crystalline

water molecules localized in the channels of the δ - $\text{KY}_3\text{F}_{10}\cdot x\text{H}_2\text{O}$ host lattice. The corresponding bands are sharper and stronger. The existence of hydroxyls groups (OH^-) in sample S-7.5, with $\text{Y}(\text{OH})_{3-x}\text{F}_x$ crystal structure, is evidenced by the bands observed at around 3630 cm^{-1} and 770 cm^{-1} , which can be ascribed to the O–H stretching vibration of virtually free hydroxyls and O–H deformation, respectively [S1,S2].

S6.2. Additional SEM images

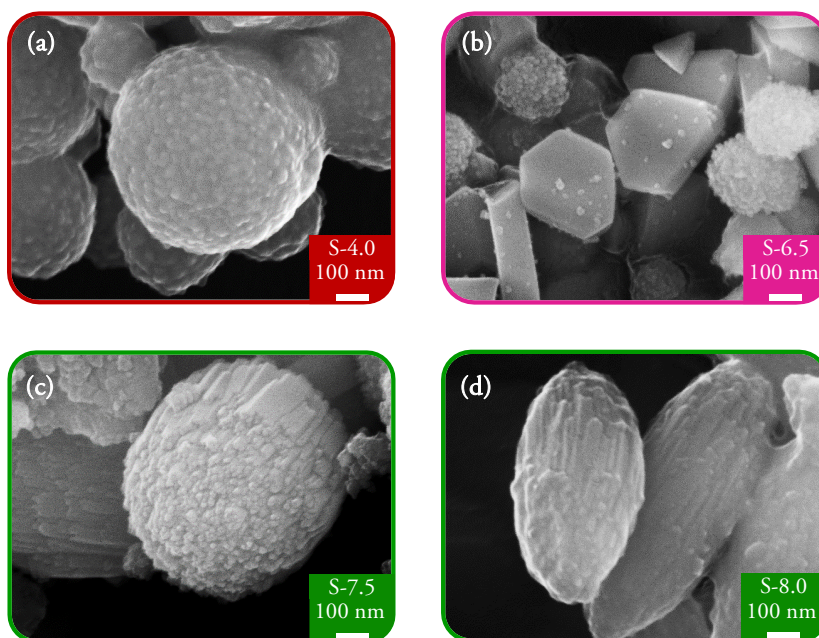


Figure S6.4. Additional SEM micrographs of samples (a) S-4.0, (b) S-6.5, (c) S-7.5, and (d) S-8.0.

Figure S6.4 shows additional SEM images of the Eu^{3+} -doped powders. The magnifications in (a), (c), and (d) highlight the subunits that constitute the particles: nanospheres for S-4.0, and nanorods for S-(7.5, 8.0). **Figure S6.4(b)** shows the mixture of spherical particles (α - KY_3F_{10} structure) and truncated triangular nanoplates (δ - $\text{KY}_3\text{F}_{10}\cdot x\text{H}_2\text{O}$ structure).

S6.3. Photoluminescence measurements

The emission bands have been assigned to their respective transitions according to reference [S3]. For samples S-(4.0-7.0), with α/δ phase of KY_3F_{10} , the assignment is as follows: ${}^5\text{D}_1 \rightarrow {}^7\text{F}_0$ (526 nm), ${}^5\text{D}_1 \rightarrow {}^7\text{F}_1$ (534 nm), ${}^5\text{D}_1 \rightarrow {}^7\text{F}_2$ (550–562 nm, with the most intense peak at 554 nm), ${}^5\text{D}_1 \rightarrow {}^7\text{F}_3$ (584 nm), ${}^5\text{D}_1 \rightarrow {}^7\text{F}_4$ (625 nm), ${}^5\text{D}_1 \rightarrow {}^7\text{F}_5$ (667 nm), ${}^5\text{D}_0 \rightarrow {}^7\text{F}_1$ (586–599, with the most intense peak at 593 nm), ${}^5\text{D}_0 \rightarrow {}^7\text{F}_2$ (610–624 nm, with the most intense peak at 621 nm for samples S-(4.0-6.5), and 613 nm for sample S-7.0), ${}^5\text{D}_0 \rightarrow {}^7\text{F}_3$ (650 nm), and ${}^5\text{D}_0 \rightarrow {}^7\text{F}_4$ (690–710 nm). For samples S-(7.5-9.0), with $\text{Y}(\text{OH})_{3-x}\text{F}_x$ structure, ${}^5\text{D}_1 \rightarrow {}^7\text{F}_j$ transitions were not appreciated. The assignment of bands is as follows: ${}^5\text{D}_0 \rightarrow {}^7\text{F}_0$ (580 nm), ${}^5\text{D}_0 \rightarrow {}^7\text{F}_1$ (593 nm), ${}^5\text{D}_0 \rightarrow {}^7\text{F}_2$ (616 nm), ${}^5\text{D}_0 \rightarrow {}^7\text{F}_3$ (652 nm), and ${}^5\text{D}_0 \rightarrow {}^7\text{F}_4$ (684–708 nm).

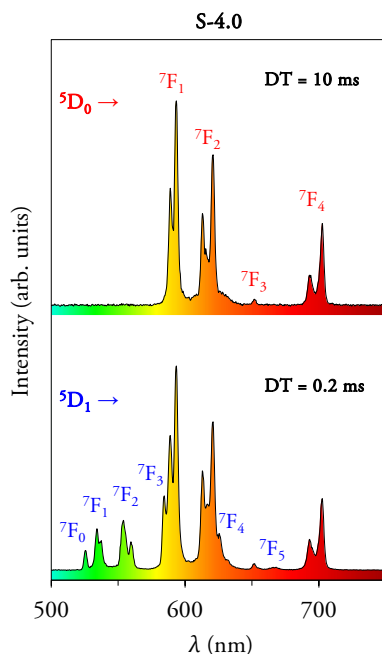


Figure S6.5. Room temperature emission spectra of sample S-4.0 obtained with a delay time (DT) of 0.2 and 10 ms upon excitation at 395 nm highlighting the different ${}^5\text{D}_{0,1} \rightarrow {}^7\text{F}_j$ transitions.

S6.4. Calculation of the asymmetry ratio and JO parameters

The asymmetry ratio has been calculated according to:

$$R = \frac{I_{02}}{I_{01}} \quad (\text{S1})$$

where I_{0J} is the intensity associated with the transition ${}^5\text{D}_0 \rightarrow {}^7\text{F}_J$ that takes place at a λ_{0J} average wavelength. The formula for the calculation of Ω_2 and Ω_4 Judd-Ofelt parameters, which has been previously derived in reference [S4], is expressed as:

$$\Omega_\lambda (\lambda = 2, 4) = A_{01} \cdot \frac{I_{0J}}{I_{01}} \cdot \frac{\lambda_{0J}^4}{\lambda_{01}} \cdot \frac{3h}{64e^2\pi^4 \chi \|U^\lambda\|} \quad (\text{S2})$$

where h is the Planck constant; e denotes the elementary charge; χ is the Lorentz local field correction term (which is equal to $\frac{n(n^2+2)^2}{9}$, n is the refractive index at λ_{0J}); $\|U^\lambda\|$ corresponds to the reduced matrix element of the unit tensor operator connecting levels $0-\lambda$ [S5]. The value reported in the literature for $\|U^2\|$ is 0.0032 and for $\|U^4\|$ is 0.0023 [S6]. A_{01} is the magnetic dipole transition rate, which is defined as $A_{01} = n^3 \cdot (A_{01})_{\text{vac}}$, where n denotes the refractive index of the material and $(A_{01})_{\text{vac}}$ is the magnetic dipole transition rate in vacuum (14.65 s^{-1}).

All the calculations were performed using the data extracted from the emission spectra recorded with a DT = 10 ms for samples synthesized with a pH ≤ 7 to avoid the small contributions from the ${}^5\text{D}_1$ level. For the rest of samples, the data were extracted from the emission spectra recorded with a DT = 0.2 ms.

On the other hand, the refractive indices for each host lattice are required to obtain the Judd-Ofelt parameters. A detailed description of the calculated refractive indices is addressed in the following Section.

S6.5. Calculation of the refractive indices

The mean refractive indices of the compounds (n) were calculated following the procedure described by Shannon and Fischer [S7] using the Anderson-Eggleton equation:

$$n = \sqrt{\frac{4\pi\alpha_T}{(c-b)\alpha_T + V_M} + 1} \quad (\text{S3})$$

where b and c are constants. b is the Lorentz factor ($b = 4\pi/3$), and c is the electron overlap factor ($c = 2.26$). V_M is the molar volume, which is defined as the unit cell volume (V_{Cell}) divided by the formula units (Z) of the compound. α_T is the total molar polarizability of the material and is calculated as a linear combination of individual ion electronic polarizabilities, $\alpha_e(\text{ion})$, according to:

$$\alpha_T = \sum_i m_i \cdot \alpha_e(\text{ion}) \quad (\text{S4})$$

where m_i is the number of ions of type i in the formula unit [S8,S9].

As an example, the total polarizability of $\alpha\text{-KY}_3\text{F}_{10}$ would be calculated according to $\alpha_T = \alpha_e(\text{K}^+) + 3\alpha_e(\text{Y}^{3+}) + 10\alpha_e(\text{F}^-)$. Cation polarizabilities are strictly additive after taking into account the coordination number (CN) and are tabulated in reference [S7]. However, the anion polarizabilities have to be calculated using the relationship:

$$\alpha_e(\text{anion}) = \alpha^\circ(\text{anion}) \cdot 10^{\frac{-N_0}{(V_{an})^{1.2}}} \quad (\text{S5})$$

where $\alpha^\circ(\text{anion})$ is the free-ion polarizability, N_0 is a parameter defined for each type of anion, and V_{an} is the anion molar volume (calculated from the molar volume V_M divided by the number of the corresponding anions in the formula unit). The

parameters $\alpha^\circ(\text{anion})$ and N_0 are also listed in reference [S7].

We have to note that Shannon and Fischer calculated the polarizabilities parameters from data recorded at a wavelength of 589.3 nm. Therefore, the previous equations yield the mean refractive indices at 589.3 nm. Notwithstanding, the refractive index is expected to change little in the visible spectral region, more particularly for fluorides. Indeed, the refractive index of $\alpha\text{-KY}_3\text{F}_{10}$ and YF_3 has been reported to be 1.49 and can be considered as a constant in the spectrum range 470–700 nm [S10–S12]. In addition, the spectral region in which the ${}^5\text{D}_0 \rightarrow {}^7\text{F}_{1,2,4}$ Eu^{3+} transitions occur (600–700 nm) are very close to 589.3. Consequently, the above equations are highly useful to calculate the refractive index of the different compounds.

Table S6.1 lists the calculated refractive indices that have been implemented in the calculations of this work (Judd-Ofelt parameters and radiative lifetimes). The values of cell volume were taken from the reported data in Springer Materials database [S13–S15]. As an approximation, it was considered $\delta\text{-KY}_3\text{F}_{10} \cdot 2\text{H}_2\text{O}$ (with 2 water molecules, as we reported in a previous study [S16]) and $\text{Y}(\text{OH})_{1.57}\text{F}_{1.43}$ ($\text{Y}(\text{OH})_{3-x}\text{F}_x$, $x = 1.43$ as explained in the main text). Additional calculations with small deviations from the established number of water molecules or x value were also performed with a negligible impact on the result of the mean refractive index. The Eu^{3+} contribution to the total polarizability was also neglected due to its small amount (1 mol%).

Table S6.1. Mean refractive indices calculated for the different host lattices.

Compound	V_{cell} (\AA^3)	Z	V_M (\AA^3)	α_T (\AA^3)	n
$\alpha\text{-KY}_3\text{F}_{10}$	1535.20	8	191.90	16.54	1.52
$\delta\text{-KY}_3\text{F}_{10} \cdot 2\text{H}_2\text{O}$	3717.90	16	232.40	19.96	1.51
$\text{Y}(\text{OH})_{1.57}\text{F}_{1.43}$	113.04	2	56.52	6.44	1.68

The n values for α -KY₃F₁₀ and δ -KY₃F₁₀·2H₂O (1.52 and 1.51, respectively) are in perfect agreement with the reported value of 1.49 for α -KY₃F₁₀ (as previously noted). On the other hand, for comparison purposes, the mean refractive index of La(OH)₃ is 1.75 [S17], thus corroborating the good value obtained for Y(OH)_{1.57}F_{1.43} (no data was available in the literature for Y(OH)₃ or the corresponding hydroxyfluorides).

S6.6. Time-resolved luminescence

The ⁵D₀→⁷F₁ decay profiles of samples with pH ≤ 7.0 (samples with α/δ phase of KY₃F₁₀) were fitted using the following equation:

$$I(t) = \left[I_0 + I_1 \left(1 - \exp\left(\frac{-t}{\tau_{\text{rise}}}\right) \right) \right] \exp\left(\frac{-t}{\tau_{\text{obs}}}\right) \quad (\text{S6})$$

where I refers to the intensity as a function of time (t) and τ_{rise} is the rising time. This expression can be considered as a single exponential model with a modified pre-exponential factor that modulates the population of Eu³⁺ ions [S18].

The ⁵D₀→⁷F₁ decay profiles of samples synthesized with pH ≥ 7.5, Y(OH)_{3-x}F_x compounds, were best fitted to a double exponential model without the presence of a rising part:

$$I(t) = I_1 \exp\left(\frac{-t}{\tau_{\text{obs } 1}}\right) + I_2 \exp\left(\frac{-t}{\tau_{\text{obs } 2}}\right) \quad (\text{S7})$$

For these samples, an effective lifetime (τ_{eff}) was calculated according to:

$$\tau_{\text{eff}} = \frac{I_1(\tau_{\text{obs } 1})^2 + I_2(\tau_{\text{obs } 2})^2}{I_1(\tau_{\text{obs } 1}) + I_2(\tau_{\text{obs } 2})} \quad (\text{S8})$$

The radiative lifetimes (τ_{rad}) of Eu³⁺ ions for the ⁵D₀ level were calculated from the emission spectra (DT = 0.2/10 ms depending on the sample) using the following

expression [S19–S21]:

$$\tau_{\text{rad}} = \frac{I_{01}}{n^3 \cdot I_{\text{total}} \cdot (A_{01})_{\text{vac}}} \quad (\text{S9})$$

where n denotes the refractive index of the material, and $(A_{01})_{\text{vac}}$ is the magnetic dipole transition rate in the vacuum (14.65 s^{-1}). Finally, the quantum efficiency of the phosphors was calculated as:

$$\eta = \frac{\tau_{\text{obs}}}{\tau_{\text{rad}}} \quad (\text{S10})$$

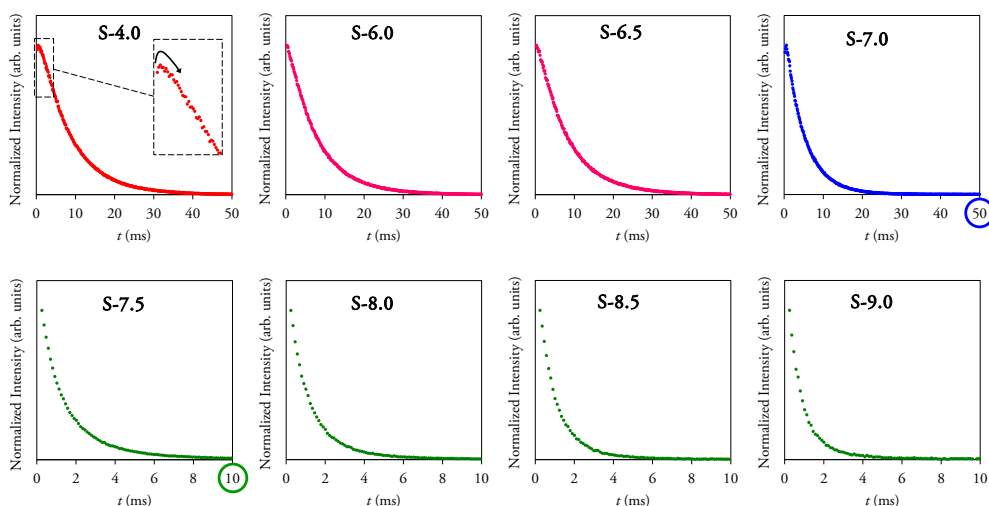


Figure S6.7. Normalized decay curves of the phosphors acquired at room temperature with a DT of 0.2 ms under the excitation of 395 nm for samples S-(4.0–7.0) and 397 nm for samples S-(7.5–9.0) monitoring the emission at 593 nm (${}^3\text{D}_0 \rightarrow {}^7\text{F}_1$). Note the difference in the time-axis scale (50 to 10 ms) for samples synthesized with $\text{pH} \geq 7.5$. The inset in sample S-4.0 highlights the rising part of the curve. All the correlation coefficients of the fits (R^2) were ≥ 0.999 .

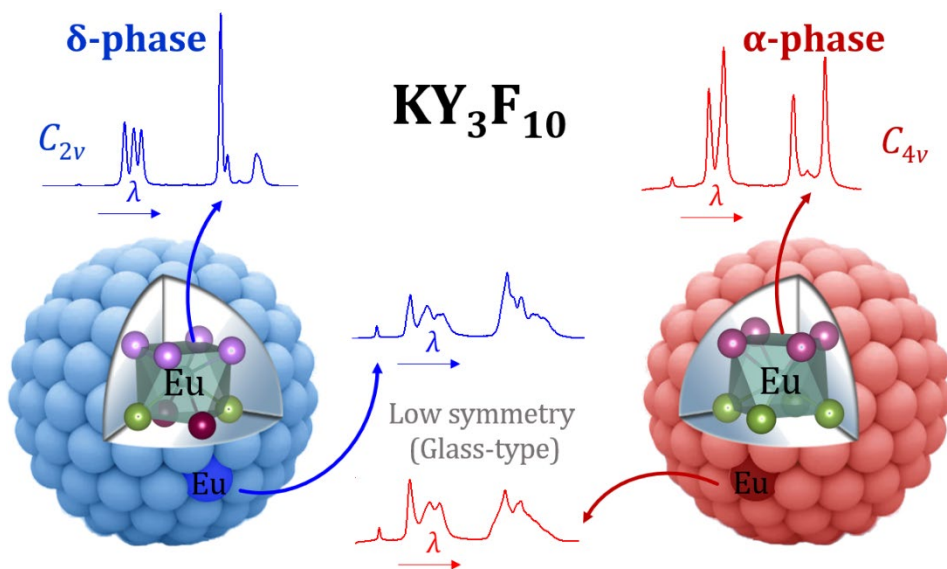
S4.3. References for the Supporting Information

- [S1] T.Y. Sun, D.Q. Zhang, X.F. Yu, Y. Xiang, M. Luo, J.H. Wang, G.L. Tan, Q.Q. Wang, P.K. Chu, *Nanoscale*. 5 (2013) 1629–1637.
- [S2] X. He, B. Yan, *CrystEngComm*. 17 (2015) 621–627.
- [S3] K. Binnemans, *Coordination Chemistry Reviews*. 295 (2015) 1–45.
- [S4] P. Serna-Gallén, H. Beltrán-Mir, E. Cordoncillo, A.R. West, R. Balda, J. Fernández, *Journal of Materials Chemistry C*. 7 (2019) 13976–13985.
- [S5] B. Julián, J. Planelles, E. Cordoncillo, P. Escribano, P. Aschehoug, C. Sanchez, B. Viana, F. Pellé, *Journal of Materials Chemistry*. 16 (2006) 4612–4618.
- [S6] S. Constantin, M.L. Stanciu, *Annals of West University of Timisoara - Physics*. 56 (2012) 127–131.
- [S7] R.D. Shannon, R.X. Fischer, *American Mineralogist*. 101 (2016) 2288–2300.
- [S8] R.D. Shannon, R.X. Fischer, *Physical Review B - Condensed Matter and Materials Physics*. 73 (2006) 1–28.
- [S9] R.C. Shannon, B. Lafuente, R.D. Shannon, R.T. Downs, R.X. Fischer, *American Mineralogist*. 102 (2017) 1906–1914.
- [S10] P. Porcher, P. Caro, *The Journal of Chemical Physics*. 68 (1978) 4176–4182.
- [S11] J. Zhang, Z. Hao, X. Zhang, Y. Luo, X. Ren, X.J. Wang, J. Zhang, *Journal of Applied Physics*. 106 (2009) 034915.
- [S12] D.F. Bezuidenhout, K.D. Clarke, R. Pretorius, *Thin Solid Films*. 155 (1987) 17–30.

- [S13] P. Villars, K. Cenzual, eds., KY_3F_{10} Crystal Structure: Datasheet from “PAULING FILE Multinaries Edition – 2012” in Springer Materials (https://materials.springer.com/isp/crystallographic/docs/sd_0552093).
- [S14] P. Villars, K. Cenzual, eds., δ - $KY_3F_{10} \cdot xH_2O$ ($KY_3F_{10}[H_2O]$) Crystal Structure: Datasheet from “PAULING FILE Multinaries Edition – 2012” in Springer Materials (https://materials.springer.com/isp/crystallographic/docs/sd_1004004).
- [S15] P. Villars, K. Cenzual, eds., $Y(OH)_{1.57}F_{1.43}$ ($Y[OH]_2F$) Crystal Structure: Datasheet from “PAULING FILE Multinaries Edition – 2012” in Springer Materials (https://materials.springer.com/isp/crystallographic/docs/sd_1900591).
- [S16] P. Serna-Gallén, H. Beltrán-Mir, E. Cordoncillo, *Journal of Materials Research and Technology*. 15 (2021) 6940–6946.
- [S17] R. Roy, H.A. McKinstry, *Acta Crystallographica*. 6 (1953) 365–366.
- [S18] M.L. Debasu, D. Ananias, A.G. Macedo, J. Rocha, L.D. Carlos, *Journal of Physical Chemistry C*. 115 (2011) 15297–15303.
- [S19] P. Ghosh, A. Patra, *Journal of Physical Chemistry C*. 112 (2008) 19283–19292.
- [S20] X.-N. Tian, G.-C. Jiang, X.-T. Wei, L.-Y. Wu, S. Li, K.-M. Deng, Y.H. Chen, M. Yin, *Journal of Nanoscience and Nanotechnology*. 14 (2014) 4490–4494.
- [S21] M.H.V. Werts, R.T.F. Jukes, J.W. Verhoeven, *Physical Chemistry Chemical Physics*. 4 (2002) 1542–1548.

Chapter 7

A site-selective fluorescence spectroscopy study of the crystal phases of KY_3F_{10} : leveraging the optical response of Eu^{3+} ions



Article 5

Journal of Alloys and Compounds, 953 (2023) 170020

A site-selective fluorescence spectroscopy study of the crystal phases of KY₃F₁₀: leveraging the optical response of Eu³⁺ ions

Pablo Serna-Gallén¹, Héctor Beltrán-Mir¹, Eloísa Cordoncillo¹, Rolindes Balda^{2,3,4},
Joaquín Fernández⁴

¹*Departamento de Química Inorgánica y Orgánica, Universitat Jaume I, Av. Vicent Sos Baynat s/n 12071, Castelló de la Plana, Spain*

²*Departamento de Física Aplicada, Escuela de Ingeniería de Bilbao, Universidad del País Vasco UPV-EHU, 48013 Bilbao, Spain*

³*Materials Physics Center CSIC-UPV/EHU, 20018 San Sebastián, Spain*

⁴*Donostia International Physics Center DIPC, 20018 San Sebastián, Spain*

Journal Impact Factor: 6.2

Quartile: Q1

Category: Metallurgy & Metallurgical Engineering

Position: 8/78

Abstract

The present work deals with the investigation of the site-selective symmetries in Eu^{3+} -doped KY_3F_{10} with different crystal phases. Employing time-resolved fluorescence line-narrowing (TRFLN), a study of the luminescent response of the dopant is reported in samples presenting a single δ -phase, a single α -phase, and a mixture of both δ and α . A new, simple, very low time-consuming and high-yield method was developed to obtain nanospheres of the δ -phase. For both crystal phases, the main site symmetry is spectrally corroborated with that expected by the crystallographic substitution position (C_{2v} in δ , and C_{4v} in α). In addition, the accuracy of the measurements also unveils the presence of significantly distorted Eu^{3+} ions in the surface of the nanoparticles in all the samples studied, a spectral behavior commonly found in glassy systems. All these findings contribute to the proper understanding of the optical response of luminescent dopants in this and related types of complex fluorides. It is worth highlighting the fact that the huge potential of the unexplored δ -phase is demonstrated, since the site-selective emission of the Eu^{3+} -doped δ -phase is up to 20 times more intense than that of the α -phase.

Keywords: Fluoride; Europium; FLN; Luminescence; Crystal Phase

7.1. Introduction

The present generation of technology calls for innovative approaches and developments which require novel materials with intriguing features. While the goals seem to be straightforward enough, they are subjected to sweeping and complex changes across the scientific community so as to give a response to several demands. On this basis, the last few decades have witnessed a huge growth in the use of fluoride hosts doped with lanthanide ions (Ln^{3+}) for important applications in photonics, biomedicine, and environmental science, to name but a few [1–5]. The implementation of these materials in such fields is based on their outstanding luminescence properties, which arise from the partially filled *f*-orbitals of Ln^{3+} ions, along with the common low phonon energy and the feasibility of being used for (up/down)conversion [6–8].

In recent years, there has been considerable interest in the complex fluoride KY_3F_{10} and its Ln^{3+} -doped counterparts. To date, researchers have been focusing only on the common α -phase of this structure in an attempt to fully describe its physicochemical properties and applications [9–13]. Notwithstanding, in 2000 Le Berre *et al.* [14] discovered a new crystal phase of this compound, the δ -phase, but it fell into oblivion and no further studies were conducted.

To fill this gap in the literature and explore the potential of this material, we recently developed a new improved method of synthesis using sonochemistry to obtain the $\delta\text{-KY}_3\text{F}_{10}\cdot x\text{H}_2\text{O}$ compound [15]. This approach yielded truncated triangular nanoplates that were also doped with Eu^{3+} as a first attempt to analyze their luminescent response. Additionally, another complementary study conducted by our laboratory has been published in which the complex formation mechanism of the δ -phase is discussed in detail [16]. The nanoplate-type morphology can be well

appropriated for some particular applications, although when it comes to surface engineering and further modifications (such as designing Ln³⁺-doped core-shell structures), it is of interest to have materials preferably with a spherical morphology. Therefore, efforts in this line have been addressed herein.

From a crystallographic point of view, both α and δ crystal phases exhibit certain similarities: they possess the same crystalline system (cubic), and the spatial groups are very similar. However, the resulting unit cells and packing have remarkable differences, which can greatly affect the optical performance of the luminescent ions embedded in such hosts. The crystallographic parameters of the different crystal phases of KY₃F₁₀ are summarized in **Table 7.1** [17,18], while the coordination polyhedra of Y³⁺ are depicted in **Figure 7.1** for better understanding. The structures were plotted with VESTA software [19].

Table 7.1. Distribution of α -KY₃F₁₀ atoms in space group $Fm\bar{3}m$ (no. 225) and δ -KY₃F₁₀·xH₂O atoms (labeled with ') in space group $Fd\bar{3}m$ (no. 227).

Name	Species	Wyckoff Position	Local Symmetry	Atomic Coordinates			Occupation Factor
				<i>x</i>	<i>y</i>	<i>z</i>	
K	K ⁺	8 <i>c</i>	<i>T_d</i> (-43 <i>m</i>)	1/4	1/4	1/4	1
Y	Y ³⁺	24 <i>e</i>	<i>C_{4v}</i> (4 <i>m.m</i>)	0.2401	0	0	1
F1	F ⁻	32 <i>f</i>	<i>C_{3v}</i> (.3 <i>m</i>)	0.1081	0.1081	0.1081	1
F2	F ⁻	48 <i>i</i>	<i>C_{2v}</i> (<i>m.m</i> 2)	1/2	0.1647	0.1647	1
K'	K ⁺	16 <i>c</i>	<i>D_{3d}</i> (.-3 <i>m</i>)	0	0	0	1
Y'	Y ³⁺	48 <i>f</i>	<i>C_{2v}</i> (2. <i>mm</i>)	0.4469	1/8	1/8	1
F1'	F ⁻	96 <i>h</i>	<i>C₂</i> (. <i>.2</i>)	0	0.3751	0.6249	1
F2'	F ⁻	32 <i>e</i>	<i>C_{3v}</i> (.3 <i>m</i>)	0.2882	0.2882	0.2882	1
F3'	F ⁻	32 <i>e</i>	<i>C_{3v}</i> (.3 <i>m</i>)	0.4462	0.4462	0.4462	1
O'	H ₂ O	48 <i>f</i>	<i>C_{2v}</i> (2. <i>mm</i>)	0.255	1/8	1/8	0.333

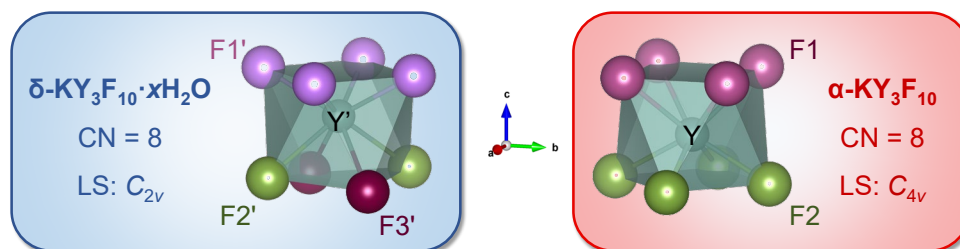


Figure 7.1. Coordination polyhedra of Y^{3+} in the different crystal phases of KY_3F_{10} . The corresponding coordination numbers (CN) and local symmetries (LS) are also included.

On the other hand, it also has to be considered that Le Berre *et al.* [14] described the isotopic $\delta\text{-(H}_3\text{O)Y}_3\text{F}_{10}\cdot x\text{H}_2\text{O}$ crystal phase (containing hydronium ions instead of potassium). Nevertheless, again there is scarce research addressing this compound in the literature [20–24]. The most interesting contribution might be that of Caron *et al.* [22], which is the only one that has focused on the properties of this compound acting as a host lattice for materials with optical applications. They reported the synthesis and characterization of low-polydispersity, luminescent $\delta\text{-(H}_3\text{O)Y}_3\text{F}_{10}\cdot x\text{H}_2\text{O}$ single-crystal nanoparticles doped with Eu^{3+} . Although the particle shape was very controllable (octahedral), the reverse microemulsion method employed required a long time (one week plus purification). Caron's paper suggested the presence of different environments for Eu^{3+} , in the core and on the surface of nanoparticles, characterized by different lifetimes and different emission probabilities. They drew this conclusion considering conventional luminescence studies, but they stated that such an explanation was somewhat speculative and required further sophisticated spectroscopic analysis.

It goes without saying that Eu^{3+} is one of the most appreciated luminescent lanthanide ions due to its particular spectral features and its ability to act as a site-sensitive structural probe [25,26]. Taking this into account, fluorescence line-

narrowing (FLN) emerges as the most powerful spectroscopic technique to discriminate among different crystal environments of luminescent ions, which is crucial for understanding their optical performance and the final properties of photonic materials.

FLN is a cryogenic technique used to obtain high-resolution fluorescence spectra [27], which was first applied in solids by Szabo to study a ruby sample [28]. This technique makes it possible to investigate the spectral transitions in solids while at the same time removing the inhomogeneous broadening. In solid-state hosts, FLN has been mainly used to analyze in detail the effects of homogeneous and inhomogeneous broadening in the emission spectra of bulk samples. While homogeneous broadening is associated with the finite linewidth inherent to the emission of “equal” ions (i.e., sensitive to the same crystal field), inhomogeneous broadening is attributed more to the impurities (or dopants) present in a host lattice that cause different Stark effects in the emitter centers (separated energetically in an inhomogeneous way) [29,30]. All this unavoidably entails the difficult interpretation of the emission spectrum of doped compounds in their bulk form. This fact is accentuated in glasses, where a greater component of disorder and thus inhomogeneous broadening, might be expected [31,32]. However, due to the *finesse* of the FLN technique, this problem can be easily overcome and it is easy to selectively discriminate among different crystal-field environments for a given dopant ion in complex systems, such as those presenting a mixture of crystal phases, as will be outlined in the present work.

FLN experiments are sensitive to local sites of the dopant ion in the host lattice because laser-selected energy levels are associated with specific single sites of distinct symmetry [33]. Hence, if the linewidth of the excitation laser is narrower than the

inhomogeneously broadened line width of a sample, only part of the ions of narrow spectral definition are excited [34]. For the particular case of Eu^{3+} , the laser frequency is tuned over the inhomogeneous bandwidth of the ${}^7\text{F}_0$ - ${}^5\text{D}_0$ transition. Since no Stark splitting can occur in the ${}^5\text{D}_0$ state under any symmetry and the ${}^7\text{F}_0$ state is also non-degenerate, the spectral profile due to ${}^5\text{D}_0 \rightarrow {}^7\text{F}_j$ emissions is only determined by the splitting of the terminal levels caused by the local crystal field of Eu^{3+} ions at different sites [35–37].

Bearing in mind everything mentioned above, in this paper a full study of the Eu^{3+} ions embedded in both α and δ crystal phases of KY_3F_{10} is reported employing FLN spectroscopy. Furthermore, a new, simple, very low time-consuming and high-yield method is presented to obtain nanospheres of the δ phase, which allows comparison of the optical response of the different phases. Our findings are vital to understand the optical response of Eu^{3+} and other dopants in these types of fluorides thanks to the description of the sites occupied by the rare earth. The results underscore the huge potential of the unknown δ -phase, since the site-selective emission of the Eu^{3+} -doped δ -phase is up to 20 times more intense than that of the α -phase.

7.2. Experimental section

7.2.1. Materials

The reagents used for the synthesis of the materials were yttrium(III) nitrate hexahydrate [$\text{Y}(\text{NO}_3)_3 \cdot 6\text{H}_2\text{O}$ 99.8%], europium(III) nitrate hexahydrate [$\text{Eu}(\text{NO}_3)_3 \cdot 6\text{H}_2\text{O}$ 99.9%], potassium fluoride [KF 99.5%], potassium tetrafluoroborate [KBF_4 96%], and hydrofluoric acid aqueous solution [HF 40% wt.]. All reagents were purchased from Sigma-Aldrich, except europium(III) nitrate hexahydrate (Strem Chemicals), and used without further purification.

7.2.2. Synthesis of materials

For all the syntheses described below, calculations were performed to obtain approximately 0.25 g of the α/δ -phase(s) of $KY_3F_{10} \cdot xH_2O$. Different amounts of the luminescent Eu^{3+} ion were employed in the three series of samples: KLn_3F_{10} ($Ln = Y, Eu; 1, 3, 5 \text{ mol\% } Eu^{3+}$). A summary of the abbreviations used according to the dopant content and the crystal phases(s) obtained is indicated in **Table 7.2**. The general scheme of the three synthetic routes is depicted in **Figure 7.2**.

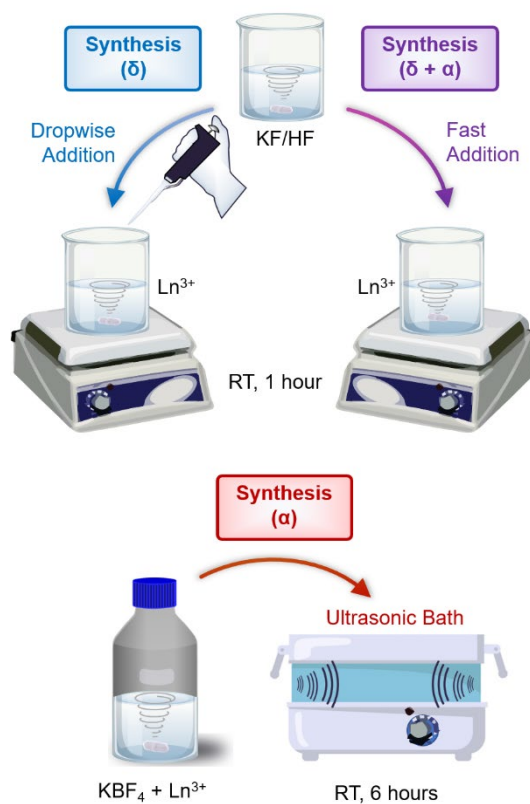


Figure 7.2. General scheme for the preparation of samples with different crystal phases of KY_3F_{10} .

Table 7.2. Nomenclature of the KY_3F_{10} fluorides prepared at different mol% Eu^{3+} .

% Eu^{3+}	Crystal Phase		
	δ	$\delta + \alpha$	α
1	1D	1DA	1A
3	3D	3DA	3A
5	5D	5DA	5A

7.2.2.1. Preparation of δ - $KY_3F_{10}:Eu^{3+}$

A new, fast, and easy coprecipitation method was developed to prepare the δ -phase compounds. First, 1.5 mmol of $Ln(NO_3)_3 \cdot 6H_2O$ were dissolved in 10 mL of water. Then, another solution was prepared by dissolving 3 mmol of KF in 10 mL of water and, subsequently, adding 135 μ L of HF aqueous solution 40% wt. (3 mmol). Later, the KF/HF solution was added dropwise to the previously prepared Ln^{3+} solution. While doing so, a white precipitate appeared and the mixture was kept under vigorous stirring for 1 hour at room temperature. After that, the precipitate was collected by centrifuging the mixture and washing it twice with water. Finally, it was dried under an infrared lamp. It is worthwhile noting that the original synthetic method proposed by Le Berre *et al.* [14] in 2000 (when this material was discovered) required the use of ≈ 20 mL of HF 40% wt. for the synthesis of similar amounts of powder. Thus, this new experimental procedure greatly reduces the use of hydrofluoric acid, which is well known for its harmful effects on human health.

7.2.2.2. Preparation of $(\delta+\alpha)$ - $KY_3F_{10}:Eu^{3+}$

The powders were prepared following the same protocol as for the synthesis of the δ -phase compounds. Notwithstanding, it is important to highlight that instead of

adding the KF/HF solution dropwise, a fast addition was required to obtain a mixture of the two crystal phases.

7.2.2.3. Preparation of α - $KY_3F_{10}:Eu^{3+}$

Eu^{3+} -doped fluorides with α -phase were obtained following a sonochemical process based on some previous studies of our research group described in references [16,38]. For that purpose, the fluoride source employed was KBF_4 . The final solution was transferred into a *Bandelin Sonorex* ultrasonic bath operating with a frequency of 35 kHz for 6 hours at room temperature.

7.2.3. Characterization

Powder X-ray diffraction (XRD) was performed at room temperature using a Bruker-AX D8-Advance X-ray diffractometer with $CuK_{\alpha 1}$ radiation from $2\theta = 15$ to 90° at a scan speed of $1.8^\circ/\text{min}$. The FT-IR spectra of the solids were recorded using an Agilent Cary 630 FT-IR spectrometer in transmission mode. Thermal analysis was carried out by a simultaneous thermogravimetric analysis (TG) and differential scanning calorimetry (DSC) using Mettler Toledo TGA/DSC3 equipment (Al_2O_3 crucible, argon atmosphere, $5^\circ\text{C}/\text{min}$ heating rate, 25 – 550°C).

Besides, the microstructure of samples was observed using a JEOL 7001F scanning electron microscope (SEM) operating with an acceleration voltage of 30 kV. For microstructural characterization, the powders were deposited on carbon double-sided stickers (previously adhered to the surface of aluminum stubs) and were sputtered with platinum. Dynamic Light Scattering (DLS) size distribution measurements were recorded using a Zetasizer Nano-ZS90 (Malvern Instruments, UK). Automatic optimization of beam focusing and attenuation was employed for each sample.

Resonant time-resolved fluorescence line-narrowing (TRFLN) spectra were performed by exciting the samples with a pulsed frequency doubled Nd:YAG pumped tunable dye laser with a 9 ns pulse width and 0.08 cm^{-1} line width, and detected by an EGG&PAR Optical Multichannel Analyzer. The measurements were carried out at 9 K in a closed cycle helium cryostat.

7.3. Results and discussion

7.3.1. Structural and thermal characterization

The XRD patterns of the Eu^{3+} -doped samples (1 mol% Eu^{3+} : 1D, 1DA, 1A) prepared using the different synthetic routes are presented in **Figure 7.3** as representatives of each series of samples. For higher percentages of dopant (3 and 5 mol% Eu^{3+}), the same XRD profiles were obtained. Sample 1D exhibits the peaks corresponding to a single phase of cubic $\delta\text{-KY}_3\text{F}_{10}\cdot x\text{H}_2\text{O}$ (ICDD card 04-016-7073). Nonetheless, the speed of the addition of the fluoride source (KF/HF solution) into the Ln^{3+} solution has a profound influence on the resulting crystal phase formation. A fast addition leads the system towards the formation of $\alpha\text{-KY}_3\text{F}_{10}$ in coexistence with the δ -phase (sample 1DA). For a better interpretation of these results, the peaks of the $\alpha\text{-KY}_3\text{F}_{10}$ structure (ICSD card 00-040-9643) can be well appreciated in the XRD pattern of sample 1A. This result underscores how delicate this fluoride system is. Further complementary and computational work, which will be the topic of an upcoming publication, is under study and corroborates that the α phase is slightly more thermodynamically favorable than the δ phase, which would explain the delicate equilibrium of coexistence between the two structures.

As outlined, the presence of both crystal phases in the same sample is a matter of study. Hence, to go deeper into this and have a semi-quantitative value of the

corresponding phase fractions in the sample, the XRD pattern of sample 1DA was refined using the Rietveld method. Further details can be found in Section S7.1 of the Supporting Information. The results revealed that sample 1DA is composed of, approximately, 69% of α -phase and 31% of δ -phase.

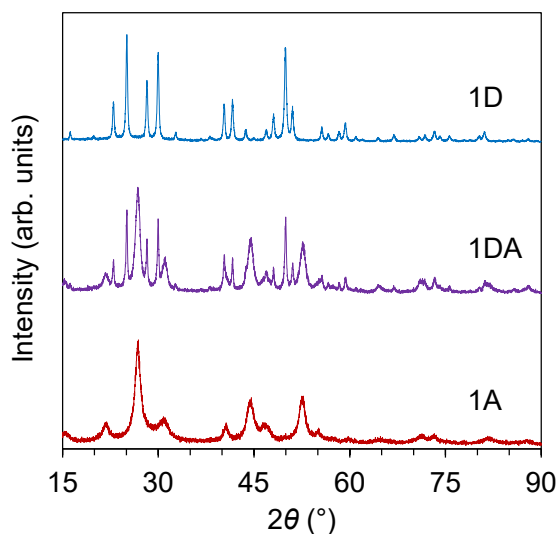


Figure 7.3. XRD patterns of samples doped with 1 mol% Eu^{3+} content.

In order to complement the structural characterization of the materials, FT-IR spectra of samples doped with 1 mol% Eu^{3+} content (i.e., 1D, 1DA, 1A) were recorded and are presented in **Figure S7.2** of the Supporting Information. The spectra showed the characteristic bands associated with the corresponding internal vibrations, and exhibited changes in the position and amplitude of the peaks depending on the different crystal phase(s). For the three compositions, the presence of absorbed/crystalline water was also noted.

To study the thermal behavior of the powders and also corroborate the existence of single/multiple crystal phase(s), simultaneous thermogravimetric analysis (TG) and differential scanning calorimetry (DSC) experiments were conducted for all the

samples. The TG/DSC curves are depicted in **Figure 7.4**, while the weight loss percentages and x values for $\text{KLn}_3\text{F}_{10}\cdot x\text{H}_2\text{O}$ ($\text{Ln} = \text{Y}, \text{Eu}$) compositions are summarized in **Table 7.3**. Each series of samples (i.e., compounds with δ , $\delta + \alpha$, and α crystal phases doped at different concentrations of Eu^{3+}) exhibited virtually the same thermal behavior. Powders with a $\delta\text{-KY}_3\text{F}_{10}\cdot x\text{H}_2\text{O}$ structure (1D, 3D, 5D) presented a progressive loss of mass associated with the crystalline water inside the channels and cavities of the crystal structure as well as with some absorbed water. According to these data, the number of water molecules in these compositions was established to be $x \approx 2.8$ (see **Table 7.3**). In addition, the absence of multiple/notable (endo/exo)thermic peaks in the temperature range 25–300 °C underscores the fact that there are no apparent traces of a possible $\delta\text{-(H}_3\text{O)Y}_3\text{F}_{10}\cdot x\text{H}_2\text{O}$ phase. The exothermic peak found at 418 °C is associated with the topotactic $\delta \rightarrow \alpha$ phase transition [14], which is in agreement with the above-mentioned stability of the α phase and the delicate equilibrium of possible coexistence between the two structures.

On the other hand, compounds with the $\alpha\text{-KY}_3\text{F}_{10}$ structure (1A, 3A, 5A) also presented a progressive loss of mass, although associated only with absorbed water rather than crystalline water, since this phase does not present any zeolitic cavities that allow the incorporation of crystalline water molecules inside the structure. This result is also corroborated by the lower percentage of weight loss in comparison to samples with the α -phase. Indeed, the number of water molecules in these compositions was established to be $x \approx 1.7$ (see **Table 7.3**). Besides, the TG/DSC results for samples with the coexistence of both crystal phases (1DA, 3DA, 5DA) are in direct connection with the FT-IR spectra (see Supporting Information for further details). The thermal behavior of these three compositions can be explained by considering an intermediate response between samples exhibiting a single δ - and α -phase. It is worthwhile pointing out that the weight loss percentage and the number of water molecules ($x \approx 1.7$) are

essentially the same as for samples with a single α -phase, which is in very good agreement with the results obtained from the Rietveld refinement that underline the prevalence of the α -phase. Therefore, this result confirms that there is a higher amount of this crystal phase, which is also in agreement with the position and amplitude of the FT-IR bands. Nonetheless, the presence of particles with a δ -phase can be well inferred from the DSC curve since the exothermic peak associated with the topotactic $\delta \rightarrow \alpha$ phase transition is also present, although with a smaller area and appearing at lower temperatures.

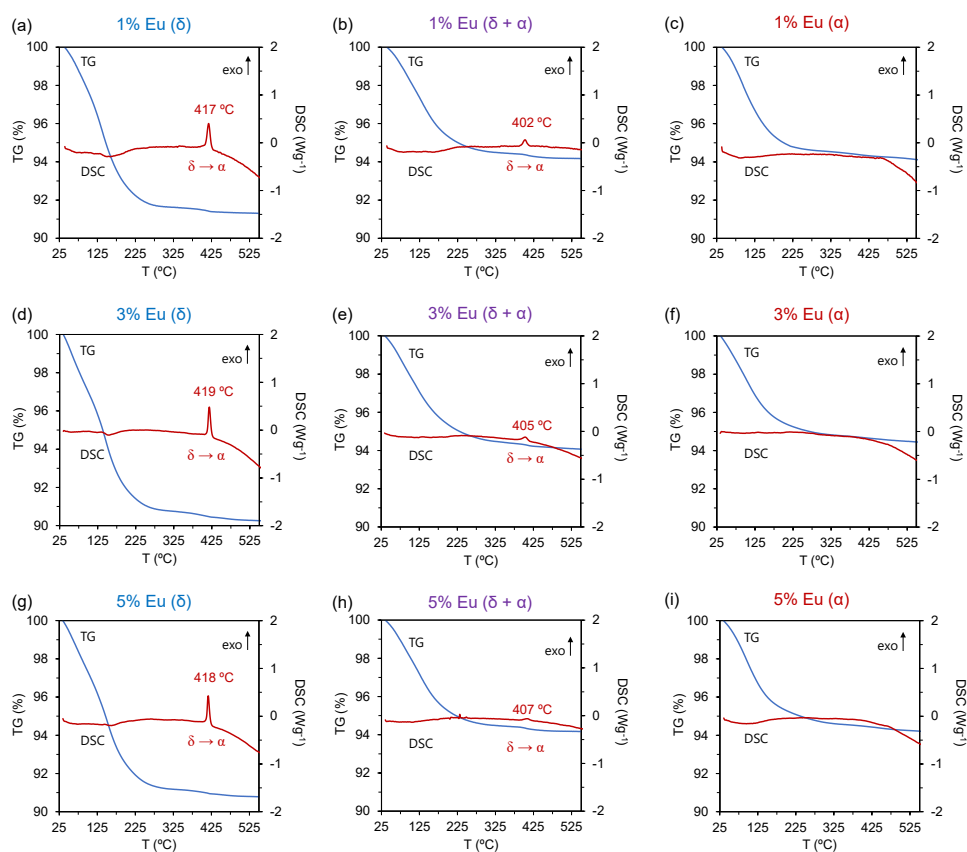


Figure 7.4. TG/DSC curves for samples 1D (a), 1DA (b), 1A (c); 3D (d), 3DA (e), 3A (f); 5D (g), 5DA (h), and 5A (i).

Table 7.3. Weight loss percentages and x values for $\text{KLn}_3\text{F}_{10}\cdot x\text{H}_2\text{O}$ ($\text{Ln} = \text{Y}, \text{Eu}$) compounds with 1 mol% Eu^{3+} content.

Sample	Weight loss (%)	x
1D	8.7	2.6
3D	9.7	3.0
5D	9.2	2.8
1DA	5.8	1.7
3DA	5.9	1.7
5DA	5.7	1.7
1A	5.9	1.7
3A	5.5	1.6
5A	5.8	1.7

7.3.2. Morphological characterization

The morphologies of the as-prepared products are illustrated in **Figure 7.5**. The SEM images correspond to samples 1D (δ), 1DA ($\delta + \alpha$), and 1A (α) as representatives of the different crystal phases. There were no appreciable morphological/size changes while increasing the dopant content in each series of samples. Powders with δ -phase exhibited a homogeneous distribution of spherical nanoparticles (between 160–190 nm). Interestingly, the higher magnification SEM image demonstrated the presence of self-assembled nanospheres around 40 nm in diameter, **Figure 7.5(a)**. Simultaneously, it is noteworthy that the new synthetic procedure herein described to prepare $\delta\text{-KY}_3\text{F}_{10}\cdot x\text{H}_2\text{O}$ compounds yields spherical particles, which can be of great interest for the development of core-shell type structures or further surface modifications/coatings. The previous method of synthesis developed by our laboratory to generate fluorides with this structure produced truncated triangular nanoplates that also formed aggregates in order to reduce the surface energy [15],

which are drawbacks that could prevent the possibility of making well-controlled and good surface engineering.

Regarding the compositions with a mixture of crystal phases – sample 1DA in **Figure 7.5(b)** – a significant change in the morphology was appreciated. The powder consists mainly of an amorphous-type matrix (highlighted in red) in which some nanospheres (highlighted in blue) are embedded. The major presence of the heterogeneous part is consistent with the previous XRD, FT-IR, and TG/DSC results since this predominant morphology might be well ascribed to the α -phase, while the nanospheres (some colored in blue as an example) correspond to the δ -phase particles. At first glance, this fact can be well corroborated by comparing **Figure 7.5(a)** and **Figure 7.5(b)**. The reason for the formation of the heterogeneous matrix is mainly due to the speed of the addition of the fluoride source (KF/HF solution) into the Ln^{3+} solution. For the latter case, a rapid addition was performed to produce the powders, while the dropwise addition used in the formation of $\delta\text{-KY}_3\text{F}_{10}\cdot x\text{H}_2\text{O}$ compounds explains the homogeneous and well-distributed nature of the nanospheres.

Finally, **Figure 7.5(c)** shows a typical SEM image of sample 1A (α -phase), which was prepared by an ultrasonication process. This sample consists of spherical particles (most of them around 400 nm) which resulted from the self-assembly of nano-sized subunits around 10–20 nm in diameter.

Furthermore, in order to get a better idea of the particle size distribution, Dynamic Light Scattering (DLS) size distribution measurements were recorded. The hydrodynamic diameters obtained were in very good agreement with the SEM results, **Figure S7.3** of the Supporting Information.

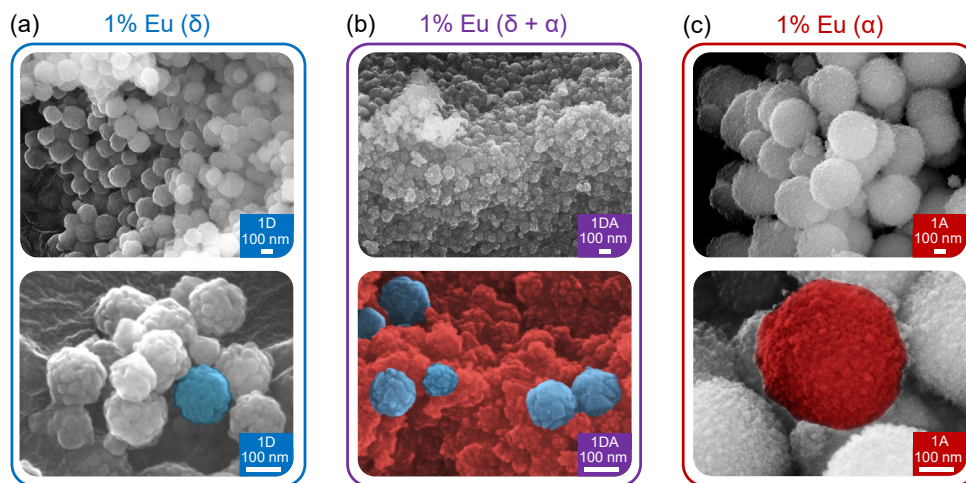


Figure 7.5. SEM images for samples 1D (a), 1DA (b), and 1A (c).

7.3.3. Site-selective time-resolved fluorescence line-narrowing spectroscopy

7.3.3.1. General grounds

The electronic energy levels of an isolated impurity in a solid are very sensitive to the positions of the nearby atoms. Since the frequency of a particular electronic transition of the impurity is directly proportional to the difference between the energies of the relevant pair of levels, it is clear that precise optical spectroscopy of the impurity can provide information about the positions and distribution symmetry of the impurity surrounding atoms in the host solid. However, the problem is far from simple. On the one hand, the electronic wave functions and the distances between the electronic levels of the chromophore depend on their environment and, on the other, in general, the electronic transitions also modify the distribution of vibrational states in the solid, which in turn can have an influence on electronic transitions. The case we are interested in concerns a substitutional rare-earth (RE) ion, used as a spectral probe, which interacts only weakly with its rigid host, so we expect the local environment to

affect only the electronic energy and not the normal mode vibrational frequencies. Thus, in the discussion that follows, we will only consider a single broadened vibrational line shape for all vibrational lines associated with a given electronic transition.

Our aim is to identify the possible crystal field (CF) symmetry distortions felt by the RE paramagnetic impurity embedded in the crystal lattice sites of the different phases of this fluoride nanocrystal, as well as to analyze the influence of the lattice distortions near the nanoparticle surface on the RE emission. Among trivalent lanthanide ions, Eu^{3+} is particularly attractive as a CF probe because of the relatively simple Stark structure of the ${}^7\text{F}_J$ and the ${}^5\text{D}_J$ states for $J = 0, 1, 2$. Moreover, excitation of Eu^{3+} fluorescence is possible at a low temperature between ${}^7\text{F}_0$ and ${}^5\text{D}_0$ singlet states. For this purpose, we have used a laser-induced site-selective time-resolved fluorescence line-narrowing technique (TRFLN). A tunable pulsed (9 ns pulse width) dye laser (0.08 cm^{-1} line width) was used as the excitation source and an optical multichannel analyzer with a gated intensified CCD detector to collect the time-resolved resonant and non-resonant ${}^5\text{D}_0 \rightarrow {}^7\text{F}_J$ emissions.

7.3.3.2. Interpretation of the TRFLN spectra

Although the fundamentals of the fluorescence line-narrowing (FLN) technique may seem simple, it is advisable to have a clear idea, from the theoretical point of view, about what interpretative complications may arise. Therefore, we are going to briefly comment on some basic aspects of the model that describes the absorption/emission processes. The aim is to use intense monochromatic laser irradiation to excite a subset of Eu^{3+} ions with nearly identical crystal strain shifts within a possible inhomogeneously broadened absorption profile. If the impurity centers exist in a distribution of environments, these spectra will be shifted with respect to each other

because the crystal host fields primarily affect the electronic transition energy. If the central electronic transition frequency for a given center is ν_0 , we can express the absorption spectrum summed for all the Eu^{3+} centers in the ensemble as

$$S(\nu) = \int D(\nu_0)A(\nu - \nu_0)d\nu_0 \quad (7.1)$$

where $A(\nu - \nu_0)$ is the intrinsic absorption spectrum shape of a center at the electronic transition frequency ν_0 and $D(\nu_0)$ is the distribution function that gives the probability that a center will have electronic transition energy ν_0 . If the sample is irradiated with a laser whose output spectrum is $\mathcal{L}(\nu - \nu_L)$, then the distribution of excited centers is given by

$$P(\nu_0) = D(\nu_0)A(\nu - \nu_0)\mathcal{L}(\nu - \nu_L) \quad (7.2)$$

and if the emission spectrum of the europium center with an electronic transition frequency ν_0 is given by $\mathcal{E}(\nu' - \nu_0)$, then the emission spectrum of the laser-irradiated fluoride crystal powder will be given by

$$S(\nu') \propto \iint D(\nu_0)A(\nu - \nu_0)\mathcal{L}(\nu - \nu_L)\mathcal{E}(\nu' - \nu_0)d\nu_0 d\nu \quad (7.3)$$

If the laser line width is very narrow, as compared to the inhomogeneously broadened absorption, the laser spectrum can be substituted by a delta function at ν_L and the above expression becomes

$$S(\nu') \propto \int D(\nu_0)A(\nu_L - \nu_0)\mathcal{E}(\nu' - \nu_0)d\nu_0 \quad (7.4)$$

Thus, the output spectrum is expressed as a convolution of both absorption and emission of a given distribution $D(\nu_0)$ of Eu^{3+} centers. It can be assumed that in the low-temperature limit the line shape for both absorption and emission of a single Eu^{3+}

center, with a very narrow strain distortion and interaction with a single phonon mode, can be described as the sum of a narrow zero-phonon line (Z) and a broad phonon wing (W) contribution weighted by a temperature-dependent Debye-Waller factor (F) [39,40].

$$S_{abs}(\nu - \nu_0) = (F)Z_{abs}(\nu - \nu_0) + (1 - F)W_{abs}(\nu - \nu_0) \quad (7.5)$$

$$S_{em}(\nu_0 - \nu) = (F)Z_{em}(\nu_0 - \nu) + (1 - F)W_{em}(\nu_0 - \nu) \quad (7.6)$$

When Eu^{3+} ions are pumped by spectrally narrow laser light of frequency ν_L , the distribution of the excited state centers is then given by

$$P(\nu_0) = D(\nu_0)\{FZ_{abs}(\nu_L - \nu_0) + (1 - F)W_{abs}(\nu_L - \nu_0)\} \quad (7.7)$$

Thus, in general, for a given $D(\nu_0)$ site distribution and temperature, by using expressions (7.4–7.7), we would have the output spectrum given by the sum of four contributions:

$$\begin{aligned} S(\nu) &= \int S_{em}(\nu_0 - \nu)P(\nu_0)d\nu_0 \\ &= F^2 \int D(\nu_0)Z_{abs}(\nu_L - \nu_0)Z_{em}(\nu_0 - \nu)d\nu_0 \\ &+ F[1 - F] \int D(\nu_0)Z_{abs}(\nu_L - \nu_0)W_{em}(\nu_0 - \nu)d\nu_0 \\ &+ F[1 - F] \int D(\nu_0)W_{abs}(\nu_L - \nu_0)Z_{em}(\nu_0 - \nu)d\nu_0 \\ &+ [1 - F]^2 \int D(\nu_0)W_{abs}(\nu_L - \nu_0)W_{em}(\nu_0 - \nu)d\nu_0 \end{aligned} \quad (7.8)$$

The first term corresponds to zero-phonon absorption followed by zero-phonon emission, the second refers to zero-phonon absorption followed by phonon wing emission, the third one gives the zero-phonon emission obtained under wing

absorption and, finally, the fourth term gives the phonon wing emission corresponding to phonon wing absorption. In our Eu-fluoride system, electron-phonon coupling seems to be weak because no phonon side band is observed under site-selective excitation at the 5D_0 level at low temperature. In addition, there is no evidence of spectral diffusion within the inhomogeneously broadened spectral profile, and so in the following discussion about the TRFLN experimental results, we will only pay attention to the first and third terms in (7.8), which account for experimentally found narrowed electronic emissions of the Eu^{3+} centers in the fluoride nanocrystals.

7.3.3.3. *Experimental results and discussion*

Figure 7.6(a) shows the $^5D_0 \rightarrow ^7F_{0,1,2}$ emission spectrum of sample 1D (1 mol% Eu^{3+} -doped δ -phase of KY_3F_{10}) obtained at 10 μs after a 578.7 nm pump pulse corresponding to the $^7F_0 \rightarrow ^5D_0$ transition. The most intense emission comes from the first component of the $^5D_0 \rightarrow ^7F_2$ emission containing at least four components. The spectral features still remain if the laser wavelength is tuned a few angstroms at both sides of the $^7F_0 \rightarrow ^5D_0$ transition but the intensity drops very quickly. The magnetic dipole and allowed $^5D_0 \rightarrow ^7F_1$ emission is much less intense, showing three spectral components that could correspond to a site with point symmetry C_{2v} , the one found by XRD for the Y^{3+} ion in this phase. On the other hand, the resonant $^5D_0 \rightarrow ^7F_0$ emission is barely visible. No changes in the shape of the spectral components are observed by changing the delay time at which the detector starts measuring (0–13 ms). All the experiments were performed at 9 K.

Figure 7.6(b) displays the $^5D_0 \rightarrow ^7F_{0,1,2}$ emission spectrum of sample 1A (1 mol% Eu^{3+} -doped α -phase of KY_3F_{10}) obtained under resonant $^7F_0 \rightarrow ^5D_0$ excitation with a 578.8 nm pulse. The intensity of the emission is more than an order of magnitude less than in the δ phase. Moreover, the intensities of both $^5D_0 \rightarrow ^7F_1$ and $^5D_0 \rightarrow ^7F_2$ transitions

are similar. However, in this case, the ${}^5D_0 \rightarrow {}^7F_1$ emission presents only two spectral components pointing to a higher site symmetry for the europium ion. In fact, this point symmetry would correspond to the C_{4v} point group [41,42] that has been found for Y^{3+} ions by XRD in the α -phase. As can be observed in these figures, from an energetic point of view, the emission efficiency of the δ phase is much higher (> 20 times) than the α one for all the spectral components. This behavior may be related to an increase in the radiative probability associated with the site symmetry distortion of the fluorine ligand crystal field in the δ -phase.

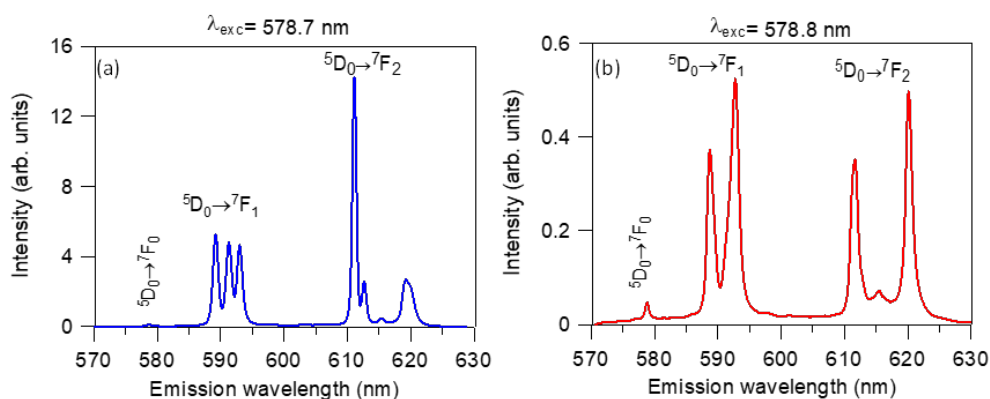


Figure 7.6. Low temperature (9 K) TRFLN emission spectra of the ${}^5D_0 \rightarrow {}^7F_{0,1,2}$ transitions for the samples (a) 1D, Eu^{3+} 1%- δ , and (b) 1A, Eu^{3+} 1%- α , obtained under excitation at 578.7 nm and 578.8 nm respectively in the ${}^7F_0 \rightarrow {}^5D_0$ transition.

The above low-temperature TRFLN results identify the energy of the 5D_0 singlet state of the Eu^{3+} in both phases in the main crystal site occupied by the rare earth (Y^{3+} site) as well as its narrowed emissions from the excited 5D_0 level. However, given the size of the crystalline nanoparticles, we expect a significant number of Eu^{3+} ions to lie at sites near the surface, where distortions of the crystal lattice can produce variable crystal fields at europium sites similar to those produced in a messy medium, like a glass. To investigate this issue, the laser tuning feature of our TRFLN spectroscopy

was used. Although the previous experiments conducted to identify the main crystal site of Eu^{3+} were obtained with 1 mol% Eu-doped samples, no significant spectral changes were observed for both lower and higher concentrations of rare earth. Therefore, in order to increase our spectral resolution, given the expected smaller TRFLN signals, in the following experiments we have used 3 mol% Eu^{3+} doped samples for both the α and δ phases.

Taking into account the theoretical predictions of expression (7.8) for the output spectrum of FLN spectroscopy in the presence of a given $D(\nu_0)$ distribution of chromophore sites in a crystalline matrix, we have performed additional experiments scanning the laser wavelength over a wide range of energies both above and below that corresponding to the main crystal field site found in both phases. The results are displayed in **Figures 7.7, 7.8, and 7.9** for δ , α , and ($\delta + \alpha$) phases, respectively.

i) δ phase: **Figure 7.7** displays a set of twelve selected spectra in the range 570–630 nm corresponding to the resonant and non-resonant emissions ${}^5\text{D}_0 \rightarrow {}^7\text{F}_{0,1,2}$. It is worth mentioning that the vertical scale gives the relative intensity of the measured spectra. As the pumping energy increases above the maximum of the ${}^7\text{F}_0 \rightarrow {}^5\text{D}_0$ electronic transition of the main Eu^{3+} site ($\lambda_{\text{ex}} = 578.7$ nm), the Eu^{3+} emission falls 85% in two angstroms, then both ${}^5\text{D}_0 \rightarrow {}^7\text{F}_{1,2}$ emissions broaden and their profiles (see $\lambda_{\text{ex}} = 578.0$ nm spectrum) are similar to those found by some authors in Eu-doped fluorophosphate glass [43]. This behavior indicates the presence of a quasi-continuous distribution of crystalline fields associated with europium ions in environments where the crystalline lattice is distorted by the presence of surface or subsurface defects that can produce variations in coordination and/or lengths and orientation of the bonds with the rare earth.

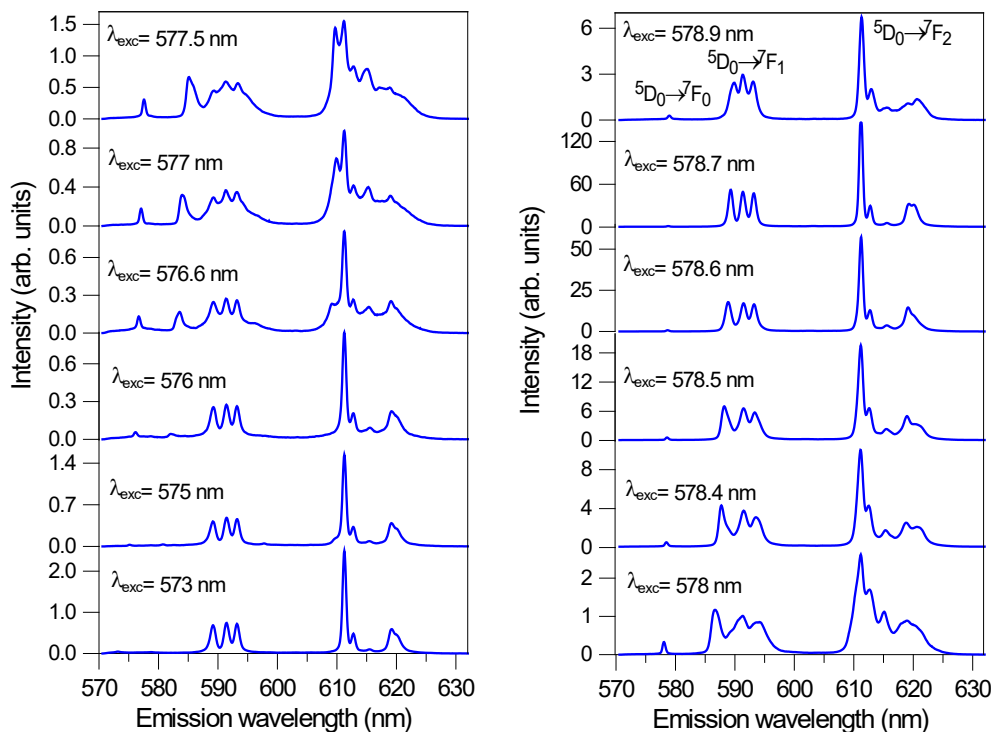


Figure 7.7. Low temperature (9 K) TRFLN emission spectra of the ${}^5D_0 \rightarrow {}^7F_{0,1,2}$ transitions for sample 3D (Eu^{3+} 3% $-\delta$) obtained at different excitation wavelengths along the ${}^7F_0 \rightarrow {}^5D_0$ transition.

If we continue exciting at higher energies (see $\lambda_{\text{ex}} = 577.5\text{--}576.6$ nm spectral range), the spectrum widens even more and in the ${}^5D_0 \rightarrow {}^7F_1$ emission profile more than the three predictable spectral components of a low symmetry site appear. By increasing the excitation energy a little more, we see, with apparent surprise, that the spectral structure of the main europium crystal site reappears and the emission energy slightly increases. The explanation for this is given by the third term of expression (7.8) mentioned above. Now the narrowed emission from 5D_0 is produced by absorption to a vibronic state in the phonon wind. In this case, the electron-phonon process consists of an electronic transition to the 5D_0 level of the Eu^{3+} occupying the main site, assisted by the emission of a low-energy phonon to the crystal lattice. As a two-body process, the probability of this kind of process is smaller than that of a direct electron

transition, as the measured intensity shows. Furthermore, although we have excited in the phonon sideband, the spectral response is the one that corresponds to the only site present in the bulk crystalline structure. If this were not the case, we could have had a spectral broadening associated with the distribution of the different crystal sites.

ii) α phase: presents a similar spectral behavior but with some differences in the spectral width and shape of the spectra. **Figure 7.8** displays a sample of the spectra obtained by scanning the laser wavelength in the range 579–573 nm.

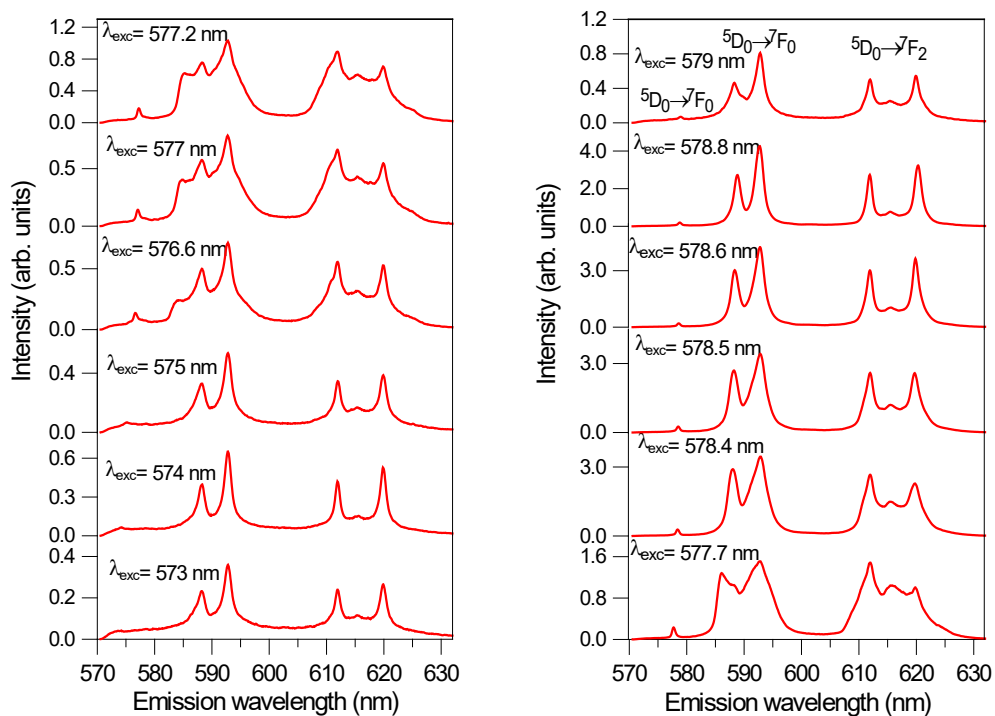


Figure 7.8. Low temperature (9 K) TRFLN emission spectra of the $^5D_0 \rightarrow ^7F_{0,1,2}$ transitions for sample 3A (Eu^{3+} 3%- α) obtained at different excitation wavelengths along the $^7F_0 \rightarrow ^5D_0$ transition.

If we decrease the excitation wavelength by more than two angstroms below that of the main Eu^{3+} site ($\lambda_{\text{ex}} = 578.8$ nm), the shape of the spectrum widens and begins to change, clearly showing a reduction in point symmetry (C_{2v} or less). An additional

component appears in the ${}^5D_0 \rightarrow {}^7F_1$ transition, and the ${}^5D_0 \rightarrow {}^7F_2$ components take on a glass-like appearance (see $\lambda_{\text{exc}} = 577.7\text{--}576.6$ nm spectral range). Then, around $\lambda_{\text{exc}} = 575$ nm, the spectral profile of the tetragonal main site of Eu^{3+} in this crystalline phase reappears again, helped, as in the δ phase, by the vibronic sideband.

iii) ($\delta + \alpha$) phases: **Figure 7.9** shows the spectral results for the 3DA (3 mol%- Eu^{3+} doped phase) mixed sample. As we can see, the best spectral resolution for both α and δ phases is obtained by exciting at 579.0 and 578.7 nm respectively.

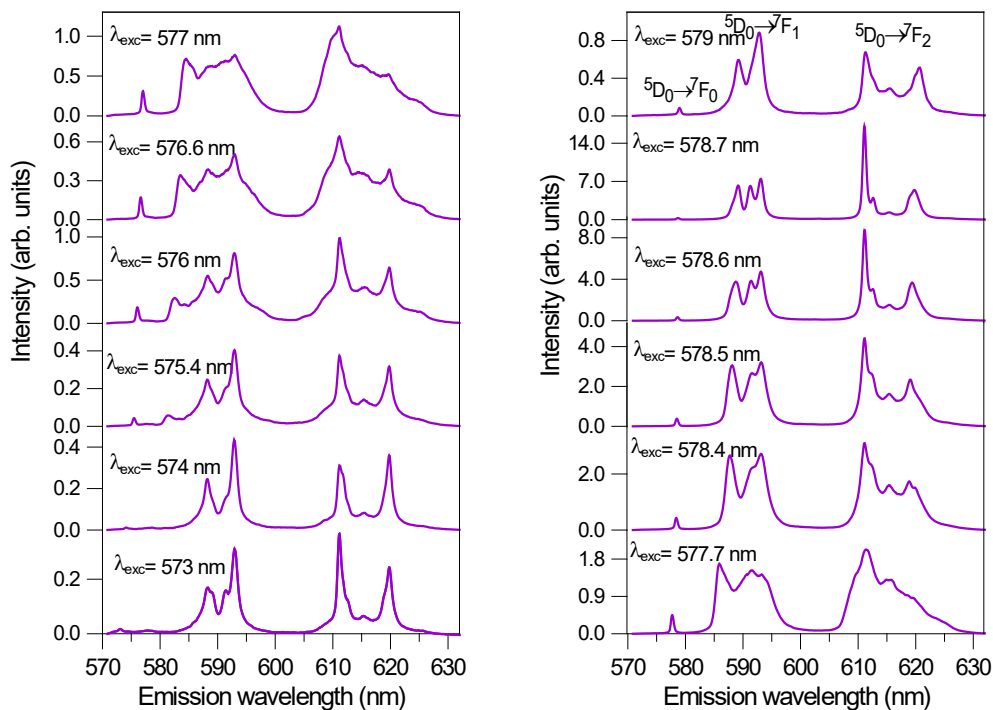


Figure 7.9. Low temperature (9 K) TRFLN emission spectra of the ${}^5D_0 \rightarrow {}^7F_{0,1,2}$ transitions for sample 3DA (Eu^{3+} 3%-($\delta + \alpha$)) obtained at different excitation wavelengths along the ${}^7F_0 \rightarrow {}^5D_0$ transition.

However, the efficiency of the δ phase drops when compared to the sample with only the δ phase. If we compare the relative intensity of the Eu^{3+} emission in α and δ single phase samples with that of the ($\delta + \alpha$) sample, we come to the conclusion that

in the sample with both ($\delta + \alpha$) phases the amount of α phase is around twice that of δ . This hypothesis is further confirmed by the emission spectrum obtained by exciting at the high energy vibronic side $\lambda_{\text{exc}} = 574$ nm. We can see that the only crystal site present is the one corresponding to the α phase. For intermediate excitation wavelengths, the ordinary glass-like behavior with higher influence of the α phase is found (see $\lambda_{\text{exc}} = 578.5\text{--}575.4$ nm spectral range). This result is also in perfect agreement with the phase fraction estimation obtained by the Rietveld refinement.

The lifetimes of the $^5\text{D}_0$ level of Eu^{3+} should reflect the different site symmetry for Eu^{3+} ions in the different phases. The experimental decays of the $^5\text{D}_0$ level were obtained for all samples at room temperature by exciting at 392.5 nm in the $^7\text{F}_0 \rightarrow ^5\text{L}_6$ transition and collecting the luminescence at 612 nm ($^5\text{D}_0 \rightarrow ^7\text{F}_2$). The decays are well described by a single exponential function for all Eu^{3+} concentrations in the different crystalline phases. As an example, **Figure 7.10** shows the decays for the samples 1D (Eu^{3+} 1% $-\delta$), 1A (Eu^{3+} 1% $-\alpha$), and 1DA (Eu^{3+} 1% $-\delta+\alpha$).

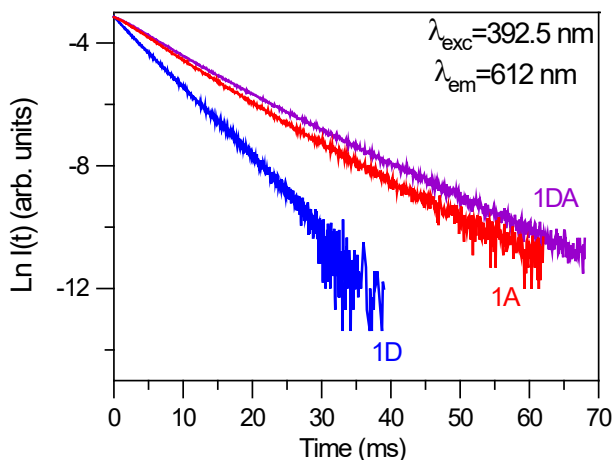


Figure 7.10. Semilogarithmic plot of the fluorescence decays of the $^5\text{D}_0$ level obtained under excitation at 392.5 nm and collecting the luminescence at 612 nm for the samples 1D (Eu^{3+} 1% $-\delta$), 1A (Eu^{3+} 1% $-\alpha$), and 1DA (Eu^{3+} 1% $-\delta+\alpha$).

As can be seen in **Table 7.4**, the lifetime values are shorter in the case of the delta phase, which agrees well with the lower site symmetry for the Eu^{3+} ions in this phase and the more electric-dipole character shown by the ${}^5\text{D}_0 \rightarrow {}^7\text{F}_2$ transition. The lifetimes of the α and ($\delta + \alpha$) phases are similar, which agrees with the results found in the TRFLN spectra.

Table 7.4. Lifetimes of the ${}^5\text{D}_0$ level obtained by exciting at 392.5 nm in the ${}^7\text{F}_0 \rightarrow {}^5\text{L}_6$ transition and collecting the luminescence at 612 nm. The coefficient of determination R^2 is also included.

% Eu^{3+}	Lifetime (ms)					
	δ	R^2	α	R^2	$\delta + \alpha$	R^2
1	4.28	0.9993	7.01	0.9996	7.79	0.9995
3	4.00	0.9997	6.16	0.9998	7.23	0.9993
5	3.69	0.9996	5.08	0.9992	6.20	0.9994

As a final comment, we would like to stress the *finesse* of TRFLN spectroscopy to detect small local crystal field variations. In our case, despite the small energy difference between the positions of the ${}^5\text{D}_0$ singlet level in both δ and α phases (0.0004 eV), it is possible not only to clearly discern the different symmetries of the main site that the rare earth occupies in the crystalline matrix but also to determine what kind of contributions in rare earth emission come from site distribution peripherals occupied by the chromophore. In the latter case, although these contributions may be small, the spectral information can be decisive when it comes to applications related to the functionalization of the nanoparticle surface. On the other hand, the top-notch optical performance of the $\delta\text{-KY}_3\text{F}_{10}\text{:Eu}^{3+}$ materials and the high chemical and thermal stability (from cryogenic up to 400 °C) make them of high interest in several photonic fields. Coupling/functionalizing these compounds with other lanthanides opens up a

vast spectrum for their application in sensing and nanothermometry (for example by using the $\text{Eu}^{3+}/\text{Tb}^{3+}$ pair), or in solid-state lighting devices (combining the yellow-orangish emission of the samples with blue InGaN chips to fabricate w-LEDs).

7.4. Conclusions

The crystallographic nature and spectroscopic features concerning the site-selective symmetries in Eu^{3+} -doped KY_3F_{10} compounds with α and δ crystal phases have been investigated in detail by TRFLN spectroscopy. For that purpose, samples containing different amounts of the luminescent Eu^{3+} ion (1, 3, 5 mol%) were synthesized yielding powders with single δ -phase, single α -phase, and a mixture of both phases. The results obtained lead to the following main conclusions:

- A new, fast, and easy coprecipitation method is developed to prepare the δ -phase compounds yielding spherical particles. This strategy represents a remarkable improvement in comparison to the existing synthesis for this structure.
- The XRD results are well corroborated with the morphological, FT-IR, DLS, and TG/DSC analyses. Samples containing the mixture ($\delta + \alpha$) exhibited a behavior very close to that of samples with the α -phase, thus suggesting the predominance of this phase in the mixture, which is supported by the estimated phase fractions obtained from the Rietveld refinement.
- TRFLN experiments confirm the existence of Eu^{3+} ions in the expected crystallographic symmetries (C_{2v} in δ , and C_{4v} in α). The laser tuning facility of this technique has made it possible to discriminate the presence of europium ions lying at low-symmetry sites near the surface of the crystalline nanoparticles, with an optical response similar to that produced in glasses.

- The lifetime values agree well with the different site symmetries for the Eu^{3+} ions and the electric-dipole character of the ${}^5\text{D}_0 \rightarrow {}^7\text{F}_2$ transition.
- From an energetic point of view, the emission efficiency of the δ phase is much higher (> 20 times) than the α one for all the spectral components in the TRFLN measurements, which is a point worthy of praise.

As per the above points, the results underscore the huge potential of the unknown δ -phase and the importance of using very precise spectroscopic techniques, as is the case of TRFLN, to shed light on the comprehension of the optical response of the luminescent dopants, which is a matter of concern when developing photonic materials for top-notch applications.

Acknowledgments

This work was supported financially by the Spanish MCIN (Grant PID2020-116149GB-I00 and PID2020-115419GB/C-22 funded by MCIN/AEI/10.13039/501100011033) and the University of the Basque Country (GIU21/006). P. Serna also thanks the Spanish MCIN for an FPU predoctoral contract (FPU18/04511 funded by MCIN/AEI /10.13039/501100011033 and by “ESF Investing in your future”).

References

- [1] J. Wu, J. Wang, J. Lin, Y. Xiao, G. Yue, M. Huang, Z. Lan, Y. Huang, L. Fan, S. Yin, T. Sato, *Scientific Reports*. 3 (2013) 1–5.
- [2] B.M. Tissue, *Chemistry of Materials*. 10 (1998) 2837–2845.
- [3] T. Grzyb, M. Węclawiak, T. Pędziński, S. Lis, *Optical Materials*. 35 (2013)

2226–2233.

- [4] A. Podhorodecki, A. Noculak, M. Banski, B. Sojka, A. Zelazo, J. Misiewicz, J. Cichos, M. Karbowski, B. Zasonska, D. Horak, B. Sikora, D. Elbaum, T. Dumych, R. Bilyy, M. Szewczyk, *ECS Transactions*. 61 (2014) 115–125.
- [5] A. Jain, P.G.J. Fournier, V. Mendoza-Lavaniegos, P. Sengar, F.M. Guerra-Olvera, E. Iñiguez, T.G. Kretzschmar, G.A. Hirata, P. Juárez, *Journal of Nanobiotechnology*. 16 (2018) 1–18.
- [6] J. Periša, J. Papan, S.D. Dolić, D.J. Jovanović, M.D. Dramićanin, *Dyes and Pigments*. 155 (2018) 233–240.
- [7] C. Sassoie, G. Patriarche, M. Mortier, *Optical Materials*. 31 (2009) 1177–1183.
- [8] F. Auzel, *Chemical Reviews*. 104 (2004) 139–173.
- [9] L. Zhu, J. Meng, X. Cao, *Materials Letters*. 62 (2008) 3007–3009.
- [10] C. Cao, *Journal of Materials Research Society*. 27 (2012) 2988–2995.
- [11] S. Goderski, M. Runowski, S. Lis, *Journal of Rare Earths*. 34 (2016) 808–813.
- [12] M. Runowski, *Journal of Luminescence*. 186 (2017) 199–204.
- [13] M. Chen, P. Loiko, J.M. Serres, S. Veronesi, M. Tonelli, M. Aguiló, F. Díaz, S.Y. Choi, J.E. Bae, F. Rotermund, S. Dai, Z. Chen, U. Griebner, V. Petrov, X. Mateos, *Journal of Alloys and Compounds*. 813 (2020) 152176.
- [14] F. Le Berre, E. Boucher, M. Allain, G. Courbion, *Journal of Materials Chemistry*. 10 (2000) 2578–2586.
- [15] P. Serna-Gallén, H. Beltrán-Mir, E. Cordoncillo, *Journal of Materials Research and Technology*. 15 (2021) 6940–6946.

- [16] P. Serna-Gallén, H. Beltrán-Mir, E. Cordoncillo, *Ultrasonics Sonochemistry*. 87 (2022) 106059.
- [17] P. Villars, K. Cenzual, eds., KY_3F_{10} Crystal Structure: Datasheet from “PAULING FILE Multinaries Edition – 2012” in Springer Materials (https://materials.springer.com/isp/crystallographic/docs/sd_0552093).
- [18] P. Villars, K. Cenzual, eds., δ - $KY_3F_{10} \cdot xH_2O$ ($KY_3F_{10}[H_2O]$) Crystal Structure: Datasheet from “PAULING FILE Multinaries Edition – 2012” in Springer Materials (https://materials.springer.com/isp/crystallographic/docs/sd_1004004).
- [19] K. Momma, F. Izumi, *Journal of Applied Crystallography*. 44 (2011) 1272–1276.
- [20] P.P. Fedorov, M.N. Mayakova, S. V. Kuznetsov, V. V. Voronov, R.P. Ermakov, K.S. Samarina, A.I. Popov, V. V. Osiko, *Materials Research Bulletin*. 47 (2012) 1794–1799.
- [21] B.E.G. Lucier, K.E. Johnston, D.C. Arnold, J.L. Lemyre, A. Beaupré, M. Blanchette, A.M. Ritcey, R.W. Schurko, *Journal of Physical Chemistry C*. 118 (2014) 1213–1228.
- [22] C. Caron, D. Boudreau, A.M. Ritcey, *Journal of Materials Chemistry C*. 3 (2015) 9955–9963.
- [23] B. Richard, J.L. Lemyre, A.M. Ritcey, *Langmuir*. 33 (2017) 4748–4757.
- [24] O. V. Andreev, I.A. Razumkova, A.N. Boiko, *Journal of Fluorine Chemistry*. 207 (2018) 77–83.
- [25] D. Das, S.K. Gupta, K. Sudarshan, *Journal of Materials Science*. 56 (2021) 17205–17220.

- [26] T.N.L. Tran, A. Chiasera, A. Lukowiak, M. Ferrari, *Materials*. 15 (2022) 1–11.
- [27] F. Ariese, A.N. Bader, C. Gooijer, *TrAC - Trends in Analytical Chemistry*. 27 (2008) 127–138.
- [28] A. Szabo, *Physical Review Letters*. 25 (1970) 924–926.
- [29] M. Reppert, V. Naibo, R. Jankowiak, *Journal of Chemical Physics*. 133 (2010) 014506.
- [30] T. Vo-Dinh, N.H. Velthorst, D.S. Moore, B. Schrader, *Pure and Applied Chemistry*. 69 (1997) 1435–1449.
- [31] L.A. Riseberg, *Physical Review Letters*. 28 (1972) 786–789.
- [32] J.A. Capobianco, P. Proulx, B. Andrianasolo, B. Champagnon, *Physical Review B - Condensed Matter and Materials Physics*. 43 (1991) 10031–10035.
- [33] J. Fidy, M. Laberge, A.D. Kaposi, J.M. Vanderkooi, *Biochimica et Biophysica Acta - Protein Structure and Molecular Enzymology*. 1386 (1998) 331–351.
- [34] L.A. Riseberg, *Physical Review A*. 7 (1973) 671–678.
- [35] V.P. Tuyen, T. Hayakawa, M. Nogami, J.R. Ducre, P. Thomas, *Journal of Solid State Chemistry*. 183 (2010) 2714–2719.
- [36] Y. Huang, H.J. Seo, *Journal of Physical Chemistry A*. 113 (2009) 5317–5323.
- [37] Y. Huang, L. Shi, E.S. Kim, H.J. Seo, *Journal of Applied Physics*. 105 (2009) 013512.
- [38] P. Serna-Gallén, H. Beltrán-Mir, E. Cordoncillo, *Optics and Laser Technology*. 136 (2021) 106734.

- [39] I.S. Osad'ko, Selective spectroscopy of chromophore doped polymers and glasses, in: *Advances in Polymer Science*, Springer, Berlin, Heidelberg, 1994: pp. 122–186.
- [40] I.I. Abram, R.A. Auerbach, R.R. Birge, B.E. Kohler, J.M. Stevenson, *The Journal of Chemical Physics*. 63 (1975) 2473–2478.
- [41] P.A. Tanner, *Chemical Society Reviews*. 42 (2013) 5090–5101.
- [42] K. Binnemans, *Coordination Chemistry Reviews*. 295 (2015) 1–45.
- [43] R. Balda, J. Fernández, J. Adam, *Physical Review B - Condensed Matter and Materials Physics*. 54 (1996) 12076–12086.

S7. Supporting Information

S7.1. Rietveld Refinement

The experimental powder X-ray diffraction pattern of sample 1DA was refined using the Rietveld method by means of GSAS software. A Pseudo-Voight function was used to simulate the peak shape and the log-interpolate function with ten coefficients was used to simulate the background. The Rietveld refinement graphic is depicted in **Figure S7.1**, while the refined parameters (including the percentage of phase fraction) are included in **Table S7.1** and **Table S7.2**.

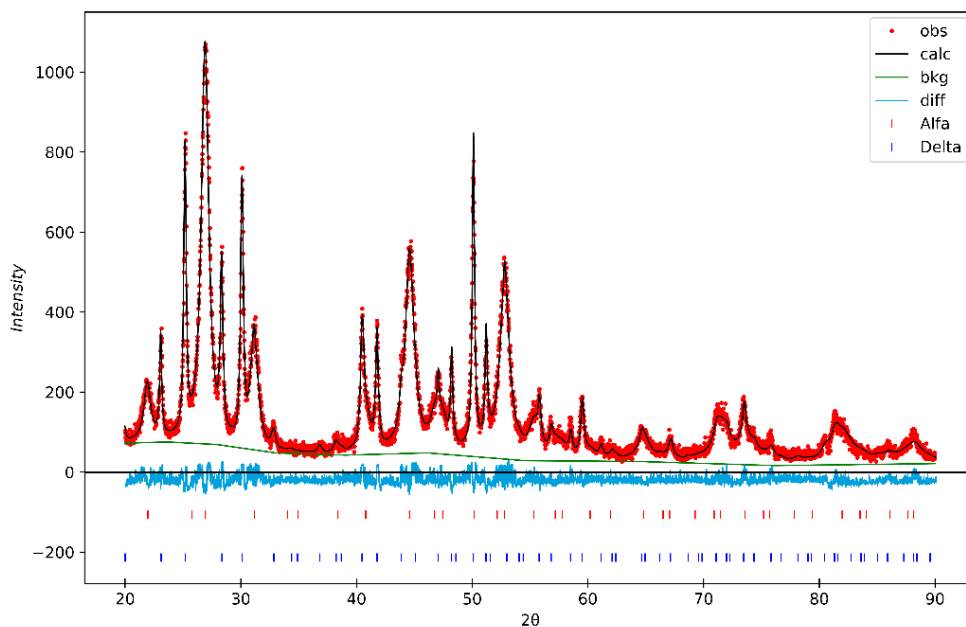


Figure S7.1. Rietveld refinement of sample 1DA, containing both α - KY_3F_{10} and δ - $\text{KY}_3\text{F}_{10}\cdot x\text{H}_2\text{O}$ crystal phases. $\chi^2 = 1.51$.

Table S7.1. Refined unit cell parameters for the XRD pattern of sample 1DA, containing both α -KY₃F₁₀ and δ -KY₃F₁₀·xH₂O crystal phases. $\chi^2 = 1.51$.

Crystal Phase	$a = b = c$ (Å)	V_{cell} (Å ³)	Phase Fraction (%)
α -KY ₃ F ₁₀	11.5231(8)	1530.1(7)	69
δ -KY ₃ F ₁₀ ·xH ₂ O	15.4831(7)	3711.7(5)	31

Table S7.2. Refined atomic positions for the XRD pattern of sample 1DA, containing both α -KY₃F₁₀ and δ -KY₃F₁₀·xH₂O crystal phases. $\chi^2 = 1.51$.

Crystal Phase	Name	Species	Wyckoff Position	Atomic Coordinates			U_{iso}
				x	y	z	
α -KY ₃ F ₁₀	K	K ⁺	8c	1/4	1/4	1/4	0.0270
	Y	Y ³⁺	24e	0.2398(8)	0	0	0.0119
	F1	F ⁻	32f	0.1113(7)	0.1113(7)	0.1113(7)	0.0109
	F2	F ⁻	48i	1/2	0.1633(5)	0.1633(5)	0.0288
δ -KY ₃ F ₁₀ ·xH ₂ O	K'	K ⁺	16c	0	0	0	0.0204
	Y'	Y ³⁺	48f	0.4465(2)	1/8	1/8	0.0105
	F1'	F ⁻	96h	0	0.3727(6)	0.6273(4)	0.0201
	F2'	F ⁻	32e	0.2866(7)	0.2866(7)	0.2866(7)	0.0112
	F3'	F ⁻	32e	0.4485(8)	0.4485(8)	0.4485(8)	0.0147
	O'	H ₂ O	48f	0.2462(9)	1/8	1/8	0.0116

S7.2. Structural Characterization

Figure S7.2 shows the FT-IR spectra of samples 1D (δ), 1DA ($\delta + \alpha$), and 1A (α) as an example of the different crystal phases. The broad, weak bands at ≈ 3100 – 3500 cm⁻¹ and ≈ 1640 cm⁻¹ are assigned to the O–H stretching vibrations and H–O–H bending mode of H₂O molecules, respectively. This indicates the presence of some absorbed

water in the materials. In sample 1D, a notable difference is appreciated in the stretching and bending vibrational modes of H₂O molecules, since they are associated with crystalline water molecules localized in the channels of the δ -KY₃F₁₀·xH₂O host lattice. These bands are sharper and stronger. For all the samples, the Y–F host lattice vibrations were observed below 600 cm⁻¹. On the other hand, the FT-IR spectrum of sample 1DA can be interpreted as a combination of the spectra of samples 1D and 1A, which is very good agreement with the results of XRD and the coexistence of δ and α crystal phases in the same sample. It is observed a major response from the response of the α -phase (see indeed the Y–F host lattice vibrations), a fact that suggests that there is a higher amount of this crystal phase.

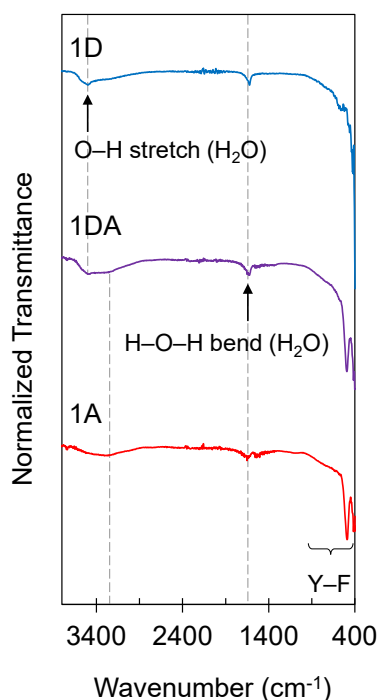


Figure S7.2. FT-IR spectra of samples doped with 1 mol% Eu³⁺ content. The dashed lines serve as guidelines to observe the change in the position and amplitude of the peaks depending on the different crystal phase(s).

S7.3. DLS measurements

Figure S7.3 shows the particle size distribution of samples doped with 1 mol% Eu^{3+} content. For the DLS measurements, the powder concentration was 1 mg/mL in distilled water. Sample 1DA ($\alpha + \delta$) was previously filtered using a 0.4 μm cellulose filter to eliminate the agglomerates corresponding to the α -phase. Otherwise, neither a good dispersion nor good data from the DLS measurements could be obtained. The maximum peak for sample 1DA-filtered was found at 195 nm (mainly due to the δ -phase nanospheres), which is quite close to the value obtained for sample 1D (δ -phase), 175 nm. The obtained hydrodynamic diameters were in very good agreement with the SEM results.

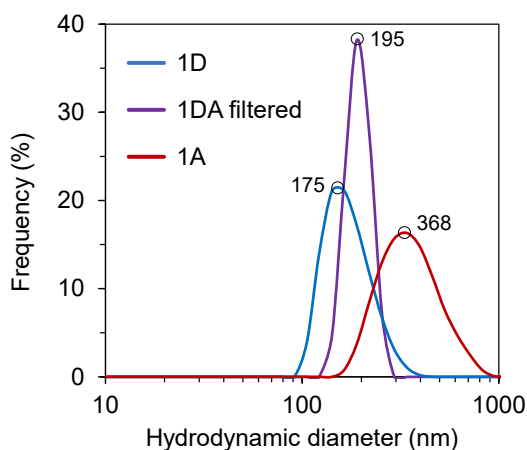
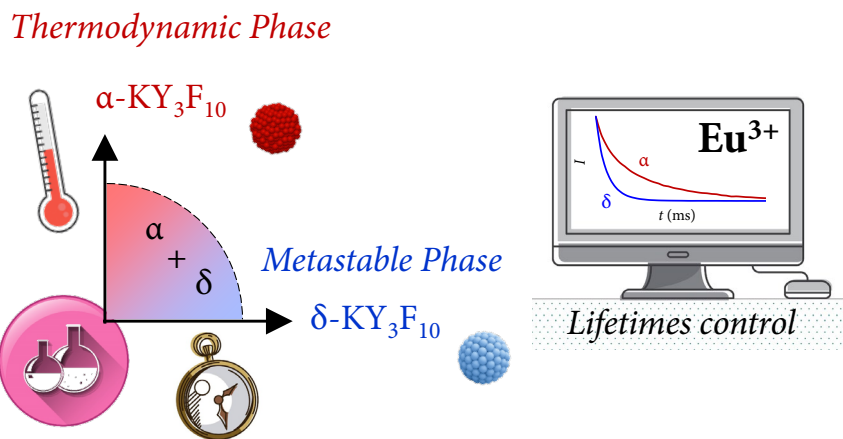


Figure S7.3. Particle size distribution of samples doped with 1 mol% Eu^{3+} content. Sample 1DA was previously filtered using a 0.4 μm cellulose filter to eliminate the agglomerates.

Chapter 8

Kinetics or thermodynamics? Extolling their role to modulate the crystal phases and luminescence of $\text{KY}_3\text{F}_{10}:\text{Eu}^{3+}$ powders



Article 6

CrystEngComm, 25 (2023) 5918–5931

Kinetics or thermodynamics? Extolling their role to modulate the crystal phases and luminescence of KY₃F₁₀:Eu³⁺ powders

Pablo Serna-Gallén, Héctor Beltrán-Mir, Eloísa Cordoncillo

Departamento de Química Inorgánica y Orgánica, Universitat Jaume I, Av. Vicent Sos Baynat s/n 12071, Castelló de la Plana, Spain

Journal Impact Factor: 3.1

Quartile: Q1

Category: Crystallography

Position: 6/26

Abstract

KY₃F₁₀, a fluoride compound with two polymorphs (α and δ), has been a subject of study due to its unique properties. Obtaining the metastable δ -phase has been challenging, but this study presents an enhanced synthetic methodology using coprecipitation to isolate specific crystal phases. Varying the reaction temperature and time allows for the modulation of polymorph formation. The structural analysis of the synthesized powders reveals the influence of kinetic and thermodynamic control. The morphology of the particles is also affected by these factors, with different reaction conditions leading to distinct particle shapes. The luminescent response of Eu³⁺-doped powders helps understand the structural stability. It is demonstrated that time-resolved fluorescence spectroscopy is a sensitive and direct measurement to follow the observed changes. Overall, this study demonstrates the interplay between thermodynamics and kinetics in materials synthesis and the impact on crystal phase formation and properties.

Keywords: Fluoride; Crystal Phase, Kinetics, Thermodynamics; Europium; Luminescence

8.1. Introduction

When it comes to materials synthesis, the corresponding thermodynamic phase diagram should be used as a starting point to yield the most stable product. However, it is not difficult to find some crystal phases that, although predicted as thermodynamically stable, cannot be synthesized experimentally and, instead of them, metastable phases are formed [1–3]. This fact evinces the competitive nature between the thermodynamic and the kinetic factors.

Thermodynamics is the cornerstone of materials and solids engineering because it helps us to study, predict, and explain the existence of different crystal phases, their range of stabilities, and their physicochemical properties [4]. On the other hand, the kinetics of a given chemical system involves the study of the concentration of reagents, reaction medium, pressure, temperature, catalysts, etc. that affect the reaction time or the formation of a specific product to the detriment of others. Given that, designing new synthetic approaches becomes a powerful strategy to tune the reaction pathways and thus the formation of the final product. Commonly, kinetic/metastable products (which are less stable thermodynamically) are favored under reaction conditions of low temperatures [5]. In contrast, high temperatures or pressures facilitate stabilizing thermodynamic products [6,7].

In materials science, the controlled synthesis of polymorphs (i.e., compounds with the same chemical formula but different crystal phases) has attracted significant interest because it opens up a plethora of possibilities regarding the functionalization and applications of solid materials [8,9]. However, understanding the involved crystal phase transformations is still a challenge in some compounds [10,11].

In that sense, the KY_3F_{10} host lattice emerges as a fluoride that deserves special attention. This compound presents two polymorphs with cubic structure [12,13] but

completely different properties: the thermodynamic α -phase and the metastable δ -phase. Indeed, a $\delta \rightarrow \alpha$ phase transformation is observed around 440 °C [14], thus corroborating the higher thermodynamic stability of α - KY_3F_{10} . α - KY_3F_{10} crystallizes in a fluorite-type cubic structure with the $Fm\bar{3}m$ (no. 225) space group (SG). The lattice parameter is $a = 11.536 \text{ \AA}$, and the cell volume is $V = 1535.20 \text{ \AA}^3$ with 8 formula units per unit cell ($Z = 8$) [12]. The structure can be described by means of square antiprisms formed by YF_8 units, having the Y^{3+} central cation a C_{4v} local symmetry, **Figure 8.1(a)**. On the other hand, the δ - $\text{KY}_3\text{F}_{10} \cdot x\text{H}_2\text{O}$ compound has also a cubic structure with a similar SG = $Fd\bar{3}m$ (no. 227), $Z = 16$, and $a = 15.492 \text{ \AA}$ (cell volume $V = 3717.90 \text{ \AA}^3$) [14]. The crystal structure is also composed of YF_8 square antiprisms, having the Y^{3+} central cation a C_{2v} local symmetry (e.g., a symmetry lower than in α - KY_3F_{10}) **Figure 8.1(b)**. Additionally, the δ -phase incorporates crystalline water molecules which gives rise to a zeolitic behavior in this unique phase.

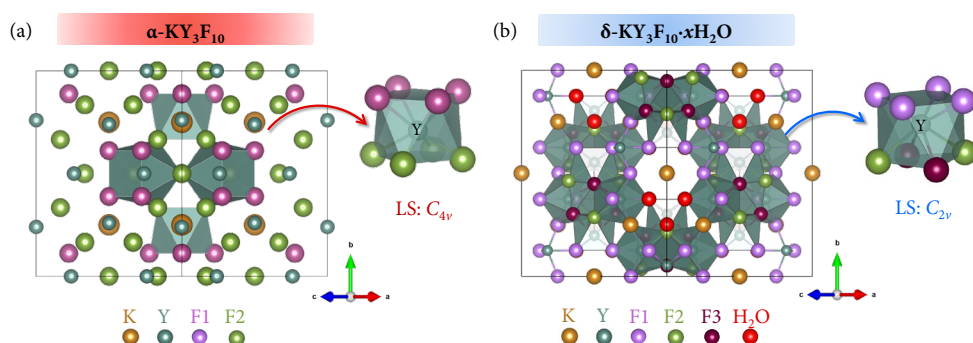


Figure 8.1. Illustrative representation of the experimental procedure followed for the synthesis of the powders. Structure of (a) α - KY_3F_{10} and (b) δ - $\text{KY}_3\text{F}_{10} \cdot x\text{H}_2\text{O}$ highlighting the coordination polyhedra of Y^{3+} ions along with their local symmetry. The labels F1, F2, and F3 refer to fluoride anions situated at different Wyckoff positions in each compound. The global structure view has been selected for simplification purposes due to the high number of atoms.

While the α -phase has been widely studied in the literature and different synthetic

procedures have been developed [15–19], the obtention of single-phase δ - KY_3F_{10} has been more challenging [20,21]. In a recent article, we employed a sonochemical synthesis to obtain both the α and δ compounds by accurately adjusting the pH of the reaction medium [22]. The complex formation mechanism of the δ -phase was discussed in detail employing equilibrium reactions. Inspired by this peculiar and delicate system, we published another study in which a novel and easy coprecipitation method was developed to obtain nanospheres of the δ -phase at room temperature [21]. The results highlighted the delicacy of this fluoride-based system because by only changing the speed of addition of the fluoride source (KF/HF solution) into the Y^{3+} solution it was possible to obtain the single δ -phase or a mixture of $\alpha + \delta$. Additionally, the site-selective emission of the Eu^{3+} -doped δ -phase was found to be 20 times more intense than that of the α -phase, a fact that illustrated the importance of exploring this metastable phase.

Therefore, this last synthesis process was a good candidate to explore the influence of kinetic and thermodynamic factors on the reaction system and the final product. However, as outlined in the Supporting Information of the present study, it is not possible to properly achieve only the thermodynamic phase (α) by performing several experiments in which the influence of temperature is implemented (thermodynamic conditions). Moreover, another secondary phase starts to appear.

Herein we introduce an enhanced synthetic methodology with some modifications of the coprecipitation strategy previously mentioned that allows to properly follow the transition-phase pathway. To consider both the kinetics and thermodynamics and see how they affect the formation of one or another polymorph, the reaction temperature was varied from 25 to 80 °C, and the reaction time was varied from 1 hour up to 7 days. The results revealed the possibility of isolating both crystal phases depending on

the experimental conditions. In addition, due to the different optical responses of both phases, the samples were doped with Eu^{3+} , and all the structural changes were followed by the luminescence of the lanthanide ion.

8.2. Experimental section

8.2.1. Materials and methods

The reagents used for the synthesis of the powders were yttrium(III) nitrate hexahydrate [$\text{Y}(\text{NO}_3)_3 \cdot 6\text{H}_2\text{O}$ 99.8%], europium(III) nitrate pentahydrate [$\text{Eu}(\text{NO}_3)_3 \cdot 5\text{H}_2\text{O}$ 99.9%], potassium fluoride [KF 99.5%], and hydrofluoric acid aqueous solution [HF 40% wt.]. All of them were purchased from Sigma-Aldrich and used without further purification.

The compounds were prepared by a coprecipitation method. Different temperatures were fixed (25, 40, 60, and 80 °C) combined with different reaction times (1 h, 1 day, and 7 days) yielding a total number of 12 samples. The amounts of reagents were adjusted to obtain approximately 0.5 g of the final product. First, 3.0 mmol of the hydrated $\text{Ln}(\text{NO}_3)_3$ were dissolved in 30 mL of water (0.1 M Ln^{3+} solution; Ln = Y, Eu; 3 mol% Eu^{3+}) in a double-necked round-bottom flask. One of the necks was fitted with a refluxing condenser and the other one was sealed with a rubber septum. The flask was put in a silicon oil bath with the desired temperature fixed. The system was maintained under stirring for 10 min to ensure that the Ln^{3+} solution had achieved the fixed temperature.

After that, the fluoride-source solution was prepared by dissolving 6 mmol of KF in 10 mL of water and, subsequently, adding 270 μL of HF aqueous solution 40% wt. (6 mmol HF). The resulting solution (0.6 M KF/HF) was added dropwise to the previous Ln^{3+} solution in the flask. For that purpose, the rubber septum was removed

and it was placed again after finalizing the addition process. Immediately, a white precipitate appeared and it was allowed to mature at the desired time under continuous stirring. Finally, the products were collected by centrifugation, washed twice with water, and dried under an infrared lamp. A summary of the abbreviations used for the samples according to the fixed temperature and reaction time is indicated in **Table 8.1** and a scheme of the experimental procedure is depicted in **Figure 8.2**.

Table 8.1. Samples prepared under different reaction conditions of time and temperature.

T (°C)	1 hour	1 day	7 days
25	R25-1h	R25-1d	R25-7d
40	R40-1h	R40-1d	R40-7d
60	R60-1h	R60-1d	R60-7d
80	R80-1h	R80-1d	R80-7d

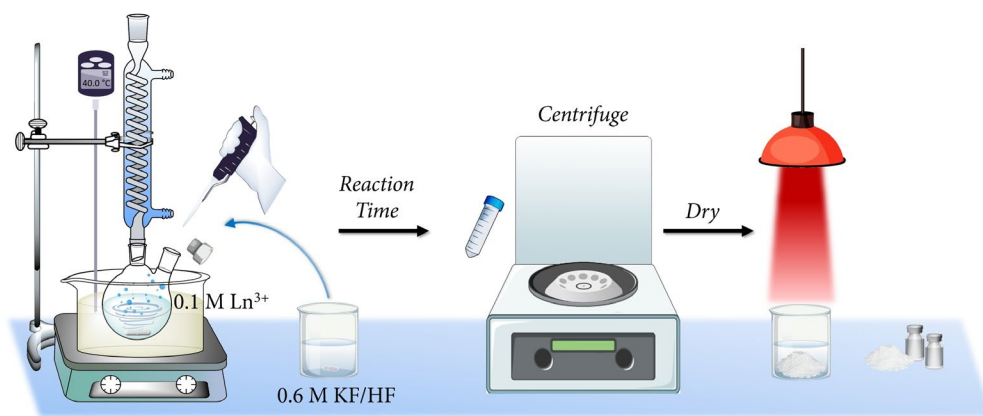


Figure 8.2. Illustrative representation of the experimental procedure followed for the synthesis of the powders.

8.2.2. Characterization techniques

Powder X-ray diffraction (XRD) of the samples was performed at room temperature using a Bruker-AX D8-Advance X-ray diffractometer with $\text{CuK}_{\alpha 1}$ radiation from $2\theta = 20^\circ$ to 90° at a scan speed of $2.25^\circ/\text{min}$. To characterize the morphology of the particles, a JEOL 7001F scanning electron microscope (SEM) was used (acceleration voltage = 30 kV, measuring time = 20 s, and working distance = 8 mm). Previously, the powders had been deposited on double-sided carbon stickers (adhered to the surface of aluminum stubs) and had been sputtered with platinum (10 s).

The photoluminescence response of the materials was recorded with an Eclipse Fluorescence Spectrophotometer (Varian). All the photoluminescence experiments were carried out at room temperature and recorded with a detector delay time (DT) of 0.2 ms to observe the contributions from the higher excited level $^5\text{D}_1$ in the emission spectra and discriminate between the optical response of α , δ , and $(\alpha + \delta)$ phases. Excitation spectra were recorded in the range 250–500 nm fixing the emission wavelength at 593 nm, while the emission spectra were collected with an excitation at 395 nm in the 500–750 nm range. Time-resolved luminescence measurements were performed at different emission wavelengths (593 nm to collect the $^5\text{D}_0 \rightarrow ^7\text{F}_1$ emission and 554 nm to record the response arising from the $^5\text{D}_1 \rightarrow ^7\text{F}_2$ transition). The excitation wavelength was monitored at 395 nm ($^7\text{F}_0 \rightarrow ^5\text{L}_6$ transition) and lifetime values were extracted from the corresponding decay profiles.

8.3. Results and discussion

8.3.1. Structural characterization

Figure 8.3 presents the XRD patterns of the resulting powders under reaction times of (a) 1 h, (b) 1 day, and (c) 7 days. To facilitate the interpretation of the XRD peaks,

especially when there is a coexistence of $\alpha + \delta$ phases, the theoretical main reflection peaks for each crystal phase have also been incorporated. The pattern standards used were ICSD card 00-040-9643 (α -KY₃F₁₀) and ICDD card 04-016-7073 (δ -KY₃F₁₀·xH₂O). Additionally, **Figure S8.2** of the Supporting Information depicts the most useful diffraction peaks that can be used to assign and/or corroborate the presence of the above crystal phases(s).

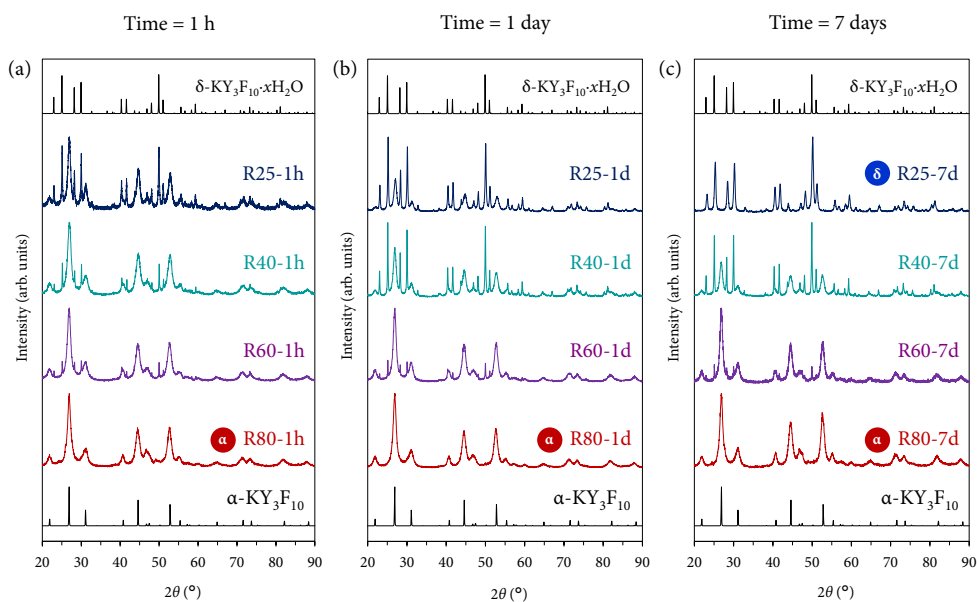


Figure 8.3. XRD patterns of the Eu³⁺-doped powders prepared under different reaction conditions of time and temperature: (a) products prepared with a reaction time of 1 h, (b) products prepared with a reaction time of 1 day, and (c) products prepared with a reaction time of 7 days. For samples that exhibit a single δ -phase (R25-7d) or single α -phase (R80-1h, R80-1d, R80-7d), the label “ α ” or “ δ ” has been added as an inset in the corresponding XRD pattern. The corresponding theoretical ICSD/ICDD cards of the α and δ crystal phases are also shown.

Regarding **Figure 8.3(a)**, with a reaction time of 1 h, it is important to note that at 25 °C a clear mixture of both crystal phases is obtained. This result is optimum to be used as a starting point to study the influence of kinetics and thermodynamics on this

particular system. Then, the kinetic factor will be ascribed to the reaction time while the thermodynamic factor, to the reaction temperature. The subsequent increase in the temperature produces a profound effect on the resulting material. The presence of the polymorph δ decreases and only α single-phase is obtained at the maximum temperature of work (80 °C). This tendency evidences the clear importance of the thermodynamic effect to yield the “thermodynamic phase”, i.e., α .

Very similar conclusions can be extracted from **Figure 8.3(b)** and **Figure 8.3(c)** if one compares the evolution of the resulting crystal phase(s) with the increase in temperature. However, to analyze the kinetic factor (time) and its influence, one can compare the XRD patterns of samples obtained at the same reaction temperature, but at different maturation times. Perhaps, the most evident and fascinating results are found evaluating the powders obtained at 25 °C. Since the temperature is mild enough to avoid thermodynamic control, it is expected that the kinetic effect becomes more prominent. Indeed, comparing samples R25-1h, R25-1d, and R25-7d, it is clearly shown that the metastable δ -phase is stabilized and R25-7d contains only this crystal phase without any traces or impurities from α -KY₃F₁₀. However, it is quite curious that the metastable phase can be stabilized in detriment of the thermodynamic α -phase, as one may expect a priori. Further explanations are given below in a subsection.

At 40 °C, the thermodynamic control starts to become slightly more important since the temperature is higher, although not enough to allow the thermodynamics to govern the whole reaction process and neglect the kinetics. The most substantial change occurs between samples R40-1h and R40-1d. The XRD pattern corresponding to the latter one presents a higher presence of the metastable δ -phase. This major contribution is even slightly higher at a long reaction time (sample R40-7d). These

results underscore that we are under experimental conditions where the competitiveness between kinetics and thermodynamics plays an important role and it is not possible to obtain either single α or δ -phase.

Following this line of reasoning, when the temperature is increased and set to 60 °C, the thermodynamic control is more than evident because all the XRD patterns of samples R60-1h, R60-1d, and R60-7d exhibit virtually the same profile regardless of the total reaction time. The powders are mainly composed of α -KY₃F₁₀ with some minor impurities of δ -KY₃F₁₀, thus highlighting that the kinetics do not play any significant contribution at this point. This fact is even accentuated considering samples synthesized at 80 °C because independently of the reaction time (1 h, 1 day, or even 7 days), the final product only exhibits the main XRD reflections ascribed to α -KY₃F₁₀. Thereby, thermodynamics governs the whole reaction pathway.

In summary, the structural analysis of the synthesized powders has revealed the possibility of modulating the desired polymorph(s) of KY₃F₁₀ thanks to the thermodynamic and kinetic control.

Additionally, all the experimental diffraction patterns of the powders were refined using the Rietveld method. The weight fractions (%) of α -KY₃F₁₀ and δ -KY₃F₁₀·*x*H₂O crystal phases are indicated in **Table 8.2**. The values are in very good agreement with the previous discussion of the XRD results and the kinetic/thermodynamic effects. **Figure 8.4** and **Figure 8.5** depict the Rietveld refinements of the XRD patterns for samples obtained at 25/40 °C, and at 60/80 °C, respectively. Further information about the Rietveld refinement can be found in **Section S8.2** of the Supporting Information. **Table S8.1** of the Supporting Information complements the results with the refined unit cell parameter ($a = b = c$) for the different experimental XRD patterns, although no substantial changes seem to take place comparing all the samples.

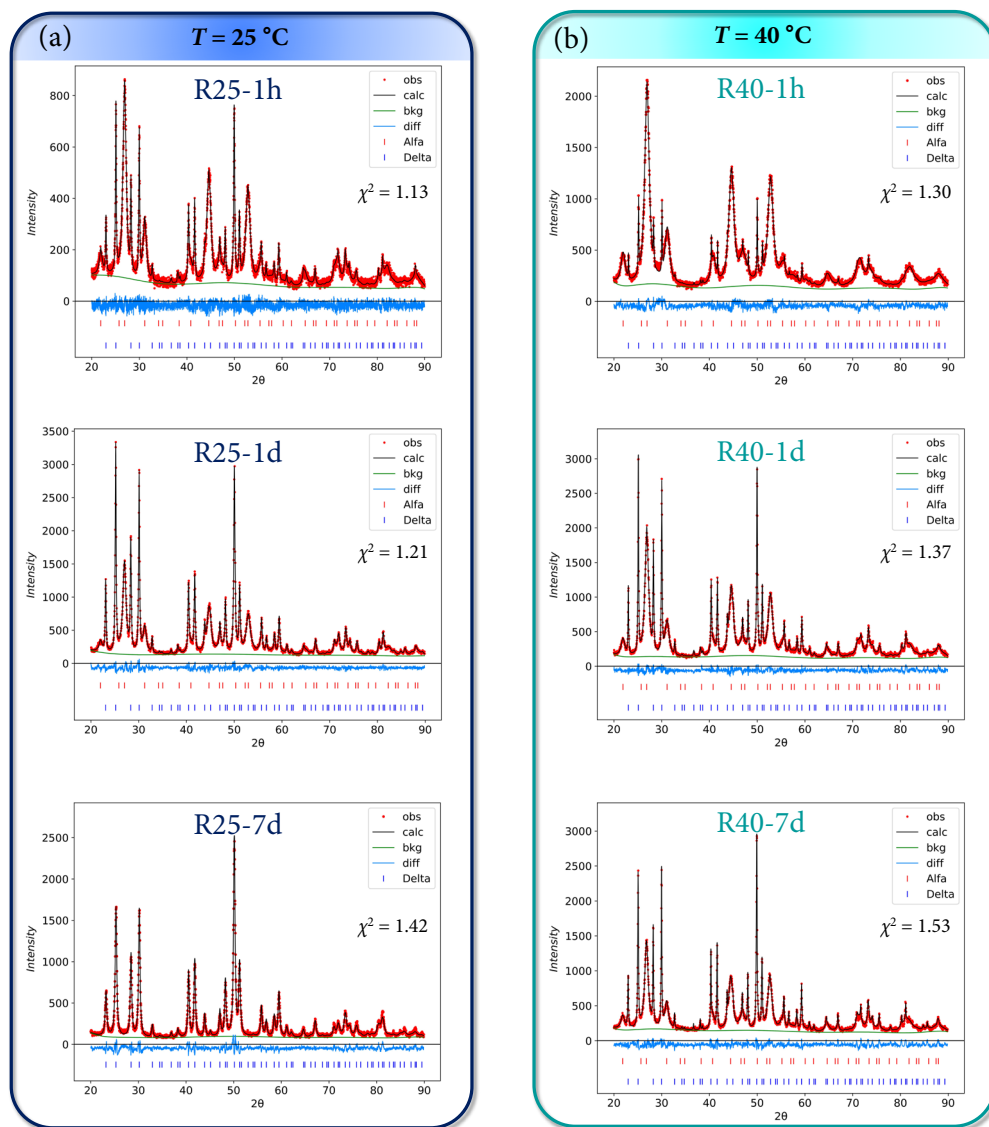


Figure 8.4. Rietveld refinements of the XRD patterns for samples obtained at (a) 25 °C and (b) 40 °C. The goodness of fit χ^2 parameter is also indicated in each plot.

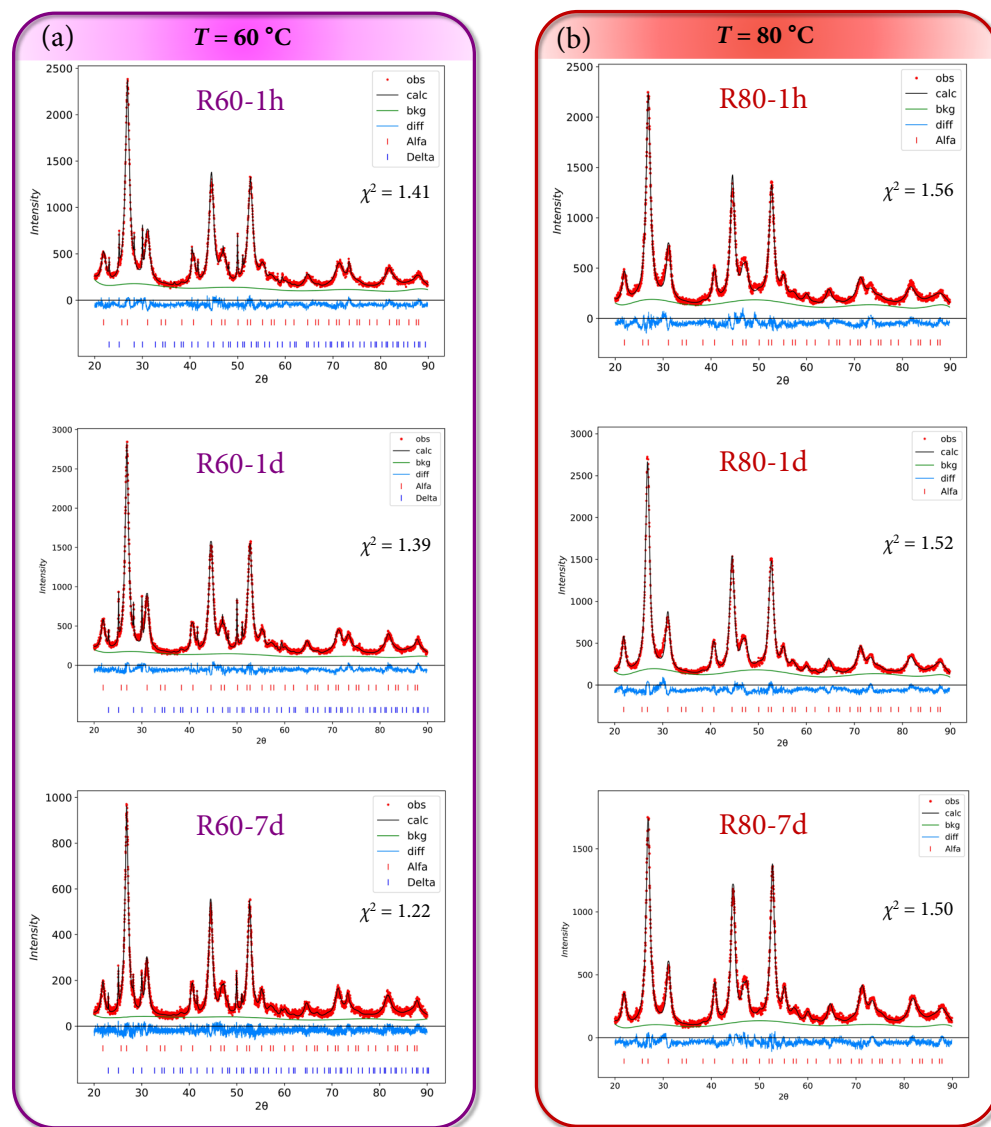


Figure 8.5. Rietveld refinements of the XRD patterns for samples obtained at (a) 60 °C and (b) 80 °C. The goodness of fit χ^2 parameter is also indicated in each plot.

Table 8.2. Weight fractions (%) of α -KY₃F₁₀ and δ -KY₃F_{10-x}H₂O crystal phases obtained using the Rietveld refinement of the different XRD patterns of the powders.

T (°C)	% α			% δ		
	1 hour	1 day	7 days	1 hour	1 day	7 days
25	68.3	41.9	0	31.7	58.1	100
40	92.8	63.7	61.3	7.2	36.3	38.7
60	95.1	93.9	93.6	4.9	6.1	6.4
80	100	100	100	0	0	0

8.3.1.1. Understanding the $(\alpha + \delta) \rightarrow \delta$ transformation

The Ostwald rule of stages, which is relevant in the study of polymorphism, describes the sequential formation of different crystal structures during crystallization, with less stable phases appearing first and more stable phases following as the process continues [23]. Therefore, one could expect that when exposing sample R25-1h ($\alpha + \delta$) to long maturing times (R25-7d, 7 days of maturation), the product would evolve toward the formation of the most thermodynamic polymorph, which in this case is α -KY₃F₁₀. Surprisingly, the opposite behavior occurs, being able to isolate the δ -phase in sample R25-7d.

To shed some light on the mechanism underlying such crystal phase transformation, further experiments were conducted to prove whether it would be possible, or not, for α to dissociate into the corresponding ions in the reaction medium and then form the less stable δ -phase. For that purpose, the pure α -KY₃F₁₀ was synthesized following the same experimental conditions as those described for sample R80-1h ($T = 80$ °C, reaction time = 1 hour). Then, the resulting precipitate in the reaction medium was allowed to cool down until room temperature under continuous

stirring. To have a better understanding of the process of transformation, several aliquots of the mixture were taken during one week. The dried powders were characterized by XRD diffraction and the results showed that the sample did not experience any partial α to δ phase transformation (see **Figure S8.3** of the Supporting Information).

Although this fact seems to be somewhat counterintuitive, there are several studies in the literature that address the crystallization of polymorphs that do not follow Ostwald's rule of stages [24–26]. Quite often, a process can result in the simultaneous crystallization of multiple polymorphic structures, further complicating the control of polymorphism, as is our case (e.g. sample R25-1h). Various mechanisms have been suggested to explain this occurrence, which is referred to as concomitant polymorphism. This phenomenon has been attributed to competing processes of nucleation that can lead to the cross-nucleation of a metastable polymorph on the stable polymorph and finally obtain the less stable polymorph [27]. Therefore, the observed results could indicate that the α to δ phase transformation might undergo a cross-nucleation mechanism, as depicted schematically in **Figure 8.6**.

Following this line of reasoning, the formation of crystal nuclei consisting of α particles would take place first and fast. Then, nuclei of δ particles would start to crystallize on the surfaces of the most stable α -nuclei. Subsequently, the amount of δ -phase would start to become more prominent until finally this polymorph is isolated despite being less stable thermodynamically. We believe that these interesting results should be subjected to further study and confirmed with future lines of research.

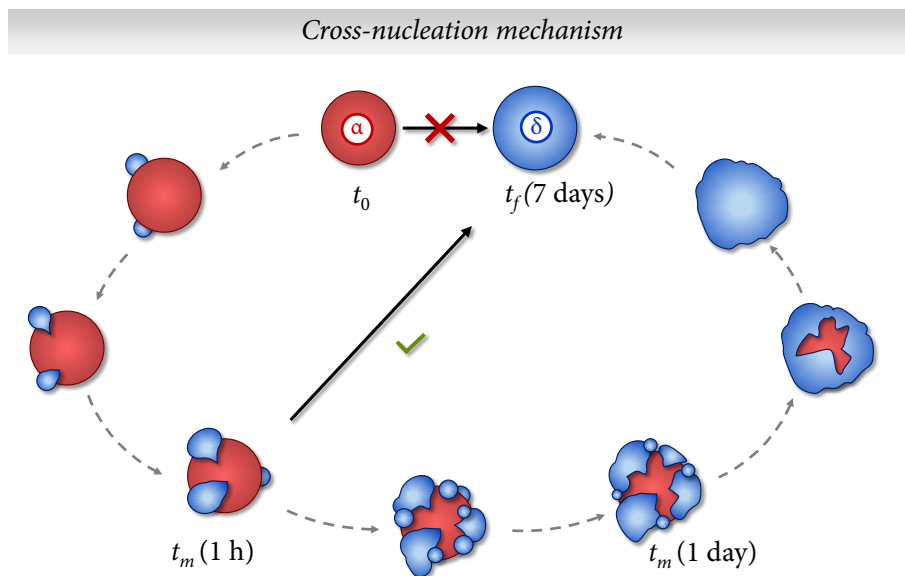


Figure 8.6. Schematic representation of the suggested cross-nucleation mechanism that explains the obtention of the metastable δ -phase instead of the thermodynamic α -phase when exposing the precipitate ($\alpha + \delta$) at long times of maturing. t_m indicates an intermediate time of maturing.

8.3.2. Morphological characterization

Given the structural results, it is of interest to analyze the morphology of the particles in order to illustrate their evolution and corroborate the kinetic/thermodynamic effects. **Figure 8.7** presents the SEM images of the Eu^{3+} -doped powders prepared under different reaction conditions of time and temperature.

Figure 8.7(a) shows the micrographs of samples synthesized at $25\text{ }^\circ\text{C}$ with different maturing times. Sample R25-1h is mainly composed of particle aggregates without a morphology clearly defined. Notwithstanding, with the evolution of time, the aggregates tend to form spherical particles, with the most notable effect appreciated in sample R25-7d (single δ -phase), in which the coalescence of spheres is demonstrated. Thus, not only does the kinetics serve as a director of the crystal structure but also as a morphological modulator.

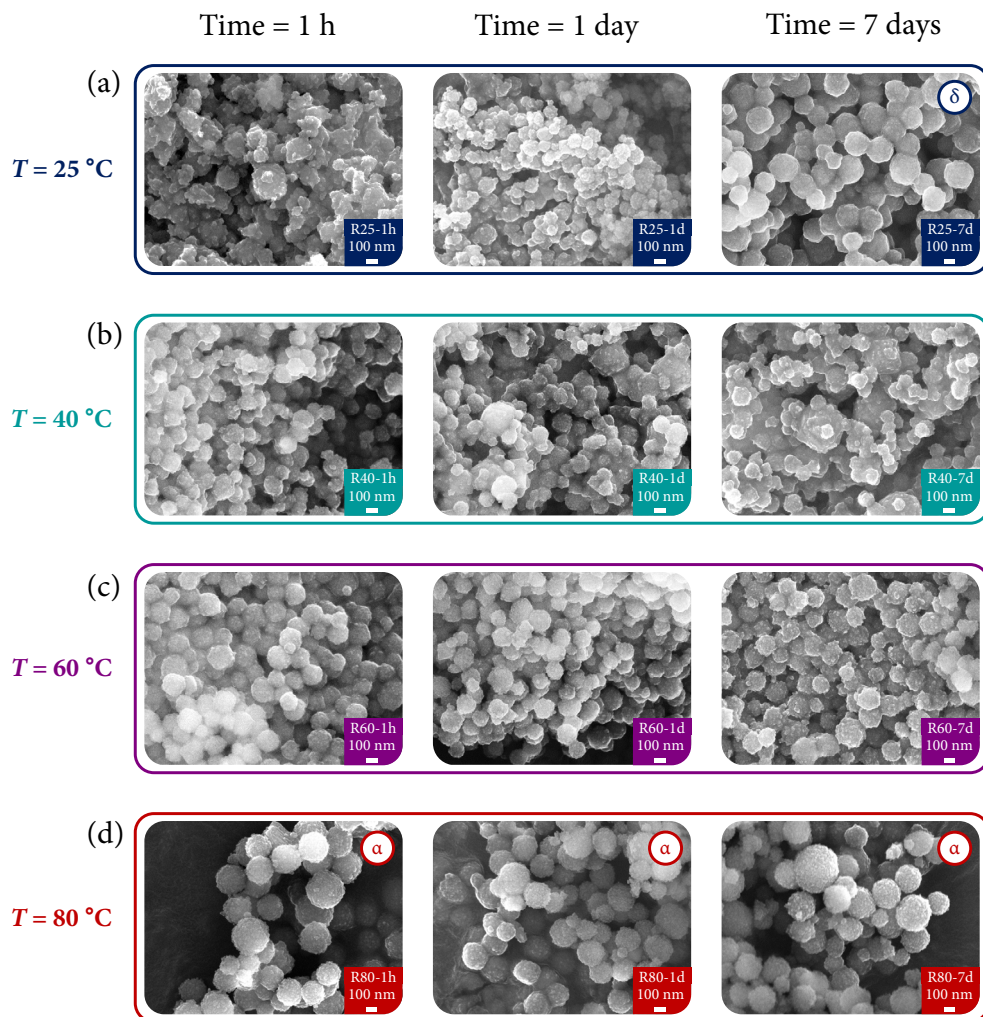


Figure 8.7. SEM images of the Eu^{3+} -doped powders prepared under different reaction conditions of time and temperature: (a) compounds prepared at $25\text{ }^{\circ}\text{C}$, (b) compounds prepared at $40\text{ }^{\circ}\text{C}$, (c) compounds prepared at $60\text{ }^{\circ}\text{C}$, and (d) compounds prepared at $80\text{ }^{\circ}\text{C}$. For samples that exhibit a single δ -phase (R25-7d) or single α -phase (R80-1h, R80-1d, R80-7d), the label “ α ” or “ δ ” has been added as an inset in the corresponding micrograph.

Regarding **Figure 8.7(b)**, i.e., samples synthesized at $40\text{ }^{\circ}\text{C}$, no substantial changes can be appreciated depending on the reaction time. However, a major degree of order (particles with more regular shapes instead of large aggregates) is formed at this

temperature. Compare for instance sample R40-1h with R25-1h.

In a similar way to the results issued by the XRD analysis, where no difference was appreciated among the samples at different reaction times, the SEM images of **Figure 8.7(c)** corresponding to powders obtained at 60 °C reflect the same behavior. As previously commented with samples of **Figure 8.7(b)**, the temperature (and, thus the thermodynamic factor) also contributes to the formation of more regular sphere-shaped particles.

Finally, **Figure 8.7(d)** underscores two main points: (1) the good correlation between the structural and morphological characterization, and (2) the prevalence of the thermodynamic control over the particle shapes. Interestingly, all the powders (which present the α -KY₃F₁₀ polymorph) exhibit the same morphology regardless of the reaction time: spherical particles resulted from the self-assembly of subunits around 20 nm. More intriguing is the fact that this morphology is the same that has been possible to obtain under the aforementioned process of synthesis mediated by sonochemistry [22].

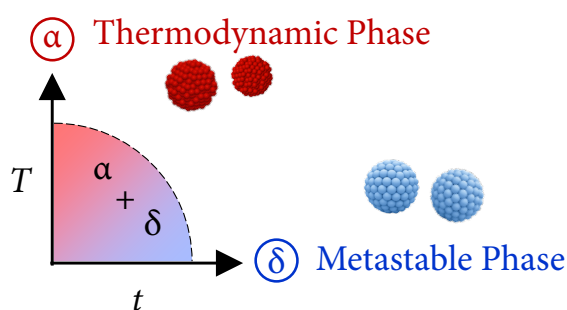


Figure 8.8. Schematic representation of the influence of the thermodynamic (temperature) and kinetic (time) factors that allow to obtain both crystal phases.

Hence, the evolution of the polymorphs is governed by kinetic and/or

thermodynamic control, also reflected in the evolution of the morphology of particles. As a schematic representation, **Figure 8.8** summarizes the above effects. At the beginning (sample R25-1h), a mixture of both α and δ phases is obtained, but with the incorporation of the thermodynamic (temperature) or kinetic (time) factors it is possible to modulate the formation of a single crystal phase.

8.3.3. Photoluminescence properties

8.3.3.1. Excitation and emission spectra

One of the main key points of this study is the capability of relating the luminescent response of the materials with the thermodynamic and/or the kinetic effect throughout the reaction pathway. Thus, a direct measurement, as it is the luminescence of the Eu^{3+} -doped powders, serves to easily interpret the structure-stability conjunction because the two polymorphs of interest exhibit some particular differences regarding the optical response.

Figure 8.9 shows the room temperature excitation spectra for different samples as an example of the δ -phase (R25-7d), α -phase (r80-1h), and $\alpha + \delta$ (R25-1h). Regardless of the sample composition, there are no substantial changes in the excitation spectra of the different powders. All the bands can be attributed to the transitions of Eu^{3+} from the ground ${}^7\text{F}_0$ level to higher excited levels. As outlined with the dashed line, the maximum intensity corresponds to the band associated with the ${}^7\text{F}_0 \rightarrow {}^5\text{L}_6$ transition (395 nm).

In addition, there are no bands associated with charge transfers (CTs) from the anions of the host lattice (F^-) to the Eu^{3+} ion. For Eu^{3+} -doped fluorides, the F^- - Eu^{3+} CT appears at high-energy positions in comparison with oxidic matrices because of the band gap of compounds and the optical electronegativity of the ions implied [28–30].

These CTs usually have low intensity and are expected to appear in the 150–170 nm spectral region so they might be difficult to detect sometimes due to instrumental limitations [31]. Therefore, the emission spectra of the powders have been recorded under an excitation wavelength of 395 nm.

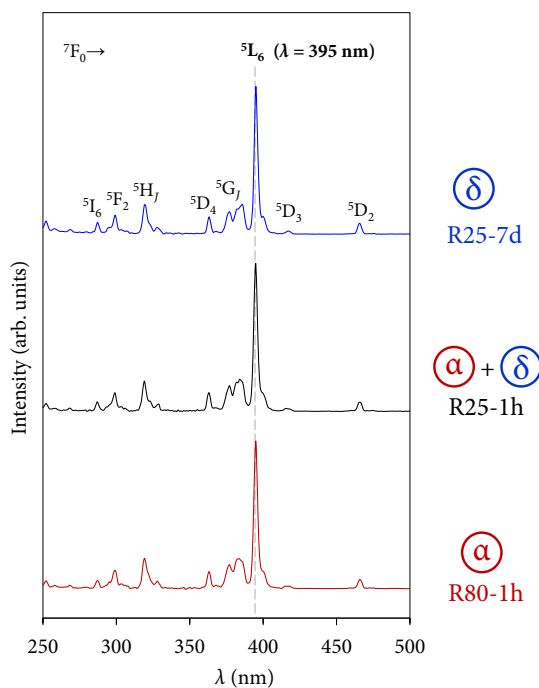


Figure 8.9. Room temperature excitation spectra obtained with a $DT = 0.2$ ms for different samples as an example of the δ -phase, α -phase, and $\alpha + \delta$. The dashed line at 395 nm serves as a guideline to observe that there are no substantial changes in the excitation spectra of the different powders and the maximum intensity corresponds to the band associated with the ${}^7F_0 \rightarrow {}^5L_6$ transition (395 nm).

Regarding the emission profiles of the powders, **Figure 8.10** depicts a selection of four spectra as an example to appreciate at first glance the modulation and changes in the photoluminescence response of the compounds depending on the polymorph(s). The observed bands correspond to the common ${}^5D_0 \rightarrow {}^7F_j$ transitions of Eu^{3+} but, due to the different electronic nature of the α and δ phases, the presence of bands

associated with transitions arising from the higher excited state 5D_1 can also be observed (marked with black stars in **Figure 8.10**) [32]. The presence of transitions from higher excited states is attributed to the typical low phonon energies of fluorides ($300\text{--}550\text{ cm}^{-1}$) [33,34]. The internal vibrations of the host lattice are low enough to avoid fast and non-radiative multiphonon relaxation processes from the 5L_6 state to the lowest-lying excited state 5D_0 , allowing the observation of such ${}^5D_1 \rightarrow {}^7F_j$ emissions [35,36].

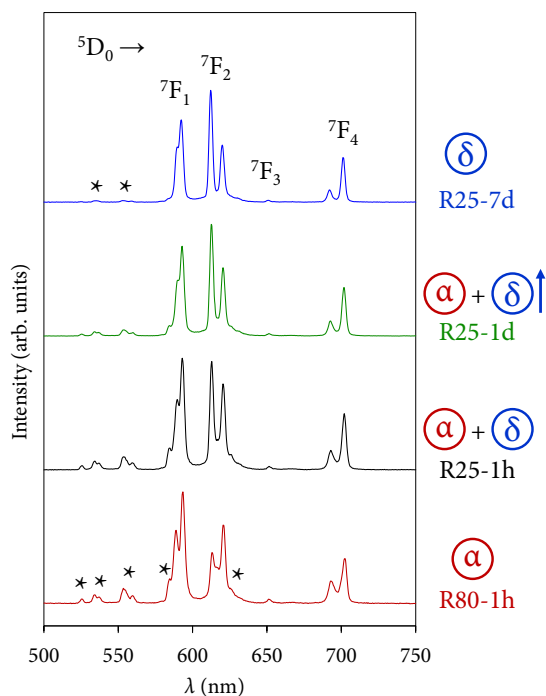


Figure 8.10. Room temperature emission spectra obtained with a $DT = 0.2\text{ ms}$ for different samples where the modulation of the crystal phases is reflected in the optical response. The stars in the emission spectra indicate bands associated with ${}^5D_1 \rightarrow {}^7F_j$ transitions from the higher excited state 5D_1 .

Sample R80-1h (α) is dominated by the ${}^5D_0 \rightarrow {}^7F_1$ magnetic dipole transition, whose main peak appears at 395 nm. Samples R25-1h ($\alpha + \delta$) and R25-1d ($\alpha + \delta$, with a major contribution of the δ -phase) exhibit an intermediate optical response between the two

crystal phases. It can be well appreciated how the peaks corresponding to the ${}^5D_1 \rightarrow {}^7F_j$ transitions start to almost disappear and the ${}^5D_0 \rightarrow {}^7F_2$ electric dipole transition (with the most intense peak at 621 nm) becomes more prominent. Finally, the photoluminescence of sample R25-7d (δ) is governed by the ${}^5D_0 \rightarrow {}^7F_2$ transition and the ${}^5D_1 \rightarrow {}^7F_j$ emissions are still present, albeit with very low intensity, a fact that will be directly related to the lifetimes of these states in the next section.

8.3.3.2. *The crystal environment of Eu^{3+} ions*

In contrast to other rare earth (RE) ions, the distinctive attributes intrinsic to the electronic configuration of Eu^{3+} render this trivalent ion particularly esteemed within the realm of photoluminescence, especially due to its ability to act as a site-sensitive structural probe [37,38]. This unique characteristic engenders a significant advantage, as it facilitates the extraction of pivotal insights regarding the crystal field surroundings of europium ions that have been incorporated into a host lattice. The analysis of the emission spectrum, therefore, emerges as a powerful and informative tool for elucidating the intricacies of the host matrix and its interaction with Eu^{3+} ions, which is of the utmost interest in this case since the optical response and associated physicochemical parameters are expected to be different for both α and δ crystal phases.

The great advantage is that these physicochemical parameters (such as the well-known asymmetry ratio R , or the Judd Ofelt parameters) can be directly extracted from the emission spectra, a fact that allows for the avoidance of many complex mathematical and computational calculations, as it is the case in other rare earth ions. Probably, the most popular parameter of Eu^{3+} is the asymmetry ratio, which can be calculated from the ratio between the integrated intensities of the ${}^5D_0 \rightarrow {}^7F_2$ electric dipole (ED) and ${}^5D_0 \rightarrow {}^7F_1$ magnetic dipole (MD) transitions. This ED transition has a

hypersensitive character to the ion's environment, while the intensity of the above MD transition is relatively independent of the Eu^{3+} symmetry for a given material. Thereby, R provides some useful information about the local symmetry of the luminescent ion.

In direct connection with the structural analysis from the emission spectrum of the luminescent centers, the Judd Ofelt (JO) theory and the corresponding parameters emerge as a robust framework for understanding and predicting the optical properties of rare earth ions. The Ω_2 parameter is linked to the polarizability and covalent nature of the RE^{3+} ion, offering valuable insights into the surrounding crystal structure of Eu^{3+} . Consequently, it is regarded as a parameter that primarily reflects the local environment [39]. In fact, $\Omega_2 \propto R$ for the europium ions of the material under consideration [40]. Hence, larger values of R and Ω_2 tend to indicate lower symmetry of Eu^{3+} ions in the host lattice [41,42]. On the other hand, Ω_4 is known as the long-range JO parameter because it is sensitive to macroscopic properties such as viscosity and rigidity [43].

The above parameters can be calculated by making use of some physical equations [44,45], although recent application software packages incorporate them and highly facilitate the calculus [46,47]. The JO and R parameters were calculated using the LUMPAC software package and are presented in **Table 8.3**. It must be noted that these parameters refer exclusively to the ${}^5\text{D}_0 \rightarrow {}^7\text{F}_j$ transitions. Therefore, to accurately calculate them, they were extracted from the emission spectra of the samples that were recorded again setting a detector delay time (DT) of 10 ms, which ensures the avoidance of contribution from the higher excited state ${}^5\text{D}_1$ [34]. An example of the emission spectrum at different DTs is presented in **Figure S8.4** of the Supporting Information.

Table 8.3. Asymmetry ratio (R) values and Judd-Ofelt parameters (Ω_2, Ω_4) for the Eu^{3+} -doped powders synthesized at different temperatures and reaction times.

T (°C)	R			Ω_2 (10^{-20} cm ²)			Ω_4 (10^{-20} cm ²)		
	1 hour	1 day	7 days	1 hour	1 day	7 days	1 hour	1 day	7 days
25	1.11	1.24	1.49	2.02	2.19	2.62	1.87	1.90	1.99
40	1.09	1.12	1.17	1.89	1.99	2.08	1.87	1.99	1.94
60	1.08	1.07	1.05	1.97	1.94	1.88	2.04	2.00	1.91
80	0.99	0.95	0.92	1.82	1.78	1.69	1.86	1.89	1.92

As mentioned, $\Omega_2 \propto R$, therefore, the discussion of the obtained results will be addressed for the asymmetry ratio (the same conclusions can be extracted from the analysis of Ω_2). Theoretically, the Eu^{3+} ions occupying the yttrium positions in the α phase would have an ideal C_{4v} local symmetry, while it would be C_{2v} for Eu^{3+} ions incorporated into the δ phase. As a result, it is expected to obtain, a priori, lower values of R (more symmetric sites) for samples containing major fractions of the α phase.

The analysis of the results presented in **Table 8.3** confirms this hypothesis. The evolution of the α/δ content was more remarkable in samples synthesized at 25 and 40 °C. For example, the weight fractions of α phase in samples R25-1h (68.3 %), R25-1d (41.9 %), and R25-7d (0 %) are directly related to the occupation of C_{2v} sites in a major proportion, as reflected in the increase of the asymmetry ratio values: R25-1h (1.11), R25-1d (1.24), and R25-7d (1.49). To appreciate at first glance the correlation between the weight fractions and R , 3D plots (fraction-time-temperature and asymmetry-time-temperature) are depicted in **Figure 8.11**. For visual purposes, instead of plotting the R values, it has been plotted the negation of the asymmetry ratio (i.e., $-R$). Thus, higher values of $-R$ indicate more symmetry in the crystal environment of Eu^{3+} ions (more fraction of α phase).

On the other hand, it must be recalled that the Ω_4 JO parameter is ascribed to bulk properties. For this reason, due to the wide range of morphologies observed and other macroscopic properties that can present the materials, it is complicated to establish a direct relationship among the different series of samples.

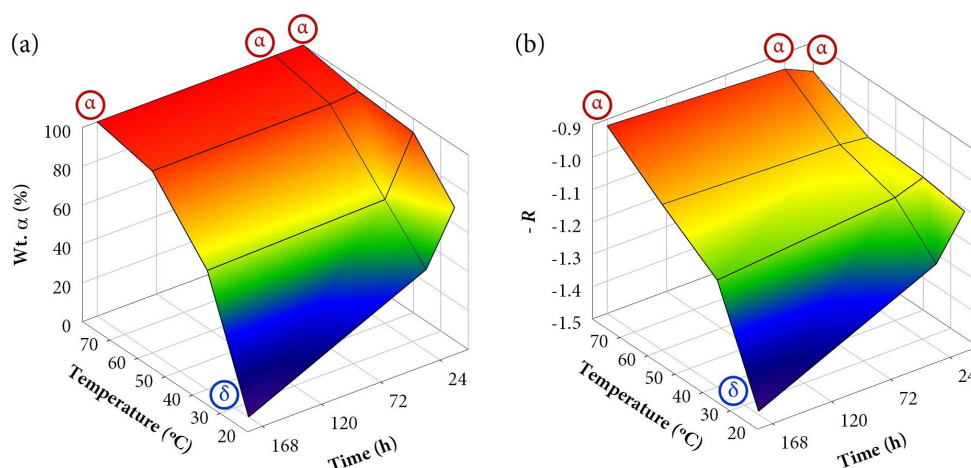


Figure 8.11. 3D plots of (a) the weight fractions of α - KY_3F_{10} and (b) the negation of the asymmetry ratio as a function of temperature and time. For samples that exhibit a single δ -phase (R25-7d) or single α -phase (R80-1h, R80-1d, R80-7d), the label “ α ” or “ δ ” has been added as an inset in the corresponding point.

8.3.3.3. Time-resolved luminescence

The lifetimes associated with a specific electronic transition can serve as a probe to check structural/local distortions [48,49], and phase transformations between different polymorphs [50,51]. Therefore, lifetimes are of the utmost interest to follow the changes produced in the synthesized powders by kinetic and thermodynamic effects during the reaction pathway.

Herein, taking advantage of the presence of $^5\text{D}_1 \rightarrow ^7\text{F}_j$ transitions, it is possible to measure the lifetimes of the materials for different excited states ($^5\text{D}_0$ and $^5\text{D}_1$) since

their sensitivity to the structural changes might be different. Thus, it is pretended to extract more information about the photoluminescence properties of the compounds and check to what extent such an inherent relationship can be established.

In direct connection with the emission results previously discussed, **Figure 8.12** displays the decay curves of some selected samples (the same used in **Figure 8.10**). For the 5D_0 state, **Figure 8.12(a)**, the emission was collected at 593 nm (${}^5D_0 \rightarrow {}^7F_1$ transition), while for the 5D_1 , **Figure 8.12(b)**, it was collected at 554 nm (${}^5D_1 \rightarrow {}^7F_2$ transition). At first glance, it can be observed that the decay profiles change during the phase transformation. In both cases, the red (R80-1h, α) and blue curves (R25-7d, δ) are very different. The decay curves were best fitted to a double exponential model ($R^2 \geq 0.999$) following the expression:

$$I(t) = I_1 \exp\left(\frac{-t}{\tau_{\text{obs } 1}}\right) + I_2 \exp\left(\frac{-t}{\tau_{\text{obs } 2}}\right) \quad (8.1)$$

where I refers to the intensity as a function of time (t). To easily compare the results, an effective lifetime (τ_{eff}), presented in **Table 8.4**, was calculated according to:

$$\tau_{\text{eff}} = \frac{I_1(\tau_{\text{obs } 1})^2 + I_2(\tau_{\text{obs } 2})^2}{I_1(\tau_{\text{obs } 1}) + I_2(\tau_{\text{obs } 2})} \quad (8.2)$$

The results indicate that the lifetimes corresponding to the 5D_1 state are shorter than those of the 5D_0 , a phenomenon strictly linked to the cross-relaxation process in which Eu^{3+} ions populating the higher excited level decay to the metastable 5D_0 [52]. Further information about the fitting procedure can be found in **Section S8.4** of the Supporting Information.

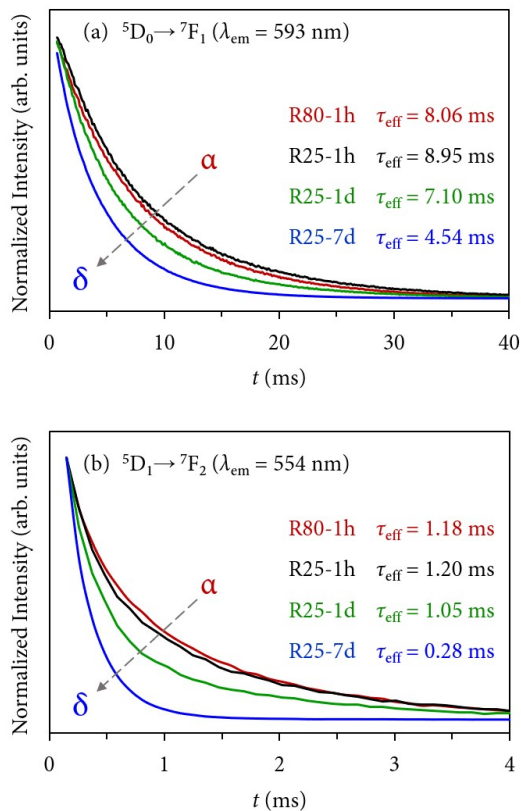


Figure 8.12. Normalized decay curves acquired at room temperature with a DT = 0.2 ms exciting the samples at 395 nm and collecting the emission at (a) 593 nm (${}^5D_0 \rightarrow {}^7F_1$ transition) for the lowest-lying excited state 5D_0 , and (b) 554 nm (${}^5D_1 \rightarrow {}^7F_2$ transition) for the higher excited state 5D_1 .

Table 8.4. 5D_0 and 5D_1 lifetimes calculated from the corresponding decay profiles of the samples. All the correlation coefficients of the fits (R^2) were ≥ 0.999 .

T ($^{\circ}\text{C}$)	$\tau_{eff} {}^5D_0 \rightarrow {}^7F_1$ (ms)			$\tau_{eff} {}^5D_1 \rightarrow {}^7F_2$ (ms)		
	1 hour	1 day	7 days	1 hour	1 day	7 days
25	8.95(6)	7.10(4)	4.54(1)	1.20(3)	1.05(3)	0.28(4)
40	8.72(4)	7.87(3)	7.49(3)	1.15(2)	1.09(3)	1.03(2)
60	8.63(4)	9.15(1)	9.25(5)	1.17(3)	1.23(2)	1.22(2)
80	8.06(3)	8.37(1)	8.68(4)	1.18(2)	1.20(2)	1.23(2)

First, the ${}^5\text{D}_0$ lifetimes will be analyzed, which are also in good agreement with the XRD and SEM results. Samples synthesized at 25 °C display a progressive shortening of the lifetimes (from 8.95 ms of the $\alpha + \delta$ mixture to 4.54 ms of single δ). Similarly, samples obtained at 40 °C also exhibit shorter lifetimes with the evolution of time, which can be well ascribed to the major presence of the δ -phase. On the other hand, although the XRD results showed that the crystal structure composition of samples synthesized at 60 °C (mainly α + some minor contribution of δ) and at 80 °C (α) was constant regardless of the maturing time because the thermodynamic control governed the reaction pathways, there is a tendency in the lifetimes to become longer as the reaction time increases, which is the opposite trend in comparison with the above series of samples. A priori, one could think that this fact could be associated with morphological aspects, however, the micrographs outlined that there were no substantial changes among each series of samples. Therefore, the main possible explanation could be associated with a local rearrangement or ordering of Eu^{3+} ions when the precipitate is exposed to high reaction times that allow for a more uniform distribution of the dopant in the crystal lattice, as might be inferred from the asymmetry ratio and the Ω_2 JO parameter, see **Table 8.3**. Thus, even though the thermodynamics govern the crystallization of the compound in the latter samples, the kinetics (maturation time) has also some particular influence.

Moreover, it is interesting to note that when both polymorphs coexist in the sample, slightly longer lifetimes are obtained. The most evident examples can be found comparing samples synthesized in 1 h at different temperatures: the τ_{eff} shortens progressively from 8.95 ms (R25-1h) to 8.06 ms (R80-1h). This behavior has also been reported previously [21] and might be related to different coupling mechanisms between Eu^{3+} ions embedded in the different host lattices that, as a result, tend to elongate the lifetime.

On the other hand, regarding the lifetimes associated with the 5D_1 state, similar conclusions can be drawn. However, the optical response of the ${}^5D_1 \rightarrow {}^7F_1$ transitions is primarily attributed to the presence of Eu^{3+} ions in $\alpha\text{-KY}_3\text{F}_{10}$ with an almost negligible contribution of the dopant in $\delta\text{-KY}_3\text{F}_{10}$ (as depicted in **Figure 8.10** for sample R25-7d). Therefore, the variation of the 5D_1 lifetime values in the different series of samples is less notable ($\tau_{\text{eff}} \approx 1.0\text{--}1.2$ ms) in comparison to the 5D_0 lifetimes. Remarkably, a drastic change is observed for sample R25-7d ($\delta\text{-KY}_3\text{F}_{10}$) whose lifetime is 0.28 ms.

Additionally, 3D plots (lifetime-time-temperature) are depicted in **Figure 8.13** to compare the kinetic and thermodynamic effects on the resulting lifetimes. As can be appreciated, both graphics evince the perfect relationship and good agreement with the tendency observed in the results previously discussed. The color gradient is very useful to easily interpret the changes. Moreover, they closely resemble the 3D plots of **Figure 8.11** (weight fractions of $\alpha\text{-KY}_3\text{F}_{10}$ and asymmetry ratio R).

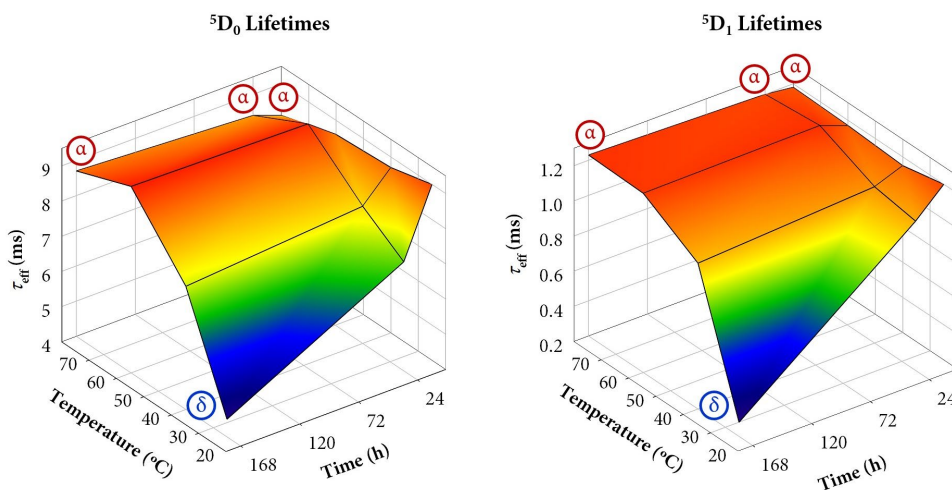


Figure 8.13. 3D plot of the lifetimes corresponding to the 5D_0 and 5D_1 states as a function of temperature and time. For samples that exhibit a single δ -phase (R25-7d) or single α -phase (R80-1h, R80-1d, R80-7d), the label “ α ” or “ δ ” has been added as an inset in the corresponding point.

8.4. Conclusions

To control and follow the transition-phase pathway of the two existent polymorphs of KY_3F_{10} (α and δ), an enhanced coprecipitation strategy has been used to synthesize different Eu^{3+} -doped powders, which contain a mixture of both crystal phases in different proportions or single-phases. The kinetics and thermodynamics effects have been able to study varying reaction conditions of temperature (25–80 °C) and time (1 hour to 7 days).

The results underscored the competitiveness between kinetics and thermodynamics. At low reaction temperature (25 °C), it is possible to modulate the crystal structure with the maturing time and the metastable δ -phase can be isolated after 7 days. However, when the temperature starts to increase (40 °C) the thermodynamic control becomes more prominent. Although the kinetics still play an important role and an evolution toward the formation of the δ -phase is evident with the reaction time, it is no longer possible to isolate this compound and only a mixture of polymorphs is obtained. Finally, higher working temperatures change dramatically the system and evidence the total thermodynamic control of the reaction pathway. Indeed, the α polymorph is always obtained at 80 °C regardless of the maturing time.

The microstructural analysis of the powders matches very well with the above structural results, being able to observe the influence of thermodynamics and kinetics in the particle morphology.

Finally, bearing in mind the good adequacy of the Eu^{3+} ion to act as a sensitive structural probe, the optical response of the prepared materials is in direct connection with the presence of one or both polymorphs and thus it serves as a perfect tool to control the kinetics and thermodynamics effects in the reaction pathway.

Author contributions

P. Serna Gallén: conceptualization, methodology, investigation, writing (original draft, review & editing). E. Cordoncillo and H. Beltrán-Mir: conceptualization, funding acquisition, writing (review & editing).

Acknowledgments

This work was supported financially by the Spanish MCIN (Grant PID2020-116149GB-I00 funded by MCIN/AEI/10.13039/501100011033). P. Serna-Gallén also thanks the Spanish MCIN for an FPU predoctoral contract (FPU18/04511 funded by MCIN/AEI/10.13039/501100011033).

References

- [1] M. Bianchini, J. Wang, R.J. Clément, B. Ouyang, P. Xiao, D. Kitchaev, T. Shi, Y. Zhang, Y. Wang, H. Kim, M. Zhang, J. Bai, F. Wang, W. Sun, G. Ceder, *Nat. Mater.* 19 (2020) 1088–1095.
- [2] B. Hu, S. Sridar, L. Hao, W. Xiong, *Intermetallics*. 122 (2020) 106791.
- [3] D. Rabadjieva, K. Sezanova, R. Gergulova, R. Titorenkova, S. Tepavitcharova, *J. Biomed. Mater. Res. - Part A*. 108 (2020) 1607–1616.
- [4] Q. Luo, Y. Guo, B. Liu, Y. Feng, J. Zhang, Q. Li, K. Chou, *J. Mater. Sci. Technol.* 44 (2020) 171–190.
- [5] T. Wang, Q. Fan, J. Zhu, *J. Phys. Chem. Lett.* 14 (2023) 2251–2262.
- [6] V. V. Gostishchev, I.A. Astapov, A. V. Seredyuk, S.N. Khimukhin, R. Hosen, *Inorg. Mater.* 52 (2016) 419–422.

- [7] X. Gong, H. Noh, N.C. Gianneschi, O.K. Farha, *J. Am. Chem. Soc.* 141 (2019) 6146–6151.
- [8] H. Liu, J. Han, C. McBean, C.S. Lewis, P. Kumar Routh, M. Cotlet, S.S. Wong, *Phys. Chem. Chem. Phys.* 19 (2017) 2153–2167.
- [9] B. Shao, Q. Zhao, Y. Jia, W. Lv, M. Jiao, W. Lü, H. You, *Chem. Commun.* 50 (2014) 12706–12709.
- [10] D. Gentili, M. Gazzano, M. Melucci, D. Jones, M. Cavallini, *Chem. Soc. Rev.* 48 (2019) 2502–2517.
- [11] R. Alvarez-Roca, A.F. Gouveia, C.C. De Foggi, P.S. Lemos, L. Gracia, L.F. Da Silva, C.E. Vergani, M. San-Miguel, E. Longo, J. Andrés, *Inorg. Chem.* 60 (2021) 1062–1079.
- [12] P. Villars, K. Cenzual, eds., KY_3F_{10} Crystal Structure: Datasheet from “PAULING FILE Multinaries Edition – 2012” in Springer Materials (https://materials.springer.com/isp/crystallographic/docs/sd_0552093).
- [13] P. Villars, K. Cenzual, eds., $\delta\text{-KY}_3\text{F}_{10}\cdot x\text{H}_2\text{O}$ ($\text{KY}_3\text{F}_{10}[\text{H}_2\text{O}]$) Crystal Structure: Datasheet from “PAULING FILE Multinaries Edition – 2012” in Springer Materials (https://materials.springer.com/isp/crystallographic/docs/sd_1004004).
- [14] F. Le Berre, E. Boucher, M. Allain, G. Courbion, *J. Mater. Chem.* 10 (2000) 2578–2586.
- [15] L. Zhu, J. Meng, X. Cao, *Mater. Lett.* 62 (2008) 3007–3009.
- [16] C. Cao, *J. Mater. Res. Soc.* 27 (2012) 2988–2995.
- [17] S. Goderski, M. Runowski, S. Lis, *J. Rare Earths.* 34 (2016) 808–813.

- [18] M. Runowski, *J. Lumin.* 186 (2017) 199–204.
- [19] M. Chen, P. Loiko, J.M. Serres, S. Veronesi, M. Tonelli, M. Aguiló, F. Díaz, S.Y. Choi, J.E. Bae, F. Rotermund, S. Dai, Z. Chen, U. Griebner, V. Petrov, X. Mateos, *J. Alloys Compd.* 813 (2020) 152176.
- [20] P. Serna-Gallén, H. Beltrán-Mir, E. Cordoncillo, *J. Mater. Res. Technol.* 15 (2021) 6940–6946.
- [21] P. Serna-Gallén, H. Beltrán-Mir, E. Cordoncillo, R. Balda, J. Fernández, *J. Alloys Compd.* 953 (2023) 170020.
- [22] P. Serna-Gallén, H. Beltrán-Mir, E. Cordoncillo, *Ultrason. Sonochem.* 87 (2022) 106059.
- [23] P.T. Cardew, *Cryst. Growth Des.* 23 (2023) 3958–3969.
- [24] S. Chen, H. Xi, L. Yu, *J. Am. Chem. Soc.* 127 (2005) 17439–17444.
- [25] J. Russo, H. Tanaka, *Soft Matter.* 8 (2012) 4206–4215.
- [26] S.F.S.P. Looijmans, D. Cavallo, L. Yu, G.W.M. Peters, *Cryst. Growth Des.* 18 (2018) 3921–3926.
- [27] C. Desgranges, J. Delhommelle, *J. Am. Chem. Soc.* 128 (2006) 10368–10369.
- [28] G. Blasse, *J. Phys. Chem. Solids.* 50 (1989) 99.
- [29] R.R. Reddy, Y. Nazeer Ahammed, K. Rama Gopal, D. V. Raghuram, *Opt. Mater. (Amst).* 10 (1998) 95–100.
- [30] P. Dorenbos, *J. Lumin.* 111 (2005) 89–104.
- [31] R.T. Wegh, H. Donker, K.D. Oskam, A. Meijerink, *J. Lumin.* 82 (1999) 93–104.

- [32] K. Binnemans, *Coord. Chem. Rev.* 295 (2015) 1–45.
- [33] A. Gulzar, J. Xu, P. Yang, F. He, L. Xu, *Nanoscale*. 9 (2017) 12248–12282.
- [34] P. Serna-Gallén, H. Beltrán-Mir, E. Cordoncillo, *Opt. Laser Technol.* 136 (2021).
- [35] T. Yamase, T. Kobayashi, M. Sugeta, H. Naruke, *J. Phys. Chem. A*. 101 (1997) 5046–5053.
- [36] R.G. Geitenbeek, H.W. De Wijn, A. Meijerink, *Phys. Rev. Appl.* 10 (2018) 1.
- [37] S.K. Gupta, C. Reghukumar, R.M. Kadam, *RSC Adv.* 6 (2016) 53614–53624.
- [38] J. Cheng, J. Cheng, S. Zhang, C. Ma, X. Bian, Z. Zhai, *J. Lumin.* 252 (2022) 119265.
- [39] T. Lan, T. Han, D. Jiang, Y. Wen, X.Y. Sun, Z. Hua, S. Qian, H. Ban, H. Cai, J. Han, H. Liu, S. Liu, L. Ma, L. Qin, J. Ren, G. Tang, Z. Wang, Z. Le Wang, Y. Zhu, *Opt. Mater. (Amst)*. 133 (2022) 113000.
- [40] P. Serna-Gallén, H. Beltrán-Mir, E. Cordoncillo, *Ceram. Int.* (2023).
- [41] D.K. Patel, B. Vishwanadh, V. Sudarsan, S.K. Kulshreshtha, *J. Am. Ceram. Soc.* 96 (2013) 3857–3861.
- [42] C. de Mello Donegá, S.A. Junior, G.F. de Sá, *J. Alloys Compd.* 250 (1997) 422–426.
- [43] S.K. Gupta, M.A. Penilla Garcia, J.P. Zuniga, Y. Mao, *J. Lumin.* 228 (2020) 117605.
- [44] Y. Tian, B. Chen, R. Hua, J. Sun, L. Cheng, H. Zhong, X. Li, J. Zhang, Y. Zheng, T. Yu, L. Huang, H. Yu, *J. Appl. Phys.* 109 (2011) 053511.

- [45] M. Luo, X. Sha, B. Chen, X. Zhang, H. Yu, X. Li, J. Zhang, S. Xu, Y. Cao, Y. Wang, X. Wang, Y. Zhang, D. Gao, L. Wang, *J. Am. Ceram. Soc.* 105 (2022) 3353–3363.
- [46] J.D.L. Dutra, T.D. Bispo, R.O. Freire, *J. Comput. Chem.* 35 (2014) 772–775.
- [47] A. Ćirić, S. Stojadinović, M. Sekulić, M.D. Dramićanin, *J. Lumin.* 205 (2019) 351–356.
- [48] N. Pathak, S. Mukherjee, B.P. Mandal, A.K. Yadav, S.N. Jha, D. Bhattacharyya, *Mater. Adv.* 1 (2020) 2380–2394.
- [49] M. Marques Fernandes, M. Schmidt, T. Stumpf, C. Walther, D. Bosbach, R. Klenze, T. Fanghänel, *J. Colloid Interface Sci.* 321 (2008) 323–331.
- [50] Y. Hui, Y. Zhao, S. Zhao, L. Gu, X. Fan, L. Zhu, B. Zou, Y. Wang, X. Cao, *J. Alloys Compd.* 573 (2013) 177–181.
- [51] P. Li, Y. Zhang, L. Zhang, F. Li, Y. Guo, Y. Li, W. Gao, *Cryst. Growth Des.* 17 (2017) 5935–5944.
- [52] X. Liu, L. Yan, J. Lin, *J. Electrochem. Soc.* 156 (2009) 1–6.

S8. Supporting Information

S8.1. Previous experiments and the scope of the present study

We recently published a paper in which a new coprecipitation method was developed to obtain nanospheres of the metastable δ -phase of KY_3F_{10} at room temperature (25 °C) [S1]. Since α - KY_3F_{10} is the thermodynamic phase, we thought that this new process could be a good candidate to explore the influence of kinetic and thermodynamic factors on the reaction system and the final product. In order to check whether it was possible to obtain single α -phase using the same experimental procedure and reagents concentration that had been employed to obtain the metastable δ -phase, several experiments were carried out in which the temperature of the reaction medium was set to 80 °C, which could, a priori, facilitate the formation of the most thermodynamic crystal structure.

However, as depicted in **Figure S8.1**, it was not possible to properly achieve only the thermodynamic phase (α). When the reaction was conducted at 80 °C for 1 hour, the presence of α - KY_3F_{10} was notable, but even at reaction times of 1 and 7 days, there were still considerable impurities of δ - KY_3F_{10} . Indeed, for high maturing times (7 days), the sample also started to decompose in YF_3 . Very similar results (not shown because they do not add significant information) were obtained at lower reaction temperatures but with the proviso that higher maturing times were necessary to achieve the higher concentration/decomposition of α - KY_3F_{10} .

These results showed that such a methodology was not successful to isolate both compounds depending on the kinetic/thermodynamic factors. As the α - δ system is extremely delicate and sensitive to any change in the reaction medium, the new idea was to modify the concentration of the reagents so as to obtain, in a controlled manner (the fast addition procedure was discarded), a mixture of both phases at room

temperature that could move the system toward the formation of one specific crystal phase depending on the kinetic and thermodynamic control. Therefore, in the present study, the reagents concentration was modified (the mmol and total amount of solvent were the same, but the water volume of each solution was changed). **Table S8.1** underscores the concentrations used in the precedent [S1] and the present study.

As outlined in the main text, this small change in the concentration of the reagents has a profound impact and allows us to properly proceed with the main scope of the study.

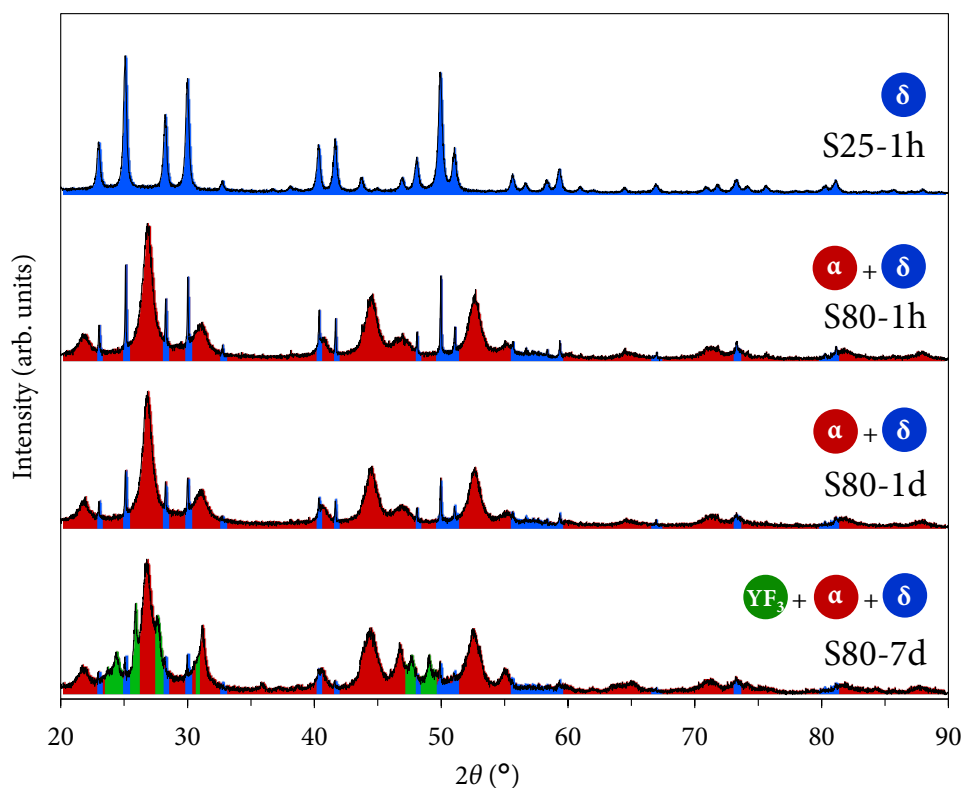


Figure S8.1. XRD patterns of the powders prepared under different reaction conditions of time and temperature. The area under the peaks corresponding to each crystal structure has been colored for clarity purposes: blue for δ -KY₃F₁₀, red for α -KY₃F₁₀, and green for YF₃. The XRD pattern corresponding to sample S25-1 h is the one published in Ref. [S1].

Table S8.1. Reagents concentration (Ln = Y, Eu). The KF/HF solution was added dropwise to the Ln³⁺ solution.

Study	[Ln ³⁺]	[KF/HF]
Ref [S1]	0.15 (10 mL)	0.30 (10 mL)
This work	0.10 (15 mL)	0.60 (5 mL)

S8.2. Crystallographic characterization

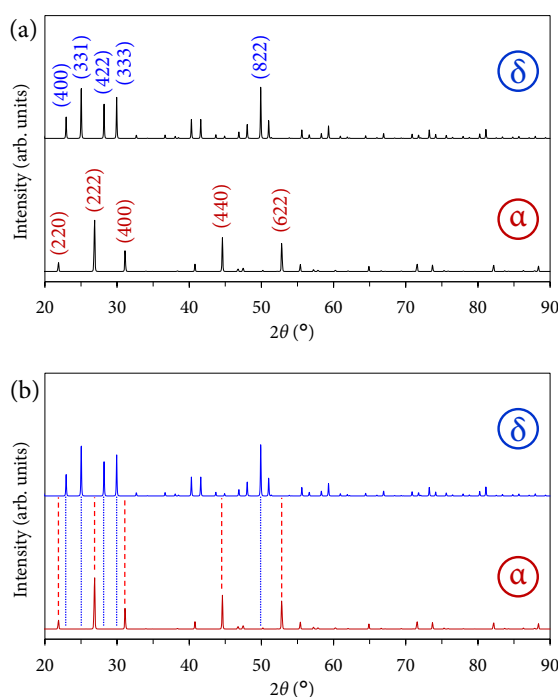


Figure S8.2. Pattern standards for δ -KY₃F₁₀·xH₂O (ICSD card 00-040-9643) and α -KY₃F₁₀ (ICDD card 04-016-7073) highlighting (a) the Miller indices of the most useful diffraction peaks that can be used to identify the presence of these crystal structures, along with (b) guidelines to see at first glance that the diffraction peaks positions are different.

All the experimental diffraction patterns of the powders were refined using the Rietveld method by means of GSAS software. Pseudo-Voigt functions were used to simulate the peaks shape and Chebyshev-1 functions with 10 coefficients were used to

simulate the background.

Table S8.1. Refined unit cell parameter ($a = b = c$) for the different XRD patterns of the powders containing α - KY_3F_{10} and/or δ - $\text{KY}_3\text{F}_{10} \cdot x\text{H}_2\text{O}$ crystal phases.

T (°C)	α , a (Å)			δ , a (Å)		
	1 hour	1 day	7 days	1 hour	1 day	7 days
25	11.5240(17)	11.5341(15)	–	15.5097(19)	15.5028(13)	15.4994(9)
40	11.5374(21)	11.5312(15)	11.5392(19)	15.5034(26)	15.5098(14)	15.5087(16)
60	11.5365(15)	11.5483(24)	11.5385(8)	15.5043(21)	15.5060(30)	15.5079(12)
80	11.5482(18)	11.5450(16)	11.5488(15)	–	–	–

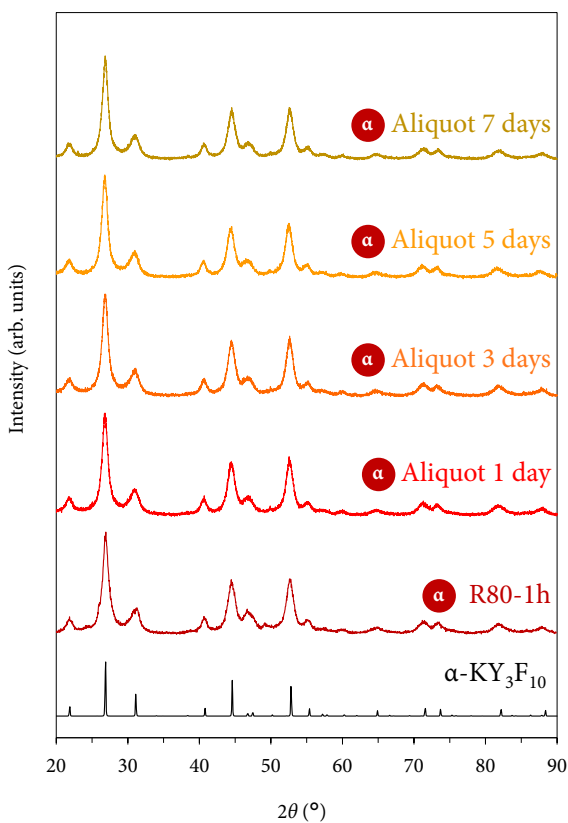


Figure S8.3. XRD patterns of the aliquots taken at different times from the reaction medium after synthesizing sample R80-1h and cooling it down to room temperature.

S8.3. Emission spectra recorded at different DTs

To accurately calculate the JO and R parameters, the emission spectra were recorded again setting a detector delay time (DT) of 10 ms, which ensures the avoidance of contribution from the higher excited state 5D_1 . An example of the emission spectrum at different DTs is presented in **Figure S8.4** for sample R80-1h.

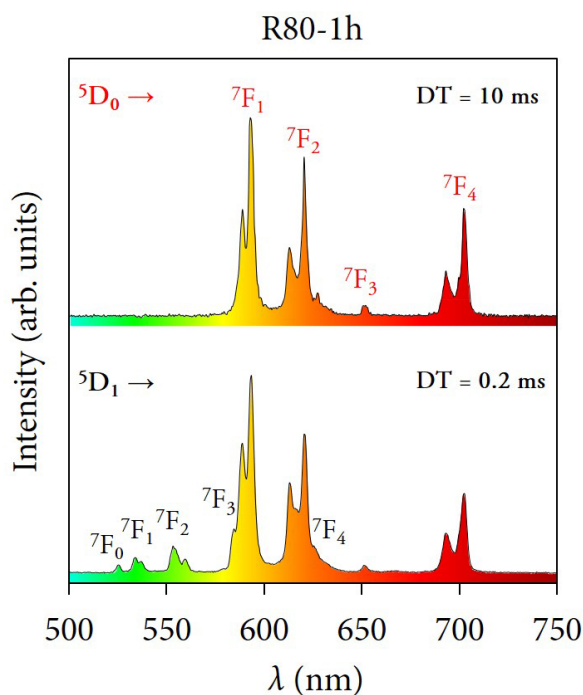


Figure S8.4. Room temperature emission spectra of sample R80-1h obtained with a delay time (DT) of 0.2 and 10 ms upon excitation at 395 nm highlighting the different ${}^5D_{0,1} \rightarrow {}^7F_j$ transitions.

S8.4. Lifetimes

Figure S8.5 depicts the results of fitting the experimental points of time-resolved luminescence for the 5D_0 state following different models for sample R25-1h as an example. As commented in the main text, the best choice is the double exponential model, since it provides the most accurate fit. The mathematical models used are the

following:

- (a) Double exponential model, **Figure S8.5(a)**, which corresponds to the formula:

$$I(t) = I_1 \exp\left(\frac{-t}{\tau_{\text{obs } 1}}\right) + I_2 \exp\left(\frac{-t}{\tau_{\text{obs } 2}}\right) \quad (\text{S8.1})$$

- (b) Single exponential model, **Figure S8.5(b)**, which corresponds to the formula:

$$I(t) = I_0 \exp\left(\frac{-t}{\tau_{\text{obs}}}\right) \quad (\text{S8.2})$$

- (c) Single logarithmic model, **Figure S8.5(c)**. It has also been contemplated because some readers might be more familiar with the semi-logarithmic plot of the luminescence intensity vs. time. Expression S8.2 is simplified into a linear equation from which the lifetime can be easily extracted from the slope of the line:

$$\ln I(t) = \ln I_0 - \frac{t}{\tau_{\text{obs}}} \quad (\text{S8.3})$$

However, this mathematical approach, along with the corresponding plot, is of interest for cases when the decay curve exhibits a single exponential decay. Applying natural logarithmic to expression S8.2 would result in a complex formula that is not straightforward to simplify as in the latter case.

Figure S8.5 also shows some insights into the plot when it can be easily appreciated that when using the single models, the experimental points are partially deviated from the fitting curve, thus obtaining worse correlation coefficients of the fits (R^2). In a similar way, **Figure S8.6** depicts the results of fitting the experimental points of time-resolved luminescence for the $^5\text{D}_1$ state following the different models. It must be noted that now the discrepancy between double and single fitting is more accentuated.

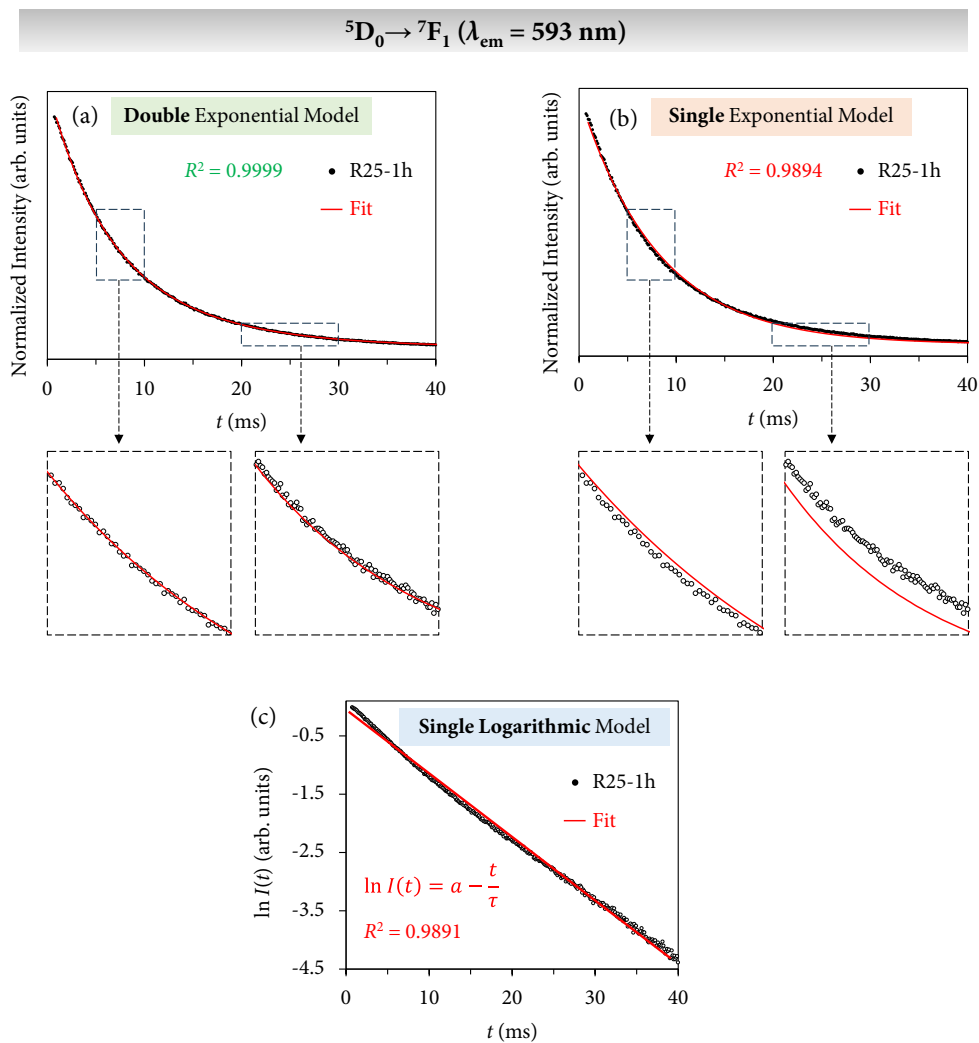


Figure S8.5. Normalized decay curves acquired at room temperature with a DT = 0.2 ms exciting the samples at 395 nm and collecting the emission at 593 nm (${}^5D_0 \rightarrow {}^7F_1$ transition) for the lowest-lying excited state 5D_0 . Different fitting models have been used: (a) double exponential, (b) single exponential, and (c) single logarithmic. For all the plots, the fitting curves are shown along with the corresponding correlation coefficients (R^2).

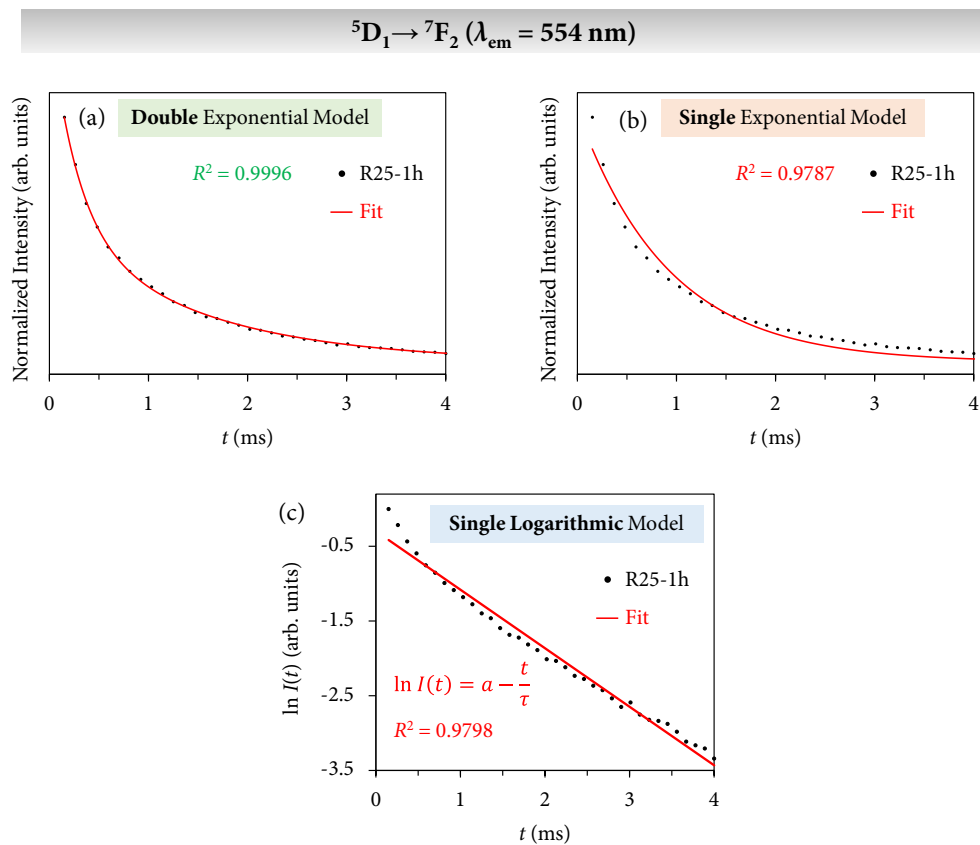


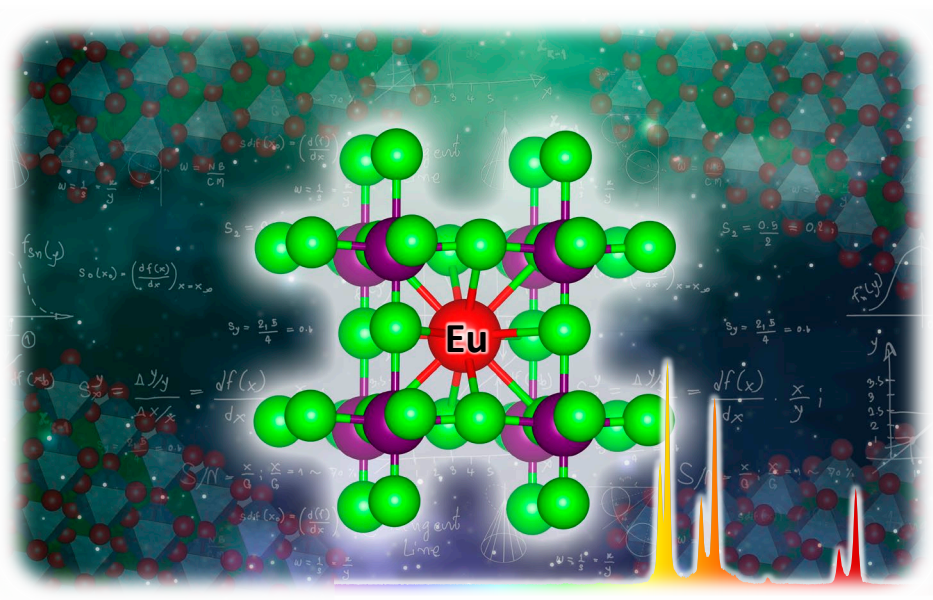
Figure S8.6. Normalized decay curves acquired at room temperature with a DT = 0.2 ms exciting the samples at 395 nm and collecting the emission at 554 nm (${}^5\text{D}_1 \rightarrow {}^7\text{F}_2$ transition) for the higher excited state ${}^5\text{D}_1$. Different fitting models have been used: (a) double exponential, (b) single exponential, and (c) single logarithmic. For all the plots, the fitting curves are shown along with the corresponding correlation coefficients (R^2).

S8.5. References for the Supporting Information

- [S1] P. Serna-Gallén, H. Beltrán-Mir, E. Cordoncillo, R. Balda, J. Fernández, *J. Alloys Compd.* 953 (2023) 170020.

Chapter 9

Practical guidance for easily interpreting the emission and physicochemical parameters of Eu^{3+} in solid-state hosts



Article 7

Ceramics International (2023)

<https://doi.org/10.1016/j.ceramint.2023.01.141>

Practical guidance for easily interpreting the emission and physicochemical parameters of Eu³⁺ in solid-state hosts

Pablo Serna-Gallén, Héctor Beltrán-Mir, Eloísa Cordoncillo

Departamento de Química Inorgánica y Orgánica, Universitat Jaume I, Av. Vicent Sos Baynat s/n 12071, Castelló de la Plana, Spain

Special Issue on Photoluminescence of Rare Earth Doped Materials

Journal Impact Factor: 5.2

Quartile: Q1

Category: Materials Science, Ceramics

Position: 3/28

Abstract

Materials doped with the luminescent Eu^{3+} ion are attracting an ever-increasing amount of attention due to their potential applications in solid-state lighting, display devices, solar cells, or bioanalytics. But, why Eu^{3+} ? Unlike other lanthanides, its electronic features make the calculation of some physicochemical parameters quite straightforward, since they can be extracted directly from the emission spectrum. Highly appreciated for its reddish emission, the luminescent ion has also been widely used as a site-sensitive structural probe. With this in mind, this paper aims to offer easy guidance with helpful advice on how to interpret measurements of the emission spectra. It also presents the most useful tools for saving time, and gives a focused and practical explanation of the theoretical concepts involved.

Keywords: Europium; Lanthanides; Emission Spectra; Luminescence; Solid State

9.1. Introduction

The term luminescence (from Latin *lumen* and *essentia*) was coined in 1888 by the physicist Eilhard Wiedemann to distinguish incandescence (emission of light caused by heat) from other physical phenomena in which the emission of light did not depend exclusively on a rise in temperature [1]. When it comes to photoluminescence (a result of the de-excitation of absorbed photons), the trivalent europium ion (Eu^{3+}) emerges as a crucial lanthanide (Ln^{3+}) due to its top-notch optical properties.

The application of Eu^{3+} -doped materials, especially inorganic solids, covers a vast range of areas such as solid-state lighting, display devices, solar cells, optical detectors, medical imaging, and tumor detection, inter alia [2–4]. The current energy scenario comprises a globally increasing demand, with prices skyrocketing, and problems to guarantee a reliable supply of energy that is starting to have a significant impact on socio-economic welfare [5]. This situation has pushed the scientific community to become more committed than ever to developing cutting-edge materials, and energy-saving and energy-efficient technologies, with a particular focus on solid-state illumination [6,7].

The vast majority of papers, reviews, or books about Ln^{3+} luminescence are intended for specialist audiences and experienced spectroscopists, and leave non-experts struggling to follow them. To overcome this, in the past decade, two reviews have been published about the interpretation and comprehension of some misconceptions concerning the emission spectra of Eu^{3+} -doped materials [8,9]. The detailed studies offer a good explanation of some interesting physical parameters of Eu^{3+} and structural properties, and provide examples of different compounds (complexes, hybrids, oxides, etc.). However, they do not go deeply enough into the common problems that scientists can find in a laboratory routine.

Given the foregoing, this review intends to offer practical, easy guidance for researchers, with helpful advice in all the sections, as well as presenting the most promising tools (free software packages, databases, examples, etc.) that can save them a lot of time in the calculation of some physicochemical parameters (phonon energies and refractive indices of the host lattices, color coordinates, branching ratios, asymmetry ratio, and Judd Ofelt parameters). In addition, to facilitate a better comprehension of the physics involved, every section has a short theoretical background that starts from a basic knowledge perspective and raises possible questions that scientists may come up with. Therefore, let scientists record the emission spectrum and *Fiat lux*.

9.2. Electronic features

9.2.1. Energy levels

The electronic configuration of Eu^{3+} is $[\text{Xe}]4f^6$. The $4f$ electrons can be arranged in different microstates in the seven $4f$ orbitals. These microstates are grouped into different terms of energy whose degeneracy is given by the expression $(2S + 1)(2L + 1)$, where S is the total spin quantum number and L is the total orbital angular momentum quantum number.

In addition, the degeneracy of terms can be lost because of spin-orbit coupling, and a new parameter is introduced: J , the total angular quantum momentum, which takes values from $|L + S|$, $|L + S| - 1$, (...), to $|L - S|$. So, each value of J gives a different level of energy. If crystal-field effects are considered, these energy levels can also be divided into sublevels, commonly called Stark levels [10]. **Figure 9.1(a)** depicts an energy diagram showing the different Eu^{3+} free-ion levels without considering the crystal-field effects because they depend on the host material. As an example, **Figure**

9.1(b) highlights the theoretical Stark splitting of the 7F_0 levels of Eu^{3+} -doped KPb_2Cl_5 with C_2/C_s site symmetry as reported by C. Cascales *et al.* [11]. The energy values were obtained from [11] and [12].

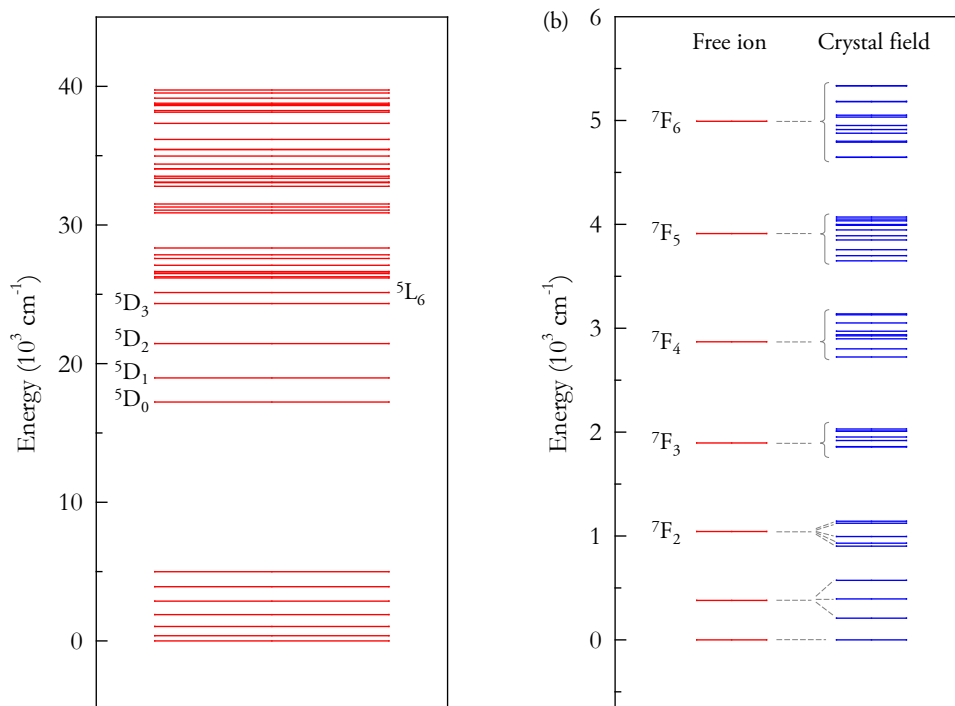


Figure 9.1. (a) Energy level diagram for the Eu^{3+} free-ion (not considering crystal field effects). (b) Example of the Stark splitting of the 7F_0 levels due to the crystal field effect in a Eu^{3+} -doped sample of KPb_2Cl_5 .

9.2.2. Some basics about symmetry and electronic transitions

In spectroscopy, electronic transitions are governed by selection rules, which determine whether such transitions can occur or not. By far one of the most widely known is the Laporte selection rule, which essentially states that for a transition to be allowed in centrosymmetric systems, the parity of the electronic states involved must change [13]. Understanding this selection rule from a theoretical point of view

commonly requires a profound solid basis in quantum mechanics and group theory, as usually found in the literature [14]. With this in mind, this paper intends to offer a proper view of the fundamentals of electronic transitions without entering into details in great depth.

The probability of an electronic transition occurring is related to the transition moment integral:

$$\int_{-\infty}^{\infty} \Psi_i^* \vec{\mu} \Psi_f d\tau = \langle \Psi_i | \vec{\mu} | \Psi_f \rangle \quad (9.1)$$

where Ψ_i and Ψ_f are the wave functions of the initial and final states, respectively, $\vec{\mu}$ is the transition moment operator, and $d\tau$ is the volume element. If this integral is zero, such electronic transition will not occur (it is forbidden). If the integral has a non-zero value, however, the transition will be allowed [15].

In order to know whether a transition is allowed or not, it is just necessary to determine the symmetry of the transition moment function $\Psi_i^* \vec{\mu} \Psi_f$. Considering the symmetry labels for the initial (Γ_i) and final (Γ_f) states, and for the operator of the transition being considered (Γ_μ), the direct product can be expressed as:

$$\Gamma_i \otimes \Gamma_\mu \otimes \Gamma_f \quad (9.2)$$

For the transition to be allowed, the decomposition of the direct product must strictly contain the totally symmetric irreducible representation Γ_1 (which is even with respect to all symmetry operations). Γ_1 can be denoted on a character table by one of the following Mulliken symbols: A , A' , A_g , A_1 , A'_1 or A_{1g} , depending on the symmetry group. Note that when considering centrosymmetric systems (with gerade, g , even symmetry) $\Gamma_1 \equiv A_g$ or A_{1g} [16,17].

The $4f$ orbitals of lanthanide ions have u (ungerade, odd) symmetry, see **Figure 9.2**. Therefore, for intraconfigurational transitions ($4f$ - $4f$ transitions), we obtain that $\Gamma_i \otimes \Gamma_f \equiv u \otimes u = g$. Consequently, the viability of the transition taking place depends on the symmetry (parity) of the transition moment operator $\vec{\mu}$, which is linked to the character of each electronic transition. If $\vec{\mu}$ has u symmetry, then the direct product yields an ungerade symmetry ($\Gamma_1 \equiv u \otimes g = u$) and the transition is forbidden, since the corresponding decomposition cannot contain the gerade A_g/A_{1g} term. In contrast, if $\vec{\mu}$ has g symmetry, the direct product yields a gerade symmetry ($\Gamma_1 \equiv g \otimes g = g$) and the transition is allowed, a priori. However, when considering the site symmetry of the Eu^{3+} ion embedded in the host lattice, it might be possible to obtain a gerade symmetry but with a term different to A_g/A_{1g} such as E_g or B_{1g} , thus making the transition forbidden.

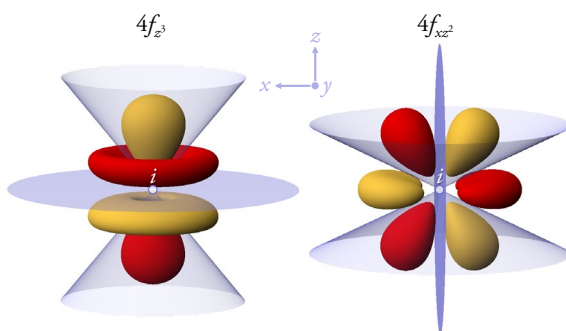


Figure 9.2. Shape of two $4f$ atomic orbitals highlighting in lilac the planar and conical nodes, whose interjection point generates the inversion center (i). Yellow zones represent regions where the wave function Ψ is positive, while the red regions denote negative values. f orbitals are ungerade, since the symmetry operation $\hat{i}\Psi(x, y, z) \neq -\Psi(x, y, z)$, where \hat{i} is the symmetry operator of i .

Additionally, it is worth mentioning the relevance of polarized measurements in the acquisition of the emission spectrum of Eu^{3+} -doped anisotropic crystals with non-cubic lattices. In these experiments, the emitted light is polarized and the presence of

the emission bands is subjected to the site symmetry that occupies the dopant in the lattice and the corresponding selection rules [9]. In this case, the transition moment function would be defined by $\Psi_i^* \vec{\mu}_\alpha \Psi_f$, with $\alpha = x, y, z$, depending on the polarization. If the operators $\vec{\mu}_x$, $\vec{\mu}_y$, and $\vec{\mu}_z$ have different irreducible representations, the selection rules for different linearly polarized light are distinguishable. Further details can be found in reference [18].

9.2.3. Understanding the character of electronic transitions in lanthanides

Depending on their dipole nature, we can group the electronic transitions of Ln^{3+} ions into three types: electric dipole (ED), magnetic dipole (MD), and electric quadrupole (EQ) transitions [9].

Most of the transitions observed in the luminescence spectra of Ln^{3+} ions are *electric dipole transitions*. Such a transition arises as a consequence of the interaction of the lanthanide ion with the electric field component of light by generating an electric dipole. The creation of a dipole involves a linear motion of the charge. The electric dipole operator \vec{P} has *u* symmetry. Therefore, intraconfigurational ED transitions are forbidden. Notwithstanding, when the Ln^{3+} ions are subjected to a crystal field, the selection rules are relaxed and the transitions become partially allowed. One of the main contributions of this relaxation is ascribed to the *J*-mixing effect, which points out that states with different *J* quantum numbers can be mixed due to the crystal field potential and can lead to a change in the energy level positions [19]. From a theoretical point of view, these mixed states are reflected on the expression of the crystal-field Hamiltonian because additional terms are introduced. As the ED transitions observed in the luminescence spectra of lanthanides come about

as a result of a perturbation, they are weaker than ordinary (or free-ion) ED transitions, so they are usually called *induced electric dipole transitions*.

On the other hand, *magnetic dipole transitions* originate from the interaction of the lanthanide ion with the magnetic field component of light by generating a magnetic dipole. Magnetic dipole radiation can be visualized as a rotational displacement of the charge. Since the direction of rotation does not change when applying an inversion with respect to an inversion center, the magnetic dipole operator \vec{M} has *g* symmetry and, therefore, *4f-4f* magnetic dipole transitions are allowed. Moreover, the intensity of this type of transition is relatively independent of the environment of the Ln^{3+} ion in the crystal lattice. This independency is ascribed to the fact that no crystal field effects are expected to affect MD transitions since the magnetic susceptibility (in a nonmagnetic medium) is the same as for vacuum. Consequently, the crystal field wave functions are not needed in the calculation of the intensities of MD transitions and only the free-ion wave functions are considered. Thus, a simple cubic dependence of the MD transition rate, A_{MD} , can be established with the refractive index of the material, n [20–22].

Finally, *electric quadrupole transitions* arise from charge displacement with a quadrupole nature. An electric quadrupole consists of four-point charges with a net charge and dipole moment equal to zero. We can visualize it as two dipoles joined in such a way that their dipole moments cancel each other out [23]. The electric quadrupole operator \vec{Q} has *g* symmetry and EQ transitions are allowed. However, although there are theoretical calculations that postulate the existence of these transitions, there is still no experimental evidence supporting them. For better comprehension, **Figure 9.3** plots the electric dipole \vec{P} , magnetic dipole \vec{M} , and electric quadrupole \vec{Q} moments for a particular distribution of point charges.

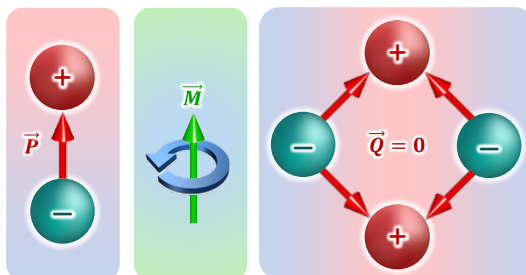


Figure 9.3. Schematic representation of the electric (\vec{P}) and magnetic (\vec{M}) dipole moment, and electric quadrupole (\vec{Q}) moment for a distribution of point charges.

9.3. Some useful considerations about the emission spectra

9.3.1. General assignment of the bands

In an emission spectrum of Eu^{3+} , the bands observed are commonly associated with the ${}^5\text{D}_0 \rightarrow {}^7\text{F}_j$ transitions, since ${}^5\text{D}_0$ is the metastable and lowest-lying excited state. Emissions from higher excited states (${}^5\text{D}_{1,2,3}$) to the ${}^7\text{F}_j$ levels can also be detected in some crystal matrices, although low phonon energy is required, as will be addressed later on. Thus, for the vast majority of researchers, special interest must be paid to ${}^5\text{D}_0 \rightarrow {}^7\text{F}_j$ transitions, especially for $J = 0-4$, since the ${}^5\text{D}_0 \rightarrow {}^7\text{F}_{5,6}$ ED transitions ($\lambda_{\text{em}} > 750 \text{ nm}$) are hardly ever detected with conventional spectrofluorometers due to sensitivity reasons [24]. **Table 9.1** summarizes the character of the main transitions and the approximate region of the emission spectrum in which the corresponding bands usually appear (in wavelength, wavenumber, and eV units) [25–27]. It has also to be mentioned that due to the crystal field effect generated by the surrounding ions of Eu^{3+} in the host lattice, the ${}^5\text{D}_0 \rightarrow {}^7\text{F}_j$ transitions can have different components depending on the site symmetry, as will be discussed later in Section 7.6. An example of this splitting has been illustrated previously in **Figure 9.1(b)**.

Table 9.1. Band assignment of the main electronic transitions of Eu^{3+} and dipole character.

Transition	Character	λ_{em} (nm)	Energy (cm^{-1})	Energy (eV)
$^5\text{D}_0 \rightarrow ^7\text{F}_0$	ED	580	17250	2.15
$^5\text{D}_0 \rightarrow ^7\text{F}_1$	MD	590	16700	2.10
$^5\text{D}_0 \rightarrow ^7\text{F}_2$	ED	615	16300	2.00
$^5\text{D}_0 \rightarrow ^7\text{F}_3$	ED	650	15400	1.90
$^5\text{D}_0 \rightarrow ^7\text{F}_4$	ED	690	14500	1.80

9.3.2. The phonon energy and how to properly discriminate emissions from higher excited states

Most of the compounds containing Eu^{3+} possess a reddish emission due to the presence of $^5\text{D}_0 \rightarrow ^7\text{F}_j$ transitions. In a common excitation spectrum of Eu^{3+} (which is recorded fixing the emission wavelength), the band corresponding to the $^7\text{F}_0 \rightarrow ^5\text{L}_6$ transition (≈ 395 nm) usually has the highest intensity (without considering possible charge transfers from the host lattice). According to the energy level diagram depicted previously in **Figure 9.1**, when Eu^{3+} ions are excited to the $^5\text{L}_6$ state, rapid non-radiative multiphonon relaxations usually occur and Eu^{3+} ions reach the metastable and lowest-lying excited state ($^5\text{D}_0$), from which the transitions to the $^7\text{F}_j$ ground state manifold take place [28]. Therefore, as this de-excitation process is fast, the luminescence from the upper $^5\text{D}_j$ states is not usually observed [29]. The presence of bands associated with emissions from the higher excited states ($^5\text{D}_{1,2,3}$) critically depends upon two factors: (1) the phonon energy of the host lattice, and (2) the concentration of Eu^{3+} ions.

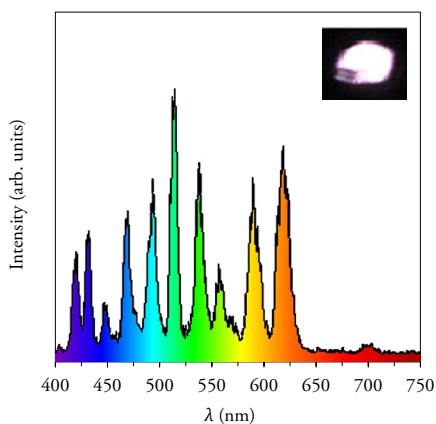
The cut-off phonon energy of a host lattice can be ascribed to the highest-energy vibrational mode. Ideal host materials should therefore have low lattice phonon

energies to avoid luminescent quenching processes and reach high quantum yields. Host materials containing heavy halides (Cl, Br, I) display very low cut-off phonon energies (generally below 300 cm^{-1}), but their hygroscopic nature and low chemical stability prevent them from being applied to practical uses. On the other hand, oxides exhibit good chemical stability, although they commonly present higher phonon energies ($> 550\text{ cm}^{-1}$) and consequently the quantum yields tend to be low [30]. In contrast, fluoride-based materials not only have good chemical stability but also low phonon energies ($300\text{--}550\text{ cm}^{-1}$), which makes them exceptional host materials for luminescent ions [31,32]. **Table 9.2** summarizes the cut-off phonon energy of some common host lattices used for Ln^{3+} doping [33–35]. For the specific examples, most of the values were obtained from the JARVIS-DFT database [36]. This repository is focused on density functional theory (DFT) predictions of material properties, especially for crystalline materials. JARVIS-DFT is a part of the NIST-JARVIS project (National Institute of Standards and Technology-Joint Automated Repository for Various Integrated Simulations). This database and tools contain very useful information for the description of host lattices, especially taking into account their (electro/thermo)dynamic features.

On this basis, host lattices with low phonon energy that also contain low doping concentrations of trivalent europium will probably exhibit emission lines from the different $^5\text{D}_j$ excited states covering the whole visible spectral region that can yield a global white light emission: $^5\text{D}_3$ (blue), $^5\text{D}_2$ (blue-green), $^5\text{D}_1$ (green-yellow), and $^5\text{D}_0$ (orange-red) [37]. As an example, **Figure 9.4** shows the emission spectrum of 1 mol% Eu^{3+} -doped CaIn_2O_4 prepared by X. Liu *et al.* [38].

Table 9.2. Cut-off phonon energy (PE) of some common host lattices used for Ln³⁺ doping and some specific examples.

Host lattice	PE (cm ⁻¹)	Example	PE (cm ⁻¹)
Borate	1300–1400	YBO ₃	1300
Phosphate	1000–1200	YPO ₄	1050
Silicate	900–1100	Y ₂ Si ₂ O ₇	1060
Vanadate	800–900	YVO ₄	890
Titanate	600–800	CaTiO ₃	640
Aluminate	600–800	YAlO ₃	650
Simple oxide	550–900	Y ₂ O ₃	600
Indium-based oxide	450–600	CaIn ₂ O ₄	475
Oxyfluoride	400–600	YOF	470
Fluoride	300–550	YF ₃	475
Chloride	200–300	YCl ₃	260
Bromide	170–250	YBr ₃	215
Iodide	150–200	YI ₃	190

**Figure 9.4.** Emission spectrum of 1 mol% Eu³⁺-doped CaIn₂O₄ recorded under an excitation wavelength of 397 nm. The inset shows a luminescent photograph with the resulting white light emission. Adapted with permission from reference [38].

Furthermore, as previously outlined, another substantial aspect to take into account is the Eu^{3+} concentration in the material. If the concentration is high, the Eu^{3+} – Eu^{3+} distance shortens and cross-relaxation phenomena become more probable. This non-radiative process involves partial energy transfer between two neighboring Eu^{3+} ions in the crystal lattice. Thus, the energy emission is quenched in favor of the lower energy level emission according to different mechanisms [39,40]. In order to make this physical process easier to understand, **Figure 9.5** depicts different schemes regarding the cross-relaxation process that can occur from the different excited states between two Eu^{3+} ions. The energy levels of each ion are represented in different colors (red and blue) and the partial energy diagrams have been plotted so as to visualize the similarity between the energy gaps at first glance.

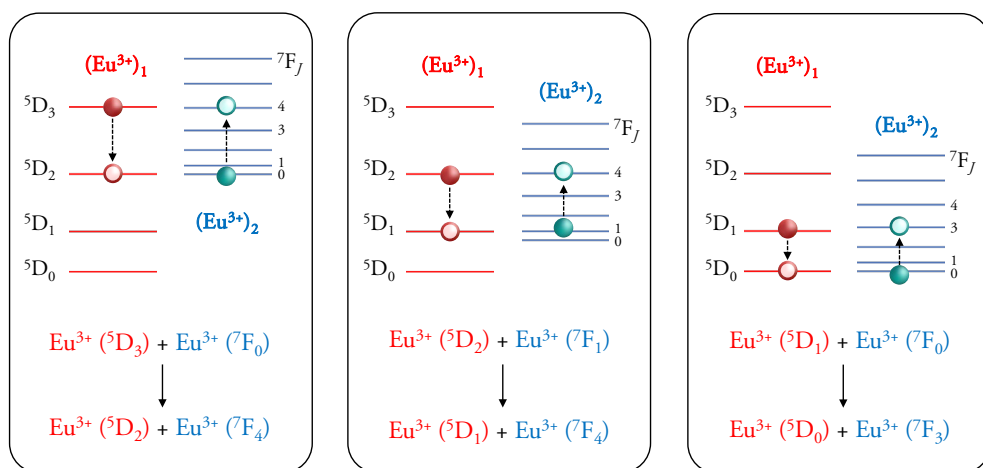


Figure 9.5. Possible cross-relaxation mechanisms occurring between two neighboring Eu^{3+} ions in the crystal lattice.

After addressing the main concepts concerning the emission from higher excited states, one of the major problems to face is how to discriminate these emissions and properly assign the corresponding bands of the whole emission spectrum of a Eu^{3+} -

doped sample. When emissions from all the 5D_j excited states (or some of them) take place, the mixing (convolution) of some bands is expected due to the small energy difference of different transitions, especially in the yellow-orange region of the spectrum, where the significant ${}^5D_0 \rightarrow {}^7F_{1,2}$ transitions appear. The simplest way to discriminate the transitions occurring from the higher excited states (${}^5D_{1,2,3}$) from those occurring from the lowest-lying excited state (5D_0) is to record the emission spectrum of a sample at different detector delay times (DT). Increasing the DT will suppress the emissions from the ${}^5D_{1,2,3}$ higher energy states, since they have shorter lifetimes in comparison with transitions from the 5D_0 ground state.

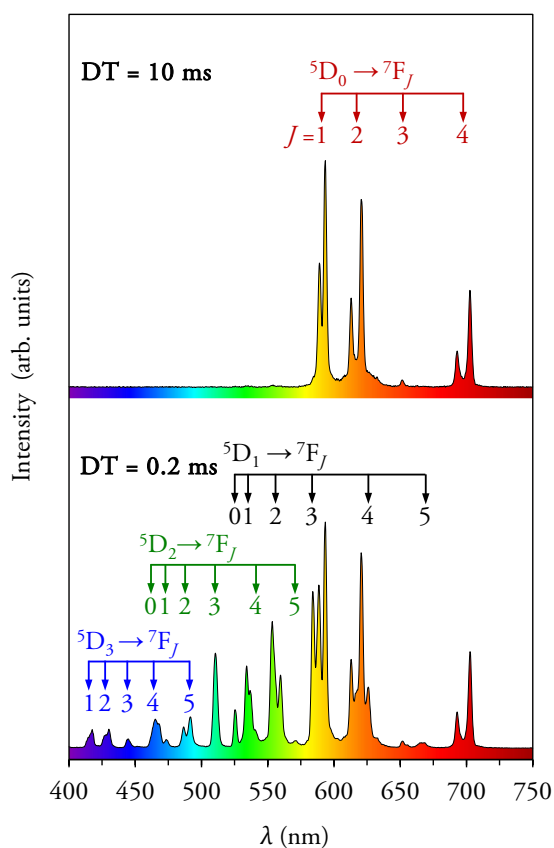


Figure 9.6. Emission spectra obtained with delay times (DT) of 0.2 and 10 ms upon excitation at 395 nm for 1 mol% Eu^{3+} -doped $\alpha\text{-KY}_3\text{F}_{10}$. Reprinted with permission from reference [41].

As an example, **Figure 9.6** shows the emission spectra of α -KY₃F₁₀ powder doped with 1 mol% Eu³⁺ [41]. With a DT = 0.2 ms, the spectrum exhibits a complex behavior due to the mixing of ⁵D₀₋₃→⁷F_J transitions. However, when the DT is increased to 10 ms, only the contribution of ⁵D₀→⁷F_J transitions is observed. See, for instance, the difference in the peak splitting in the yellow-orange region of the spectrum (three components with DT = 0.2 ms, and two components with DT = 10 ms).

9.3.3. The emission color: CIE *xy* coordinates

In Solid State Science, the description and quantification of the emission color of a phosphor are of paramount relevance, since it allows comparison with other materials and provides a direct connection with the luminescence spectral features. The color of any visible light emission can be illustrated using the CIE (*Commission Internationale de l'Eclairage*) 1931 chromaticity diagram, also known as the CIE *xy* diagram, which is a universally accepted system for representing the composition of color through three primary colors (blue, green, and red) [42,43].

The calculation of color coordinates is based on the formulations of the CIE system set up in 1931. As color is three-dimensional, it can be characterized by an (*x*, *y*, *z*) set, where the different coordinates correspond to the red, green, and blue components, respectively. Notwithstanding, given that $x + y + z = 1$, it is enough to define an (*x*, *y*) pair to represent the color in a plane (2D) graph, since the *z* coordinate can be inferred from the other two. The white light emission point is located at the center of a CIE *xy* diagram, **Figure 9.7**, with chromatic coordinates $x = 0.33$ and $y = 0.33$ [44,45].

The *xy* coordinates can be calculated from the emission spectrum of a phosphor using different equations described in the literature [46]. However, sometimes it can be time-consuming but different free software packages and computational tools are

available online. Some useful examples are: GoCIE [47], CIE Coordinate Calculator (works with a MATLAB routine) [48], and Chromaticity Diagram (a complement to be used in Origin) [49]. The file containing the emission spectrum data can be uploaded, the chromatic coordinates are calculated, and they can also be plotted in a CIE diagram.

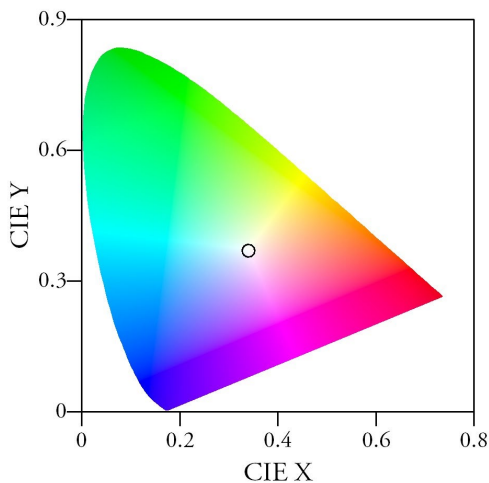


Figure 9.7. CIE chromaticity diagram. The white light emission point is located at its center (indicated with an empty circle in the figure).

9.4. The asymmetry ratio

9.4.1. Determination of the branching ratios

A theoretical approach for branching ratios can be used to predict the intensity of different emission lines [50]. However, most of the emphasis is commonly placed on the experimental branching ratios (β_j), which can be obtained directly from the emission spectra of the lanthanide ion taking into account the relative areas of the bands. For example, considering the $^5D_0 \rightarrow ^7F_j$ transitions of Eu^{3+} , the general expression for β_j is:

$$\beta_J = \frac{I_{0J}}{\sum I_{0J}} \quad (9.3)$$

where I_{0J} is the integrated intensity of the ${}^5D_0 \rightarrow {}^7F_J$ transition.

Once the different β_J have been calculated, several physicochemical parameters can be obtained. As regards studies about Eu^{3+} luminescence in the literature, the most calculated and discussed parameter is the asymmetry ratio (R). Europium is highly appreciated among the scientific community due to its feature of acting as a symmetry-sensitive spectroscopic probe, as will be discussed later on. The intensity of the ${}^5D_0 \rightarrow {}^7F_1$ MD transition is relatively independent of the site symmetry of Eu^{3+} ions, while the ${}^5D_0 \rightarrow {}^7F_2$ ED transition has a hypersensitive character, i.e., it is affected to a large extent by the surroundings and crystal field of Eu^{3+} [51]. Therefore, the asymmetry ratio can shed some light on the local environment of this particular lanthanide. Defining I_{02} and I_{01} as the integrated intensity of the ${}^5D_0 \rightarrow {}^7F_2$ and ${}^5D_0 \rightarrow {}^7F_1$ transitions, respectively, R can be extracted from the branching ratios:

$$R = \frac{I_{02}}{I_{01}} = \frac{\beta_2}{\beta_1} \quad (9.4)$$

It is important to note that researchers must avoid the calculus of this parameter using absolute intensities of the bands rather than integrated intensities.

9.4.2. The Jacobian transformation: to do, or not to do

The most common way of recording and presenting the signal data of absorption, emission, or excitation spectra as a function of the electromagnetic spectrum is in wavelength units. However, from a physical point of view, the data should be presented as a function of energy for the cases in which the quantitative analysis of the emission spectra is required. Converting wavelength to energy units (e.g., eV) is quite

straightforward using the familiar equation:

$$E = \frac{h c}{\lambda} \quad (9.5)$$

where h is Planck's constant and c , the speed of light in vacuum. Expressing h in eV·s, c in nm·s⁻¹, and λ in nm, the above expression results in:

$$E \text{ (eV)} = \frac{1239.84}{\lambda \text{ (nm)}} \quad (9.6)$$

Although it might appear that with this transformation everything is solved, it must be recalled that a change in the units of the abscissa axis must also imply a conversion of the signal values (intensity), if not, the integrated area under the curve will differ [52]. This conversion of $I(\lambda)$ to $I(E)$ is called Jacobian transformation. Then, in order to express the signal values properly, the following operation must be applied:

$$I(E) = I(\lambda) \frac{h c}{E^2} = I(\lambda) \frac{\lambda^2}{h c} = I(\lambda) \frac{\lambda(\text{nm})^2}{1239.84} \quad (9.7)$$

At this point, the question that probably comes to mind is whether or not the Jacobian transformation should be performed to calculate the asymmetry ratio accurately, since it is derived from integrated areas.

The use of the Jacobian transformation in an emission spectrum with narrow bandwidth peaks, as is normally the case for Ln³⁺-doped materials, does not have any prominent effects. However, if the spectra have broad bands, this transformation plays a crucial role and must be applied. For further details, see the work of Mooney and Kambhampati addressing this issue [53]. To prove that the Jacobian transformation is not usually required in well-defined emission spectra of Eu³⁺, **Figure 9.8** presents the same data in different units and the resulting asymmetry ratio value. As

highlighted, the difference in the value of R (0.02) is more than negligible. To summarize, the Jacobian transformation can be neglected for the calculation of the asymmetry ratio in the majority of cases.

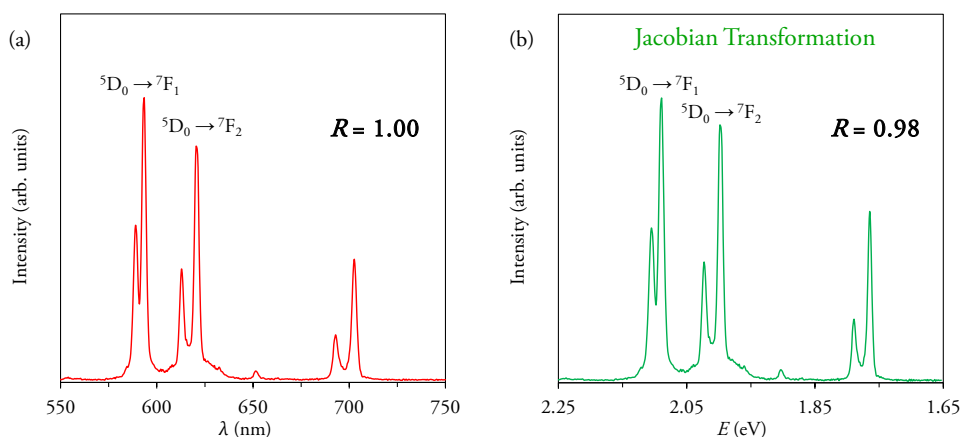


Figure 9.8. Emission spectra of 1 mol% Eu³⁺-doped α-KY₃F₁₀ presented in (a) wavelength and (b) energy units. The asymmetry ratio is indicated for both cases.

9.4.3. Avoid emissions from higher excited states

As previously discussed in Section 9.3.2, when a Eu³⁺-doped sample exhibits emission lines corresponding to transitions from higher excited states (⁵D_{1,2,3}), the emission spectra should also be recorded increasing the DT of the detector so as to effectively suppress the contribution of these transitions. If this experiment is not carried out, substantial errors can be made in the calculation of some physicochemical parameters of Eu³⁺. To underscore this fact, **Figure 9.9** (**Figure 9.6** magnified in the region of interest) depicts the emission spectra of a sample recorded at two different DT. The values of the asymmetry ratio change notably (0.21).

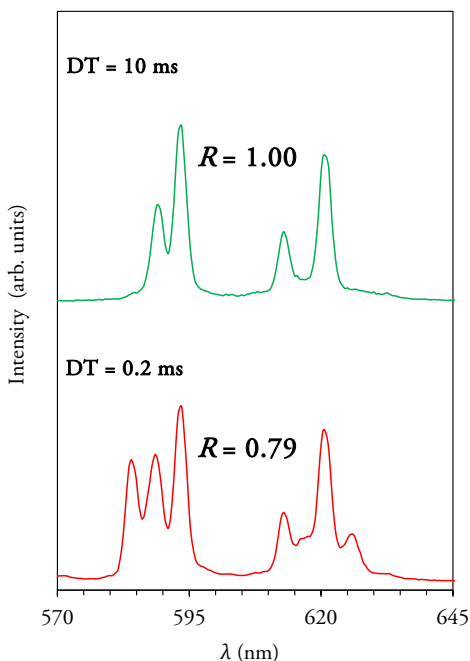


Figure 9.9. Emission spectra obtained with a delay time (DT) of 0.2 and 10 ms upon excitation at 395 nm for 1 mol% Eu^{3+} -doped $\alpha\text{-KY}_3\text{F}_{10}$.

9.4.4. “Unexpected” values and controversy about the asymmetry ratio

A broad statement in the literature about the asymmetry ratio is that the higher the R values are, the more deviation of the Eu^{3+} site from a centrosymmetric geometry there is. In other words, low values of the asymmetry ratio are expected, a priori, when Eu^{3+} ions are located in crystal sites with an inversion center [54]. The detailed works of Tanner [8] and Binnemans [9] highlighted that distortions or deviations from the centrosymmetric geometry of Eu^{3+} generally increase R , but great caution must be paid when comparing the asymmetry ratios of different crystal structures because the ${}^5\text{D}_0 \rightarrow {}^7\text{F}_2$ transition probability also depends on the shape of the coordination polyhedra (as well as the coordination number), and the nature of the ligands (or

surrounding ions) [55]. Therefore, sometimes it can be obtained “unexpected” R values (very small or large) that do not follow the incorrect general statement of the asymmetry ratio tendency.

A good example can be found considering Eu^{3+} -doped YF_3 . In the orthorhombic YF_3 crystal structure, Y^{3+} ions are located at a site with C_s symmetry (which is also the crystallographic symmetry for Eu^{3+} ions replacing Y^{3+}). Of course, C_s is a low symmetry point group (only σ_h and E operations are possible), and without an inversion center. Hence, one could wrongly expect to obtain high R values (higher than unity, since the lack of an inversion center could imply the domination of the ${}^5\text{D}_0 \rightarrow {}^7\text{F}_2$ transition in the emission spectrum), but asymmetry ratio values in the range 0.3–0.5 are obtained [41,56,57]. In fluoride-based materials, it has been quite common to find that the ${}^5\text{D}_0 \rightarrow {}^7\text{F}_1$ MD transition dominates over the ${}^5\text{D}_0 \rightarrow {}^7\text{F}_2$ ED transition. The explanation lies in the high ionicity of $\text{Eu}-\text{F}$ bonds, which allows only a little admixture of opposite parity states to the Eu^{3+} f -states, and it makes the ED transition less favorable and thus with low intensity [58].

Hence, it would be wrong stating that Eu^{3+} ions are located at centrosymmetric sites in orthorhombic YF_3 due to the low R values obtained.

9.5. Judd-Ofelt parameters of Eu^{3+}

9.5.1. Theory and applications: a 60-year history

Occasionally, history is witness to unprecedented, peculiar, unique coincidences in science, as was the appearance of the Judd Ofelt (JO) theory 60 years ago. On August 1, 1962, two independent papers (by two authors who had never met in person) saw the light simultaneously: Brian R. Judd published his work *Optical Absorption*

Intensities of Rare-Earth Ions in the journal *Physical Review* [59], while George S. Ofelt's paper entitled *Intensities of Crystal Spectra of Rare-Earth Ions* appeared in *The Journal of Chemical Physics* [60]. These two articles have been considered a breakthrough in the field of rare-earth spectroscopy. They laid the foundations of what we now know as the JO theory, which in essence is the most powerful tool in optical spectroscopy for the theoretical calculation and prediction of physicochemical parameters of lanthanides and actinides in solids and solutions. The great advantage of the JO theory is that physical parameters such as dipole oscillator strengths, emission intensities, radiative lifetimes, or quantum efficiencies can be calculated by simply using three material-dependent parameters (the famous JO parameters Ω_2 , Ω_4 , and Ω_6) and material-independent squared reduced matrix elements of the unit tensor operator connecting the levels of the transitions of interest (abbreviated as U^2 , U^4 , and U^6) [61,62]. The values of U^λ ($\lambda = 2, 4, 6$) have been tabulated [63,64] and are widely considered invariant for a given Ln^{3+} ion because the position of the J levels is weakly affected by the surrounding ions/atoms [65].

After this brief introduction, one could ask oneself: what is the practical application of the JO parameters in Eu^{3+} -doped materials? Does this theory deserve its prestige? The answer is an unequivocal "yes". Since the appearance of those two initial pieces of research, a plethora and constantly growing number of papers have been published. To support this phenomenon, **Figure 9.10(a)** shows the number of papers including the word "Judd Ofelt" published over the years as determined by Scopus (accessed in October 2022). Perhaps the most outstanding feature is the rapid growth of use of this theory for Eu^{3+} -doped compounds, as highlighted in **Figure 9.10(b)**. The number of papers published was also determined by Scopus by combining the word "Judd Ofelt" with "europium", "Eu", or " Eu^{3+} ".

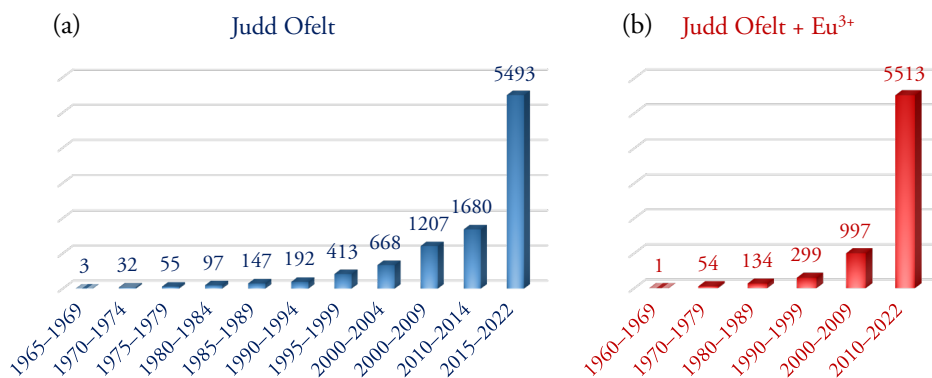


Figure 9.10. Number of papers published including the word (a) “Judd Ofelt”, and (b) “Judd Ofelt” plus “europium”, “Eu”, or “Eu³⁺”. Data were extracted from the Scopus database (accessed in October 2022).

9.5.2. The particular case of Eu³⁺

Traditionally, JO parameters are determined from the absorption spectra of Ln³⁺-doped materials [50]. For the vast majority of rare-earth ions, the calculation of the JO parameters requires a complex mathematical algorithm and also extensive knowledge of quantum mechanics. Readers interested in an in-depth explanation can consult some worthy detailed works in the literature [66,67]. However, the scope of this paper is to provide practical, easy guidance for researchers so they do not have to deal with tedious calculations, rather than just describing the JO equations in full once again, which is something that has already been carried out in many studies.

Unlike other trivalent lanthanide ions, the electronic characteristics of Eu³⁺ make the calculation of the JO parameters quite straightforward, since they can be extracted directly from the emission spectrum. Among all the ⁵D₀→⁷F_{*j*} transitions, only ⁵D₀→⁷F₁ has a magnetic dipole character, while the rest of the transitions are (induced) electric dipole, see **Table 9.1**. As previously stated, the dipole strength of MD transitions is independent of the environment of the Ln³⁺ ion in the host lattice and can be calculated by theory. The dipole strength is directly related to the emission rate (A_{if})

of a $\Psi_i \rightarrow \Psi_f$ transition. Thus, the emission rate for the ${}^5D_0 \rightarrow {}^7F_1$ transition is defined as:

$$A_{01} = n^3 (A_{01})_{\text{vac}} \tag{9.8}$$

where n denotes the refractive index of the material and $(A_{01})_{\text{vac}}$ is the MD transition rate in vacuum (14.65 s^{-1}). Such electronic particularity allows us to use this transition as a reference for the rest of the ${}^5D_0 \rightarrow {}^7F_J$ transitions.

In addition, another important aspect that makes the calculation of Ω_λ quite easy is the fact that all the squared reduced matrix elements U^λ are zero except for the ${}^5D_0 \rightarrow {}^7F_{2,4,6}$ transitions [68], as outlined in **Table 9.3**.

Table 9.3. Reduced matrix elements for the ${}^5D_0 \rightarrow {}^7F_J$ ED transitions of Eu^{3+} .

Transition	U^2	U^4	U^6
${}^5D_0 \rightarrow {}^7F_0$	0	0	0
${}^5D_0 \rightarrow {}^7F_2$	0.0032	0	0
${}^5D_0 \rightarrow {}^7F_3$	0	0	0
${}^5D_0 \rightarrow {}^7F_4$	0	0.0023	0
${}^5D_0 \rightarrow {}^7F_5$	0	0	0
${}^5D_0 \rightarrow {}^7F_6$	0	0	0.0002

The Ω_2 parameter has been associated with the polarizable and covalent character of the Ln^{3+} ion. Thus, it provides useful information about the crystal environment of Eu^{3+} and is considered a short-range parameter [60,69,70]. The reason why the asymmetry ratio R and the Ω_2 parameter in practice provide the same information is that a direct relation between them can be derived for a given material:

$$\Omega_2 = kR \quad (9.9)$$

where k is a constant (see reference [71] for further details). Therefore, interpreting the Ω_2 requires the same caution as with the asymmetry ratio in order to avoid misleading conclusions.

Conversely, Ω_4 and Ω_6 show the long-range effects and are affected by the viscosity and rigidity of the host lattice [72], although it is quite complicated to obtain the Ω_6 parameter from the emission spectra due to the instrumental limitations and the low intensity of the ${}^5D_0 \rightarrow {}^7F_6$ transition. In most cases, this is why only the discussion of Ω_2 and Ω_4 is contemplated for Eu^{3+} -doped materials. It should also be noted that for a correct calculation of the JO parameters from the emission spectrum, the emission from higher excited states, if present, must be suppressed by increasing the DT of the detector, as previously discussed.

9.5.3. Calculus by computational programs

In this section, the most promising tools are briefly presented to calculate the aforementioned parameters of Eu^{3+} using free software packages available online.

To calculate the physicochemical parameters from the experimental emission spectrum, there are two main application software packages of interest: LUMPAC [73] and JOES [74]. LUMPAC was developed in 2014 and allows the calculation of the JO parameters (Ω_2 and Ω_4), radiative (A_{rad}) and non-radiative (A_{nrad}) emission rates, and quantum efficiencies (η). It must be highlighted that if we are only interested in these parameters, the application interface is very easy. LUMPAC also integrates three additional modules that are devoted to other luminescent features, such as calculating ground state geometries of systems containing Ln^{3+} ions. However, to be able to use

these extra modules, it is necessary to work with MOPAC [75] and ORCA [76], which are programs based on semiempirical quantum chemistry that require a higher degree of knowledge about computation.

Some years later, in 2019, the JOES software package was released to complement and improve the existing JO parameterization of the emission spectrum. In addition to the physicochemical parameters obtained by LUMPAC, JOES derives other quantities: the branching ratios (both experimental and theoretical), emission cross-sections (σ_e), and the CIE xy coordinates. It must be highlighted that although the CIE coordinates and diagram can be plotted, we suggest using the previously mentioned GoCIE program for graphical representations because colors, legends, text size/font, and so on can be configured as desired.

As explained above, the Ω_6 parameter is seldom obtained from the emission spectra because the ${}^5D_0 \rightarrow {}^7F_6$ transition (810–840 nm) is commonly outside the limits of detection of the equipment. Moreover, this transition is also very weak due to the low value of the reduced matrix element U^6 (0.0002) and is therefore practically irrelevant for describing the emission features. Notwithstanding, we must recall that in the absorption and excitation spectra, the ${}^7F_0 \rightarrow {}^5L_6$ transition (see Section 3.2) tends to be the dominant one. Hence, for these spectra, Ω_6 (which is only related to this transition) has far more relevance. To overcome this problem, recently, in 2022, the JOEX software has been developed [77], which allows calculation of the three JO parameters from the excitation spectrum. **Figure 9.11** compares the JO parameterization with the corresponding transitions using the excitation and emission spectra.

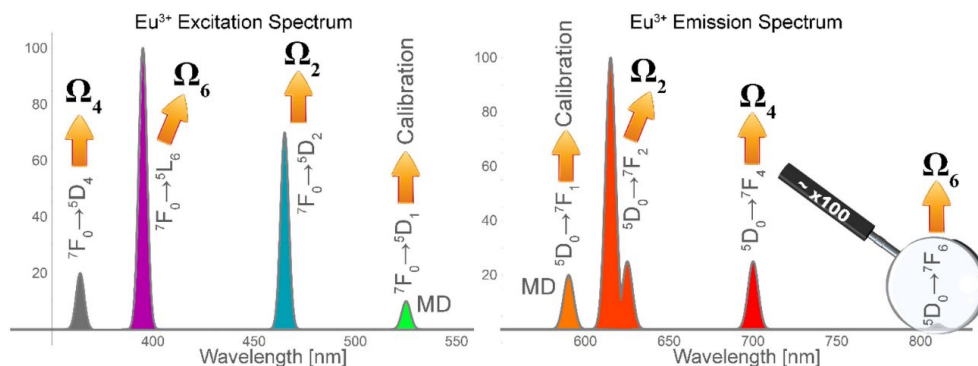


Figure 9.11. Comparison of the JO parameterization with the corresponding transitions using the excitation and emission spectra. Reprinted with permission from reference [77].

9.5.4. No data available for the refractive index

Even though refractive indices for the most common materials can be found in the literature, it could be that some of them are not included in such databases, especially when working with novel materials, different crystal phases, solid solutions, or different doping concentrations. Since the refractive index is required for the calculation of the JO parameter and derivation of other substantial physicochemical parameters, finding an alternative solution is a matter of concern, since having no data available for the refractive index means that no calculations are possible. Herein it is referred a simple theoretical approach that can overcome this problem, without the need to perform ellipsometry measurements that might be complicated for some kinds of materials.

Previous to going deeper into this approach, it is worth mentioning the concept of birefringence, which is defined as the optical property of a material that differs by polarization and light propagation [78]. Birefringence occurs in anisotropic crystals with non-cubic lattices. Therefore, different refractive indices of the materials can be determined depending on the light polarization [79]. Mainly, two types of crystals can

be distinguished: uniaxial and biaxial. Uniaxial crystals are characterized by one optical axis and two refractive indices: n_o (ordinary) and n_e (extraordinary). On the other hand, biaxial crystals can be described by two optical axis and three refractive indices: n_x , n_y , and n_z . The calculation of the birefringence for biaxial crystals is complex, while for the uniaxial materials, it is expressed as:

$$\Delta n = n_e - n_o \quad (9.10)$$

For some crystals, the birefringence value is relevant since it can be in the order 0.1–0.2, as in phosphate-type lattices [80]. After these considerations, the mean refractive index of a material (n) can be calculated for anisotropic crystals as $n = (2n_o + n_e)/3$ for uniaxial crystals, and $n = (n_x + n_y + n_z)/3$ for biaxial crystals [81].

The mean refractive index of a compound can be calculated following the procedure described by Shannon and Fischer using the Anderson-Eggleton equation, which is based on ion polarizabilities [81–83]. They calculated the polarizability parameters from data recorded at a wavelength of 589.3 nm. Therefore, the equations yield the mean refractive indices at 589.3 nm. However, the spectral region in which the ${}^5D_0 \rightarrow {}^7F_{1,2,4}$ transitions occur (600–700 nm) is very close to 589.3 and only small changes in n values are expected. For most compounds, only the second decimal would be affected and this theoretical approach can be of high relevance. See as an example **Figure 9.12**, which highlights the minor deviation of the refractive index in the 600–700 nm range for a simple oxide (Y_2O_3), complex oxides ($Y_3Al_5O_{12}$, $MgAl_2O_4$), and a fluoride (LaF_3). The values were taken from the Mikhail Polyanskiy database [84].

In order to prove the validity of this method, the theoretical mean refractive indices

of the above-mentioned compounds were calculated using the Anderson-Eggleton equation. The crystal structure data were taken from the Springer Materials database [85–88]. The results are summarized in **Table 9.4** and, as highlighted with the relative errors, the theoretical values are extremely close to the reported ones.

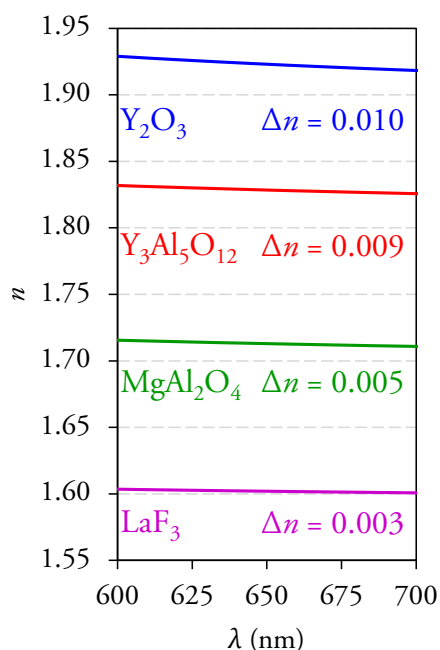


Figure 9.12. Evolution and deviation (Δn) of the refractive index in the 600–700 nm range for Y₂O₃, Y₃Al₅O₁₂, MgAl₂O₄, and LaF₃ compounds.

Table 9.4. Cell volume of the different host lattices (V_{cell}), number of formula units (Z), total polarizability (α_T), mean refractive index calculated (n_{calc}) at 589.3 nm, and relative error (δn) in the calculation of n .

Compound	V_{cell} (Å ³)	Z	α_T (Å ³)	n_{calc}	n_{real}	δn (%)
Y ₂ O ₃	1060.50	16	10.34	1.95	1.93	1.0
Y ₃ Al ₅ O ₁₂	1731.46	8	29.13	1.81	1.83	1.1
MgAl ₂ O ₄	542.34	8	8.01	1.71	1.72	0.6
LaF ₃	329.98	6	6.04	1.65	1.60	3.1

9.6. Inferring the site-selective symmetries of Eu^{3+}

When Eu^{3+} ions are embedded in a host lattice, they usually substitute other cations. This replacement can be isoelectronic (e.g., $\text{Y}^{3+} \leftrightarrow \text{Eu}^{3+}$ in Y_2O_3) or non-isoelectronic (e.g., $\text{Ca}^{2+} \leftrightarrow \text{Eu}^{3+}$ in CaF_2 , or $\text{Ti}^{4+} \leftrightarrow \text{Eu}^{3+}$ in TiO_2 , which imply the generation of ionic vacancies [89–91]). Quite often, these substitutions produce low deviations in the crystal lattice, breaking the ideal site-symmetry of the host ions. One of the reasons explaining these deviations is the difference in the ionic radius between the host and the dopant ion. To have a better comprehension of the site-substitution, knowing the values of Eu^{3+} ionic radii for different coordination numbers (CN) is of great interest. However, the well-known Shannon's radii database lacks all the values for Eu^{3+} in a $\text{CN} > 9$ [92], which is a drawback since host ions with such CN are quite common in solid-state materials, e.g., $\text{CN}(\text{Ca}^{2+}) = 12$ in CaTiO_3 perovskite. To fill this gap, Jia [93] proposed an empirical formula to calculate the unknown crystal radii of trivalent and divalent rare earth ions with $6 \leq \text{CN} \leq 12$. **Table 9.5** shows the ionic radii of Eu^{3+} with different coordination numbers. Apart from that, dopants can also be distributed irregularly in the particles of a compound, resulting in different site occupations. One recurrent example can be found in the interfaces or grain boundaries of a particle, since Eu^{3+} ions occupying their vicinities tend to possess low symmetries and present broad signals and non-well-resolved emission spectra [94,95].

Table 9.5. Ionic radii (\AA) of Eu^{3+} with different coordination numbers (CN).

CN = 6	CN = 7	CN = 8	CN = 9	CN = 10	CN = 11	CN = 12
0.947	1.01	1.066	1.12	1.17	1.23	1.28

Widely discussed in the literature, the particular features of the trivalent europium ion make it possible to use it as a site-sensitive structural probe. Both the $^5\text{D}_0$ and $^7\text{F}_0$

states are non-degenerate ($J = 0$). Thus, if the frequency of the pumping excitation source is tuned over the inhomogeneous bandwidth of the ${}^7F_0-{}^5D_0$ transition, the Stark splitting observed in the emission spectrum will only result from the local crystal field of Eu^{3+} ions situated at a given site with a corresponding point group symmetry [96]. However, it must be highlighted that to record an emission spectrum with high resolution, the temperature must be as low as possible to avoid vibronic contributions. Because of this, the most powerful spectroscopic technique to perform these experiments is laser-induced fluorescence line narrowing (FLN), which requires the use of cryogenic working conditions [97].

Table 9.6. Point group assignment according to the number of emission bands of ${}^5D_0 \rightarrow {}^7F_{0-4}$ transitions. Adapted with permission from reference [8].

Symmetry class	Point group	7F_0	7F_1	7F_2	7F_3	7F_4	Symmetry class	Point group	7F_0	7F_1	7F_2	7F_3	7F_4
Icosahedral	I_h	0	1	0	0	0	Tetragonal	C_4	1	2	2	3	5
Cubic	O_h, T_h	0	1	0	0	0		S_4	0	2	3	4	4
	O	0	1	0	1	1		D_{2d}	0	2	2	3	3
	T_d	0	1	1	1	1	Trigonal	D_{3d} C_{3i}	0	2	0	0	0
	T	0	1	1	2	2		D_3	0	2	2	4	4
Octagonal	D_{4d}	0	2	0	1	2		C_{3v}	1	2	3	3	5
Hexagonal	D_{6h}, C_{6h}	0	2	0	0	0		C_3	1	2	3	5	6
	D_6	0	2	1	2	1	Orthorhombic	D_{2h}	0	3	0	0	0
	C_{6v}, C_6	1	2	2	2	2		D_2	0	3	3	6	6
	D_{3h}	0	2	1	2	3		C_{2v}	1	3	4	5	7
	C_{3h}	0	2	1	3	4	Monoclinic	C_{2h}	0	3	0	0	0
Tetragonal	D_{4h}, C_{4h}	0	2	0	0	0		C_2, C_s	1	3	5	7	9
	D_4	0	2	1	3	3	Triclinic	C_1	1	3	5	7	9
	C_{4v}	1	2	2	2	4		C_i	0	3	0	0	0

Therefore, it is reasonable to infer the site-selective symmetries of Eu^{3+} ions by analyzing the emission profile and the number of Stark components for each ${}^5\text{D}_0 \rightarrow {}^7\text{F}_j$ transition (see **Table 9.6**). Special attention should be paid to the ${}^5\text{D}_0 \rightarrow {}^7\text{F}_{0-4}$ splitting, and care should be taken with the ${}^5\text{D}_0 \rightarrow {}^7\text{F}_{5,6}$ transitions because the number of J components observed is usually lower than the predicted ones due to overlapping between the emission lines.

9.7. Conclusions

In this review, a brief introduction to the electronic features of the luminescent Eu^{3+} ion is first presented in order to lay the foundations for some remarks on optical spectroscopy in Sections 9.1 and 9.2. This description is followed by some important symmetry concepts that allow a good comprehension of the character of electronic transitions in lanthanides (ED, MD, and QD).

Section 9.3 provides some useful insights that help properly interpret the emission spectrum of Eu^{3+} . Aspects discussed include how to assign the bands correctly while being careful to consider possible emissions associated with transitions from higher excited states (${}^5\text{D}_{1,2,3}$). Detailed information regarding the phonon energy of solid materials with some common examples is also included. Moreover, the cross-relaxation phenomena are discussed in order to have a deeper understanding of the physical processes involved when emissions from different excited states occur. The quantification of the color emission of a phosphor by the CIE xy diagram is presented, focusing on the low time-consuming free software packages available for researchers.

Section 9.4 gives practical advice about the calculation and interpretation of the asymmetry ratio, which is probably the most discussed parameter in the literature on the Eu^{3+} emission. The asymmetry ratio should be calculated from the emission

spectrum with a proper detector delay time, while the Jacobian transformation is not required in most cases. Additionally, a short explanation of some misconceptions about this parameter is also presented.

Section 9.5 is devoted to the famous Judd Ofelt parameters. After explaining the history and some minor concepts of this theory, it is noted how the explosion of works using this parameter (most of them about Eu^{3+} -doped materials) is mainly due to the electronic peculiarities of this lanthanide. Following on with the practical character of this review, the most interesting computational programs are commented on to facilitate the scientist's work. Attention is also drawn to the methodology presented, which allows the refractive indices of a material to be calculated theoretically when there is no data available.

Finally, Section 9.6 briefly reviews some interesting facts and advice about the utility of using Eu^{3+} as a site-sensitive structural probe that can be useful for understanding the structure-property relation of a material.

Acknowledgments

This work was supported financially by the Spanish MCIN (Grant PID2020-116149GB-I00 funded by MCIN/AEI/10.13039/501100011033) and the Universitat Jaume I (Project UJI-B2019-41). P. Serna also thanks the Spanish MCIN for an FPU predoctoral contract (FPU18/04511 funded by MCIN/AEI /10.13039/501100011033 and by “ESF Investing in your future”).

References

- [1] B. Valeur, M.N. Berberan-Santos, *J. Chem. Educ.* 88 (2011) 731–738.
- [2] J. Song, C. Zhang, C. Xu, Y. Qiang, A. Lu, L. Han, *Appl. Phys. A Mater. Sci. Process.* 128 (2022) 1–10.
- [3] H. Groult, J. Ruiz-Cabello, J. Pellico, A. V. Lechuga-Vieco, R. Bhavesh, M. Zamai, E. Almarza, I. Martín-Padura, E. Cantelar, M.P. Martínez-Alcázar, F. Herranz, *Bioconjug. Chem.* 26 (2015) 153–160.
- [4] B. Song, M. Li, J. Ren, Q. Liu, X. Wen, W. Zhang, J. Yuan, *New J. Chem.* 46 (2022) 9658–9665.
- [5] A. Omri, F. Belaïd, *J. Environ. Manage.* 278 (2021) 111483.
- [6] R. Devi, R. Boddula, J. Tagare, A.B. Kajjam, K. Singh, S. Vaidyanathan, *J. Mater. Chem. C* 8 (2020) 11715–11726.
- [7] B. Verma, R.N. Baghel, D.P. Bisen, N. Brahme, V. Jena, *Opt. Mater. (Amst)*. 123 (2022) 111787.
- [8] P.A. Tanner, *Chem. Soc. Rev.* 42 (2013) 5090–5101.
- [9] K. Binnemans, *Coord. Chem. Rev.* 295 (2015) 1–45.
- [10] R. Reisfeld, *AIMS Mater. Sci.* 2 (2015) 37–60.
- [11] C. Cascales, J. Fernández, R. Balda, *Opt. Express*. 13 (2005) 2141–2152.
- [12] K. Binnemans, *Bull. Des Soc. Chim. Belges*. 105 (1996) 793–798.
- [13] O. Laporte, W.F. Meggers, *J. Opt. Soc. Am. Rev. Sci. Instruments*. 11 (1925) 459–463.

- [14] M.S. Dresselhaus, G. Dresselhaus, A. Jorio, *Group theory. Application to the Physics of Condensed Matter*, Springer, 2008.
- [15] R.C. Maurya, J.M. Mir, *Molecular Symmetry and Group Theory. Approaches in Spectroscopy and Chemical Reactions*, De Gruyter, 2019.
- [16] A. De Bettencourt-Dias, *Introduction to Lanthanide Ion Luminescence*, in: A. De Bettencourt-Dias (Ed.), *Lumin. Lanthan. Ions Coord. Compd. Nanomater.*, Wiley, 2014: pp. 1–48.
- [17] I. Gutman, O.E. Polansky, *Mathematical Concepts in Organic Chemistry*, Springer, 1986.
- [18] Y. Wang, G. Yu, M. Rösner, M.I. Katsnelson, H.Q. Lin, S. Yuan, *Phys. Rev. X* 12 (2022) 21055.
- [19] A.S. Souza, M.A. Couto Dos Santos, *Chem. Phys. Lett.* 521 (2012) 138–141.
- [20] G. Nienhuis, C.T.J. Alkemade, *Phys. B+C* 81 (1976) 181–188.
- [21] C. Görller-Walrand, L. Fluyt, A. Ceulemans, W.T. Carnall, *J. Chem. Phys.* 95 (1991) 3099–3106.
- [22] Z. Wang, T. Senden, A. Meijerink, *J. Phys. Chem. Lett.* 8 (2017) 5689–5694.
- [23] N. Papasimakis, V.A. Fedotov, V. Savinov, T.A. Raybould, N.I. Zheludev, *Nat. Mater.* 15 (2016) 263–271.
- [24] M. Upasani, *J. Adv. Ceram.* 5 (2016) 344–355.
- [25] Y.-C. Li, Y.-H. Chang, Y.-F. Lin, Y.-S. Chang, Y.-J. Lin, *J. Alloys Compd.* 439 (2007) 367–375.
- [26] C. Görller-Walrand, K. Binnemans, Chapter 167 *Spectral intensities of f-f*

- transitions, in: J.K.A. Gschneidner, E. LeRoy (Eds.), *Handb. Phys. Chem. Rare Earths*, Elsevier, 1998: pp. 101–264.
- [27] J.-C.G. Bünzli, S. V. Eliseeva, *Basics of Lanthanide Photophysics*, in: P. Hänninen, H. Härmä (Eds.), *Lanthan. Lumin.*, Springer, 2010: p. 1.45.
- [28] A. Jose, T. Krishnapriya, T.A. Jose, C. Joseph, N. V. Unnikrishnan, P.R. Biju, *Ceram. Int.* 47 (2021) 6790–6799.
- [29] M. Dejneka, E. Snitzer, R.E. Riman, *J. Lumin.* 65 (1995) 227–245.
- [30] F. Wang, X. Liu, *Rare-earth doped upconversion nanophosphors*, in: D.L. Andrews, R.H. Lipson, T. Nann (Eds.), *Compr. Nanosci. Nanotechnol.*, Elsevier Ltd., 2019: pp. 359–384.
- [31] A. Gulzar, J. Xu, P. Yang, F. He, L. Xu, *Nanoscale.* 9 (2017) 12248–12282.
- [32] P. Serna-Gallén, H. Beltrán-Mir, E. Cordoncillo, *Opt. Laser Technol.* 136 (2021).
- [33] G. Gao, A. Turshatov, I.A. Howard, D. Busko, R. Joseph, D. Hudry, B.S. Richards, *Adv. Sustain. Syst.* 1 (2017) 1600033.
- [34] X. Tian, C. Wang, J. Wen, S. Lian, C. Ji, Z. Huang, Z. Chen, H. Peng, S. Wang, J. Li, J. Hu, Y. Peng, *J. Lumin.* 214 (2019) 116528.
- [35] K.K. Markose, R. Anjana, A. Antony, M.K. Jayaraj, *J. Lumin.* 204 (2018) 448–456.
- [36] NIST (National Institute of Standards and Technology), JARVIS-DFT, (n.d.). <https://jarvis.nist.gov/jarvisdft/>.
- [37] G. Li, J. Lin, *Phosphors for Field Emission Display: Recent Advances in*

- Synthesis, Improvement, and Luminescence Properties, 2016.
- [38] X. Liu, C. Lin, J. Lin, White light emission from Eu³⁺ in CaIn₂O₄ host lattices, in: *Appl. Phys. Lett.*, 2007: p. 081904.
- [39] T. Yamase, T. Kobayashi, M. Sugeta, H. Naruke, *J. Phys. Chem. A*. 101 (1997) 5046–5053.
- [40] R.G. Geitenbeek, H.W. De Wijn, A. Meijerink, *Phys. Rev. Appl.* 10 (2018) 1.
- [41] P. Serna-Gallén, H. Beltrán-Mir, E. Cordoncillo, *J. Alloys Compd.* 883 (2021) 160847.
- [42] R. Nagaraj, P. Suthanthirakumar, R. Vijayakumar, K. Marimuthu, *Spectrochim. Acta - Part A Mol. Biomol. Spectrosc.* 185 (2017) 139–148.
- [43] R. Nagaraj, A. Raja, S. Ranjith, *J. Alloys Compd.* 827 (2020) 154289.
- [44] R. Jagannathan, S.P. Manoharan, R.P. Rao, R.L. Narayanan, N. Rajaram, *Bull. Electrochem.* 4 (1988) 597–600.
- [45] B. Rigg, Colour description/specification systems, in: J.H. Xin (Ed.), *Total Colour Manag. Text.*, Woodhead Publishing Limited, 2006: pp. 22–43.
- [46] M.R. Luo, *Encyclopedia of Science and Technology*, Springer, 2016.
- [47] K.R. Justin Thomas, GoCIE V2 software (2009), downloaded from <http://faculty.iitr.ac.in/~krjt8fcy/index.html>
- [48] P. Patil, CIE Coordinate Calculator, (2022). <https://www.mathworks.com/matlabcentral/fileexchange/29620-cie-coordinate-calculator>.
- [49] OriginLab Technical Support, Chromaticity Diagram, (2022). <https://www.originlab.com/fileExchange/details.aspx?fid=446>.

- [50] P. Babu, C.K. Jayasankar, *Phys. B Condens. Matter*. 279 (2000) 262–281.
- [51] K. Vuković, M. Medić, M. Sekulić, M.D. Dramićanin, *Adv. Condens. Matter Phys.* 2015 (2015) 1–7.
- [52] E. Marín, A. Calderón, *J. Phys. Chem. Lett.* 13 (2022) 8376–8379.
- [53] J. Mooney, P. Kambhampati, *J. Phys. Chem. Lett.* 4 (2013) 3316–3318.
- [54] I.E. Kolesnikov, A. V. Povolotskiy, D. V. Mamonova, E.Y. Kolesnikov, A. V. Kurochkin, E. Lähderanta, M.D. Mikhailov, *J. Rare Earths*. 36 (2018) 474–481.
- [55] A.M. Srivastava, M.G. Brik, W.W. Beers, W. Cohen, *Opt. Mater. (Amst)*. 114 (2021) 110931.
- [56] G. Phaomei, W.R. Singh, *J. Rare Earths*. 31 (2013) 347–355.
- [57] Z. Yuan, C. Shen, Y. Zhu, A. Bai, J. Wang, Y. Liu, Y. Lyu, *Ceram. Int.* 42 (2016) 1513–1520.
- [58] M.M. Lezhnina, T. Jüstel, H. Kätker, D.U. Wiechert, U.H. Kynast, *Adv. Funct. Mater.* 16 (2006) 935–942.
- [59] B.R. Judd, *Phys. Rev.* 127 (1962) 750–761.
- [60] G.S. Ofelt, *J. Chem. Phys.* 37 (1962) 511–520.
- [61] M.P. Hehlen, M.G. Brik, K.W. Krämer, *J. Lumin.* 136 (2013) 221–239.
- [62] G. Yao, C. Lin, Q. Meng, P. Stanley May, M.T. Berry, *J. Lumin.* 160 (2015) 276–281.
- [63] M.J. Weber, *Phys. Rev.* 157 (1967) 262–272.
- [64] W.T. Carnall, P.R. Fields, K. Rajnak, *J. Chem. Phys.* 49 (1968) 4424–4442.

- [65] C.K. Jørgensen, R. Reisfeld, *J. Less-Common Met.* 93 (1983) 107–112.
- [66] B.M. Walsh, Judd-Ofelt theory: principles and practices, in: B. Di Bartolo, O. Forte (Eds.), *Adv. Spectrosc. Lasers Sens.*, Springer, Dordrecht, 2006: pp. 403–433.
- [67] L. Smentek, Judd-Ofelt Theory–The Golden (and the Only One) Theoretical Tool of *f*-Electron Spectroscopy, in: M. Dolg (Ed.), *Comput. Methods Lanthan. Actin. Chem.*, Wiley, 2015: pp. 241–268.
- [68] A. Ćirić, S. Stojadinović, M.G. Brik, M.D. Dramićanin, *Chem. Phys.* 528 (2020) 110513.
- [69] D.K. Patel, B. Vishwanadh, V. Sudarsan, S.K. Kulshreshtha, *J. Am. Ceram. Soc.* 96 (2013) 3857–3861.
- [70] C. de Mello Donegá, S.A. Junior, G.F. de Sá, *J. Alloys Compd.* 250 (1997) 422–426.
- [71] P. Serna-Gallén, H. Beltrán-Mir, E. Cordoncillo, A.R. West, R. Balda, J. Fernández, *J. Mater. Chem. C* 7 (2019) 13976–13985.
- [72] M. İlhan, M.K. Ekmekçi, İ.Ç. Keskin, *RSC Adv.* 11 (2021) 10451–10462.
- [73] J.D.L. Dutra, T.D. Bispo, R.O. Freire, *J. Comput. Chem.* 35 (2014) 772–775.
- [74] A. Ćirić, S. Stojadinović, M. Sekulić, M.D. Dramićanin, *J. Lumin.* 205 (2019) 351–356.
- [75] J.J. Stewart, MOPAC2012, (2012). <http://openmopac.net/>.
- [76] F. Neese, The ORCA program system, *WIREs Computational Molecular Science*. 2 (2012) 73–78. <https://doi.org/10.1002/wcms.81>.

- [77] A. Ćirić, Ł. Marciniak, M.D. Dramićanin, *Sci. Rep.* 12 (2022) 1–10.
- [78] M.J. Bin Murshed Leon, S. Abedin, M.A. Kabir, *Sensors Int.* 2 (2021) 100061.
- [79] L. Cao, G. Peng, W. Liao, T. Yan, X. Long, N. Ye, *CrystEngComm.* 22 (2020) 1956–1961.
- [80] M. Zhao, Y. Sun, Y. Wu, D. Mei, S. Wen, T. Doert, *J. Alloys Compd.* 854 (2021) 0–10.
- [81] R.D. Shannon, R.X. Fischer, *Am. Mineral.* 101 (2016) 2288–2300.
- [82] R.D. Shannon, R.X. Fischer, *Phys. Rev. B - Condens. Matter Mater. Phys.* 73 (2006) 1–28.
- [83] R.C. Shannon, B. Lafuente, R.D. Shannon, R.T. Downs, R.X. Fischer, *Am. Mineral.* 102 (2017) 1906–1914.
- [84] M.N. Polyanskiy, Refractive index database, (n.d.).
<https://refractiveindex.info>.
- [85] P. Villars, K. Cenzual, eds., C-Y₂O₃ Crystal Structure: Datasheet from “PAULING FILE Multinaries Edition – 2012” in Springer Materials (https://materials.springer.com/isp/crystallographic/docs/sd_0305868).
- [86] P. Villars, K. Cenzual, eds., Y₃Al₅O₁₂ Crystal Structure: Datasheet from “PAULING FILE Multinaries Edition – 2012” in Springer Materials (https://materials.springer.com/isp/crystallographic/docs/sd_0309606).
- [87] P. Villars, K. Cenzual, eds., MgAl₂O₄ Crystal Structure: Datasheet from “PAULING FILE Multinaries Edition – 2012” in Springer Materials (https://materials.springer.com/isp/crystallographic/docs/sd_0310018).

- [88] P. Villars, K. Cenzual, eds., LaF₃ Crystal Structure: Datasheet from “PAULING FILE Multinaries Edition – 2012” in Springer Materials (https://materials.springer.com/isp/crystallographic/docs/sd_0379018).
- [89] J.G. Li, X. Wang, K. Watanabe, T. Ishigaki, *J. Phys. Chem. B.* 110 (2006) 1121–1127.
- [90] Ž. Antić, R.M. Krsmanović, M.G. Nikolić, M. Marinović-Cincović, M. Mitrić, S. Polizzi, M.D. Dramićanin, *Mater. Chem. Phys.* 135 (2012) 1064–1069.
- [91] D. Avram, A.A. Patrascu, M.C. Istrate, B. Cojocar, C. Tiseanu, *J. Alloys Compd.* 851 (2021) 156849.
- [92] R.D. Shannon, *Acta Crystallogr.* A32 (1976) 751–767.
- [93] Y.Q. Jia, *J. Solid State Chem.* 95 (1991) 184–187.
- [94] C. Cascales, R. Balda, S. García-Revilla, L. Lezama, M. Barredo-Zuriarrain, J. Fernández, *Opt. Express.* 26 (2018) 16155.
- [95] H. Lösch, A. Hirsch, J. Holthausen, L. Peters, B. Xiao, S. Neumeier, M. Schmidt, N. Huittinen, *Front. Chem.* 7 (2019) 1–16.
- [96] V.P. Tuyen, T. Hayakawa, M. Nogami, J.R. Duclre, P. Thomas, *J. Solid State Chem.* 183 (2010) 2714–2719.
- [97] R. Balda, J. Fernández, J. Adam, *Phys. Rev. B - Condens. Matter Mater. Phys.* 54 (1996) 12076–12086.

Chapter 10

Conclusions

The main conclusions of the research conducted in this Doctoral Thesis are integrated into their respective chapters. Some general conclusions concerning the most interesting results are briefly presented hereafter.

- Different solid-state hosts based on yttrium complex fluorides have been synthesized, with particular emphasis on the KY_3F_{10} compound. Other host lattices under study include YF_3 and $Y(OH)_{3-x}F_x$. In that sense, each chapter incorporates new and improved synthetic methodologies that allow for proper modulation of the macroscopic and microscopic properties of these materials, ultimately influencing the luminescent characteristics the Eu^{3+} -doped powders.
- The KF - YF_3 system is very sensitive to the experimental conditions of the synthesis. It is worthwhile noting the huge impact of the pH in the reaction medium (outlined in **Chapters 4–6**), the fluoride source (KBF_4 or KF/HF) that allows to systematically obtain different compounds (deep details provided in **Chapters 5–7**), and the reaction time and temperature (described in **Chapter 8**).
- The different crystal structures of KY_3F_{10} (α - KY_3F_{10} and δ - $KY_3F_{10}\cdot xH_2O$) have been compared in terms of structural stability (**Chapters 6,7**), luminescence efficiency (**Chapter 7**), and phase transitions (**Chapters 6,8**).
- For the first time since it was discovered more than twenty years ago, the uncharted δ - $KY_3F_{10}\cdot xH_2O$ compound has been studied, providing alternative and improved synthesis (**Chapters 5,7**). The δ -phase has shown an outstanding optical response since the site-selective emission of the Eu^{3+} -doped δ -phase is up to 20 times more intense than that of the α -phase for the same dopant concentration (**Chapter 7**).
- The mechanisms that underlie the optical response of the compounds have been analyzed and unraveled for all the series of samples presented in each chapter.

From a photophysical point of view, the energy transfers and related phenomena have been studied particularly in **Chapters 3,4** (cross-relaxation between neighboring Eu^{3+} ions), and **Chapter 7** (presence of electron-phonon processes).

Appendix 1

Co-authors' consent

Rolindes Balda de la Cruz, as a co-author, hereby **authorize** Pablo Serna Gallén to include the publications listed below in his Doctoral Thesis.

List of publications:

- A site-selective fluorescence spectroscopy study of the crystal phases of KY₃F₁₀: leveraging the optical response of Eu³⁺ ions

In addition, I **waive the right** to use those articles as part of any other Doctoral Thesis.

In witness thereof, I hereby sign this document



Bilbao, 06 June 2023

In accordance with article 28 of the Regulations on doctoral studies of the Universitat Jaume I in Castelló, regulated by RD 99/2011, at the Universitat Jaume I (Approved by the Governing Council at its meeting no. 8/2020 held on 2 October 2020): "(...) 4. *In the case of joint publications, all the co-authors must explicitly state their approval that the doctoral student presented the work as part of her/his thesis and the express waiver of presenting this same work as part of another doctoral thesis. This authorization must be attached as documentation when the evaluation of the thesis begins.*"

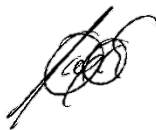
Joaquín Manuel Fernández Rodríguez, as a co-author, hereby **authorize** Pablo Serna Gallén to include the publications listed below in his Doctoral Thesis.

List of publications:

- A site-selective fluorescence spectroscopy study of the crystal phases of KY₃F₁₀: leveraging the optical response of Eu³⁺ ions

In addition, I **waive the right** to use those articles as part of any other Doctoral Thesis.

In witness thereof, I hereby sign this document



Bilbao, 06 June 2023

In accordance with article 28 of the Regulations on doctoral studies of the Universitat Jaume I in Castelló, regulated by RD 99/2011, at the Universitat Jaume I (Approved by the Governing Council at its meeting no. 8/2020 held on 2 October 2020): "(...) 4. *In the case of joint publications, all the co-authors must explicitly state their approval that the doctoral student presented the work as part of her/his thesis and the express waiver of presenting this same work as part of another doctoral thesis. This authorization must be attached as documentation when the evaluation of the thesis begins.*"

Eloísa Cordoncillo Cordoncillo, as a co-author, hereby **authorize** Pablo Serna Gallén to include the publications listed below in his Doctoral Thesis.

List of publications:

- Tuning the optical and photoluminescence properties of high efficient Eu^{3+} -doped KY_3F_{10} phosphors by different synthetic approaches
- Unraveling the superior role of dicarboxylic acids as surface chelators in Eu^{3+} -doped yttrium fluorides: A systematic modulation of the crystal phases and morphologies for highly tuned optical performance
- The unexplored δ -phase of KY_3F_{10} : Toward novel Eu^{3+} -doped nanoplates with a 'super-diamond' structure for optical applications
- The pH-dependent reactions in the sonochemical synthesis of luminescent fluorides: the quest for the formation of KY_3F_{10} crystal phases
- A site-selective fluorescence spectroscopy study of the crystal phases of KY_3F_{10} : leveraging the optical response of Eu^{3+} ions
- Practical guidance for easily interpreting the emission and physicochemical parameters of Eu^{3+} in solid-state hosts
- Kinetics or thermodynamics? Extolling their role to modulate the crystal phases and luminescence of $\text{KY}_3\text{F}_{10}:\text{Eu}^{3+}$ powders

In addition, I **waive the right** to use those articles as part of any other Doctoral Thesis.

In witness thereof, I hereby sign this document



Castelló de la Plana, 29 September 2023

In accordance with article 28 of the Regulations on doctoral studies of the Universitat Jaume I in Castelló, regulated by RD 99/2011, at the Universitat Jaume I (Approved by the Governing Council at its meeting no. 8/2020 held on 2 October 2020): "(...) 4. In the case of joint publications, all the co-authors must explicitly state their approval that the doctoral student presented the work as part of her/his thesis and the express waiver of presenting this same work as part of another doctoral thesis. This authorization must be attached as documentation when the evaluation of the thesis begins."

Héctor Beltrán Mir, as a co-author, hereby **authorize** Pablo Serna Gallén to include the publications listed below in his Doctoral Thesis.

List of publications:

- Tuning the optical and photoluminescence properties of high efficient Eu^{3+} -doped KY_3F_{10} phosphors by different synthetic approaches
- Unraveling the superior role of dicarboxylic acids as surface chelators in Eu^{3+} -doped yttrium fluorides: A systematic modulation of the crystal phases and morphologies for highly tuned optical performance
- The unexplored δ -phase of KY_3F_{10} : Toward novel Eu^{3+} -doped nanoplates with a 'super-diamond' structure for optical applications
- The pH-dependent reactions in the sonochemical synthesis of luminescent fluorides: the quest for the formation of KY_3F_{10} crystal phases
- A site-selective fluorescence spectroscopy study of the crystal phases of KY_3F_{10} : leveraging the optical response of Eu^{3+} ions
- Practical guidance for easily interpreting the emission and physicochemical parameters of Eu^{3+} in solid-state hosts
- Kinetics or thermodynamics? Extolling their role to modulate the crystal phases and luminescence of $\text{KY}_3\text{F}_{10}:\text{Eu}^{3+}$ powders

In addition, I **waive the right** to use those articles as part of any other Doctoral Thesis.

In witness thereof, I hereby sign this document



Castelló de la Plana, 29 September 2023

In accordance with article 28 of the Regulations on doctoral studies of the Universitat Jaume I in Castelló, regulated by RD 99/2011, at the Universitat Jaume I (Approved by the Governing Council at its meeting no. 8/2020 held on 2 October 2020): "(...) 4. In the case of joint publications, all the co-authors must explicitly state their approval that the doctoral student presented the work as part of her/his thesis and the express waiver of presenting this same work as part of another doctoral thesis. This authorization must be attached as documentation when the evaluation of the thesis begins."

Appendix 2

Lanthanide photophysics

The Hamiltonian plays a crucial role in describing the electronic structure and properties of lanthanides. It takes into account various factors such as the interactions between the electrons, the CF effects, and the spin-orbit coupling. The Hamiltonian enables the calculation of energy levels, magnetic properties, and spectroscopic transitions in lanthanides, providing valuable insights into their behavior and facilitating the understanding of their unique characteristics. In order to calculate the energy levels, the Schrödinger equation for a given system must be solved:

$$\mathcal{H}\Psi_n = E_n \Psi_n \quad (\text{A.1})$$

where \mathcal{H} is the Hamiltonian operator, the eigenfunctions Ψ_n are the wavefunctions describing different n electron states, and E_n are the energy eigenvalues associated to each state.

The effective Hamiltonian of an ion embedded in a host lattice can be expressed as the sum of two contributions:

$$\mathcal{H} = \mathcal{H}_{\text{FI}} + \mathcal{H}_{\text{CF}} \quad (\text{A.2})$$

The initial one represents the effective Hamiltonian of a free ion (FI), while the subsequent one refers to the crystal field (CF) Hamiltonian, which encompasses the interactions between the lanthanide ion and the surrounding host material.

The \mathcal{H}_{FI} for a $4f^N$ configuration of lanthanides can be written as follows [1]:

$$\begin{aligned} \mathcal{H}_{\text{FI}} = E_{\text{avg}} + \sum_k F^k f_k + \zeta_f A_{\text{so}} + \alpha L(L + 1) + \beta G(G_2) \\ + \gamma G(R_7) + \sum_i T^i t_i + \sum_h M^h m_h + \sum_k P^k p_k \end{aligned} \quad (\text{A.3})$$

E_{avg} considers the kinetic energy of the electrons and their interaction with the nucleus. The Coulomb interaction between the $4f$ electrons is parametrized by the radial electrostatic integrals F^k ($k = 2, 4, 6$), and the respective angular parts of the electrostatic repulsion is given by f_k . \mathcal{H}_{FI} also includes the spin-orbit coupling constant ζ_f , being A_{so} the angular part.

Higher-order terms are included to consider multiple-body Coulomb contributions. The parameters associated with two-electron interactions are represented by α , β , and γ ; which multiply the term $L(L + 1)$, being L the total orbital angular momentum, and the Casimir operators $G(G_2)$ and $G(R_7)$, respectively [2]. The three-electron Coulomb interactions are also expressed by T^i parameters ($i = 2, 3, 4, 6, 7, 8$) multiplying the t_i operators. Four-body and higher-order terms could be defined but they are unnecessary to a good representation of the experimental data. Magnetic effects are also parametrized by M^h ($h = 0, 2, 4$) and P^k with the corresponding operators given by m_h , and p_k .

On the other hand, according to Wybourne [3], the crystal field Hamiltonian can be expressed by

$$\mathcal{H}_{\text{CF}} = \sum_{k,q,i} B_q^{(k)} C_q^{(k)}(i) \quad (\text{A.4})$$

where $B_q^{(k)}$ are the CF parameters and $C_q^{(k)}$ are the Racah spherical tensor operators [4] which are defined as

$$C_q^{(k)} = Y_{q,k} \left(\frac{4\pi}{2k+1} \right)^{1/2} \quad (\text{A.5})$$

where $Y_{q,k}$ are the spherical harmonic functions.

Additionally, the scalar crystal field strength N_v , defined by Auzel and Malta [5], is

a valuable measure for comparing crystal field parameters across various symmetries of host sites:

$$N_v = \left[\sum_{k,q} (B_q^k)^2 \left(\frac{4\pi}{2k+1} \right) \right]^{1/2} \quad (\text{A.6})$$

References of Appendix 2

- [1] W.T. Carnall, G.L. Goodman, K. Rajnak, R.S. Rana, *J. Chem. Phys.* 90 (1989) 3443–3457.
- [2] K. Rajnak, B.G. Wybourne, *Phys. Rev.* 132 (1963) 280–290.
- [3] B.G. Wybourne, *Spectroscopic properties of rare earths*, Wiley-Interscience, New York, 1965.
- [4] G. Racah, *Phys. Rev.* 62 (1942) 438–462.
- [5] F. Auzel, O.L. Mata, *J. Phys.* 44 (1983) 201–206.
- [6] O. Laporte, W.F. Meggers, *J. Opt. Soc. Am. Rev. Sci. Instruments.* 11 (1925) 459–463.

Appendix 3

Honour Science & Chemistry event

As part of the 50th anniversary of the European Chemical Industry Council (Cefic), I had the great privilege of attending a special event held in Brussels on May 30, 2022: the *Honour Science & Chemistry* event. Cefic wished to bring together leading scientists and chemists from all over Europe, and together with the young generation, pave the way to a bright future of chemistry. 34 of Europe's top chemistry professors, including two Nobel Prize laureates, and 21 Ph.D. outstanding students from all across the EU gathered that day at the Brussels Metropole Hotel to recreate the iconic picture made in 1911 and 1927 during the Solvay International Conferences.

I had the great honor to be selected as the Spanish student representative by Cefic with the support of Feique (Federación Empresarial de la Industria Química Española), and I must admit that this experience will be truly unforgettable.

25 CEOs and Chief Technology Officers (CTOs) of Europe's leading chemical manufacturers also joined us to reinforce the alliance between science and business to ensure scientific progress and innovation find their way to the market and contribute to the EU's Green Deal agenda.

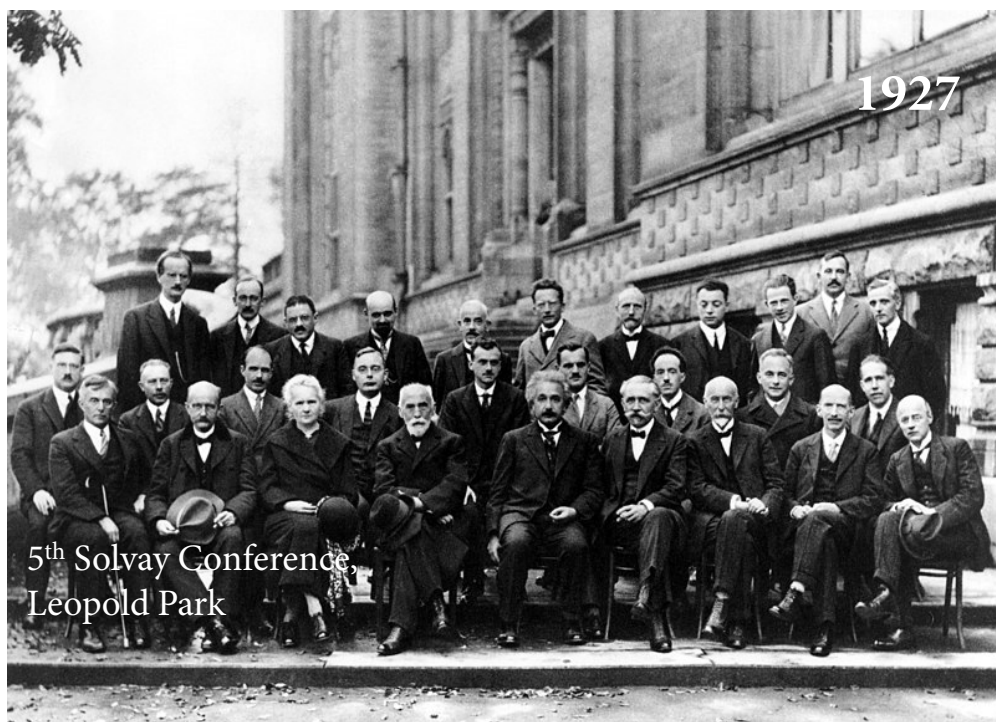
As the European institution stated, more than ever, chemistry is necessary to tackle some of the biggest challenges in our lifetime, such as fighting climate change, saving natural resources, or improving the well-being of a growing and aging population. Only cooperation between all societal stakeholders will make it possible to develop the best ideas to jointly address these challenges.

The occasion was able to go beyond remaking the famous Solvay conference pictures (presented below) and we participated in interactive discussions with professors, CEOs, and Cefic's members to address questions about the future of chemistry, how to help to achieve the Green Deal commitments and make a more sustainable world.



1st Solvay Conference,
Hotel Metropole





Moreover, we also had the opportunity to join different working groups for an assignment related to the Green Deal Call. In that sense, the development of such a cooperative and multidisciplinary project in the following months with other Ph.D. students from Europe (that today have become truly friends) supervised by Cefic's managers was a fruitful tool for being embarked firsthand in European politics about the new chemical demands.

We also had the opportunity to present the outcome of our assignment at the Cefic premises to the members of the Innovation Department and to our coaches on October 30, 2022. But that was not all. On the same day, I had the huge privilege of participating in the special Academic Session of the Solvay Conference of 2022. That session was organized as part of the 100th Anniversary of the First Solvay Conference on Chemistry (which took place in 1922), and I was chosen to participate in the panel "Future and social responsibility of chemistry: the view of the young generation" organized by the International Solvay Institutes. Certainly, it was an unforgettable experience in which I had the warmth of my European colleagues.

Images and information provided by Cefic at: <https://cefic.org/media-corner/newsroom/renowned-chemistry-professors-and-young-european-scientists-recreate-the-iconic-photo-featuring-curie-and-einstein/>

